NEODYMIUM OXIDE THIN FILM GATE OXIDE ON SILICON SUBSTRATE

HETHERIN A/P KARUPPIAH

FACULTY OF ENGINEERING
UNIVERSITY OF MALAYA
KUALA LUMPUR

2018

NEODYMIUM OXIDE THIN FILM GATE OXIDE ON SILICON SUBSTRATE

HETHERIN A/P KARUPPIAH

THESIS SUBMITTED IN FULFILMENT OF THE REQUIREMENTS FOR THE DEGREE OF DOCTOR OF PHILOSOPHY

FACULTY OF ENGINEERING
UNIVERSITY OF MALAYA
KUALA LUMPUR

2018

UNIVERSITI MALAYA

ORIGINAL LITERARY WORK DECLARATION

Name of Candidate: HETHERIN KARUPPIAH

Registration/Matric No:**KHA140071**

Name of Degree:**DOCTOR OF PHILISOPHY**

Title of Project Paper/Research Report/Dissertation/Thesis ("this Work"):
NEODYMIUM OXIDE THIN FILM GATE OXIDE ON SILICON SUBSTRATE
Field of Study:
ENGINEERING MATERIALS

I do solemnly and sincerely declare that:

(1) I am the sole author/writer of this Work;
(2) This Work is original;
(3) Any use of any work in which copyright exists was done by way of fair dealing and for permitted purposes and any excerpt or extract from, or reference to or reproduction of any copyright work has been disclosed expressly and sufficiently and the title of the Work and its authorship have been acknowledged in this Work;
(4) I do not have any actual knowledge nor do I ought reasonably to know that the making of this work constitutes an infringement of any copyright work;
(5) I hereby assign all and every rights in the copyright to this Work to the University of Malaya ("UM"), who henceforth shall be owner of the copyright in this Work and that any reproduction or use in any form or by any means whatsoever is prohibited without the written consent of UM having been first had and obtained;
(6) I am fully aware that if in the course of making this Work I have infringed any copyright whether intentionally or otherwise, I may be subject to legal action or any other action as may be determined by UM.

Candidate's Signature Date

Subscribed and solemnly declared before,

Witness's Signature Date

Name:
Designation:

NEODYMIUM OXIDE THIN FILM GATE OXIDE ON SILICON SUBSTRATE

ABSTRACT

Metallic neodymium (Nd) films were sputtered on silicon substrates. The films then underwent thermal oxidation andthermal oxynitridation at various durations of 5 min, 10 min, 15 min, and 20 min. The optimized time was utilized to carry out thermal oxidation and thermal oxynitridation at various temperatures of 500°C, 700°C, 900°C, and 1100°C.Thermal oxidation in oxygen (O_2) ambient produced neodymium oxide (Nd_2O_3) and thermal oxynitridation in nitrous oxide (N_2O) ambient producednitrogen-incorporated neodymium oxide ($Nd_xO_yN_z$). Both thermal oxidation and thermal oxynitridationproducedfilms with compositions of cubic neodymium oxide (c-Nd_2O_3), orthorhombic neodymium silicate (o-$Nd_2Si_2O_7$), monoclinic (m)-, tetragonal (t)-, and hexagonal (h)-silicon dioxide (SiO_2). These compositions and phases were identified through X-ray diffraction (XRD). The existence of semicrystalline interface layer was further supported by Fourier transform infrared (FTIR) analysis, Raman analysis, energy dispersive X-ray (EDX) spectroscopy analysis, and X-ray photoelectron spectroscopy (XPS) analysis. As for thermal oxynitridation, nitrogen (N) element was detected through XPS analysis. A physical model describing theformation of Nd_2O_3 and $Nd_xO_yN_z$ together withsemicrystalline interface layer is proposed and explained. In the study of the effects of thermal oxidationdurationat a fixed temperature of 700°C, 15-min sampleproducedthebest electrical properties through the measurement and analysis of current-voltage (I-V) and capacitance-voltage (C-V) characteristics. This sample also demonstrated single interfacial layer with inclusion of $Nd_2Si_2O_7$ and SiO_2.Scratch test is conducted in order to characterize the mechanical adhesion strength of the samples, in which, this testrevealed that the samples have scratch resistance up to 700N. By using the optimized thermal oxidation time of 15 min to study the effects of temperature, it was found that 900°C sample produced thebest I-V and C-V characteristics. The optimized thermal oxidation parameter,that is900°C for 15 min, yieldedthebest electrical properties withthehighestelectrical breakdown field of 5.26 MV/cm at thelowestleakage value of 2.02 x 10^{-6} A/cm^2, thehighest barrier height ($Ø_B$) of2.91eV, thelowest effective oxide charge (Q_{eff}) of 4.03 x 10^{24} cm^{-2}, and thelowest average interface trap density (D_{it}) of ~ 10^{31} eV^{-1} cm^{-2}with effective dielectric constant value of 7.03. Similar trend was observed for the formation of $Nd_xO_yN_z$, whereby the optimized thermal oxynitridation parameters of 900°C for 15 min,exhibited the best electrical properties of with highest electrical breakdown fieldof 5.27 MV/cm, thelowest leakage current of 9.96 x 10^{-6} A/cm^2, thehighest $Ø_B$of 2.94eV, thelowest Q_{eff} of 6.59 x 10^{24} cm^{-2}, and thelowest D_{it} of ~ 10^{30} eV^{-1} cm^{-2} with effective dielectric constant value of 8.42.By comparing both Nd_2O_3 and $Nd_xO_yN_z$, nitrogen content in the films has improved the electrical properties. Based on this study, it is highly possible for Nd_2O_3 and $Nd_xO_yN_z$to be applied as high dielectric constant gate oxide material in advanced metal-oxide-semiconductor (MOS)-based technology.

Keyword: neodymium oxide, nitrogen-incorporated neodymium oxide, sputtering, thermal oxidation, thermal oxynitridation

NEODYMIUM OKSIDA SEBAGAI FILEM NIPIS GET OKSIDA PADA SUSBSTRAT SILIKON

ABSTRAK

Filem nipis neodymin (Nd) telah dipercitkan pada substrat silikon. Filem nipis tersebut telah menjalani pengoksidaan terma dan pengoksinitridaan terma. Kesan masa pengoksidaan dan pengoksinitridaan (5 min, 10 min, 15 min, dan 20 min) telah dijalankan. Tempoh masa yang optimum telah digunakan untuk menjalankan eksperimen kesan suhu pengoksidaaan terma dan pengdioksinitridakan terma (500°C, 700°C, 900°C, dan 1100°C). Pengoksidaan terma dalam ambien gas oksigen (O_2) telah menghasilkan neodymium oksida (Nd_2O_3), manakala pengoksinitridaan terma dalam ambien gas nitrous oksida (N_2O) telah menghasilkan neodymium oksida yang diterapkan nitrogen ($Nd_xO_yN_z$). Kedua-dua pengoksidakan terma dan pengoksinitridaan terma menghasilkan filem dengan komposisi dan fasa berikut, iaitu neodymium oksida (c-Nd_2O_3) berfasa kubik, neodymium silikat (o-$Nd_2Si_2O_7$)berfasa ortorombik, silikon dioksida (SiO_2) berfasa monoklinik (m), tetragonal (t), dan heksagonal (h). Kesemua komposisi dan fasa telah dikenalpasti melalui teknik pembelauansinar-X (XRD). Kewujudan antara muka lapisan yang bersifat separuh hablur telah dikenalpasti melalui analisis menggunakan inframerahjelmaan Fourier (FTIR), spektroskopi Raman, spektroskopi komposisi tenaga serakan sinar-X (EDX), dan spektroskopi fotoelektron sinar-X (XPS). Unsur nitrogen (N) bagi pengoksinitridaan terma, telah dikesan melalui analisis XPS. Satu model mekanisme fizikal berkaitan dengan penghasilan Nd_2O_3 dan $Nd_xO_yN_z$ serta lapisan antara muka yang separuh hablur telah dicadangkan dan dijelaskan. Dalam kajian kesan masa bagi pengoksidakan terma pada suhu tetap 700°C, tempoh pengoksidaan 15 min menghasilkan sifat elektrik terbaik melalui pengukuran dan analisis arus-voltan (I-V) dan kapasitan-voltan (C-V). Ini disebabkan sampel tersebut mempunyai satu lapisan antara muka yang mengandungi komposisi $Nd_2Si_2O_7$ dan SiO_2. Ujian calar telah dijalankan keatas sampel bagi mengkaji sifat kekuatan melekat secara mekanikal dimana ia mempunyai rintangan calar sehingga 700N. Dengan menggunakan tempoh pengoksidaan terma yang optimum, iaitu 15 min untuk mengkaji kesan suhu yang berbeza, suhu pengoksidaan 900°C menghasilkan sifat elektrik terbaik bagi pengukuran dan analisis I-V dan C-V. Bagi parameter optimum untuk pengoksidakan terma, iaitu 900°C selama 15 min, menghasilkan sifat elekrik terbaik dengan medan pecah tebat yang tertinggi pada 5.26 MV/cm dimana, kebocoran ketumpatan arus terendah ialah 2.02×10^{-6} A/cm^2, ketinggian sawar yang tertinggi($Ø_B$) iaitu 2.91eV, caj oksida (Q_{eff}) yang terendah pada 4.03×10^{24} cm^{-2}, Ketumpatan perangkap antara muka oksida-semikondukor (D_{it}) yang terendah pada ~ 10^{31} eV^{-1} cm^{-2} dengan pemalar dielektrik setinggi 7.03. Trend yang sama telah diperhatikan bagi pembentukkan $Nd_xO_yN_z$ dimana, parameter optimum bagi pengoksinitridaan terma adalah 900°C selama 15 min. Sampel tersebut mempunyai medan pecah tebat yang tertinggi pada 5.27 MV/cm, kebocoran ketumpatan arusterendah pada 9.96×10^{-6} A/cm^2, $Ø_B$ yang tertinggi pada 2.94eV, Q_{eff} yang terendah pada 6.59×10^{24} cm^{-2}, D_{it} yang terendah iaitu ~ 10^{30} eV^{-1} cm^{-2} dengan pemalar dielektrik setinggi 8.42. Dengan membandingkan kedua-dua Nd_2O_3 dan $Nd_xO_yN_z$, penerapan nitrogen kedalam filem telah menambahbaikkan sifatelekrik. Berdasarkan kajian ini, Nd_2O_3 dan $Nd_xO_yN_z$ mempunyai potensi yang tinggi untuk diaplikasikan sebagai get oksida pemalar dielektrik tinggi dalamteknologi berasaskan logam-oksida-semikonduktor (MOS).

Kata Kunci: neodymium oksida, neodymium oksida yang diterapkan nitrogen, pemercitan, pengoksidaaan terma, pengoksinitridaan terma

ACKNOWLEDGEMENT

First and foremost, I would like to thank God for his blessings and strength that He provided to complete my research work on time. Next, I would like to thank my supervisor **Ir. Dr. Wong Yew Hoong** and co-supervisor **Prof. Ir. Dr. Ramesh Singh** for their guidance throughout my candidature in terms of their support, suggestions, patience, and valuable insights sharing.

Special thanks to **Dr.Bushroa binti Abdul Razak** for her guidance in conducting mechanical testing of thin film. I also would like to thank **Mrs. Hartini binti Bharum** for her assistance in sample preparation. Great thanks to all academic and administrative staffs of Faculty of Engineering for their assistances. Besides that, I would like to thank technicians and engineers from **Malaysian Institute of Microelectronic System (MIMOS)** for their assistance in physical characterization service.

In addition, I also would like thank fellow colleagues for the physical and mental support throughout my candidature period. I also would like thank by father **Mr. Karuppiah** and mother **Mrs. Sisilamari,** include rest of my family members for their supports and encouragements includes my friends **Miss. Mahaletchumy, Miss. Aaina Aqilah, Miss.Pushpapriya, Dr. Shamini and Dr. Anithambigai.**

Last but not least, I would like to thank MyBrain scholarship (Kementerian Pendidikan Malaysia), University of Malaya Research Grant (UMRG), and Postgraduate Research Grant (PPP) for their financial support.

With thanks and love,
Hetherin Karuppiah

TABLE OF CONTENTS

LIST OF FIGURES

LIST OF TABLES

LIST OF SYMBOLS AND ABBREVIATIONS

CMOS	Complementary metal oxide semiconductor
k	Dielectric constant
Si	Silicon
SiO_2	Silicon dioxide SiO_2
D_{it}	Interface trap defect density
ZrO_2	Zirconium dioxide
HfO_2	Hafnium dioxide
Al_2O_3	Aluminium oxide
PDA	Post-deposition annealing
REO	Rare earth oxide
EOT	Equivalent oxide thickness
Nd_2O_3	Neodymium oxide
EBE	Electron beam evaporation
MBE	Molecular beam evaporation
MOCVD	Metalorganic chemical vapour deposition
ALD	Atomic layer deposition
CSD	Chemical solution deposition

O_2 : Oxygen

N_2O : Nitrous oxide

Nd : Neodymium

RF : Radio frequency

XRD : X-ray diffraction

FTIR : Fourier transformed infrared

HRTEM : High-Resolution Transmission Electron Microscopy

XPS : X-ray photoelectron spectroscopy

SCS : Semiconductor characterization system

MOS : Metal oxide semiconductor

SB : Soft breakdown

HB : Hard breakdown

F-N : Fowler-Nordheim

ITRS : International Technology Roadmap for Semiconductors

Al : Aluminum

OTFT : Organic thin film transistor

Pr_2O_3 : Praseodymium oxide

Sm_2O_3 : Samarium oxide

Gd_2O_3 : Gadolinium oxide

Dy_2O_3	:	Dysprosium oxide
N_2	:	Nitrogen
UHV	:	Ultra high vacuum
C	:	Carbon
Eu_2O	:	Europium oxide
RTA	:	Rapid thermal annealing
EIS	:	Electrochemical impedance spectroscopy
LPCVD	:	Low pressure chemical vapor deposition
P	:	Phosphorous
$NdTiO_3$	:	Neodymium titanium oxide
HF	:	Hydrofluoric acid
DI	:	Deionized
Ar	:	Argon
$(Nd(tmhd)_3)$	:	2,2,6,6-tetramethyl-3,5-heptanedionium, Nd preseodymium oxide
La_2O_3	:	Lanthanum oxide
MOSFET	:	Metal oxide semiconductor field effect transistor
Ln_2O_3	:	Lanthanide oxide
Ho_2O_3	:	Holmium oxide
Er_2O_3	:	Erbium oxide

Tm_2O : Thulium oxide

$NdAlO_3$: Neodymium aluminate

$((CH_3)_3Al)$: Trimethyl aluminum

NH_3 : Ammonia

I-V : Current-voltage

C-V : Capacitance-voltage

J : Current density

$Nd_xSi_yO_z$: Neodymium silicate

ZnO : Zinc oxide

H_2O_2 : Hydrogen peroxide

HCl : Hydrochloric acid

NH_4OH : Ammonia hydroxide

RCA : Radio Corporation of America

W-H : Williamson-Hall

J-E : Leakage current density versus electrical breakdown field

ΔV_{FB} : Flatband voltage

Q_{eff} : Effective oxide charge

STD : Slow trap density

c : Cubic

ICSD : Inorganic Crystal Structure Database

m : Monoclinic

h : Hexagonal

t : Tetragonal

o : Orthogonal

L_c : Critical load

L_{e-p} : Elastic-plastic deformation

TZDB : Time-zero dielectric breakdown

EBD : Dielectric breakdown field

ZrON : Zirconium oxynitride

HfON : Hafnium oxynitride

$Nd_xO_yN_{Z:}$: Nitrogen-incorporated neodymium oxide

SiON : Silicon oxynitride

$Nd_aSi_bO_cN_d$: Nitrogen-incorporated neodymium silicate

Sm_xO_yN : Samarium oxynitride

CHAPTER 1: INTRODUCTION

1.1 Background

The semiconductor industries have today evolved into an established industry with the advancements of semiconductor materials. These advancements have led to the development of a wide range of electronic and optoelectronics devices (Yacobi, 2003). They can be categorized into various categories such as semiconductor substrates, gate oxides, methods producing gate oxide, gate oxide thickness variation and others. The most active advancement is the miniature version of the devices which is not only cost-efficient, but is also 25 times faster than the devices produced 40 years ago and reduces power consumption (Rathee, Kumar, & Arya, 2010; Sze, 2001).

Generally, the development of complementary metal oxide semiconductor (CMOS) is classified into four main categories which are, i) multigate structures, ii) channel strain, iii) high dielectric constant (*k*) materials, and iv) metal gates. Multigate structure refers to technology incorporation of more than one gate into a single device to suppress leakage current. Meanwhile, channel strain refers to induced crystalline distortion which will enhance carrier mobility. Lastly, high-*k* material and metal gates are technologies to replace polysilicon gates. This development will lead to lower OFF leakage and increasing ON current(Shima & Ryuzaki, 2007). This is also the most vital development in order to proceed with miniature devices.

At present time, Silicon (Si) is the dominant semiconductor in the industry (Kano, 1998). Replacing it with other available semiconductor material is also another key development in CMOS technology . This is attributed by Si limitation theoretically, due to higher voltage and current handling included increased packaging density (Ambriz-Vargas et al., 2017; Chow & Tyagi, 1993).

1.2 Problem Statement

Downscaling of devices leads to higher power consumption due to higher gate leakage current as the thickness approaches few atomic layers or nanometers. As the insulating layer of silicon dioxide (SiO_2) gets thinner, tunneling current density increases(Tseng, 2010). For example, when the oxide's thickness is 2.0 nm, direct tunneling current of the oxide bias at 1 V is almost 10^{-2} A/cm^2 and with every decrease in 0.2 nm, the direct tunneling current increases by approximately one order of magnitude(Gerald Lucovsky, 2005). As the Si channel interface reaches two monolayers, oxygen atoms do not own the full arrangement of oxygen neighbours; thus, it affects the full band gap which results in undesired leakage(Wilk, Wallace, & Anthony, 2001). These negative impacts lead to the need to find replacement for SiO_2(Gopalan, Dutta, Ramesh, & Prathapan, 2017).

A high-*k* thin film is a potential material to replace SiO_2 since it is able to provide similar capacitance as physically larger capacitance (Chiu, Lee, & Pan, 2009). Additionally, the selection of material is also influenced by other criteria such as permittivity, band gap of ≥ 5 eV to ensure hot carrier injection below specified level for gate current dielectric reliability property and band alignment to Si, stability in terms of thermodynamic when in contact with Si, high quality interface with Si, low interface trap defect density (D_{it}) to reduce degradation of mobile carrier, low flat band voltage (V_{FB}) for better reliability, process compatibility, and compatible with current and expected material for CMOS (Chin, Cheong, & Hassan, 2010; A. Dakhel, 2004a; Houssa et al., 2006; Osten, Bugiel, Kirfel, Czernohorsky, & Fissel, 2005).

Various materials which meet those requirements were investigated to serve as alternative material to SiO_2. Among them are zirconium dioxide (ZrO_2), hafnium dioxide (HfO_2), tantalum pentoxide , titanium dioxide, aluminium oxide (Al_2O_3), cerium (IV) oxide, yttrium (III) oxide and more(Osten et al., 2005). Among those materials, HfO_2 and ZrO_2 are widely accepted materials to replace SiO_2 due to their high *k*-value, chemical stability, thermodynamically stable on Si and large bandgap (Han, Kang, Lin, & Han, 2003; Jin et al., 2017; Wong & Cheong, 2010). However, the electrical property degradation with post-deposition annealing (PDA) is a drawback for these materials. Upon high temperature annealing such as at 900˚C or 1000˚C, voids are formed in the oxide layer, which leads to decomposition process. Subsequently, silicide layer which are zirconium disilicide and hafnium silicide are formed (Zeman, Fulton, Lucovsky, Nemanich, & Yang, 2006). These interfacial layers tend to degrade the electrical properties.

Currently, researchers are focusing on rare earth oxide (REO) due to its excellent characteristics including a large bandgap (4-6 eV), high resistivity (10^{12}-10^{15}Ωcm), high crystallization temperature, high relative permittivity (7-20), thermodynamic stability when in contact with Si substrate at high temperature (above 800 ˚C) under high vacuum or nitrogenous ambient and most importantly high-*k* value (7-20) (A. Dakhel, 2004a, 2004c; Wilk et al., 2001; Zaumseil & Schroeder, 2005). These are among the important properties for REO to survive as gate oxide, since it provides chemical stability, inhibits formation of interfacial layer, low leakage of electron across dielectric pad at higher equivalent oxide thickness (EOT) and processing suitability. Additionally, a large bandgap produces deeper trapping levels for electron injected form substrate. Hence, reduces back tunneling probability (Pan & Yu, 2009).

In addition to the replacement of SiO_2 with REO, incorporation of nitrogen into these oxides has also gained researchers' attention. Nitrogen has been proven to improve the stability against crystallization and suppressing dopant diffusion(Watanabe et al., 2005). In addition, it also provides higher diffusion resistance of oxygen towards Si substrate(Sano & Ohmi, 2011). This could prevent the formation of undesirable interfacial layer. Nitrogen incorporation into HfO_2 reduces boron penetration from polysilicon gate, increases stability of the high-*k* film and improves overall electrical properties (Aibin & Qiuxia, 2009; Gavartin, Shluger, Foster, & Bersuker, 2005).

Neodymium oxide (Nd_2O_3) is one of the REOs that is notable as gate dielectric. It has high *k*-value (10-15), large bandgap (5.8 eV), good lattice matching with Si, thermodynamically stable when in contact with Si, good insulating properties and appropriate conduction band offset with Si, which makes it suitable for microelectronic application (Fan, Liu, & Zhang, 2014a). Additionally, it also poses low interface trap density and small hysteresis (Pan et al., 2009). Due to its excellent properties, $Nd_2O_3$was also investigated for its membrane sensing application of and high density dynamic random access memory (C.H. Kao, Chan, Chen, Chung, & Luo, 2010; Pan et al., 2009).

In addition to physical and electrical properties, mechanical property of a thin film also plays a role in the application of the investigated thin film as a replacement of SiO_2. The lattice mismatch leads to stress and dislocations which will affect the optical and structural properties of the film (D Geetha, Sophia, Radhika, & Arivuoli, 2017). Besides, contact loading during processing or packaging will affect the performance of the device (Yau, Tseng, & Lian, 2011). The mechanical property also influences the wear resistance, thermal cycling and process-induced stress(Fu, Chang, Chang, Yao, & Liao, 2013).

Up to date, Nd_2O_3 has been investigated through various methods such as thermal evaporation, electron beam evaporation (EBE), molecular beam evaporation (MBE), sputtering, metalorganic chemical vapour deposition (MOCVD), atomic layer deposition (ALD) and chemical solution deposition (CSD). In this work, Nd_2O_3 was formed by thermal oxidation and thermal oxynitridation upon sputtered Nd thin film on Si substrate. The effect of thermal oxidation and thermal oxynitridation temperature and durations on the structural, chemical and electrical properties were further determined.

1.3 Research Objectives

The main objective of this research is to form Nd_2O_3 and Nitrogen-incorporated Nd_2O_3 on Si substrate by thermal oxidation in oxygen (O_2) ambient and thermal oxynitridation in nitrous oxide (N_2O) ambient upon sputtered Neodymium (Nd) thin film. With this main objective, the following aspects were examined:

1. To investigate the effects of thermal oxidation in O_2 ambient at different oxidation temperatures and durations on the physical and electrical properties of the oxidized sputtered pure Nd metal thin film on Si substrate.

2. To investigate the effects of thermal oxynitridation in N_2O ambient at different oxynitridation temperatures and durations on the physical and electrical properties of the oxidized sputtered pure Nd metal thin films on Si substrate.

3. To compare the physical, chemical and electrical properties of oxidized and oxynitrided sputtered pure Nd metal thin films on Si substrate.

4. To determine the wear resistant property of Nd_2O_3, which is formed by thermal oxidation in O_2 ambient at different oxidation durations.

5. To develop possible mechanism model of oxidation and oxynitridation to explain the formation of oxidized and oxynitrided sputtered metal thin films on Si substrate.

1.4 Scope of Studies

The research involved the deposition of Nd thin film upon Si substrate through radio frequency (RF) sputtering. Later, the Nd_2O_3 was formed by thermal oxidation and thermal oxynitridation. Initially, formation was carried out by varying durations at fixed temperature. Once the optimized duration was determined, the formation was carried out by varying temperatures at fixed duration.

Structural and chemical properties were determined using X-ray diffraction (XRD) analysis, Fourier transformed infrared (FTIR) spectroscopy, Raman analysis, High-Resolution Transmission Electron Microscopy (HRTEM) and X-ray photoelectron spectroscopy (XPS) measurements. Meanwhile, the electrical properties were determined by semiconductor characterization system (SCS). The mechanical property of the film was determined using Ltd micro scratch tester.

1.5 Structure of the Thesis

The thesis consists of five chapters. In Chapter I, brief introduction of this research is provided. Meanwhile, Chapter II provides literature review pertaining to REO and Nd_2O_3, followed by Chapter III, where design of the experiment, implementation, tools and process flow were discussed. Chapter IV focuses on discussions of the test results including the comparison with some of previous research works. Finally, Chapter V concludes the research with some future recommendations and problems encountered.

CHAPTER 2: LITERATURE REVIEW

2.1 Metal Oxide Semiconductor

Metal oxide semiconductor (MOS) consists of metal such as aluminum or high-conductivity polycrystalline silicon deposited upon oxide. The general structure of MOS is as shown in Figure 2.1. The insulator layer separates both metal and semiconductor substrate. Negative charges exist on top plate where, positive charge at bottom of the plate. This will lead to induction of electric field between them (Neamen, 2003). Generally, oxide is a class of material comprising of full spectrum of optical, electronic and magnetic behaviors such as ferroelectric, pyroelectric, insulating, semiconducting, metallic, superconducting, multiferroic and nonlinear optical effects(Schlom, Chen, Pan, Schmehl, & Zurbuchen, 2008) . Thus, it will act as an excellent insulating layer.

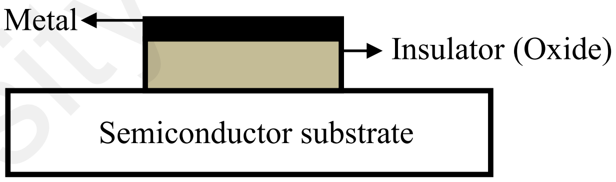

Figure 2.1: Basic MOS structure (Neamen, 2003)

SiO_2 is the dominant oxide for MOS technology (Schlom et al., 2008). Even though a variety of techniques are available to produce oxide, thermal oxidation is the most common method (May & Spanos, 2006). Thermal oxidation was carried out by heating Si wafer vertically into quartz boat in quartz tube, where it passed through a resistant heated furnace in oxygen ambient at about 1000°C (Kano, 1998). Oxygen ambient was produced through dry oxygen or wet oxygen as shown in Equations 2.1 and 2.2 (May & Spanos, 2006). EventhoughSi is an average semiconductor, SiO_2 is excellent insulator and easy formation method to ensure the survival of Si(Kumar, 2012).

$$Si + O_2 \rightarrow SiO_2 \tag{2.1}$$

$$Si + 2H_2O \rightarrow 2SiO_2 + \ 2H_2 \tag{2.2}$$

2.1.1 Silicon Dioxide Breakdown

Generally, the oxide wasbroken down due to previous degradation which were defects that arisen from stress. Some of them were interface states, hole traps, neutral electron traps and slow states. These breakdowns are classified into soft breakdown (SB) and hard breakdown (HB). Both of these breakdowns are results of the same kind of defect-relatedconduction path(Dumin, 2002). Several models have been proposed to explain the breakdown.

Initial modal was time-dependant dielectric breakdown (Klein, 1966, 1971; Osburn & Ormond, 1974; Shatzkes, Av-Ron, & Anderson, 1974). The modal stated that driving force such as voltage or resulting tunneling electrons create defects in the oxide and it is accumulated by time. Upon reaching the critical density, it loses the dielectric properties (Suehle, 2002). The modal raises questions upon substrate hot electron injection experiments, the thickness and polarity breakdown dependence (Degraeve, Groeseneken, De Wolf, & Maes, 1995; DiMaria, 1999; Shi, Ma, Prasad, & Dhanda, 1998; Umeda, Tomita, & Taniguchi, 1997; Vogel et al., 2000; E. Y. Wu, Abadeer, Han, Lo, & Hueckel, 1999). These experiments suggest that life time decreases with the increase in direct tunneling current as a function of oxide thickness. Injection of holes developed by tunneling current is captured by Si-O bonding. In the capturing situation, bond breakage rate by a field driven mechanism is improved (Suehle, 2002).

Another modal to explain breakdown in thin SiO_2 film is Anode Hole Injection. The modal proposes that electron is injected to oxide by Fowler-Nordheim (F-N) tunneling, hole generation by impact ionization or other mechanism and hole-trapping in the oxide. Trapping of holes increases cathode field and leads to electron trap, followed by increase in tunneling current density, where it eventually leads to oxide breakdown (Yeo, Lu, & Hu, 2001). Additionally, Anode Hydrogen Release is also used to explain the breakdown of thin SiO_2 film. The release of atomic hydrogen from anode takes place by energetic tunneling electrons, which then leads to defect formation. Trap is created at Si/SiO interface due to the release of atom (DiMaria & Stasiak, 1989). Basically, both of these models use the principles of electron injection through oxide followed by energy loss at the interface. This principle releases some positively-charged species which is then injected into oxide and travels towards cathode where it produces defects by reaction with unspecified precursor (Strong et al., 2009).

2.2 Replacement of Silicon Dioxide

Thinner equivalent gate has high influence on channel, which subsequently will lead to better short channel performance (Yeo, King, & Hu, 2003). When the International Technology Roadmap for Semiconductors (ITRS) was projected, the channel length was 9 nm in 2016 (Zhao, Zhao, Werner, Taylor, & Chalker, 2012). Further predictions are as shown in Figure 2.2. In order to achieve high drive current, smaller equivalent oxide thickness (EOT) has to be achieved, as shown in Equation 2.3,

$$EOT = t_{ox}\,\frac{k_{SiO_2}}{k_{dielectric}} \qquad (2.3)$$

where, t_{ox} is physical thickness of the dielectric, k_{SiO_2} is k-value of SiO_2 which is 3.9 and $k_{dielectric}$ is k-value of dielectric(Vaz, Martin, & Fenker, 2013).

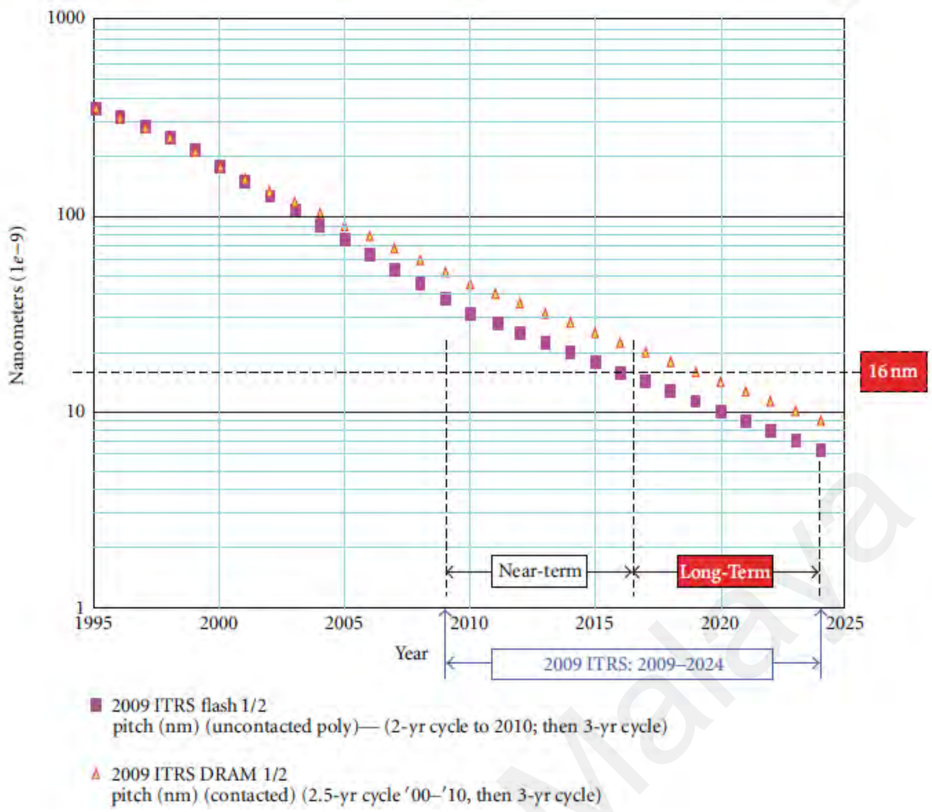

Figure 2.2: ITRS prediction (Zhao et al., 2012)

As the EOT value reaches 1 nm, leakage current, power consumption, reliability issues and difficulty in process capability increases(Vaz et al., 2013). Strain engineering (where strain is applied to Si channels) is an alternative method to control the transport properties of channel electron, but it is also limited to extremely scaled devices(B. H. Lee, Oh, Tseng, Jammy, & Huff, 2006). As the thickness of SiO_2 reduces, tunneling current increases exponentially. Thus, high-*k* material has been proposed as an alternative material to replace SiO_2. By doing so, the occurrence of leakage current can be minimized while maintaining low EOT(Gopalan et al., 2017; Oniki, Iwazaki, Hasumi, Ueno, & Kuroiwa, 2008; Osten et al., 2005; Wang et al., 2009). Several high-*k* oxides such as HfO_2, ZrO_2, Al_2O_3 and several REOs together with their silicates and aluminates were studied using various preparation methods(Jayanti, Yang, Lichtenwalner, & Misra, 2010a; Kosola, Päiväsaari, Putkonen, & Niinistö, 2005; B. H. Lee, Kang, Nieh, Qi, & Lee, 2000; Oniki et al., 2008). HfO_2 and ZrO_2caught the attention of researchers in this field and have been extensively studied due to their composition-tunable structure and ability to significantly improve electrical properties. Moreover, incorporation of SiO_2 onto these oxides, leads to stabilization of silicate layer and eliminates the formation of low *k* interfacial layer (Tahir et al., 2009).

2.3 Neodymium Oxide as Potential Replacement Silicon Dioxide

As mentioned earlier, methods employed to deposit Nd_2O_3 in semiconductor substrates are based on physical and chemical deposition methods. The earliest method employed for the investigation was thermal evaporation with the most recent one being ALD. The history of Nd_2O_3development based on methodology employed are as summarized in Figure 2.3. It can be seen that after almost two decades of thermal evaporation production researchers have been actively investigating Nd_2O_3 as a replacement for SiO_2.

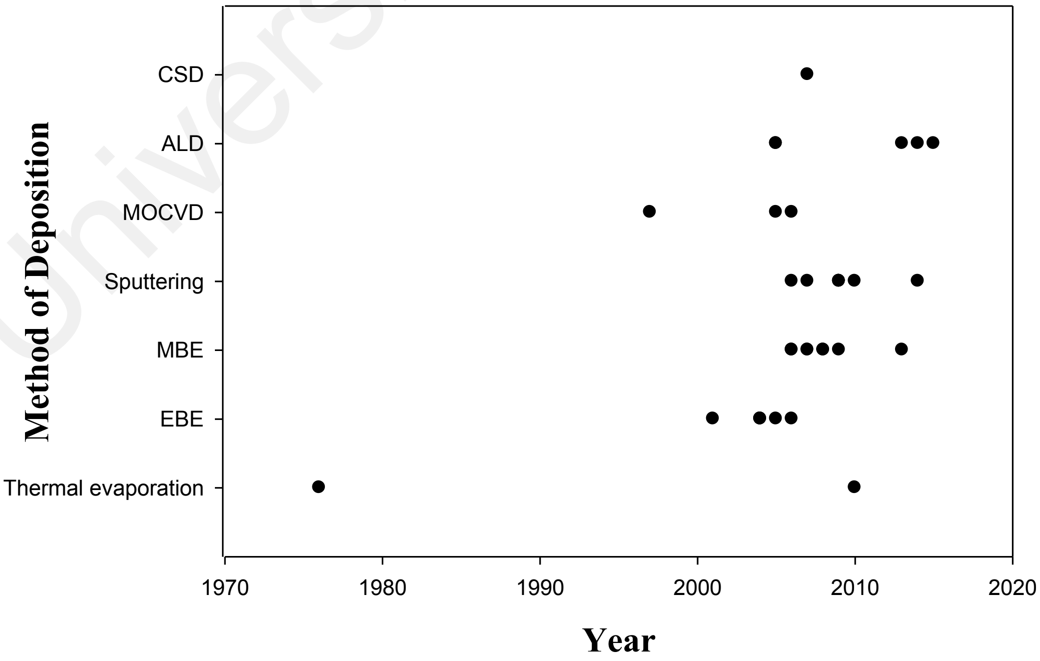

Figure 2.3: History of methodology employed to deposit Nd_2O_3

2.3.1 Thermal Evaporation

Thermal evaporation involves the concept of evaporating material from hot source and condenses it on a cold surface by which is known as deposition. The equipment setup is simpler since the main source energy for this method is thermal energy. The whole process takes place under high vacuum condition; thus, evaporated atoms and ion will not collide with each other upon leaving source until they reach the substrate. The kinetic energy is low (0.1 eV to 0.5 eV) since the substrate is not often biased. This method enables high deposition rate and large substrate size. However, at the same time, this method can only be employed to material that has low sublimation or evaporation temperature (Guo & Tan, 2009).

Fromhold et.al (1976) employed this method to deposit Nd_2O_3 and other rare earth oxides on microscopic glass. This is one of the earliest surveys on REO that studied their experimental properties. As discussed earlier, characterization of electrical properties requires pretreatment of the slide. Initially, the slide was heated to 600°C and silver tabs were fired onto it. This was then followed by soldering copper wire to the silver tabs. This process should be carried out before evaporation occurs to avoid heat damages to the substrate. Then, it was vibrated in deionized water and dried in hot air blast, which was approximately 100°C for 5 to 10 minutes (Fromhold Jr & Foster, 1976).

The oxides were evaporated form tungsten boats and the electrode was evaporated from tungsten filament. The ultimate pressure was at a range of 3×10^{-6} and 4×10^{-7} torr. Meanwhile, the evaporation pressure for electrode was at the range of 5×10^{-6} to 6×10^{-7} torr while the oxides were between 2×10^{-5} to 8×10^{-5} torr. However, prior to evaporation, filaments, boats, oxides and electrode materials out-gassed and substrate were shielded to avoid contamination during this process. The distance between evaporated source and substrate was 5 inches. Initially, strip of aluminum (Al) was evaporated to act as base electrode, followed by oxide evaporation on top of it. Later, counter electrodes were evaporated upon oxide, which were perpendicular to the oxide. The sequence is as shown in Figure 2.4. The evaporation temperature of REO varied from 2000°C to 2300°C, the temperature of substrate was 25°C during deposition of electrode and 50°C during deposition of oxide(Fromhold Jr & Foster, 1976).

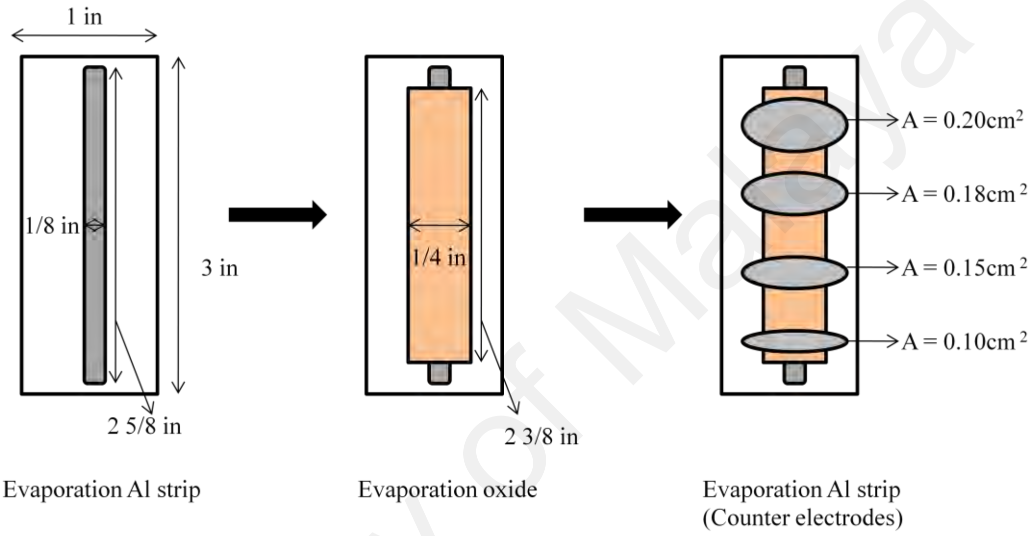

Figure 2.4: Evaporation sequence of rare earth oxide (Fromhold Jr & Foster, 1976)

Sarma et.al (2010) employed thermal evaporation method to develop organic thin film transistor (OTFT) in order to study its structural and electrical properties. The pentacene-based OTFT was fabricated in staggered electrode structures by series of vacuum evaporations using suitable mask as shown in Figure 2.5 (a). All of the depositions were carried out at room temperature (27°C) and higher vacuum than 5 x 10^{-6} torr. Initially, Al electrode with thickness of 1010 Å was deposited upon glass substrate and followed by Nd_2O_3 deposition with thickness of 650 Å. The oxide degassed in vacuum for a long period of time. Later, pentacene was deposited using two-step layer depositions. The first deposition (120 Å) was done at a deposition rate of 0.5 Å/s and the second (260 Å) was deposited at a rate of 0.1 Å/s. Finally, Au with thickness of 1430 Å was deposited as drain and source using shadow mask with channel length of 50 µm and width of 0.14 cm. The experimental arrangement to study electrical properties as shown in Figure 2.5 (b).

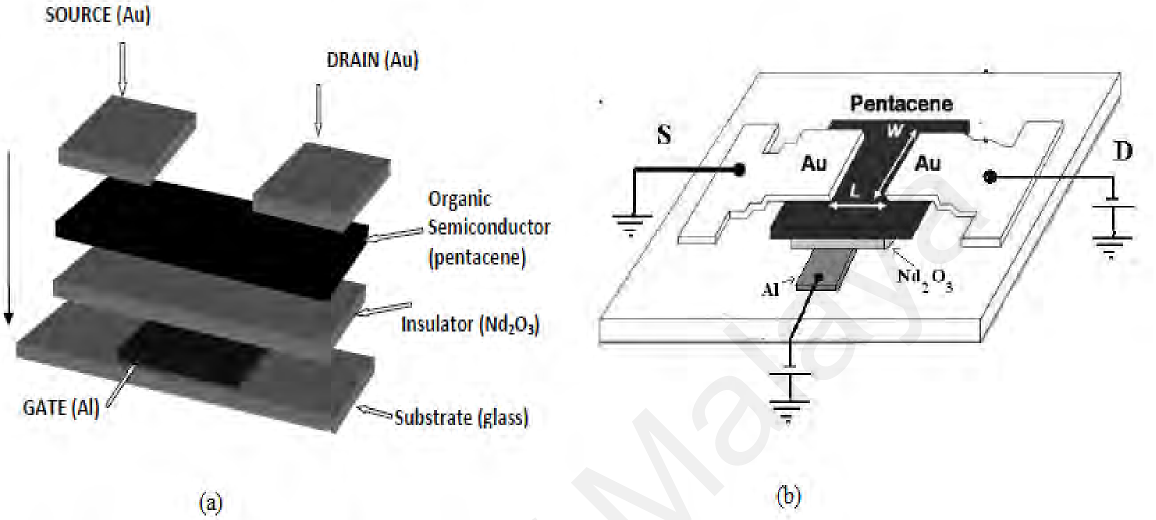

Figure 2.5 (a): Deposition order of OTFT (b): Electrical experimental arrangement (Sarma, Saikia, 2010).

2.3.2 Electron Beam Evaporation

This method involves the evaporation of target material by the bombardment of electron. Filament source is heated to high temperature to generate electron which will be accelerated at a field of 5-10 kV, whereby it will be channeled towards target by electric and magnetic fields. Upon reaching the target, the kinetic energy converts to thermal energy and the material on surface starts to evaporate. The evaporated material will be deposited on preheat substrate (Chin et al., 2010; J. George, 1992).

Jeon et al. (2001) used this method to compare electrical characteristics of several REOs deposited by EBE with praseodymium silicate deposited by sputtering. Praseodymium oxide (Pr_2O_3), Nd_2O_3, samarium oxide (Sm_2O_3), gadolinium oxide (Gd_2O_3), dysprosium oxide (Dy_2O_3) and praseodymium titanium oxide were deposited upon *p*-Si, but no defined parameter was given. This was followed by the deposition of platinum with a thickness of 150 nm. Later, gate area 9 x 10^6cm^{2}was deposited through photolithography and etching. Additionally, n$^+$ polysilicon was deposited upon REO at 560°C followed by active anneal at various temperatures in order to study polysilicon's compatibility with temperature(Jeon et al., 2001).

In another study, Dakhel et.al (2004) employed this method to studycrystalline and amorphous Nd_2O_3 in terms of their structural, optical and electrical propertiesthrough three different studies. Upon cleaning *p*-Si (100), it was degassed through heating in vacuum of 10^{-4} Pa ambient at 150°C for 3 hours followed by evaporation of Nd in O_2 ambient at pressure of 10^{-4} Pa. Different crystalline structures were imposed through annealing in air and vacuum at different temperatures and at the same time as shown in Table 2.1. Upon annealing, Al film with thickness of 150 nm was deposited at the front and back of Si (A. Dakhel, 2004b, 2004c; A. A. Dakhel, 2004).

Table 2.1: Annealing parameter

Annealing ambient	**Annealing temperature (°C)**	**Annealing duration (min)**	**Annealing pressure (Pa)**	**Reference**
Air	300	15	-	(A. Dakhel, 2004b, 2004c; A. A. Dakhel, 2004)
Air	800	15	-	
Vacuum	800	15	10^{-4}	
Air	800	15	-	(A. Dakhel, 2004b)

Meanwhile, Busani et. al (2006) used EBE to deposit Nd_2O_3 on *p*-Si (100) in order to study the structural effect on the properties of the film. The target material was Nd_2O_3 and evaporation was carried out in O_2 ambient at a pressure of 2.5 x 10^{-5} torr. Different structures were achieved through deposition at different temperatures, deposition rate and different annealing parameter. The deposition parameters are as shown in Table 2.2. Meanwhile, two types of annealing parameters were used. First, annealing at 600°C for 3 hours in O_2 ambient and the second is 800°C for 30 minutes in nitrogen (N_2) ambient. Lower temperature annealing was used in O_2 ambient to ensure re-oxidation and higher temperature in N_2 ambientis necessary to minimize oxidation Nd_2O_3 and Si interface (Busani, Devine, & Gonon, 2006). Bugiel et.al (2005) also used this similar method to produce Nd_2O_3 on Si(001) and Si(111) to study their interface and layer formation. Other than Nd_2O_3, they also deposited Pr_2O_3 and Gd_2O_3 on Si. However, no clear method was described except that they used granular REO (E. Bugiel, Osten, Fissel, Kirfel, & Czernohorsky, 2005).

Table 2.2: Deposition parameter of Nd_2O_3 (Busani et al., 2006)

Deposition temperature (°C)	**Deposition rate (Ås^{-1})**
Room temperature	2
280	2
280	0.4

2.3.3 Molecular Beam Evaporation

MBE is a method to produce epitaxial layers. It refers to layers with the same crystallographic orientation and crystal structure as substrate (Yacobi, 2006). This structure will have large dielectric constant, high thermodynamic stability and high band offset. At the same time, it also produces sharp interface between silicon and oxide without interfacial layer, which is a high quality single crystalline oxide (Kakushima et al., 2007). Additionally, this method can also be used to overcome polycrystalline problem whereby it will lead to high defect density and leakage (H. Kim, Marshall, McIntyre, & Saraswat, 2004; Sun et al., 2008a).

The growth of material is done under ultra-high vacuum condition on a heated crystalline substrate by the interaction of absorbed species supplied by atomic or molecular beam. The beam is accompanied with thermal energy. It is produced by evaporation or sublimation of suitable materials contained in ultra-pure crucibles (Franchi, 2013). Initially, a precise beam of heated molecules was fired on a substrate from effusion cells. The molecule lands surface on substrate. It will condense and build up very slowly, which then forms ultra-thin layers and subsequently produces one atomic layer at a time (Herman & Sitter, 2012).

Fissel et.al (2006), Bugiel et.al (2007) and Osten et.al (2007) employed MBE method to produce Nd_2O_3 on Si to study the interface and layer formation. There were no clear experimental details discussed by Bugiel et.al. but the experimental procedures employed by the other two researchers are similar except on Si orientation and growth orientation as shown in Table 2.3. The growth is done in multi-chamber ultra high vacuum (UHV) system which poses growth, annealing and analysis. Upon cleaning, the substrate was inserted into a vacuum system and followed by ex situ annealing. The purpose of this was to create an order and clean surface. Later, the evaporation of granular $Nd_2O_3$was carried out to deposit the film (Eberhard Bugiel, Fissel, Czernohorsky, Laha, & Osten, 2007; Fissel et al., 2006; Osten et al., 2007). Osten et.al's (2007) study also enable this current research to have a reference in understanding the effect of different Si orientations in oxide growth.

Table 2.3: Si orientation and growth temperature

Reference	(Fissel et al., 2006)	(Eberhard Bugiel et al., 2007)	(Osten et al., 2007)
Si Orientation	(001)	(001)	(001), (111)
Growth temperature	800 K	-	800 K – 1000 K

Besides that, Afanas'ev et.al (2008) employed the MBE method to produce three types of REO on two different Si orientations; 1) Nd_2O_3 and Gd_2O_3 on Si(100) and2) Gd_2O_3 and lutetium oxide on Si(111). The growth temperature was 650°C -750°C and low O_2 pressure which resulted in abrupt Si/REO interface. The objective of this study was to investigate the effect of 4*f*-shell occupancy as it will contribute to interface band offset (Afanas' ev et al., 2008).

Meanwhile, Sun et.al (2008) grew Nd_2O_3 on *p*-Si(111) by utilizing the MBE method to investigate electrical properties. Upon cleaning, the substrate was loaded into multi-chamber UHV system and it was passivated at 300°C for 7 minutes at lower power than the deposition. Granular Nd_2O_3 was evaporated and deposited on substrate at a temperature of 675°C. At the same time, MBE's growth was modified by additional molecular oxygen partial pressure of 5×10^{-7} mbar. Later, it was annealed in forming gas at 450°C for 10 minutes before Pt deposition. Pt metal electrode with area of 0.96×10^{-3} $cm^2$was evaporated by e-beam evaporation through a shadow mask(Sun et al., 2008a).

Wang et.al (2009) employed this method to study the mechanical properties in terms of structural and strain relaxation of Nd_2O_3 on Si(111). After being loaded into multi-chamber UHV MBE system upon cleaning, substrate was heated up to 706°C to create an ordered surface, followed by evaporation of granular Nd_2O_3 and deposition on Si at a temperature of 670°C. Additional oxygen was then supplied into the chamber at partial a pressure of 6.3×10^{-7} mbar. Finally, the grown Nd_2O_3 was protected by amorphous Si cap layer, which was deposited in situ (Jinxing et al., 2009).

Lastly, Laha et.al (2013) used MBE method to study the effect of carbon (C) incorporation onto Si(111) and Si(001)'s prior deposition of REO in their electrical properties. The incorporation of C will improve the interface quality, which will then affect the electrical properties. The growth is carried out in multi-chamber UHV MBE system. The C passivation was carried at a temperature in between 500°C to 600°C on a reconstructed (well orderly surface) Si. The growth of Nd_2O_3 and Gd_2O_3 was carried out at a temperature of 650°C at O_2 partial pressure of 5 x 10^{-7} mbar. Finally, Pt metal electrode was evaporated through a shadow mask at different chamber, without leaving the vacuum ambient(Laha, Fissel, & Osten, 2013).

2.3.4 Sputtering

Sputtering is a widely used method for the deposition of thin film(Depla, Mahieu, & De Gryse, 2008). It has been a widely employed method in the last 10 decades and it involves the concept that is similar to EBE. However, instead of using accelerated electron, sputtering utilizes energetic ions. Bombardment of these ions on the surface of a target material will result in a backward scattering of target atom due to collision (Depla et al., 2008). Initially, negative charge is applied to target material, which will lead to plasma discharge. Thus, the positively charged gas ions are attracted to the negatively charged target and the two will collide at high speed. Particles of the target will be ejected out as a result of the momentum and then deposited upon the substrate(Chin et al., 2010; Depla et al., 2008).

Pan et.al (2006, 2007, 2009) employed sputtering method to study structural and electrical properties including the pH characteristic of Nd_2O_3, Pr_2O_3 and europium oxide (Eu_2O_3). The parameters involved in these researches are as summarized in Table 2.4. As the study involved structural and electrical characterization, titanium nitride film of 500 Å was deposited, followed by photolithography and wet etching to produce gate area of 3.14 x 10^{-4} cm^2. Later, 4000 Å of Al was deposited for back contact (Pan, Lee, Shu, & Chen, 2006b; Pan, Lee, & Yeh, 2007). Meanwhile, to compare the structural and electrical properties of Nd_2O_3, Pr_2O_3 and Eu_2O_3, the experimental method was modified since the study was carried out using high-*k,* metal oxide high-*k* silicon - type memory structure. Prior to the deposition of the oxide, tunnelling oxide with a thickness of 2 nm was grown by rapid thermal annealing (RTA). This improved the interface quality. Upon deposition, the samples were again annealed. After annealing, a ~20 nm-thick blocking oxide layer was deposited by a plasma-etched chemical vapour deposition. Prior to Al deposition, it was densified at 900°C for 30 s in N_2 ambient to reduce the number of defects. Finally, Al gate was deposited(Pan & Yu, 2009).

Table 2.4: Parameters of sputtering by Pan et.al

Reference	**(Pan et al., 2006b)**	**(Pan et al., 2007)**	**(Pan et al., 2009)**	**(Pan & Yu, 2009)**	**(Pan et al., 2009)**
Substrate	*p*-Si (100)	*p*-Si (100)	*p*-Si (100)	*p*-Si (100)	*p*-Si (100)
Oxide film	Nd_2O_3	Nd_2O_3	Nd_2O_3	Nd_2O_3, Pr_2O_3, Eu_2O_3	Nd_2O_3
Thickness (nm)	6.5	7-8	18-20	12	18-20
Target	Nd	Nd	Nd	Pr, Nd, Er	Nd
Power (W)	175	100	-	-	100
Base pressure (Torr)	10^{-6}	10^{-6}	-	-	10^{-6}
Sputtering ambient	$Ar:O_2$ 12.5:12.5	$Ar:O_2$ 20:15, 15:10, 12.5:12.5	$Ar:N_2$ 20:15 15:10 10:15.	$Ar:O_2$ 5:2	$Ar:N_2$ 20:15 15:10 10:15.
RTA ambient	N_2	N_2	O_2	O_2	O_2
RTA temperature (°C)	600, 700, 800	600, 700, 800	600, 700, 800	700, 800, 900	600, 700, 800
RTA duration (s)	30	30	30	30	30
Purpose	Structural and electrical	Structural and electrical	Structural and pH	Structural and electrical	Structural and pH

Meanwhile, electrochemical impedance spectroscopy (EIS) capacitor structure as shown in Figure 2.6 was fabricated to study the structural and pH properties. After annealing, 400 nm of Al was deposited at the backside of the substrate using thermal coater. Later, sensing membrane size was defined through photolithographic processing under photosensitive epoxy which behaves as anti-acid polymer. This was then followed by the fabrication of EIS device on Cu lines of printed circuit board by using Argentum gel to form conductive lines. Finally, handmade epoxy package was used to encapsulate the device and Cu line (Pan et al., 2009).

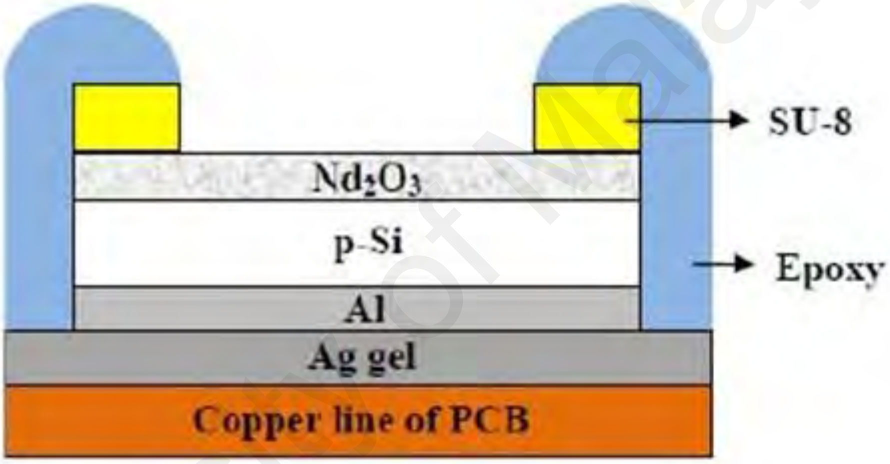

Figure 2.6: EIS capacitor structure (Pan et al., 2009)

Kao et.al (2010) developed polyoxide structure as shown in Figure 2.7 using sputtering method to study the structural and electrical properties. Initially, *p*-Si thermally oxidized to form oxide layer with thickness of 550 nm. This was then followed by deposition of polysilicon film with a thickness of 300 nm at 625°C by low pressure chemical vapor deposition (LPCVD). Later, the implantation of phosphorous (P) was carried out at a dosage of 5 x 10^{-15} cm^{-2} and 30 keV energy. Then, the activation in N_2 ambient at 950°C for 30 s was done to obtain a sheet resistance of 70 - 80 Ω/sq. Afterwards, Nd_2O_3 with a thickness of 25 nm was deposited by sputtering system and followed by annealing in N_2 for 30 s at varying temperatures of 600°C, 700°C, 800°C, 900°C and 950°C. Al gate with a thickness of 300 nm was deposited on the oxide film. Finally, self aligned defining Al gate and gate dielectric pattern formed polyoxide capacitors by a two step wet etching process (C.H. Kao et al., 2010).

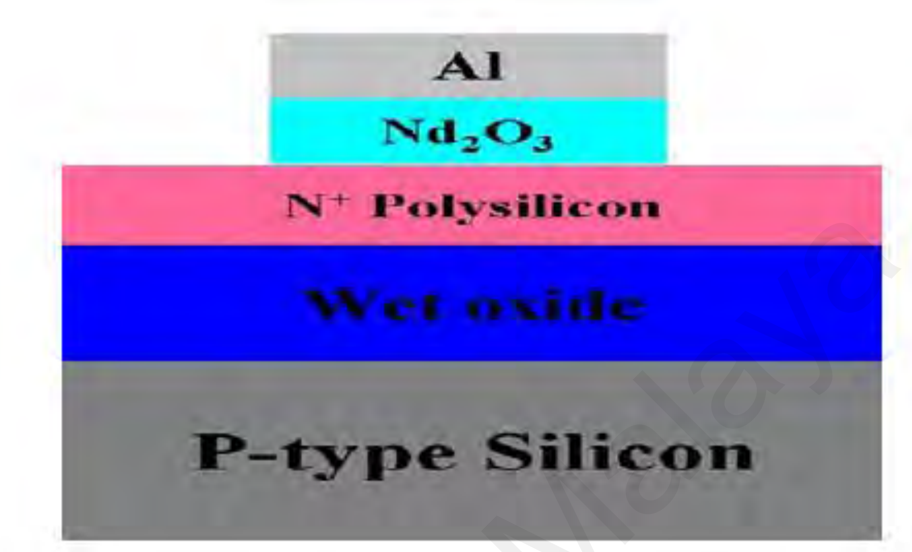

Figure 2.7: High-*k* Nd_2O_3 polyoxide structure (C.H. Kao et al., 2010)

In another study, Kao et.al (2014) compared physical and electrical characteristics of polyoxide with Nd_2O_3 and neodymium titanium oxide ($NdTiO_3$). The experimental procedure was slightly modified compared to previous studies. Initially, oxide with 600 nm thickness was grown on *p*-Si by thermal oxidation at 650°C. Then, polysilicon with thickness of 300 nm was deposited at 625°C by LPCVD. It was then followed by annealing in N_2 ambient. Nd_2O_3 film was sputtered at two different thicknesses which are 27 nm and 18 nm. Later, Ti with thickness of 9 nm was sputtered upon 18 nm Nd_2O_3 to form $NdTiO_3$. All the sputtering was carried out at Ar:O_2 (12.5:12.5) ambient with operating pressure at 1.5 x 10^{-4} Pa and power of 150 W. Then, the samples were annealed for 30 s at various temperatures (600°C, 700°C, 800°C and 900°C) and at different ambients; Nd_2O_3 polyoxide (in N_2 ambient) and $NdTiO_3$ polyoxide (in O_2 ambient). 3000 Å was deposited using thermal evaporation. The capacitor area was defined by wet etching and hydrofluoric acid (HF) whereby deionized (DI) water (1:10) was used to etch away Nd_2O_3 and $NdTiO_3$(C. H. Kao et al., 2014).

2.3.5 Metalorganic Chemical Vapour Deposition

MOCVD is specialized CVD. Metal organic refers to compound whereby the atom of an element is bonded with one or more carbon atoms of organic hydrocarbon group. Most of these elements are non-transitional(Pierson, 1999). This process involves the deposition of thin solid oxide film on a heated substrate by using a vapor-phase mixture of metal containing precursors and an oxidant. The reactor is operated at an intermediate pressure, usually in the range of 1 – 200 mbar. This is to ensure that the process takes place at both gas phase and on, or close to, the substrates(Jones et al., 2004). Most of MOCVD takes place at a temperature in the range of 300°C - 800°C. The temperature window between precursor evaporation and decomposition should be controlled so that the process will take place without degrading the device. For many electronics application, it is always around 500°C and below(Jones et al., 2004). At the same time, the process requires high purity reactant and the most accurate control to fulfill the requirement of a highly critical semiconductor application(Pierson, 1999). Precursor should also have appropriate physical and decomposition characteristics. For example, adequate volatility is needed in order to have efficient vapor phase transport which will lead to high purity films.

MOCVD process has several advantages which lead to the production of high quality film. Some of its contributions are notable in terms of providing a large area growth as well as presents a highly uniformed film, good composition and doping control and excellent conformal step coverage on non-planar device geometries(Jones et al., 2004). At the same time, it is a also flexible technique since it allows controllable growth of highly conformal films on planar and high-aspect ratio (Jones et al., 2005). However, the one downside of this application is that it is limited due to high production cost. Thus, it is applicable when a high quality film is needed (Pierson, 1999). Additionally, the growth of Nd_2O_3 through MOCVD is also limited due to the lack of suitable precursors with suitable decomposition characteristics, volatility and decomposition characteristics (Jones et al., 2004).

Another study by Tasaki et.al (1997) employed this method to investigate precursor of 2,2,6,6-tetramethyl-3,5-octanedionato (TMOD). The TMOD complexes of yttrium and neodymium (Nd) were developed and later deposited upon magnesium oxide. Hot-wall-type MOCVD was used in this study where substrate was heated by an electric furnace. Vessel was used to hold the precursor and argon (Ar) at a flow rate of 100 cm^3/min was utilized to transport the precursor's vapor. The temperature of the gas line between the vessel of the precursor and reactor was kept at 10°C higher than the vessel. O_2 gas was introduced into quartz reactor. Meanwhile, the source temperature was in the range of 120°C - 150°C for Y-based TMOD and 130°C - 160°C for Nd-based TMOD. This is because the melting point of Nd-based TMOD is higher than the other. The substrate temperature was 800°C (Tasaki, Satoh, Yoshizawa, Kataoka, & Hidaka, 1997).

On the other hand, Song et.al (2005) utilizes direct liquid injection-MOCVD to investigate the properties of 2,2,6,6-tetramethyl-3,5-heptanedionium, Nd ($Nd(tmhd)_3$) as precursor. Tetrahydrofuran was used as solvent for 0.05 mol/l $Nd(tmhd)_3$ and deposited upon *p*-Si(100). A precise amount of precursor was introduced through syringe pump at a speed of 0.1 ml/min into flash evaporator at vaporizer temperature of 220°C and pressure of 5 torr. Meanwhile, the reactor pressure was set at 1.2 torr, O_2 was flowed at a rate of 350 sccm and carrier gas Ar was flowed at a rate of 150 sccm. The deposition was carried out at a temperature range of 400°C - 625°C. Finally, the samples were annealed in O_2 ambient at a temperature of 600°C, 800°C and 1000°C for 1 hour (Song & Rhee, 2005b).

Frohlich et.al (2006) used MOCVD to compare structural and electrical properties of Nd_2O_3, Gd_2O_3, preseodymium oxide (Pr_6O_{11}) and lanthanum oxide (La_2O_3). Gd_2O_3 and La_2O_3 were deposited by thermal evaporation of MOCVD, meanwhile, Nd_2O_3 and Pr_6O_{11} were deposited by pulsed injection MOCVD (Frohlich et al., 2006). Precursor based on $(tmhd)_3$ was utilized in this study. The growth method of Gd_2O_3 and La_2O_3 was similar. The growth took place at a reactor temperature of 500°C and pressure of 133 Pa. The reaction gas was O_2 and flowed at a rate of 100 sccm and the carrier gas Ar flowed at a rate of 15 sccm. The growth rate was 40 nm/hour(Lupták et al., 2005; Pisecny et al., 2004). There were no clear trace of experimental procedures concerning Nd_2O_3 and Pr_6O_{11}.

2.3.6 Atomic Layer Deposition

ALD is a variation of CVD. In MOCVD, the precursor forms the first monolayer and the second reactant introduced in chamber will produce the second layer. Meanwhile, ALD is a two-step process whereby one reactant will form self-limiting monolayer on the surface. Self-limiting refers to a process which involves one complete layer of reactant bond to the surface where bonding of any other molecules to the reactant will be prohibited. Later, a second reactant will be introduced and converted the earlier layer to desired solid materials (Kääriäinen, Cameron, Kääriäinen, & Sherman, 2013). The process details are as shown in Figure 2.8. The international ITRS included ALD in high-*k* gate oxide in metal oxide semiconductor field effect transistor (MOSFET) and for copper diffusion barriers in backend interconnect. This leads to the rise of studies involving ALD in semiconductor application (S. M. George, 2009).

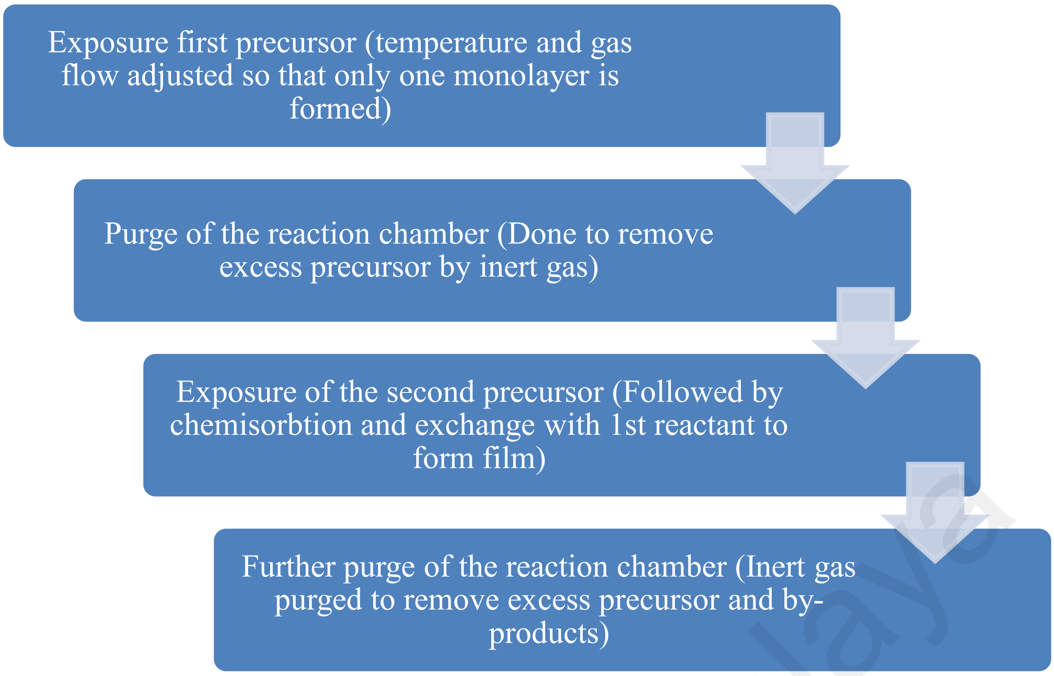

Figure 2.8: Process flow of ALD (Chin et al., 2010; S. M. George, 2009)

Päiväsaari et.al (2005) employed ALD method to compare the structural and chemical properties of lanthanide oxide (Ln_2O_3) thin films. The investigated oxides wereNd_2O_3, Sm_2O_3, Eu_2O_3, Gd_2O_3, Dy_2O_3, holmium oxide (Ho_2O_3), erbium oxide (Er_2O_3) and thulium oxide (Tm_2O_3). These oxides were deposited upon *n*-Si (100). One of the major differences in this experimental is that the native oxide of substrate was not removed before deposition. Volatile β-diketone type chelates $Ln(thd)_3$ and ozone were the precursors. N_2 was used as carrier and purge gas. The pulse length was 1.25 s and 2.5 s for $Ln(thd)_3$ and O_3. Other parameters are as shown in Table 2.5 and it can clearly be seen that the deposition temperature of $Nd_2O_3$is higher compared to the others since the temperature produces film with the best quality (Päiväsaari, Putkonen, & Niinistö, 2005).

Table 2.5: ALD deposition parameters (Päiväsaari et al., 2005)

Material	**Evaporation temperature (°C)**	**Deposition temperature (°C)**	**Growth rate (Å/cycle^{-1})**
Nd_2O_3	161-164	310	0.435
Sm_2O_3	148-152	300	0.36
Eu_2O_3	135	300	0.32
Gd_2O_3	155-160	300	0.31
Dy_2O_3,	125	300	0.305
Ho_2O_3	130	300	0.25
Er_2O_3	130	300	0.235
Tm_2O_3	125-128	300	0.22

On the other hand, Kosola et.al (2005) utilizes ALD method to compare physical and electrical properties of Nd_2O_3 and neodymium aluminate ($NdAlO_3$) by depositing on Si (100) and soda lime glass. For Nd_2O_3,$Nd(thd)_3$ and O_3 used as precursors, N_2 (>99.999%) was used as carrier and purging gas. The evaporation temperature was 161°C - 164°C. The film deposition was carried out at reduced pressure of 2 mbar – 3 mbar in the temperature range of 200°C - 450°C. Meanwhile, to study the effect of pulse and purge time, the deposition was carried out at a temperature of 310°C. Later, the samples underwent RTA to study the effect of heat on crystallinity. Finally, samples deposited at 230°C and 310°C were annealed at 400°C -700°C for 10 minutes in N_2 ambient (>99.999). On the other hand, trimethyl aluminum ($(CH_3)_3Al$) and water vapour (O_2 source) were used as precursors for $NdAlO_3$. The deposition was only carried out on Si (100) at 300°C by pulsing sequence of N x [$(Nd(thd)_3/O_3)$ x x + $((CH_3)_3Al/H_2O)$ x y]. Initially, film composition was altered by changing the pulsing ratio of Nd to Al (x:y). Different thicknesses were achieved by varying pulsing cycles (N).The reactant pulse times were 1 s for $(CH_3)_3Al$ and water vapor, 1s for $Nd(thd)_3$ and 1.5 s – 2 s for O_3. The purge times between the reactant pulses were between 1 s – 2 s. Finally, samples were annealed in both N_2 and O_2 ambient at temperature in the range of 800°C - 950°C (Kosola et al., 2005).

Meanwhile, Hansen et.al (2013) compared optical properties of several Ln_2O_3. Similar like Päiväsaari et.al (2005), the study involved additional two oxides which are Pr_2O_3 and ytterbium oxide. Ln_2O_3 were deposited on *p*-Si (100) and soda lime glass. Native oxide of Si was not removed prior to deposition. $Ln(thd)_3$ (pulse time 1.5 s) and O_3 (pulse time 4 s) were used as precursors with deposition cycle of 2000 while N_2 was carrier and purging gas. Additionally, in this study, two different O_3 generators were used. This was done to verify that it will not affect the deposition. The deposition was carried out in the temperature range of 200°C - 400°C. The evaporation temperatures are as shown in Table 2.6. Purge time after each precursor was 1.5 s (Hansen, Fjellvåg, Finstad, & Nilsen, 2013).

Table 2.6 : Evaporation temperature of $Ln(thd)_3$ (Hansen et al., 2013)

Ln	**Pr**	**Nd**	**Sm**	**Eu**	**Tb**	**Dy**	**Ho**	**Er**	**Tm**	**Yb**
T (°C)	155	155	145	145	140	130	130	130	125	122

In another study, Fan et.al (2014) employed ALD method to study optical property of Nd_2O_3 on *p*-Si (100). Even in both studies carried out by Hansen et.al (2013) and Fan et.al (2014), the native oxide is not removed. $Nd(thd)_3$ and O_3 were used as precursors while N_2 was carrier and purging gas. The evaporation temperature was at 185°C. The deposition was carried out in a vacuum pressure as reduced pressure of 10 mbar - 12 mbar in a temperature range of 270°C to 330°C (Fan et al., 2014a). This was followed by another study in 2015 whereby the same methodology was employed but more detailed experimental procedure was shared. The deposition was carried out at a temperature of 320°C, pulse length was 1 s for $Nd(thd)_3$ and 1.5 s for O_3. Later, samples were annealed in N_2 at temperatures of 700°C and 900°C for 5 minutes(Fan et al., 2015).

2.3.7 Chemical Solution Deposition

CSD is also known as chemical bath deposition. The method involves chemical transformation of precursor and the exchange of defined unit during the reaction. This unit can be electron, chemical element or chemical group(Lincot & Hodes, 2006). This method has been employed in coating of SiO_2 on glass substrate for optical application since the 20th century and in electronic applications since the 1980's. Initially, precursor which is carboxylate or metallo-organic compound will be prepared and dissolved in a solvent. The mixing is done based on desired composition of film. Later, it will be deposited on substrate by spin coating or dip coating. Finally, the wet deposited film will be dried, pyrolyzed (conversion of solid materials into gases and liquid by indirect heat under exclusion of air or O_2 and crystallized. Sometimes, it may have to undergo post annealing for densification or microstructure modification(Schwartz, Schneller, & Waser, 2004).

Meanwhile, Hardy et.al (2007) employed CSD method to develop Nd_2O_3, Pr_2O_3, Eu_2O_3 and Sm_2O_3 on SiO_2/Si (100) to study the effectiveness of this method in preparing a a high quality ultra thin film (3.3 nm). Deposition on bare Si is not possible since it has hydrophobic surface. Initially, precursor was prepared from Ln_2O_3 (Ln = Nd, Pr, Eu and Sm), citric acid and extra pure ammonia (NH_3). Later, the precursor was spin coated at 3000 rpm for 30s onto SiO_2/Si, followed by heat treatment on hot plate to remove organic residual. Finally, samples underwent thermal annealing by preheated tube furnace in dynamic dry air at 0.51 min^{-1}(Hardy et al., 2007).

2.4 Electrical Properties of Neodymium Oxide

The ultimate goal of investigating Nd_2O_3 is to determine its potential in replacing SiO_2. The main characteristic for this replacement is that it will reduce gate leakage current and maintain gate capacitance. This can be achieved if it could provide physically thicker film for the same EOT (Pan et al., 2006b). At the same time, physical characteristic such as interface formation will also affect the electrical properties. For instance, Song et.al (2005) discovered that crystallinity and roughness of film affect the electrical characteristics (Song & Rhee, 2005b). Current transfer in MOS devices is controlled by one or more of the following mechanisms: Richardson-Schottky emission, Poole-Frenkel emission, F-N tunneling (FN) and/or space charge limited current mechanism (A. Dakhel, 2004c).

The electrical characteristics will mainly be studied and determined through current-voltage (I-V) and capacitance-voltage (C-V) tests. The main difference between current and capacitance measurement is the absence of the ac probing signal in the dc current measurement (Dieter K Schroder, 1987).

The capacitance of semiconductor can be easily measured and it is always affected by physical parameters. Thus, determination of capacitance will be followed by characterization analysis to understand the geometry of devices component materials and interface (Rahmawati, Ekawita, Budiman, Abdullah, & Khairurrijal, 2012).

2.4.1 Current-Voltage Analysis

I-V characteristics have unique properties as far as extraction generation of lifetimes and surface generation velocity are concerned. For this test, the device has to be treated as diode with a surrounding gate. The nearby gate is responsible to alternate the diode’s current. Meanwhile, diode is meant to collect the current generated by capacitor. The diode biased at constant voltage, thus, the gate voltage is varied (Dieter K Schroder, 1987). Sometimes, the current data can also be presented in the form of current density (J).

The film deposited by ALD method at 310°C has the lowest leakage current of 3.2 x 10^{-9} A/cm^2 and breakdown strength at 1.3 MV/cm. This film poses cubic structure and smoother surface. There were no conclusion that can be driven since the electrical test was only carried out for film deposited at 310°C and not for other temperatures (Kosola et al., 2005). Thermal evaporation method leads to much lower current leakage at atmospheric pressure compared to pressure ranging from 1.2 x 10^{-6} to 5 x 10^{-6} torr. At atmospheric pressure, the leakage was 1 x 10^{-3} A at 32 V with initial erratic behavior. Meanwhile, at a higher pressure, it exhibits smoother initial behavior and leakage current was 1 A at 4.4 V at non-linear region. Non-linear region was obtained at higher voltage region. The data obtained were limited since some samples had short or open circuit (Fromhold Jr & Foster, 1976). Meanwhile, OTFT developed using this method poses very low leakage current density which makes it suitable for this kind of structure (Sarma, Saikia, 2010). On the other hand, CSD method shows the trend of decreasing gate leakage current with increasing thickness (Hardy et al., 2007).

MOCVD employed by Song et. al (2005) shows that leakage characteristics of the film improved with annealing at higher temperature. The sample deposited at 475°C poses leakage current of 2.8 x 10^{-4} A/cm^2 at 5V and no breakdown until 20V. Meanwhile, film annealed at 800°C has leakage current of 2.2 x 10^{-6} A/cm^2 at 5V. The highest leakage current was shown by sample annealed at 1000°C. This is due to crystallinity and roughness which increase with rising temperature whereby it will cause carrier flows easily via grain boundaries(Song & Rhee, 2005b). Similarly, sputtering and EBE methods also show the same observation whereby the leakage properties improved with higher annealing temperature; however, upon reaching too high of a temperature, they would start to deteriorate.

Sputtering method shows a decrease in leakage current density with the increase of electric breakdown field and RTA temperature. The initial discovery was that RTA at

800°C encourages the best electrical result. Annealing causes the EOT to be increased as a result of an increment in the thickness of interfacial layer between Nd_2O_3 and Si (Pan et al., 2006b). RTA passivate the dangling bond and trap state at Nd_2O_3 include interface of Nd_2O_3 and polysilicon. However, at a temperature of above 900°C (950°C), the quality of polyoxide film starts to deteriorate which then leads to lower breakdown electric field (C.H. Kao et al., 2010; C. H. Kao et al., 2014). The electrical field breakdown value is as summarized in Table 2.7. On the other hand, Pan et.al (2007) showed that deposited sample has higher leakage current than annealed sample. However, the best gate leakage current was at 700°C even though the highest annealing temperature was 800°C (Jinxing et al., 2009). This difference can be due to different capacitor structures employed by these researchers. Kao et al. (2010, 2014) utilized polyoxide structure and Pan et.al (2006) used EIS capacitor structure. At 2V, leakage current of sample deposited at a ratio 20:5 ($Ar:O_2$) was four times higher than 12.5:12.5 ($Ar:O_2$) ratio. Equal ratio of Ar and O_2 suppressed the formation of amorphous silica. Additionally, optimization of annealing temperature removed the crystal defect. These resulted in lower leakage current density (Strong et al., 2009).

Table 2.7: Electric field breakdown summary (C.H. Kao et al., 2010; C. H. Kao et al., 2014; Pan & Yu, 2009)

RTA Temperature	**Electric field breakdown (MV/cm)**				
	Pan et.al (2007)	**Kao et al. (2010)**		**Kao et al. (2010)**	
	Positive bias	**Positive bias**	**Negative bias**	**Positive bias**	**Negative bias**
As deposited	3.4	1.6	-2.9	2	-4.1
600°C	3.4	2.1	-2.1	3	-4.6
700°C	4.6	3	-4	3.7	-5.6
800°C	5.4	6.25	-6.6	4.3	-6.3
900°C	-	11.2	-11.4	6.4	-9.1
950°C	-	7.6	-7.9	-	-

The EBE method substantiates similar characteristics as other methods. A study performed by Dakhel (2004) proved that in addition to annealing temperature, annealing ambient also affected the electrical result. Sample annealed at 300°C and 800°C in air, exhibited partially linear behavior at lower voltage (< 1.5V). Meanwhile, sample annealed at 800°C in vacuum is totally linear. It follows SCLC mechanism. At the same time, Arrhenius plot of temperature dependence leakage J indicated that the sample was annealed at 300°C in air deviated from linear shape when the temperature is higher than 373K. The result indicates that current carrier trapping was enhanced which then led to lower leakage J. This is because -OH started to leave the film(A. A. Dakhel, 2004).

Each of these methods produces various leakage values. However, it can be clearly seen that annealing plays a vital role in improving the leakage properties of the thin film.

2.4.2 Capacitance-Voltage Analysis

C-V is an important test that reveals the internal structure of MOS. The measured capacitance varies as function of applied gate voltage. It measures the capacitance between two more terminals with respect to a common ground plane. The characteristics will be used to determine deviation from the ideal oxide and semiconductor I-V (Pierret, 1990; Tummula, Rymaszewski, & Klopfenstein, 1997).

EBE method employed by Jeon et.al (2001) shows that accumulation capacitance of various Ln_2O_3 is between 20-21 fF/um^2 (Jeon et al., 2001). However, this value is much lower than the one reported by Kosola et.al (2005) through ALD method whereby the accumulation capacitance was ~340 fF/um^2 (Kosola et al., 2005). The same method also produced very close result in another experiment which is 336 fF/um^2(Päiväsaari et al., 2005).

Dakhel (2004) utilized correlated barrier-hopping to explain the C behavior. In this model, CBH of bipolarons (or a single polaron) was proposed to interpret the frequency dependence of insulator conductivity according to the following equation:-

$$\sigma_{ac}(\omega) = A\omega^{s} = \left\{\frac{\pi^2 N_{LS}^2 \varepsilon_0 \varepsilon}{24\tau_0^{\beta}}\left(\frac{8e^2}{\varepsilon_0 \varepsilon W_m}\right)^6\right\}\omega^{s} \qquad (2.4)$$

where N_{LS} is the density of the localised state, $\varepsilon_0\varepsilon$ is the permittivity, τ_0 is the effective relaxation time, $s = 1 - \beta$, where $\beta = \frac{6TK_B}{W_m}$ and W_m is the effective hopping barrier height between adjacent sites. Based on these, the calculated value of W_m is (1/4)E_g for sample annealed at 800°C in vacuum and (1/25) E_g for sample annealed at 300°C and 800°C in air. These findings support the result of I-V, where annealing ambient also influences the electrical result. The temperature dependence capacitance under accumulation at 1kHz shows linear proportion with temperature coefficient of capacitance (TCC) of 5.54 x $10^{-3}K^{-1}$ at 300°C for sample annealed at 300°C in air. Meanwhile, it varies slowly for the sample annealed at 800°C in air with TCC +5.57 x 10^{-3} K^{-1} at 300°C (A. Dakhel, 2004c).

Additionally, PDA treatment also contributed in improving the highest capacitance accumulation value. However, upon reaching higher temperature of 800°C, the value started to deteriorate which is similar to the observation by Song et. al (2005) through I-V testing. The value was reduced from ~500 pF at 700°C, to 380 pF at 800°C, which is close to the deposited sample value (Pan, Lee, Shu, & Chen, 2006a). Thus, high temperature treatment tends to degrade the quality of the film (C.H. Kao et al., 2010; C. H. Kao et al., 2014; Song & Rhee, 2005a). At the same time, no frequency dispersion in accumulation of dielectric was observed. This can be attributed to series resistance which results in lowering the accumulation of capacitance. Thus, it can be concluded that interface states of the film have been reduced and there was no lattice mismatch due to PDA treatment (Pan et al., 2006a).

From the C-V curve, it can also be observed for frequency dispersion in accumulation region. This region was larger when the sputtering was carried out under lower O_2 to Ar ratio. This condition reduces the capacitance value by 13% due to the formation of large crystal defect(Pan et al., 2007). Different trends of C-V curve were observed by Sun et.al (2009), as illustrated in Figure 2.9, whereby anomalous hump is observed. This indicates the presence of near interface oxide trap. This trap is located within oxide and interferes with Si(Sun et al., 2008b).

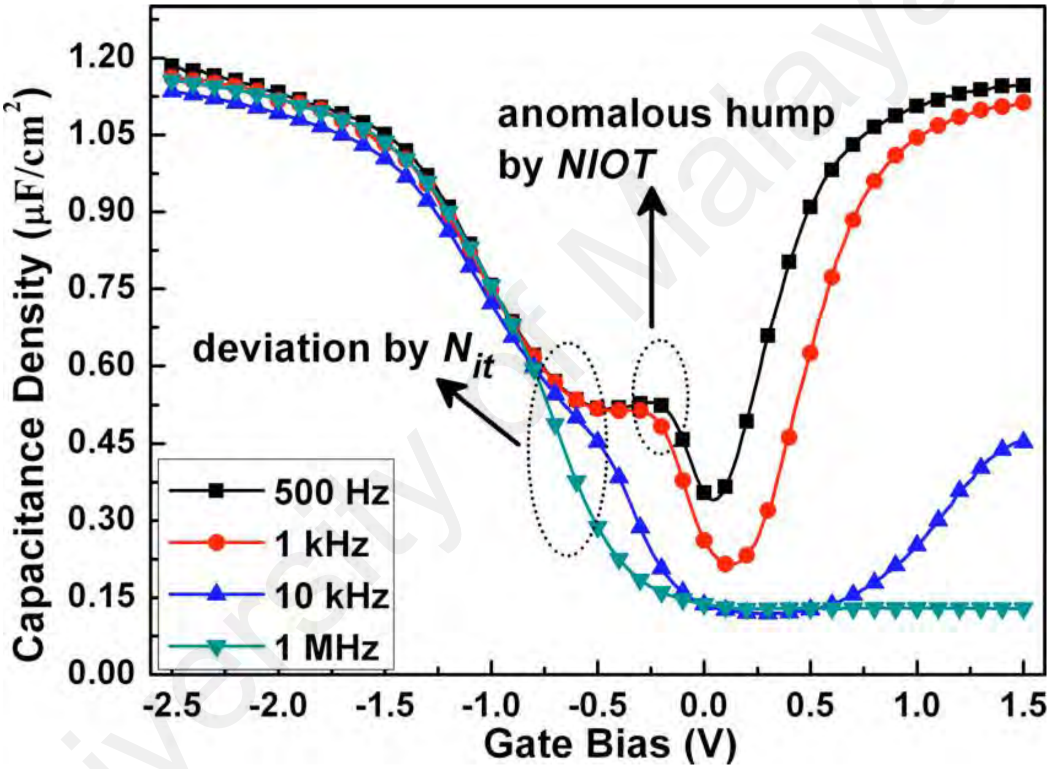

Figure 2.9: C-V curve with anomalous hump (Sun et al., 2008b)

2.4.2.1 Flatband Voltage

V_{FB} is another electrical property which uses the C value to determine the work function difference between metal semiconductor and various oxide charges (D.K. Schroder, 2006). Dakhel et.al (2004) employed equation 2.5 below in order to determine V_{FB},

$$Q_{ox} = (C_{ox}^{'}/e)\ (\o_{ms} - V_{FB}) \qquad (2.5)$$

where, $C_{ox}^{'}$ is the capacitance per unit area of the oxide insulator, e is the electron charge and $\o_{ms}$ = –0.9 for Al gate. The value is less negative when annealed in vacuum but more positive when annealing in air. At the same time, annealing in air and at a higher temperature resulted in more negative value (A. Dakhel, 2004b). The same trend was observed by Song et.al (2005) and together, these findings show that annealing in air and higher temperature reduces negative charges(Song & Rhee, 2005a).

In addition, Pan et.al (2009) also observed the same trend and suggested that higher annealing temperature indeed increases the density of trapped in the charged trapped layer due to rougher surface and higher content of silicate compared to silica(Pan & Yu, 2009). Frohlich et.al (2006) also discovered that PDA before gate electrode deposition reduces fixed oxide charges compared to annealing the whole structure with gate electrode (Frohlich et al., 2006).

The rest of researches utilized C-V test result to determine V_{FB}. The predicted V_{FB} value for Al/Nd_2O_3/native – SiO_2/ Al capacitor is -0.2 V. However, the value recorded through ALD method by Kasola et. al (2005) and Paivasaari et.al (2005) showed negative bias with the deposited sample. This shows the presence of positive fixed charge (Kosola et al., 2005; Päiväsaari et al., 2005). On the other hand, Laha et.al (2013) were able to study the effect of C on the C-V properties. Their study signified monotonic shift of V_{FB} which indicates that C passivating interface defected the stem from dangling bond from Si surface, thus, the effect of fixed charge is reduced(Laha et al., 2013).

2.4.2.2 Hysteresis

V_{FB} is information which can be gathered from C-V test as it also reveals the defect in dielectric film. It is measured through the difference between forward and reverse bias in C-V curve(Päiväsaari et al., 2005). The value is directly proportional to the amount of defects. It is common in high-*k* materials as a result from charge trapping under negative bias. Additionally, hysteresis can also be due to chemical contamination, stress-induced deformation or mobile ions(Pan et al., 2007). Pan et.al (2007) also detected very small hysteresis for a sample PDA at 700°C which is < 30 mV. This indicates that the sample has very small charge density and high crystalline quality. At the same time, PDA enables the reduction of O_2 related defects(Pan et al., 2006a; Pan et al., 2007; Pan et al., 2009; Pan & Lin, 2009). They further found that contamination from precursors increases the density of impurity and change in hysteresis direction. The hysteresis was 0.70 V and faces counter-clockwise hysteresis which is reverse sweep shifted towards negative bias voltages(Päiväsaari et al., 2005).

2.4.2.3 *k*-value

Fromhold et.al (1976) found that the *k*-value is not only affected by thickness but also by the evaporation parameter including ultimate and evaporation pressure, current and time. Recorded average *k*-value was 12.7 for oxide with a thickness 30 nm (Fromhold Jr & Foster, 1976). Song et.al (2005) also found that lower thickness have lower *k*-value compared to thicker oxide (Song & Rhee, 2005a). However, the MOCVD shows opposite trend where thicker sample poses lower *k*-value than thinner. This is attributed by an admixture of SiO_2 lower density or carbon contamination (Frohlich et al., 2006).

Meanwhile, Pan et.al (2007) discovered that oxygen content plays a vital role in determining the *k*-value. Higher O_2 reduces lower *k*-value interface and neodymium silicate ($Nd_xSi_yO_z$) interface formation due to higher diffusion O_2 rate through Nd_2O_3(Pan et al., 2007). On the other hand, Fan et.al (2014) found that *k*-value decreases as the annealing temperature increases to 900°C, whereby the refractive index increases. Refractive index is indirectly related to the quality of the film (Fan et al., 2014a). The results of *k*-values are as shown in Table 2.8. The thinnest and highest *k*-value is achieved through MBE method which is attributed by the structure of atom.

Table 2.8: *k*-values of Nd_2O_3 deposited through various methods

Method of deposition	**Thickness (nm)**	***k*-value**	**Reference**
Thermal evaporation	30	12.7	(Fromhold Jr & Foster, 1976)
MOCVD	>25	13 ± 2	(Song & Rhee, 2005a)
	>25	14 ± 2	
MOCVD	6 - 20	14 ± 0.3	(Frohlich et al., 2006)
MBE	8.5	15	(Sun et al., 2008b)
Sputtering	28	11.7	(Pan et al., 2007)

The thickness of film highly influences *k*-value of the oxide. As stated in Equation 2.6,

$$C = \frac{kA\epsilon_0}{t} \tag{2.6}$$

where, C is the capacitance of the oxide, *k* is the effective dielectric constant, A is the area of the capacitor, ϵ_0 is the permittivity of free space (8.85×10^{-12} Fm^{-1}), and t is the thickness of the oxide film (Goh et al., 2016a; Kurniawan, Wong, et al., 2011). Based on this equation, the thickness have inverse relationship with the *k*-value. As thickness increases, the *k*-value decreases. As a result, sample with lowest thickness which produces through MBE method has the higher *k*-value. On the other hand, sample deposited by MOCVD have more or less the similar *k*-value as MBE even their thickness higher. The PDA treatment done on oxide deposited through MOCVD reduces surface roughness and increases grain size (Song & Rhee, 2005a). This larger grain size, will reduces electrical trapping site at grain boundary. Hence, result in better electrical property include *k*-value (Zeng et al., 2013).

2.5 Structural Properties of Neodymium Oxide

As stated earlier, the parameters and method of deposition play vital roles in determining the electrical properties. This is because the electrical properties highly depend on the quality of the oxide, chemical composition and interface.

2.5.1 Quality of the Oxide

Basically, most of these methods produce cubic – Nd_2O_3 (Frohlich et al., 2006; A. Laha, A. Fissel, E. Bugiel, & H. J. Osten, 2007b; Pan & Lin, 2009). The deposited Nd_2O_3 through sputtering produces amorphous oxide(Pan et al., 2006a). However, the cubic Nd_2O_3 through sputtering method was achieved after annealing(Pan & Lin, 2009). Annealing form 600°C to 900°C produces stronger spectra of Nd_2O_3 in XPS. Optimum electrical result was obtained for sample annealed at 900°C as it forms well crystalline structure, thus, it has a stronger Nd-O bonding (C.H. Kao et al., 2010; C. H. Kao et al., 2014; Pan & Yu, 2009). As the result defect and trap states reduces (C.H. Kao et al., 2010). However, annealing at a very high temperature increases the crystallinity and makes the cubic Nd_2O_3 disappears. This leads to the formation of silicate layer (C.H. Kao et al., 2010; Song & Rhee, 2005a). At this stage, diffusion of Nd into Si atom increases and forms lower *k*-value of interfacial layer which degraded the quality of the oxide forms (C.H. Kao et al., 2010; Pan et al., 2009).

An almost similar trend was observed when $NdTiO_3$is annealed. XRD peak intensity of $NdTiO_3$ increases up to annealing temperature of 900°C. At 900°C, titanium has insufficient kinetic energy to react with Nd_2O_3. Thus, O atoms leave $NdTiO_3$ layer and move towards $NdTiO_3$ / Nd_2O_3 interface resulting in lower *k*-value interfacial layer (C. H. Kao et al., 2014). Different O contents in sputtering also influence the oxide growth. Preferred orientation crystalline cubic Nd_2O_3 that is parallel to substrate was achieved at the same and higher O ratio to Ar. Annealing of these samples from 600°C - 800°C does not impart any change in the structure (Pan et al., 2007).

As annealing affects the morphology of the oxide, it also directly affects the grain size. Oxide deposited through MOCVD has dense and fine grain film with an average size of 20 nm. The surface roughness decreases and the grain size increases as annealing temperature increases. However, as the annealing temperature increases up to 1000°C, the surface roughness increases as a result of silicate formation supported by sputtering findings (Pan et al., 2009; Pan & Lin, 2009; Song & Rhee, 2005a). Crystalline Nd_2O_3 with C- type structure was achieved at a deposition temperature of > 450°C with preferred orientation of (1 0 0). At lower temperature, amorphous disorder structure was achieved. However, oxide that is deposited on gallium arsenide exhibits amorphous structure at higher temperature due to degradation or reaction with surface (Jones et al., 2005).

Additionally, deposited oxide through ALD also produces amorphous phase when deposited below the threshold temperature of 300°C. Above this temperature, crystalline oxide was achieved but without any preferred direction. For example, a study by Hansen et al. (2013) produced hexagonal Nd_2O_3, while a study by Kosola et.al (2005) produced the amorphous oxide at a much more lower temperature in between 200°C and 250°C. The preferred orientation on Si (1 0 0) is (1 0 0) (Hansen et al., 2013; Kosola et al., 2005). In addition, oxide produced by Paivasaari et.al (2005) by the same method also consists of both cubic and hexagonal Nd_2O_3, with preferred orientation of

(4 0 0). However, this preferred orientation changed as the function of deposition temperature (Päiväsaari et al., 2005).

Kosola et.al (2005) also found that oxide started to crystallize at a temperature in between 250°C and 270°C. Amorphous $Nd_2O_2CO_3$ and crystalline Nd_2O_3 were achieved with temperature of 270°C to 325°C. Exposure to air led to the formation of neodymium oxide hydroxide, NdO(OH). However, the exposure to air has no effect on $Nd_2O_2CO_3$. Additionally, reaction of water in the air was strongly affected by the deposition temperature in terms of its degree of crystallinity and carbonate contamination. As carbon contamination was lowering, the crystallinity contrarily got higher. Thus, the tendency to absorb water was higher. This condition was achieved with a sample deposited at 350°C to 375°C. Annealing of the amorphous oxide had no change until the annealing temperature reached 650°C where it started to crystallize as cubic. Meanwhile, crystalline sample annealed at 700°C showed preferred growth orientation in (2 2 2) direction (Kosola et al., 2005).

EBE also produces almost same structure as ALD, where as deposited produces amorphous oxide which is combination of hexagonal and cubic Nd_2O_3, where at annealing at 700°C changes it to crystalline (Busani et al., 2006). However, the annealing in both air or vacuum improved the crystallinity with large differences in grain size from (2 2 2) line. The sample annealed in vacuum was 68 nm and while the sample annealed in air was 8.5 nm At the same time, the sample annealed in vacuum had more orderly structure(A. Dakhel, 2004b, 2004c). Increasing the annealing temperature up to 1000°C enhances the cubic structure with a preferred (1 0 0) orientation (A. Dakhel, 2004b).

Meanwhile, MBE formed a well ordered growth of oxide layer compared to other methods. This is due to the formation of 3-fold periodic structure (Laha et al., 2007b; Wang et al., 2009). However, this layer-by-layer growth is only limited to thickness up to 10 nm and for > 10 nm, transition to three dimensional growths was observed (Laha et al., 2007b). Additionally, the oxide also formed layers of cubic structure consisting of two domains in {110}-orientation on Si(001) (Sun et al., 2008b). However, Laha et.al (2013) found that Si orientation has no impact on growth and structure of oxide (Laha et al., 2013).

2.5.2 Interface

Interface was studied in detail through MOCVD and MBE methods. MOCVD revealed that the thickness of amourphous silicate layer depends on the system and deposition condition (Frohlich et al., 2006). At the same time, annealing at > 1000°C leads to the reaction with Si and forms a silicate layer. Resulting phase changes and affects the surface morphology and surface characteristics as stated earlier (Song & Rhee, 2005a).

In the interface formation of MBE, silicate such as bonding appears even before Nd-O-Nd peaks start dominating in XPS. During initial growth stage, O atoms bonded to Si by Nd or movement of oxygen atoms from a Si–O–Nd interface site into the layer during the initial stage of growth. At initial stage of growth where the thickness is < 1 nm, formation of Si–Nd bonds occurred due to UHV condition. In addition, Si suboxide like bonds were also formed. As the thickness increases, silicide bonding increases compared to suboxide like. During the next growth step, Si bonds in higher oxidation states were also formed, which are attributed by silicate like bonding. During the second layer, Nd-O continues to increase as the thickness increases. Annealing in oxygen rich environment leads to the disappearances of silicide layer but also leads to the formation of amorphous interface layer (E. Bugiel et al., 2005; Fissel et al., 2006;

Laha et al., 2007b). Osten et.al (2007) discovered that as a single valence REO, Nd_2O_3 have fewer tendencies to form SiO_2 interfacial layer due to their exposure to air, which is also supported by findings through EBE (Busani et al., 2006; Laha et al., 2007b). Wang et.al (2009) discovered that the oxide consists of sharp and smooth interface (Wang et al., 2009).

Sputtering method also produces similar interface as MOCVD and MBE. As the oxygen is sufficient, there is no silicide formation from the initial growth stage. Annealing facilitates the diffusion of Nd and O atoms into Si to form $Nd_xSi_yO_z$(Pan et al., 2007). ALD also produces the same result as sputtering, whereby the deposited has no interfacial layer and annealing induces the formation of interfacial layer of $Nd_xSi_yO_z$. As the annealing temperature increases, $Nd_xSi_yO_z$ poses high ratio of SiO_2 to $Nd_xSi_yO_z$(Fan et al., 2015). Generally, all of these findings and different methods produce the same interfacial layer as proposed by Fan et.al (2014), as shown in Figure 2.10.

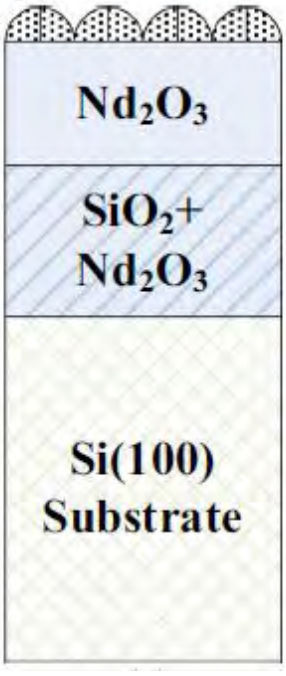

Figure 2.10: Schematic diagram of oxide formed through various methods (Fan et al., 2015)

2.5.3 Band Gap

Energy band diagram of thicker oxide layer was determined for oxide produced through MBE. From the energy-loss spectrum (O 1*s* Plasmon energy-loss and the valence-band spectrum) energy band gap were determined from threshold energy of the energy loss. It is estimated that the gap energy was 5.8±0.2 eV. Meanwhile, the valence-band offset for Nd_2O_3 / Si (0 0 1) heterostructure was 2.57 eV for Nd_2O_3 and 0.07 eV for Si (0 0 1). It was determined by evaluating the energies of the valence-band maximum of Si and Nd_2O_3. The differences of these values represent valence-band offset of 2.5 eV. The energy band diagram is as shown in Figure 2.11 (Fissel et al., 2006).

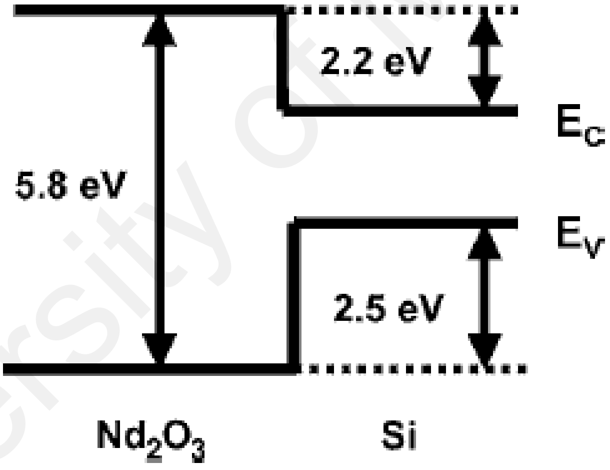

Figure 2.11: Energy band diagram of Nd_2O_3 /Si (0 0 1) heterostructure determined for oxide formed by MBE (Fissel et al., 2006)

The energy band diagram for oxide formed by sputtering method is as shown in Figure 2.12. The gap energy is similar as the oxide formed by MBE. However, there is a difference in the conduction and valence band offset(Pan & Yu, 2009). Even when the thicknesses of both oxides are the same, the difference can be due to organized atomic arrangement which result in better electrical properties.

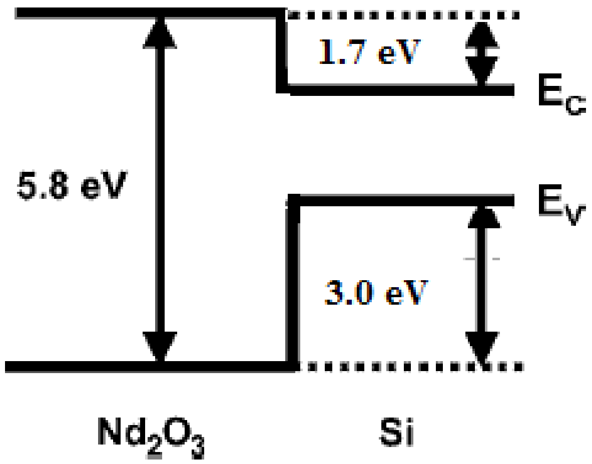

Figure 2.12: Energy band diagram of Nd_2O_3 /Si (0 0 1) heterostructure determined for oxide formed by sputtering

2.6 Mechanical Properties of Thin Oxide Film

As stated in the introduction section, mechanical properties play vital role in determining a possible replacement for SiO_2. However, the literature pertaining to mechanical properties of Nd_2O_3 is found to be scarce to none. Nevertheless, mechanical properties of thin oxide film of zinc oxide (ZnO) and HfO_2 were determined through nanoindentation and nanoscratch tests. Nanoindentation is a method most frequently implemented to investigate mechanical properties of thin-film such as Young's modulus and hardness. On the other hand, nanoscratch is used to evaluate mechanical properties of ultra-thin film (Fang, Chang, & Lin, 2005).The test involves scratching the surface with a diamond tip in order to determine the coefficient of friction(Yau et al., 2011).

The type of scratch failure can be classified to three types. The first is significant creep which is associated with plastic deformation whereby at this stage, no debris was found. The second type is scratch mark pile-up appear at the side of the mark. The third type is indenter edge occurred and film is removed through ploughing mechanism. Scratch debris were found inside or around the scratch track (Jian et al., 2008). This is due to normal and lateral forces which result in the creation of dislocation loops underneath the point of scratch. Increment of the debris also indicate increased plastic deformation which leads to wider scratches (D Geetha et al., 2017).

Investigation on ZnO revealed that smaller grain size has higher coefficient of friction, thus resulting to better resistance to scratch. At the same time, the plane orientation also affects coefficient of friction (Yau et al., 2011). Additionally, lower surface roughness also result in better scratch resistance. Higher roughness level leads to point-on orientation of the tip or the layered structure of thin films or it could be resulting to nanoscale fracture events (Jian et al., 2008). Critical load is the normal force applied to the scratch probe at the time that the interfacial failure is detected. The higher the critical load, the higher the critical depth as it is affected by the thickness of the film. In addition, higher critical load also means higher interfacial adhesion (D Geetha et al., 2017).

As stated earlier, annealing improves the oxide structure. Thus, annealing also affects the coefficient of friction. As the annealing temperature increases for HfO_2, the scratch depth decreases. This indicates that wear resistance increases as the annealing temperature increases (Fu et al., 2013).

2.7 Research Gap

Based on the published results, it can be observed that even the replacement material for SiO_2 have been actively searched since almost half a century, but researchers are actively looking Nd_2O_3 as option since 20 years back. This is due to the identification of this material as higher *k*-value material compared with ZrO_2 and HfO_2.

Even the investigation have been carried out by using variety different deposition technology, thermal oxidation never been carried out. This is an essential method, as current industries are using this method in order to produce SiO_2. This will leads to result of feasibility study for ensure this material to be adopted in MOS technology in industry production scale.

Besides that, by using variety of deposition of technology, researchers deposited Nd_2O_3 at different thickness. As thickness of thin film affects the electrical property, no clear relationship between deposition methods and electrical property was able to determined. Better understanding could be achieved is the research if it has been carried at constant thickness. However, the effect of deposition method to interfacial layer and electrical property has been determined.

In addition, even lattice mismatch leads to stress and dislocations none of the researches have address mechanical properties of this thin film. This is vital as contact loading during processing or packaging processing or packaging, will affect the processability and/ reliability of MOS.

CHAPTER 3: MATERIALS AND METHODOLOGY

3.1 Introduction

In this chapter, the materials and experimental methodologies employed in this research are discussed in detail. Figure 3.1, 3.2, and 3.3 show the experimental overview, sample preparation overview, and characterization technique overview applied in this research, respectively. This can be further divided into three main parts, as follows:

(i) Materials;

(ii) Experimental procedure; and

(iii) Characterization techniques.

The materials and chemicals involved in this research are categorized below:

(i) Substrate material;

(ii) Chemicals utilized in Si substrate and quartz tube cleaning process;

(iii) Materials for sputtering;

(iv) Materials for the oxidation/oxynitridation process; and

(v) Materials for the electrode metallization and photolithography process.

The steps involved in preparing the sample are described below and in Section 3.3. An overview of these steps is shown in Figure 3.2.

(i) Si substrate cleaning;

(ii) Nd thin film sputtering;

(iii) Thermal oxidation/oxynitridation of sputtered Nd thin film on Si substrate in O_2/ N_2O gas ambient; and

(iv) MOS capacitor fabrication process via Al sputtering.

The physical, chemical, mechanical, and electrical characterization techniques employed in this research are discussed in Section 3.4 and shown in Figure 3.3. The physical and chemical characterization techniques used are XRD, FTIR analysis, Raman spectroscopy, HRTEM, EDX, and XPS. The mechanical test employed is the microscratch test. On the other hand, electrical properties were characterized via I-V and C-Vmeasurements.

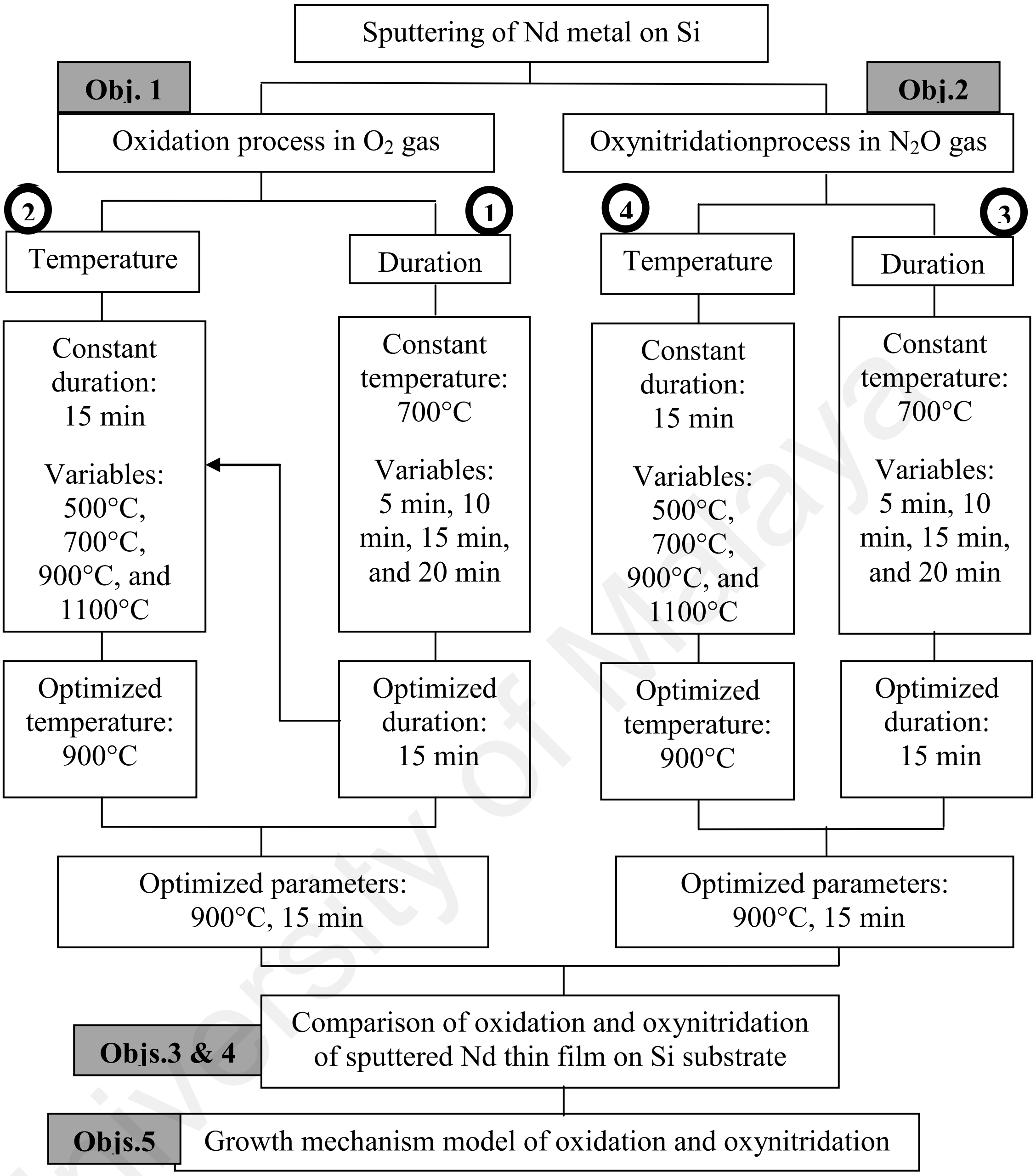

Figure 3.1: An experimental overview of this study

Notes:

(i) Obj. 1, Obj., 2, Obj. 3, and Obj. 4 refer to the objectives numbered 1, 2, 3, and 4, respectively, as outlined in Subsection 1.3 of Chapter 1.

(ii) The numbers 1–4 represent the parameters, as discussed in Chapter 4.

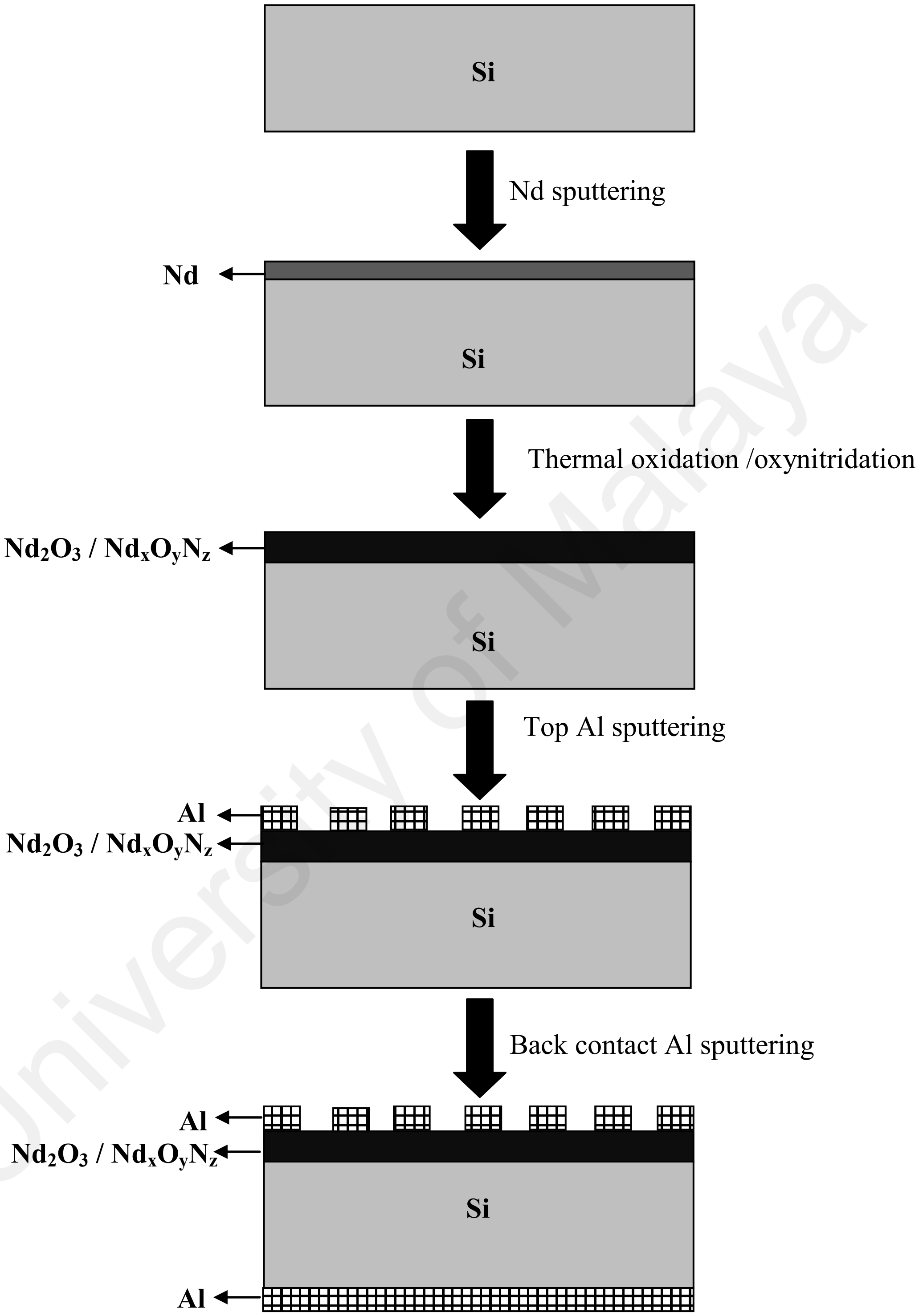

Figure 3.2: An overview of the sample preparation for this study

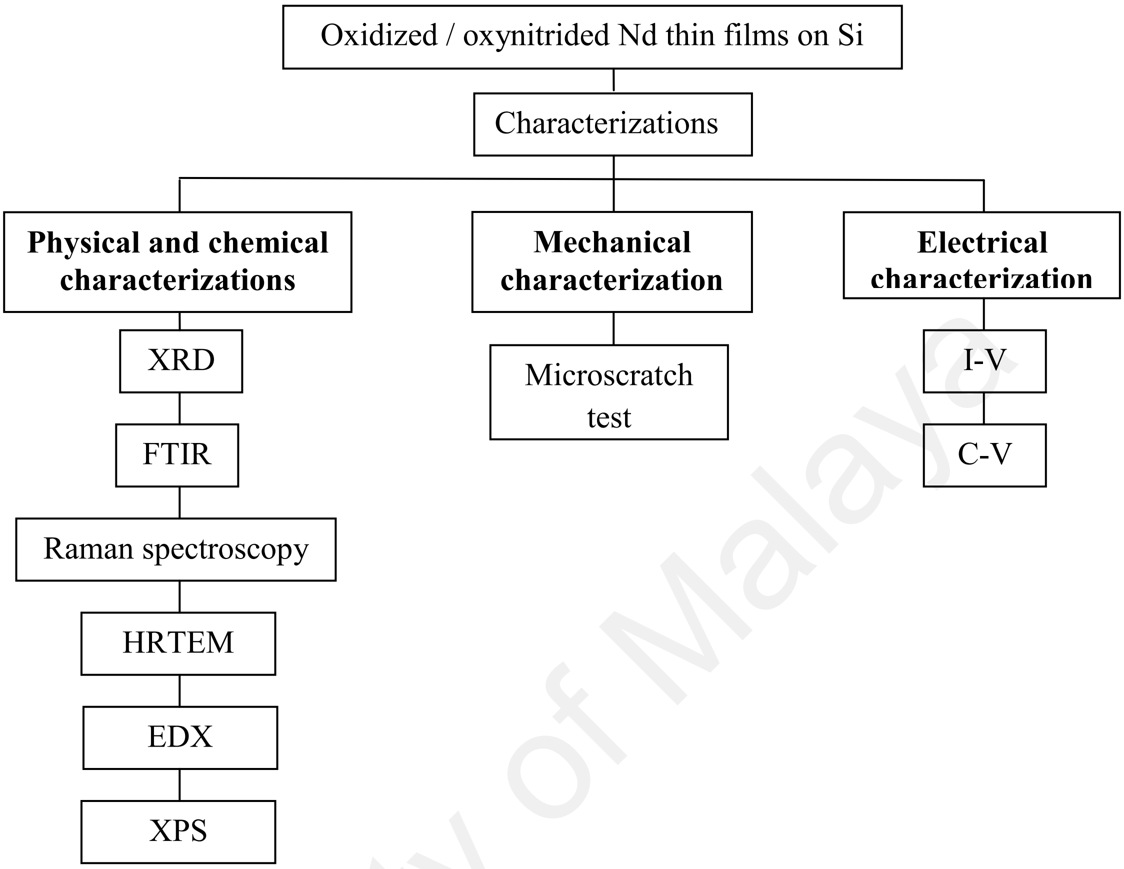

Figure 3.3: An overview of the sample characterization techniques used in this study

3.2 Materials

3.2.1 Substrate Materials

Si wafers were utilized as substrate materials. The wafers were supplied by Technologies Sdn.Bhd and are *n*-type, (100)-oriented, with 1–10 Ω cm resistivity, and phosphorus-doped with a polished surface on one side.

3.2.2 Chemical Used in Si Substrate and Quartz Tube Cleaning Process

The chemicals used for the Si substrate and quartz tube cleaning are shown in Table 3.1. Further chemical details such as the chemical formula, assay percentages, supplier, and Chemical Abstracts Service (CAS) numbers are also given.

Table 3.1: List of chemicals used in Si substrate and the quartz tube cleaning process

No	**Chemical**	**Chemical Formula**	**Assay**	**Supplier / CAS No.**
1	Hydrogen Peroxide	H_2O_2	30%	R&M Chemicals / 7722-84-1
2	Hydrogen Fluoride	HF	49%	R&M Chemicals / 7664-39-3
3	Hydrochloric Acid	HCl	37%	R&M Chemicals / 7647-01-0
4	Ammonia Hydroxide	NH_4OH	29%	R&M Chemicals / 1336-21-6
5	Acetone	$(CH_3)_2CO$	> 99%	R&M Chemicals / 67-64-1

3.2.3 Chemical used in Nd and Al Sputtering

Nd pure metal and Al sputtering was carried out using the Nd target, Al target, and in Ar gas ambient. Prior to sputtering, the chamber was cleaned with acetone. Details on materials and chemicals involved in the sputtering process are shown in Table 3.2.

Table 3.2: List of materials and chemicals used in the sputtering process

No	**Chemical**	**Chemical Formula**	**Supplier / CAS No.**	**Specifications**
1	Neodymium target	Nd	Kurt J. Lesker	Purity: 99.9% Diameter: 101.6 mm Thickness: 3.175 mm
2	Aluminium target	Al	Kurt J. Lesker	Purity: 99% Diameter: 101.6 mm Thickness: 3.175 mm
3	Argon gas	Ar	Gaslink / 7440-37-1	Purity: 99.99%

Table 3.2: *(continued)* List of materials and chemicals used in the sputtering process

No	**Chemical**	**Chemical Formula**	**Supplier / CAS No.**	**Specifications**
4	Acetone	NH_4OH	R&M Chemicals / 67-64-1	Purity: 99.99%

3.2.4 Materials used in Thermal Oxidation/Oxynitridation

O_2 gas was used for thermal oxidation, N_2O for thermal oxynitridation, and Ar gas to cool down the location to room temperature upon completion of the thermal oxidation/oxynitridationprocess. More details of these gases are shown in Table 3.3.

Table 3.3: List of gases used in the oxidation/oxynitridation process

No	**Chemical**	**Chemical Formula**	**Supplier / CAS No.**	**Purity**
1	Oxygen	O_2	Gaslink /7782-44-7	99.99%
2	Nitrous oxide	N_2O	Gaslink /10024-97-2	99.99%
3	Argon	Ar	Gaslink /7440-37-1	99.99%

3.3 Experimental Procedures

3.3.1 Substrate Cleaning Process

Prior to the cleaning process, the Si wafers were cut into square shapes with dimensions of 1 cm× 1 cm using a diamond cutter. The wafers then undergo a series of cleaning processes including a standard cleaning procedure as per Radio Corporation of America (RCA), which is shown in Table 3.4.

Table 3.4: Steps in the Si cleaning process

Process	Purpose	Procedures
Step 1 Ultrasonic cleaning	To remove physical debris from the substrate.	(i) The Si wafers are put in a sample holder and placed in a container, which contains DI water. (ii) The container is transferred into an ultrasonic bath for 10 min. (iii) The Si wafers are rinsed with DI water before proceeding to the next step.
Step 2 RCA-1	To remove organic dirt from the substrate.	i) The chemicals (NH_4OH:H_2O_2:H_2O) are prepared according to a ratio of 1:1:5. (ii) 100 ml of DI water is heated to 90°C on a hot plate. (iii) Once the temperature reaches 90°C, 20 ml ofNH_4OH is added to the heated DI water. (iv) 20 ml of $H_2O_2$is added into the DI water when the temperature decreases to 80°C. (v) The solution starts to bubble after one minute. (vi) The Si wafers are soaked for 15 minutes and the temperature maintained at 80°C. (vii) Then, the Si wafers are rinsed with the DIwater.
Step 3 HF dipping	To remove native oxide from the substrate.	i) Diluted HF solution is prepared according to a ratio of 1:50 (HF:H_2O). (ii) The Si wafers are soaked in diluted HF solution for 10 seconds. (iii) After 10 seconds, the Si wafers are rinsed with DI water immediately.

Table 3.4: *(continued)* Steps in the Si cleaning process

Process	Purpose	Procedures
Step 4 RCA-2	To remove metal ions from the substrate.	i) The chemicals ($HCl:H_2O_2:H_2O$) are prepared according to a ratio of 1:1:6. (ii) 120 ml of DI water was heated to 90°C on a hot plate. (iii) Once the temperature reaches 90°C, 20 ml ofNH_4OH is added into the heated DI water. (iv) 20 ml of $H_2O_2$is added into the DI water when the temperature decreases to 80°C. (v) The solution starts to bubble after one minute. (vi) The Si wafers are soaked for 15 minute sand the temperature maintained at 80°C. (vii) Lastly, the Si wafers are rinsed with DI water and dried with an air gun.

3.3.2 Nd Thin Film Sputtering

A TF 450 physical vapor deposition (PVD) RF sputtering system was utilized for the Nd thin film deposition. The sputter chamber, substrate holder, target holder, and shutter were cleaned with acetone before the sputtering process is started. This is followed with fixing the Nd target onto the target holder with the Si substrates placed on thesubstrate holder. Before sputtering, the chamber was evacuated to a base pressure of 1.5×10^{-3} Pa. Afterwards, Ar gas is introduced at a RF power of 170 W. Prior to the sputtering of Nd, pre-sputtering was carried out for 2 minutes in order to remove native oxide from the Nd target. Upon completing the pre-sputtering, the shutter was opened followed with Nd sputtering at a working pressure of 3×10^{-3} Pa. The distance between Si substrates and the target was about 20 cm. An Nd thin film with a thickness of about

11 nm was sputtered on the Si substrate. The thickness was measured and controlled by elipsometry.

3.3.3 Thermal Oxidation / Oxynitridation of Sputtered NdThin Film on Si Substratein O_2 / N_2O Gas Ambient

A horizontal tube furnace was used to carry out the thermal oxidation and oxynitridation processes in this study. Thermal oxidation was carried out in O_2 gas ambient and thermal oxynitridation was carried out in N_2O gas ambient. The quartz boat and quartz tube werecleaned with diluted HF solution prior to thermal oxidation and oxynitridation. Then, the Nd-sputtered Si substrate was placed on a quartz boat and transferred into the horizontal tube furnace. The experimental setup for thermal oxidation/oxynitridation is shown in Figure 3.4.

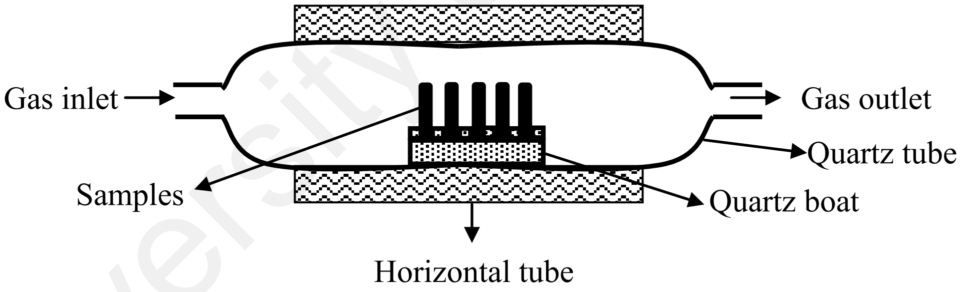

Figure 3.4: Setup of the thermal oxidation/oxynitridation processes

SiO_2 is the dominant oxide in MOS technology (Schlom et al., 2008). Even though a variety of techniques are currently available for producing this oxide, thermal oxidation is the most common method(May & Spanos, 2006). Thermal oxidation is carried out via the heating of the Si wafer vertically on a quartz boat in a quartz tube.

i) Effects of thermal oxidation duration on sputtered Nd thin film on Si substrate.

The samples were heated to 700°C in Ar gas with a heating rate of 10°C/min. Once the temperature reaches 700°C, O_2 gas is introduced into the quartz tube with a flow rate of 150ml/min for set durations (5 min, 10 min, 15 min, and 20 min). The oxidized samples werethen cooled down to room temperature in Argas ambient.

ii) Effects of thermal oxidation temperature on sputtered Nd thin film on Si substrate.

The samples were heated up to a set of temperatures (500°C, 700°C, 900°C, and 1100°C) in Ar gas with a heating rate of 10°C/min. Once the set temperature wasachieved,O_2 gas was introduced into the quartz tube with a flow rate of 150 ml/min for 15 min. Theoxidized samples were then cooled down to room temperature in Ar gas ambient.

iii) Effects of thermal oxynitridation duration on sputtered Nd thin film on Si substrate.

The samples were heated to 700°C in Ar gas with a heating rate of 10°C/min. Once it reached700°C, N_2O gas was introduced into the quartz tube with a flow rate of 150ml/min for one of a set of durations (5 min, 10 min, 15 min, and 20 min). The oxynitrided samples werethen cooled down in Ar gas.

iv) Effects of thermal oxynitridation temperature on sputtered Nd thin film on Si substrate.

The samples were heated up to set temperatures (500°C, 700°C, 900°C, and 1100°C) in Ar gas with a heating rate of 10°C/min. Once the set temperature was reached,N_2O gas was introduced into the quartz tube with a flow rate of 150 ml/min for 15 min. Theoxynitrided samples were then cooled down in Ar gas.

3.3.4 MOS Capacitor Fabrication Process via the Al Sputtering Process

The MOS capacitor was fabricated on oxidized and oxynitrided samplesinorder toperform electrical characterization. An Al mask was used to create electrodes with a thickness of 100 nm on top of the Nd thin film, as shown in Figure 3.5. The sputtering condition is similar to the one mentioned in Section 3.3.2. Upon completion of sputtering the top layer, the sample is removed from the chamber and undergoes back contact sputtering without the mask but with similar thickness.

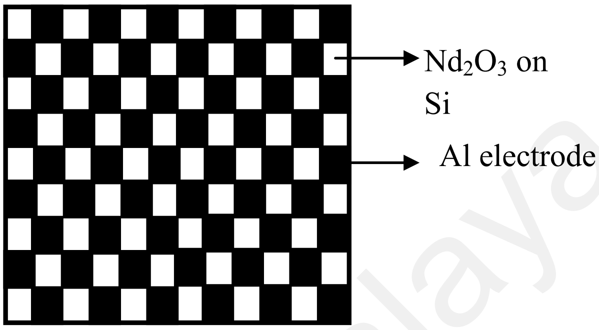

Figure 3.5: Illustration of a sample with Al electrodes

3.4 Characterizations Techniques

3.4.1 XRD Analysis

XRD is a technique for acquiring the structural parameter of metal oxides (Rodriguez & Fernández-García, 2007). This tool is essential for characterizing crystallinity, orientation of crystallites, and phase composition (Escoubas et al., 2008; Terasawa et al., 2005). Bragg's Law, as per Equation 3.1, can be used to described X-ray diffraction:

$$\lambda = 2d \sin \theta \tag{3.1}$$

where λ is the wavelength of the radiation beam (nm), d is the interplanar spacing in a crystal(nm), and $2\theta$is the angle between the diffracted and transmitted beams (°). This Law facilitates the identification of atomic or molecular structure, phases, composition, and polycrystalline state. In addition, it also enables the identification of various orientations, as most materials do not exist as a single crystal.

The crystallinity of oxidized and oxynitrided Nd thin films were characterized using a PANalytical Empyrean XRD system at diffraction angle, 2θ, of 15°-90° with a step time of 150 s and step size of 0.026°, operating at 40 kV and 30 mA with a scan rate of 0.02° per second. Copper (Cu Kα) with a wavelength (λ) of 0.154056 nm was employed by the system.A diffraction pattern plot (intensity of X-ray against angle 2θ) for each sample was obtained after scanning.

XRD peak broadening was utilized to determined crystallite size (D) and microstrain (ε) due to crystal defects such as dislocations (Venkateswarlu, Bose, & Rameshbabu, 2010). Thus, Bragg's peak is affected by D and ε, which increase the peak width and intensity, shifting the 2θ peak position(Prabhu, Rao, Kumar, & Kumari, 2014).This analysis is vital, as crystallite size results in peak broadening. This is caused by the finite size components diffracting incoherently with respect to one another. Meanwhile, non-uniform displacements of the atoms with respect to their reference-lattice positions results in broadening due to strain(Bushroa, Rahbari, Masjuki, & Muhamad, 2012). These data provide valuable information on crystal defects (K. H. Goh, A. Haseeb, & Y. H. Wong, 2016a). The number of electrical trapping sites at the grain boundary decreases with larger grain size (Zeng et al., 2013); thus,resulting in better electrical properties. On the other hand, electrical conductivity is affected by microstrain, as it is also associated with grain boundary structure (Tao, Xu, Li, & Zhu, 2012). Therefore, higher microstrain can be obtained with a larger grain size.

In this research, a simplified integral breadth method consisting of Debye-Scherrer analysis and Williamson-Hall (W-H) analysis was employed to calculate the values of crystallite size and microstrain(Fan, Liu, & Zhang, 2014b; A. Laha, A. Fissel, E. Bugiel, & H. Osten, 2007a; Pan et al., 2007). Based on Debye-Scherrer, the averagenanocrystallite size is outlined by Equation (3.2):

$$D = \frac{K\lambda}{\beta_D \cos\theta} \tag{3.2}$$

where D is the crystalline size, K is the shape factor, which is a constant (0.9), λ is the wavelength of Cu Kα (0.1541 nm), β_D is the peak width with half maximum intensity,and θ is the peak position. The strain induced due to distortion and crystal imperfection is given by Equation (3.3):

$$\varepsilon = \frac{\beta_s}{4\tan\theta} \tag{3.3}$$

where, β_s is the width at half maximum intensity. Combining Equations (3.2) and (3.3) gives Equations (3.4) and (3.5):

$$\beta_{hkl} = \beta_D + \beta_s \tag{3.4}$$

$$\beta_{hkl} = \frac{K\lambda}{D\cos\theta} + 4\varepsilon\tan\theta \tag{3.5}$$

The rearrangement of Equation (3.5) gives the W-H equation i.e. Equation (3.6):

$$\beta_{hkl}\cos\theta = \frac{K\lambda}{D} + 4\varepsilon\sin\theta \tag{3.6}$$

The graph of $\beta_{hkl}\cos\theta$ against $4\sin\theta$ was plotted. From the linear fit data, D is calculated from the y-intercept, which is $\frac{K\lambda}{D}$, and the ε calculated from the slope gradient.

3.4.2 FTIR Analysis

The FTIR spectroscopy is a characterization technique for identifying functional groups by obtaining the infrared spectrum of the absorption or emission of amaterial(Grill & Neumayer, 2003; Schmitt & Flemming, 1998). Both organic and inorganic samples can be identified via this method. Since molecules absorb infrared radiation, the chemical bonds vibrate and stretch, contract, and bend. This is classified as vibrational spectroscopy (Smith, 1998).

In this research, a FTIR analysis was conducted using a Perkin ElmerSpectrum 400 Fourier Transform infrared (FTIR) spectrometer. The scanning range was 1300–400cm^{-1} with a transmittance mode employed.

3.4.3 Raman Analysis

The Raman analysis is another type of vibrational spectroscopy. The FTIR spectroscopy is a characterization technique for identifying functional groups. Laser is used to irradiate sample with monochromatic radiation. Radiation may be reflected, absorbed, or scattered (Larkin, 2011). Even though FTIR is a great method to analyze functional groups, it is always accompanied with Raman analysis because the infrared spectrum might not have enough information or have misleading information, which makes the identification of unknown molecules more complicated (Smith, 1995).

. In this research, the Raman analysis was conducted using a Horiba Xplora One Raman spectrometer. Chemical bonding stability upon thermal oxidation and oxynitridation processes was measured. The scanning range was 0-1500 cm^{-1}.

3.4.4 HRTEM Analysis

HRTEM is a microscopy technique, which uses electron diffraction for structure characterization. It is an essential tool to characterize thin films, as electrons can pass through the sample easily (Adamson, 1990). An image is produced from the interaction between transmitted electron and sample. Later, this image is focused and magnified onto an imaging device.

Prior to the analysis, lamella preparation (Helios NanoLab 650) was used to cross-section the film. This was followed with Pt deposition on the surface for protection from ion bombardment resulting from the focused ion beam.

In this research, the cross-sectioned film was analyzed using a TECNAI G2 F20 HRTEM with an accelerating voltage of 20 to 200 kV and standard magnification of22 x to 930 kx. A field emission gun is used with a Schottky Field emitter as the electron source. Images were captured using a SC1000 ORIUS CCD camera, which enables a maximum resolution of up to 4008 ×2672 pixels with 14-bit dynamic range and 14 frames per second at 4x binning. This enables suitable sample segments to directly be displayed on screen. The thickness of the oxide and interfacial layer was also measured.

3.4.5 EDX Analysis

In this research, an EDX (Oxford Instrument X-MaxN 80T SDD detector) analysiswas used together with HRTEM to perform chemical analysis (Fitzgerald, Storey, & Fabian, 1993). Element composition of the sample is determined from the X-ray characteristics generated via the aid of an electron beam. EDX can be utilized to determine both the lateral distribution and individual point of the sample. An EDX detector measures the relativeabundance of emitted X-rays versus their energy by separating the characteristic X-raysof different elements into an energy spectrum. A typical EDX spectrum is plotted as X-raycounts versus energy (keV).

3.4.6 XPS Measurement

XPS is a common analysis tool for quantitative chemical analysis (Aydogan Gokturk et al., 2017). It is capable of defining elemental composition of the top surface of a solid up to 10 nm. It is a single-step process where electrons bound to an atom are ejected by a massless photon. As a result of this photon-electron interaction, a chargeless package of energy is produced. If the energy is adequate, an electron on the atom of the solid is emitted and the kinetic energy remaining on the emitted electron measured (van der Heide, 2011).

Measurement using XPS is done using both survey and narrow scan. The elemental chemical states were determined using a survey scan with energy of 280 eV for 10 min. Nd 3*d*, Si 2*p*, O 1*s*, N 1*s*, and C 1*s*were detected. The survey scan is followed with a narrow scan at 112-eV energy for 5 min to scan through each binding energy of the detected elements. A binding energy of 284.6 eV was used as a reference to compensate for the shifting effectof the XPS spectra. CasaXPS software was utilized to correct linear background and surface charge followed by deconvolution.

3.4.7 Scratch Testing

The scratch test is an efficient tool to analyze the interfacial adhesion of a thin film and substrate system (D Geetha et al., 2017). It is one of the nanotribological properties where a surface is scratched using a diamond tip. The load on the tip linearly increases to induce a shear force on the film, which is proportional to the applied load and transmitted throughout the sample (Yau et al., 2011; Zhang, Sun, Fu, & Du, 2005). Wear resistance is directly related to microstructure (Havey, Zabinski, & Walck, 1997).

The scratch test was conducted using a Microscratch Tester produced by Micro Material Limited. The load is applied progressively with a loading rate of 2.5 mN/s where the maximum load is 800 mN. The load is applied after 50 µm. A diamond indenter of 25.0±2.0 µm was utilized to carry out the scratch test.

3.4.8 Optical Microscope Imaging

The microscope is a tool for penetrating and gaining information at the submicroscopic level (Török & Kao, 2013). The magnified image of a sample is produced via the use of visible light, which is later reflected onto the retina of the user. This tool consists of two important elements, which are the objective lens and condenser. The objective lenscollects light diffracted by the specimen, resulting in a magnified real image. Meanwhile, the condenser focuses light from the illuminator onto a small area of the sample(Murphy & Davidson, 2012).

An Olympus optical microscope model bx61 was used to analyze the scratch path obtained from the scratch test. Magnifications of 5x, 10x, 20x, and 50x were utilized to observe the scratch mark uptothe microstructural level. This enables the determination of changes at the microstructure level before and after the critical point.

3.4.9 Current-Voltage Measurement

I-V measurements were carried out using a BPW-800 8" probe station assisted with a Keithley 4200 SCS. The sweep range and frequency were set to 0–8 V and 50 Hz. The *I-V* data was converted to leakage current density versus electrical breakdown field (*J-E*). The plot was utilized to extract current density at various electrical fields. The E value was obtained using Equation (3.7):

$$E = \frac{(V_g - V_{FB})}{t_{ox}} \tag{3.7}$$

where, V_g is the gate voltage, V_{FB} is the flatband voltage, and t_{ox} is the oxide thickness.

The MOS capacitors show two-step oxide breakdowns. This can be attributed to the pre-maturely broken down (*ES*) oxide or interface layer at a lower electrical field. Meanwhile, the second breakdown is due to the other layer, which blocks the carrier until it is broken down electrically (*EH*) at a higher electrical field(T. Kurniawan, K. Y. Cheong, K. A. Razak, Z. Lockman, & N. Ahmad, 2011b; Kurniawan, Wong, et al., 2011; Wong & Cheong, 2012a).

3.4.9.1 Fowler-Nordheim Tunneling Analysis

Current conduction in a thin gate oxide can be explained via the F-N type current conduction (Päiväsaari et al., 2005). In this type of leakage, the carrier tunnels through a triangular barrier into the conduction, where the valence band of the insulator F-N tunneling is characterized by the barrier, which is triangular, and tunneling is only through the insulator layer(Demkov & Navrotsky, 2006).

A F-N tunneling regression plot was plotted based on J-E data. The barrier height ($Ø_B$) between conduction band edge and between Si and interface was calculated as per Equations (3.8)-(3.10) below:

$$J_{FN} = AE^2 \exp(-\frac{\mathrm{B}}{\mathrm{E}}) \tag{3.8}$$

where,

$$A = 1.54\, x\, 10^{-6} \left(\frac{m}{m_{ox}}\right) ø_B \tag{3.9}$$

$$B = 6.83\, x\, 10^{7} \left(\frac{m_{ox}}{m}\right) ({ø_B}^3)^{\frac{1}{2}} \tag{3.10}$$

Rearranging Equation (3.8) gives Equation (3.11):

$$\ln\left(\frac{J}{E^2}\right) = -B\, \left(\frac{1}{E}\right) + \ln A \tag{3.11}$$

Based on the F-N tunneling regression plot (Equation (3.11)), the gradient is equal to B and the y-intercept is equal to A. Meanwhile, the effective mass of high-k is assumed to be 0.3m for calculation purposes (Salmani-Jelodar, Ilatikhameneh, Kim, Ng, & Klimeck, 2015).

3.4.10 High Frequency of Capacitance-Voltage Measurement

The same BPW-800 8" probe station together with the Keithley 4200 Semiconductor Characterization System (SCS), as mentioned in Section 3.4.8, were used for capacitance-voltage (C-V) measurements. Both forward bias (from inversion to accumulation) and reverse bias (from accumulation to inversion) were swept by a linear DC voltage ramp. The bias sweep was run at -8 V to +2V and +2 V to -8 V with a sweep rate of 0.1 V per second. From the C-Vmeasurements, the capacitance of Nd_2O_3 ($C_{Nd_2O_3}$), k-value, flatband voltage (ΔV_{FB}), effective oxide charge (Q_{eff}), slow trap density (STD), and total interface trap density (D_{it}) were determined.

3.4.10.1 *k*-value

The accumulation capacitance value was utilized to calculate the k-value of the samples, as per Equation (3.12) (Goh et al., 2016a; Kurniawan, Wong, et al., 2011),

$$C = \frac{kA\epsilon_0}{\mathrm{t}} \tag{3.12}$$

where, C is the capacitance of the oxide, k is the effective dielectric constant, A is the area of the capacitor, ϵ_0 is the permittivity of free space (8.85×10^{-12} Fm^{-1}), and t is the thickness of the oxide film. Based on Equation (3.12), C is directly proportional to k-value and inversely proportional to t. A and $\epsilon_0$have no influence on the C value, as both are constant.

3.4.10.2 Effective Oxide Charge and Slow Trap Density

Q_{eff}andSTD of the samples were calculated based on Equations (3.13) and (3.14) below (Kurniawan, Wong, et al., 2011; Wong & Cheong, 2012a),

$$Q_{eff} = \frac{C_{ox}\,\Delta V_{FB}}{\mathrm{qA}} \tag{3.13}$$

$$STD = \frac{\Delta \mathrm{V} \mathrm{C_{ox}}}{\mathrm{qA}} \tag{3.14}$$

where, C_{ox} is the capacitance of Nd_2O_3, ΔV_{FB} is the flatband voltage, q is the electronic charge (1.6×10^{-19} C), A is the area of the capacitor, and ΔV is the difference between the flatband voltages of the hysteresis curve.

3.4.10.3 Interface Trap Defect Density

D_{it} was calculated using the Terman method, as outlined in Equation (3.15) below(Kurniawan, Wong, et al., 2011; Wong & Cheong, 2012a),

$$D_{it} = \frac{\Delta \mathrm{V_g} \mathrm{C_{ox}}}{\text{ø}_\mathrm{s}\,\mathrm{qA}} \tag{3.15}$$

where, $ø_s$ is the surface potential of Si at a specific gate voltage, V_g. The surface potential of a particular capacitance is taken from an ideal MOS capacitor. The gate voltage is obtained from the experimental C-V curve of the same capacitance as that of $ø_s$. The steps were then repeated for other data points until a relevant D_{it} against (Ec – E) curve is obtained.

CHAPTER 4: RESULTS AND DISCUSSION

4.1 Introduction

This chapter presents the results and discussion of this research. It consists of two main parts, which are thermal oxidation and thermal oxynitridation. Each part is further discussed in detail, as follows:

(i) Effects of thermal oxidation duration at an oxidation temperature of 700°C on sputtered Nd thin film on Si substrate;

(ii) Effects of thermal oxidation temperature at oxidation duration of 15 min on sputtered Nd thin film on Si substrate;

(iii) Effects of thermal oxynitridation duration at an oxynitridation temperature of 700°C on sputtered Nd thin film on Si substrate; and

(iv) Effects of thermal oxynitridation temperature at oxynitridation duration of 15 min on sputtered Nd thin film on Si substrate.

4.2 Effects of Thermal Oxidation Duration on Sputtered Nd Thin Film on Si Substrate

4.2.1 XRD Analysis

Figure 4.1 shows the XRD patterns of the oxidized Nd samples at various durations (5 min, 10 min, 15 min, and 20 min). Two distinct peak peaks were observed at 33.0° and 69.0°. These peaks belongs to cubic (c)-Si(1 1 2) and c-Si(4 0 0). These peaks were confirmed based on the Inorganic Crystal Structure Database (ICSD) with reference code 98-001-6569. c-Nd_2O_3wasdetected at 68.8°, 74.9°, and 75.8°, corresponding to (1 1 8), (2 5 7), and (2 5 7), respectively. These peaks were confirmed based on ICSD 98-009-6204. Multiple phases of SiO_2-monoclinic (m), hexagonal (h), and tetragonal (t) were detected. Four peaks belonging to m-SiO_2 were detected at 46.2°, 47.8°, 54.6°, and 89.4°, corresponding to (2 2 6), ($9\ 1\ \overline{3}$), ($5\ 1\ \overline{13}$), and (2 0 1), respectively. These peaks were confirmed by ICSD 98-001-0176 and ICSD 98-002-425. On the other hand, three peaks belonging to h-SiO_2 were detected at 69.4°, 75.3°, and 75.6°, corresponding to (0 3 0), (1 0 4), and (3 0 2), respectively. These peaks were confirmed based on ICSD 98-001-6336, ICSD 98-001-6333, and ICSD 98-000-0174. In addition, a single peak belonging to t-SiO_2 was detected at 76.4°, corresponding to (0 4 0).These peaks were confirmed based on ICSD 98-000-9327. Meanwhile, five peaks belonging to orthogonal (o)-$Nd_2Si_2O_7$ were detected at diffraction angles of 55.4°, 56.3°, 61.8°, 66.5°, and 67.4°, corresponding to (2 1 6), (3 1 3), (1 3 7), (1 6 0), and (2 0 8), respectively. These peaks were confirmed based on ICSD 98-001-6051. The detection of SiO_2 and $Nd_2Si_2O_7$ shows the presence of an interfacial layer between the Si substrate and oxide layer.

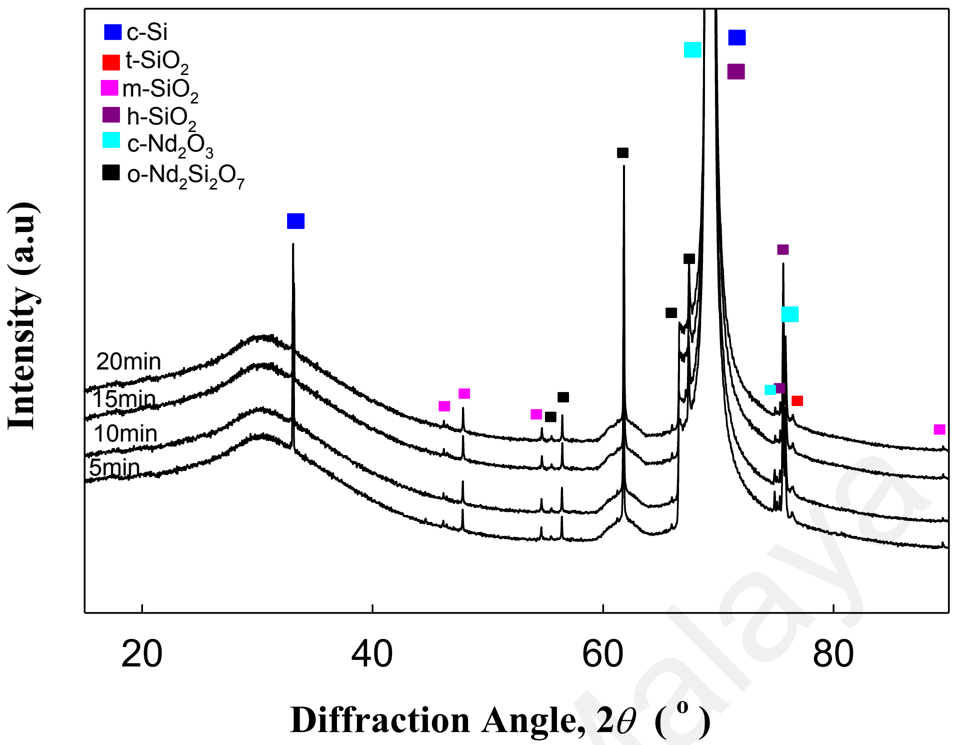

Figure 4.1: XRD patterns of oxidized Nd samples at various durations (5 min, 10min, 15 min and 20 min)

Figure 4.2 shows the highest intensities of c-Nd_2O_3, m-SiO_2, h-SiO_2, t-SiO_2, and o-$Nd_2Si_2O_7$ in order to determine the effect of oxidation duration on the interfacial layer. The plot reveals that h-SiO_2 has the highest intensity followed by c-Nd_2O_3. Meanwhile, the lowest intensity is t-SiO_2. The sample oxidized for 15 min recorded the highest intensity for c-Nd_2O_3 and o-$Nd_2Si_2O_7$. In addition, the lowest intensity is shown bym-SiO_2. The highest intensity for m-SiO_2 and t-SiO_2 is shownat10 min. Meanwhile, the sample oxidized for 20 min shows the highest intensity for h-SiO_2.

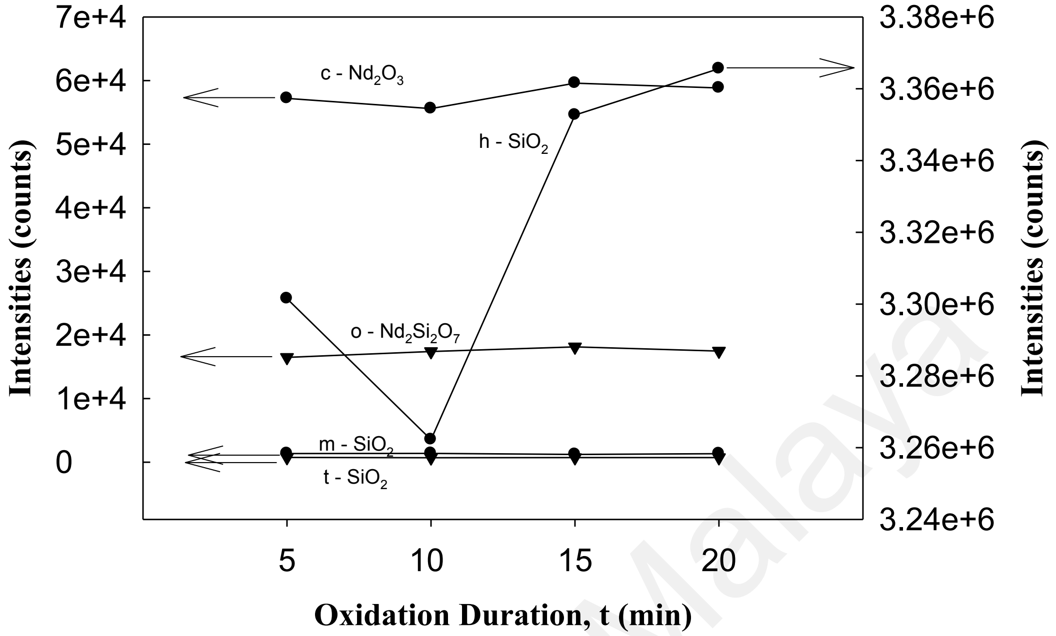

Figure 4.2: The highest intensities of c-Nd_2O_3, m-SiO_2, h-SiO_2, t-SiO_2, and o-$Nd_2Si_2O_7$ for oxidized Nd samples at various durations (5 min, 10 min, 15 min, and 20 min)

4.2.1.1 Williamson-Hall Analysis

As mentioned in Section 3.4.1, a W-H analysis was employed to determine the crystallite size and microstrain of each element detected in the XRD analysis. A graph of $\beta_{hkl}\cos\theta$ against $\sin\theta$, for Nd_2O_3, SiO_2, and $Nd_2Si_2O_7$ is illustrated in Figure.4.3.

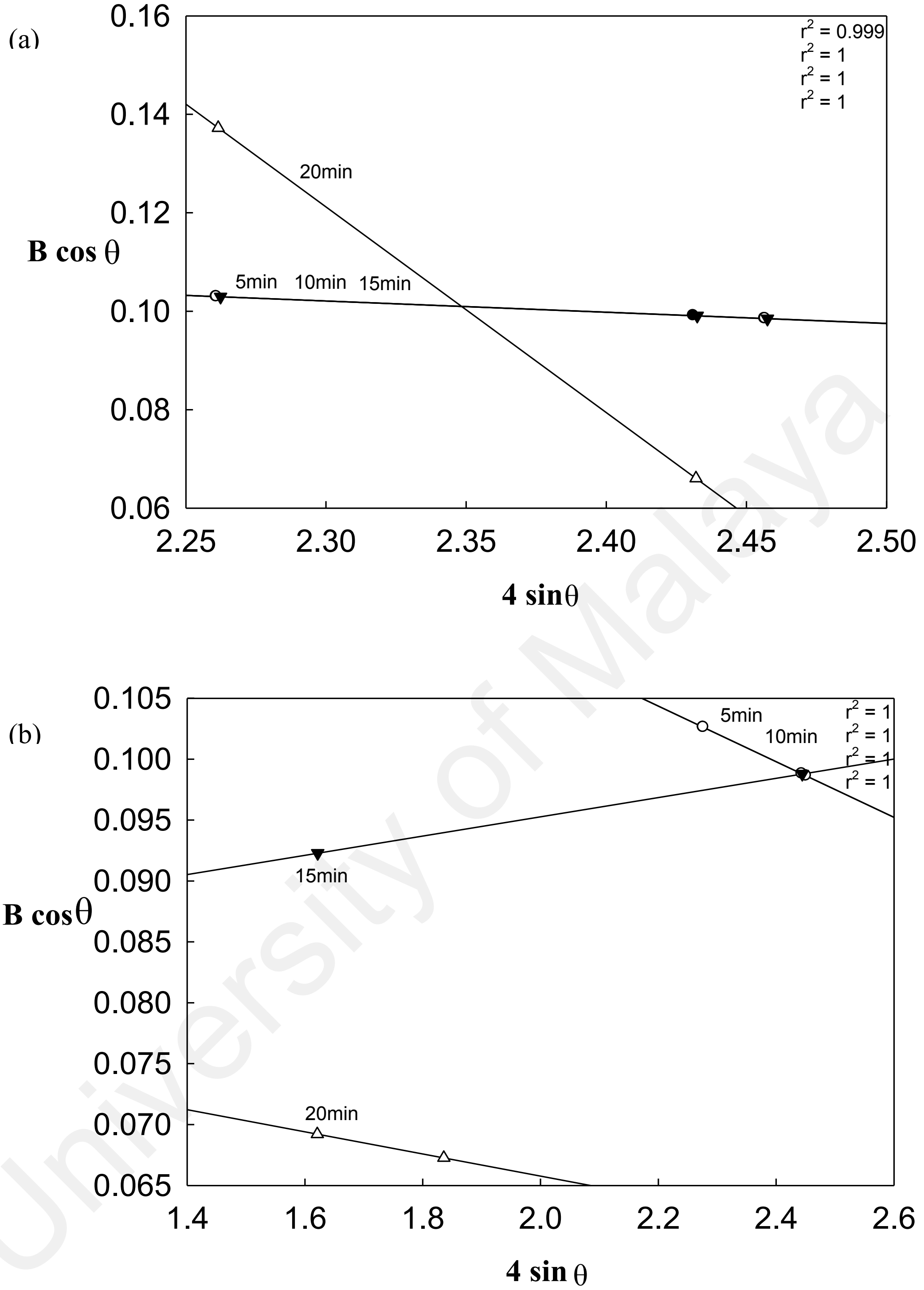

Figure 4.3: W-H plot of: (a) Nd_2O_3;(b) SiO_2; and (c) $Nd_2Si_2O_7$ of the oxidized Nd samples at various durations (5 min, 10 min, 15 min, and 20 min)

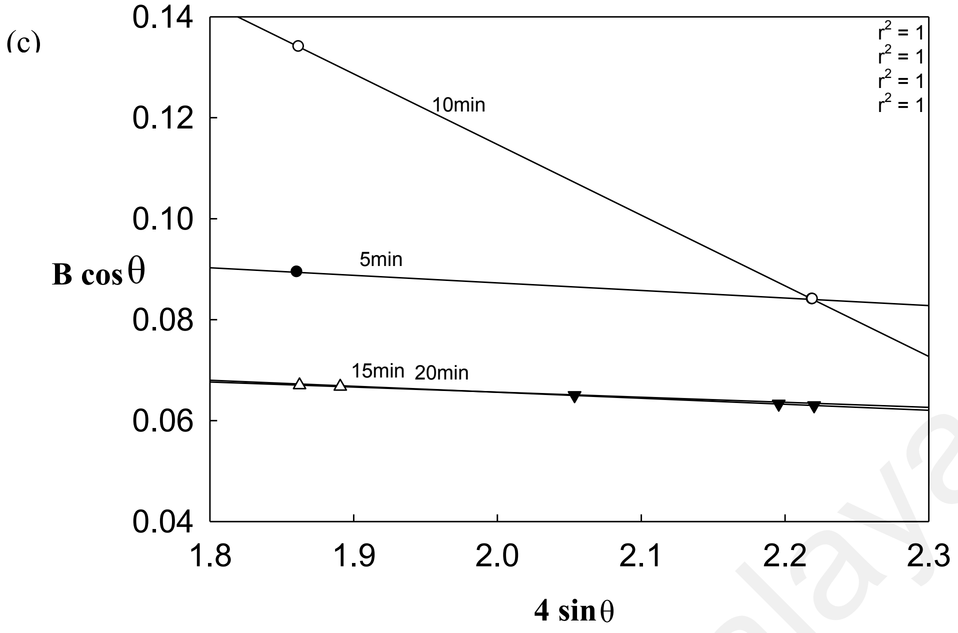

Figure 4.3: *(continued)* W-H plot of: (a) Nd_2O_3;(b) SiO_2; and (c) $Nd_2Si_2O_7$ of the oxidized Nd samples at various durations (5 min, 10 min, 15 min, and 20 min)

Figure 4.4 shows the microstrain and crystallite size of Nd_2O_3, $SiO_2$and $Nd_2Si_2O_7$. All the samples posses negative microstrain for all the compounds, except sample oxidized for 15 min for SiO_2. Sample oxidized for 5 min, 10 min and 15 min shows same microstrain values and crystallite size for Nd_2O_3. Additionally, sample oxidized for 10 min shows the lowest microstrain values for both SiO_2 and $Nd_2Si_2O_7$. Microstrain posses direct relationship with crystallite size (Tao et al., 2012). As crystallite size decreases, the microstrain also decreases until it reaches negative value. However, when the crystallite size increases at 15 min, it exhibit positive and higher microstrain. Meanwhile, sample oxidized for 20 min have the lowest crystallite size and microstrain value and of Nd_2O_3. On the other hand, sample oxidized for 15 min shows second highest values for the both characteristics.

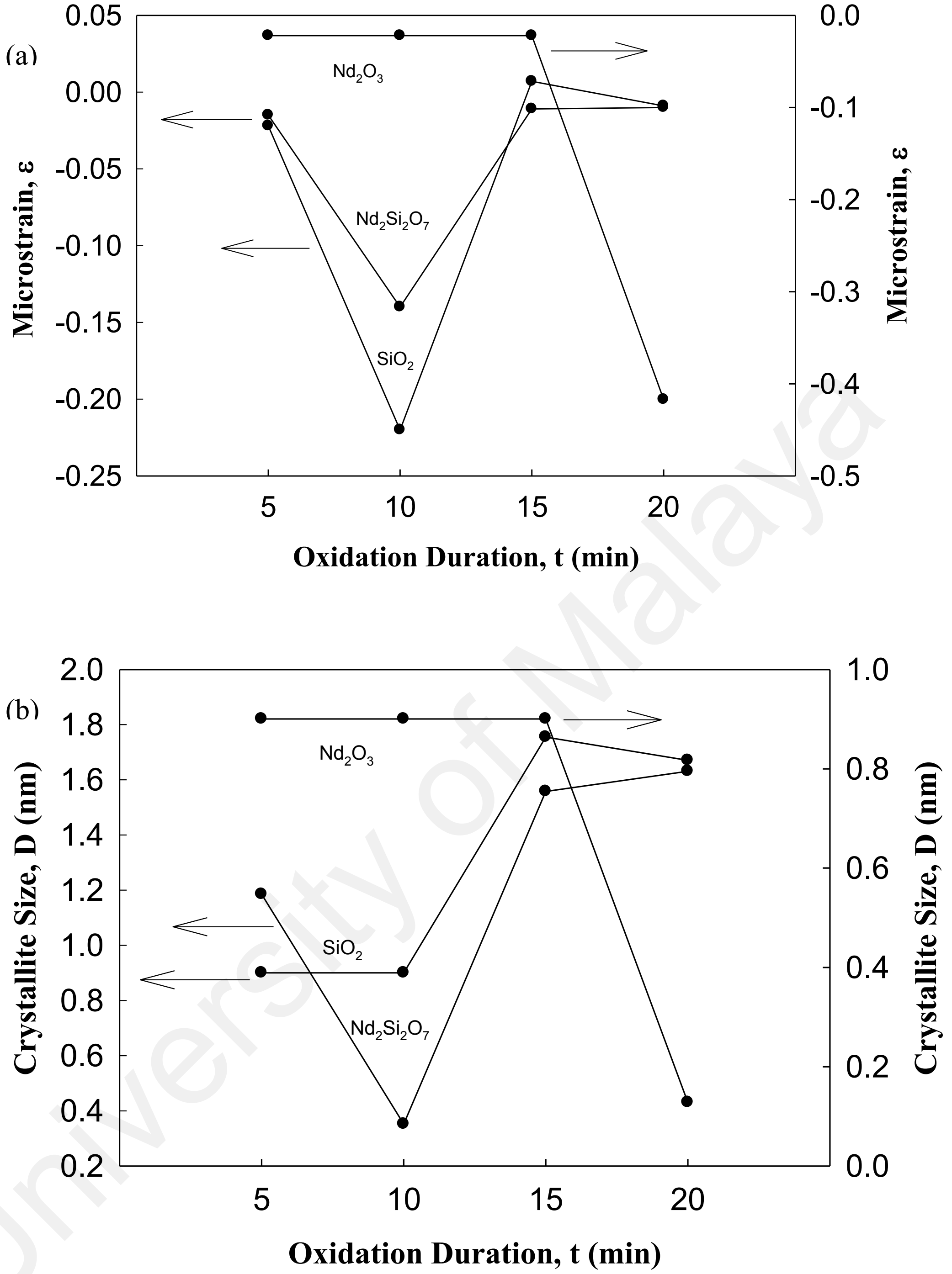

Figure 4.4: (a) Microstrain (b) crystallite size of Nd_2O_3, SiO_2, and $Nd_2Si_2O_7$ of the oxidized Nd samples at various durations (5 min, 10 min, 15 min, and 20 min)

4.2.2 FTIR Analysis

The FTIR results of the oxidized Nd samples at various durations (5 min, 10 min, 15 min, and 20 min) are shown in Figure 4.5.A Si-Si vibration mode originating from the Si substrate was detected at 613 cm^{-1} (Smith, 1998). The peak broadens until it almost disappears at 20min. A vibration mode belonging to Nd-O was detected at 558 cm^{-1} and 501 cm^{-1} (Päiväsaari et al., 2005). Both peaks sharpened as the oxidation duration increased. A Si-O-Si assymmetric stretching mode was detected at 1204 cm^{-1} and 1041cm^{-1} (T. Kurniawan, K. Cheong, K. Razak, Z. Lockman, & N. Ahmad, 2011a). The peak at 1204cm^{-1} broadens while the intensity of peak 1041 cm^{-1} increases with increased oxidation duration. A peak attributed to the rocking, bending, and stretching of Si-O was detected at 805cm^{-1}(Smith, 1998). A Si-O vibration mode was detected at 478 cm^{-1} and 471 cm^{-1}(Lippincott, Van Valkenburg, Weir, & Bunting, 1958; Viana, da Silva, & Morimoto, 2001). The peak at 478 cm^{-1} sharpened as oxidation duration increased. Meanwhile, peak 471 cm^{-1}was only visible for the sample oxidized for 5min. Additionally, a Si-O mode was detected as Si-O-Si and Si-O bending mode. Si-O-Si bending was detected at 456 cm^{-1}(Lippincott et al., 1958; Viana et al., 2001). This peak sharpens when oxidation duration increases from 5 min to 15 min and broadens at 20 min. The peak attributed to Si-O bending was detected at 443 cm^{-1}, 431 cm^{-1}, 419 cm^{-1}, 411 cm^{-1}, and 403 cm^{-1}(Lippincott et al., 1958; Viana et al., 2001). The peak at443 cm^{-1} was shifted at5 min and 10 min and then sharpened at 15 min and decreased at 20 min. The peak 431 cm^{-1}sharpenedas oxidation time increased. Meanwhile, peak 419 cm^{-1}wasonly visible at 15 min. On the other hand, peak 411 cm^{-1}wasnot visible at15 min. This peak sharpens as oxidation duration increases from 5min to 10min and then became visible at 20 min. Lastly, peak 403 cm^{-1}sharpenedwhen oxidation time increased from 5min to 10 min, and then decreased at 15 min. The last unknown peak at 925 cm^{-1} is attributed to silicate vibration (Ganesan, Dhananjeyan, Sarangapani, &Renganathan, 2008; Smith, 1998). Eventhough the actual peak list is not available, this was confirmed based on other metal silicates such as hafnium silicate, zirconium silicate, and samarium silicate. The peak shows almost negligible difference with increased oxidation duration.

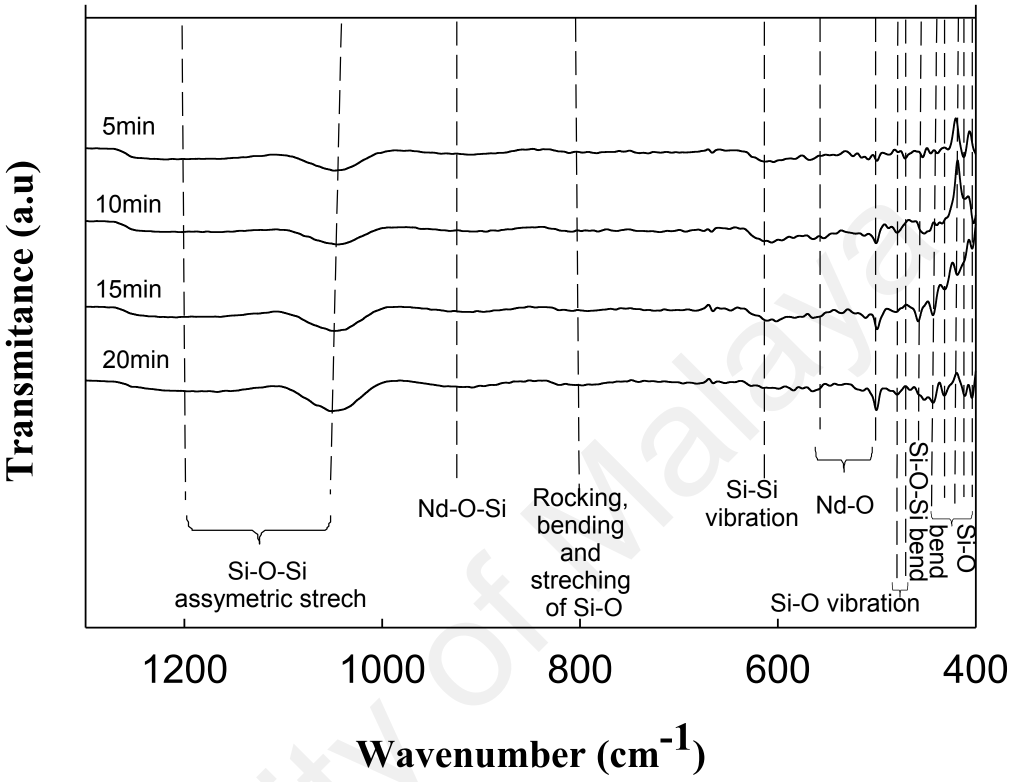

Figure 4.5: Transmittance spectra of oxidized Nd samples at various durations (5 min, 10 min, 15 min and 20 min)

4.2.3 Raman Analysis

Figure 4.6 shows the Raman analysis result of the oxidized Nd samples at various durations (5 min, 10 min, 15 min, and 20 min). Si wavelength was detected at 525 cm^{-1} (Wong & Cheong, 2011a). The intensity decreased from 5 min to 10 min and later increased up to20 min. Two different peaks belonging to Nd_2O_3 were detected at 112 cm^{-1}and 312 cm^{-1} (Kurniawan, Cheong, et al., 2011b). Both peak intensities decreased up to15 min and increased at 20 min. Peak 925 cm^{-1} was assigned to SiO_2(Nyquist & Kagel, 2012). The peak shows a similar trend to that of Nd_2O_3, where the intensity decreased until 15 min and increased at 20 min. Additionally, the unidentified peak at17 cm^{-1} was attributed to neodymium silicate, as the compound was detected in the XRD and FTIR analysis. The lowest intensity of silicate was at 5 min, followed by 15 min and 20 min with the highest intensity observed at 10 min. The Raman findings support the existence of an interfacial layer consisting of SiO_2 and $Nd_2Si_2O_7$.

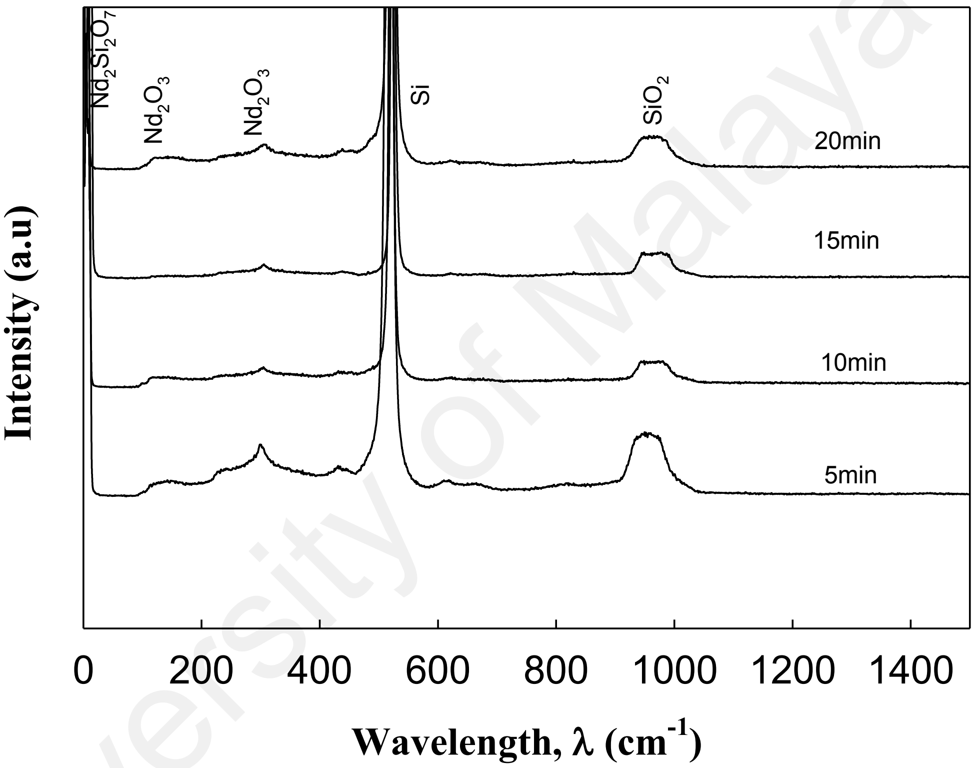

Figure 4.6: Raman spectra of oxidized Nd samples at various durations (5 min, 10 min, 15 min and 20 min)

4.2.4 HRTEM Analysis

The HRTEM analysis results of oxidized Nd samples at various durations are shown in Figure 4.7. Interfacial layers were detected in between the Si substrate and oxide layer. This observation is in agreement with the XRD, FTIR, and Raman analysis findings. The main difference that can be clearly seen is that the sample oxidized for 15 min possesses the thinnest oxide and a single interfacial layer. On the other hand, the rest of the samples showed two distinct interfacial layers. A summary of sample thickness variation is shown in Figure 4.8.

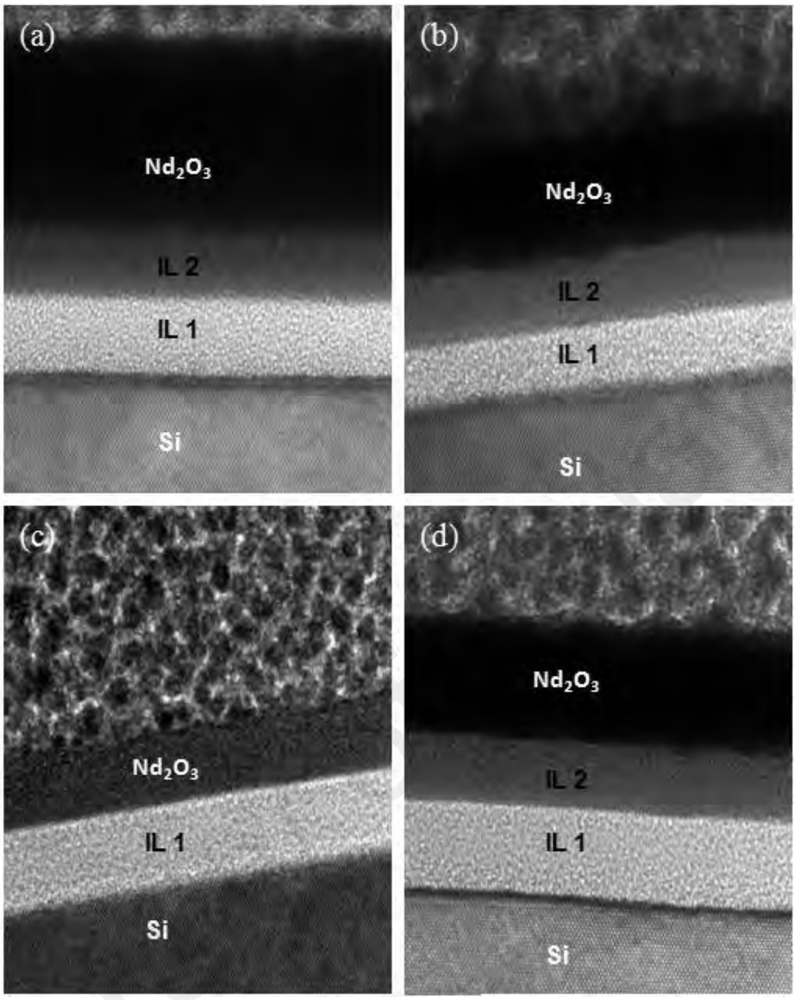

Figure 4.7: HRTEM images of oxidized Nd samples at various durations: (a) 5 min; (b) 10 min; (c) 15 min; and (d) 20 min

.

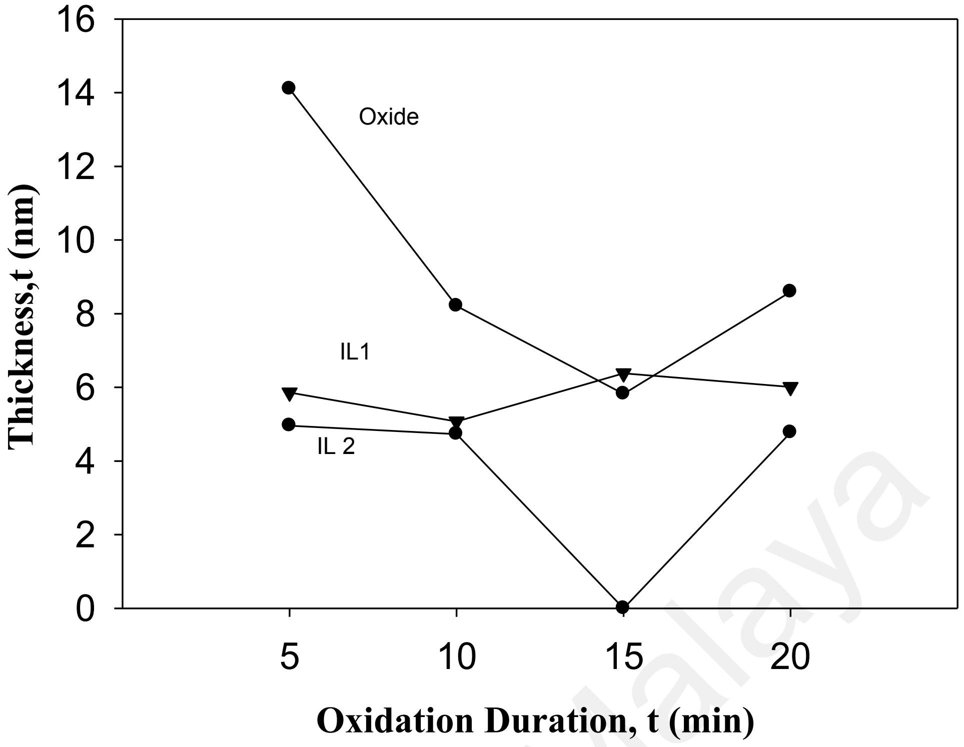

Figure 4.8: Thickness variation of each layer according to oxidation duration

Up until 15 min, the oxide layer thickness reduces and then increases at 20 min. Meanwhile, interfacial layer 1 increases until 15 min and decreases at 20 min. On the other hand, interfacial layer 2 decreases until 15 min, where it disappears at this duration and appears again at 20 min. However, the oxide layer of the sample oxidized for 15 min is thinner than the interfacial layer. This is result of temperature aided sintering effect which results in smaller grain size. Thus, atoms are more consolidate which leads to single interfacial layer. An oxidation model was proposed based on these findings, as shown in Figure 4.9.

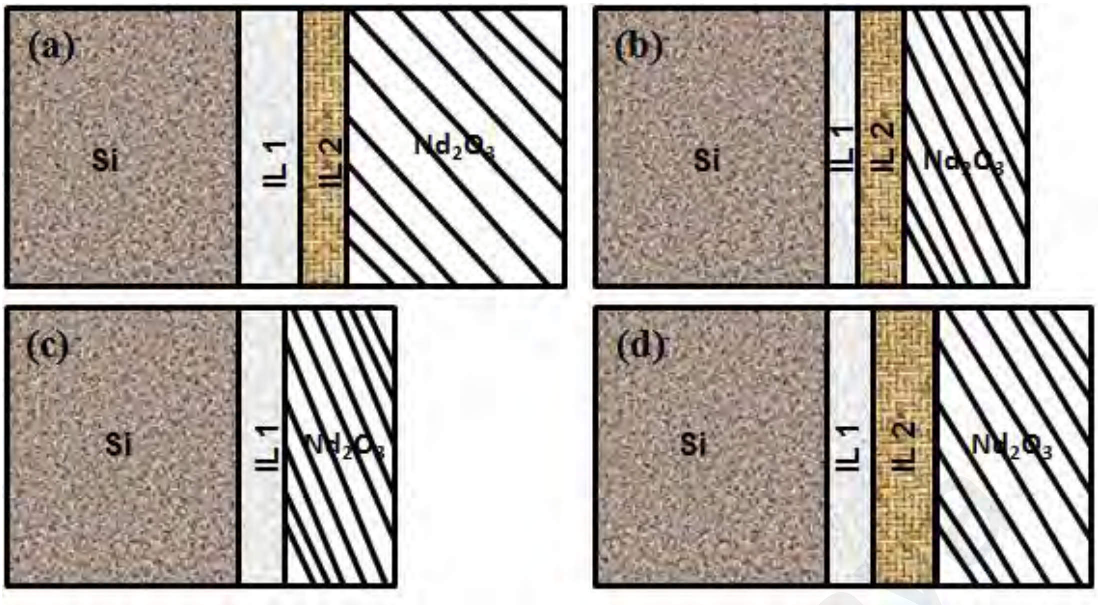

Figure 4.9: Layer distribution model for different oxidation durations: (a) 5 min; (b) 10 min; (c) 15 min; and (d) 20 min

At the initial oxidation state, the oxidation rate was 0.047 nms^{-1}, which is the highest value of all four durations. This resulted in the thickest oxide layer at 5 min. The XRD, FTIR, and Raman results reveal that the interfacial layer consists of SiO_2 and $Nd_2Si_2O_7$. Based on these findings, it can be assumed that SiO_2 is the layer closest to Si (E. Bugiel et al., 2005; Laha et al., 2007b). As the oxygen atom diffuses in, the Si and O_2 atoms bond with each other. Meanwhile, the second interfacial layer is identified as $Nd_2Si_2O_7$. This is due to the Nd atoms diffusing together with O_2 atoms; where as the Si atoms diffuse out and results in silicate bonding (Jayanti, Yang, Lichtenwalner, & Misra, 2010b). Based on these findings, the chemical compound present in each interfacial layer is summarized in Table 4.1. The thickness of the silicate interfacial layer decreases at 10 min. This could be a result of the longer oxidation duration, where the oxidation rate decreased; this rate decreases as a result of the consolidation of atoms. The thermal energy produces a sintering effect and the atoms become more compact (Kang, 2004). The duration is optimized at 15min, as only a single interfacial layer is observed. At this duration, the atoms are more compact than the 5 min and 10 min durations. The amorphous single interfacial layer consists of a mixture of both SiO_2 and $Nd_2Si_2O_7$. At this duration also, the oxidation rate and diffusion rate decreases and, as a result, the total thickness including both the interfacial layer and oxide layer does not vary much from the thickness of the deposited Nd (11 nm). The decrease in oxidation rate and diffusion rate prevents the formation of a distinct layer. On the other hand, as the oxidation duration increases to 20 min, the thickness of the oxide and interfacial layer increases again and becomes thicker than the thickness at 10 min. After the consolidation of atoms at 15 min, the oxidation rate increases due to a longer oxidation time at 20 min. At longer oxidation durations, there is more oxygen supply. As a result, the oxidation rate increases and results in more bonding formations. A reverse effect can also be seen where the consolidation of atoms become less pronounced.

Table 4.1: Interfacial layers compound by oxidation durations

Oxidation duration (min)	**Oxide layer**	**IL 1**	**IL 2**
5	Nd_2O_3	SiO_2	$Nd_2Si_2O_7$
10	Nd_2O_3	SiO_2	$Nd_2Si_2O_7$
15	Nd_2O_3	$SiO_2 + Nd_2Si_2O_7$	Does not exist
20	Nd_2O_3	SiO_2	$Nd_2Si_2O_7$

Consolidation of atoms results in smaller grain size. As the consolidation of atom more pronounce at oxidation duration of 15 min, the grain size of SiO_2 and $Nd_2Si_2O_7$ is smaller compared to rest of the durations. This results in formation of interfacial layer with inclusion of SiO_2 and $Nd_2Si_2O_7$ rather than two distinct interfacial layer.

4.2.5 Scratch Test

Figure 4.10 shows the optical micrograph of scratch tracks and the graphs of depth versus distance and load versus distance of oxidized Nd samples at various durations (5 min, 10 min, 15 min, and 20 min). The critical load (L_c) is the minimum load that results in adhesive failure. This is due to different mechanical properties of substrate and thin film, which leads to discontinuity of shear stress at the interface (Zhang et al., 2005). Optical microscope observation was used to investigate the scratched surface. L_c was determined by sudden alterations in the graph of profile of depth against distance. At the same time higher the L_c, the higher the wear resistant property. The sample oxidized for 10 min showed the highest L_c, whereas the lowest L_c was observed for the sample oxidized for l5 min. The sample with the lowest thickness had the lowest L_c. The critical load values for all samples are more than 780 mN. This proves that thickness affects mechanical properties (D. Geetha, Joice Sophia, Radhika, & Arivuoli, 2017). Although the thickness of the sample oxidized at 10 min possesses lower thickness than the rest of the samples ,it might still posses a stronger Nd-O bonding, which results in better scratch resistance (Yau et al., 2011). Prior to that, the L_c of all samples except for the sample oxidized for 10 min experienced elastic-plastic deformation (L_{e-p}), after which a more uniform width was achieved after this point. The stronger Nd-O bonding might contribute to better scratch resistance. Table 4.2 shows the L_c and scratch length of oxidized Nd samples at various durations. The sample with the highest L_c has the shortest scratch length and vice versa. Thus, the sample oxidized at 10 min has better scratch resistance.

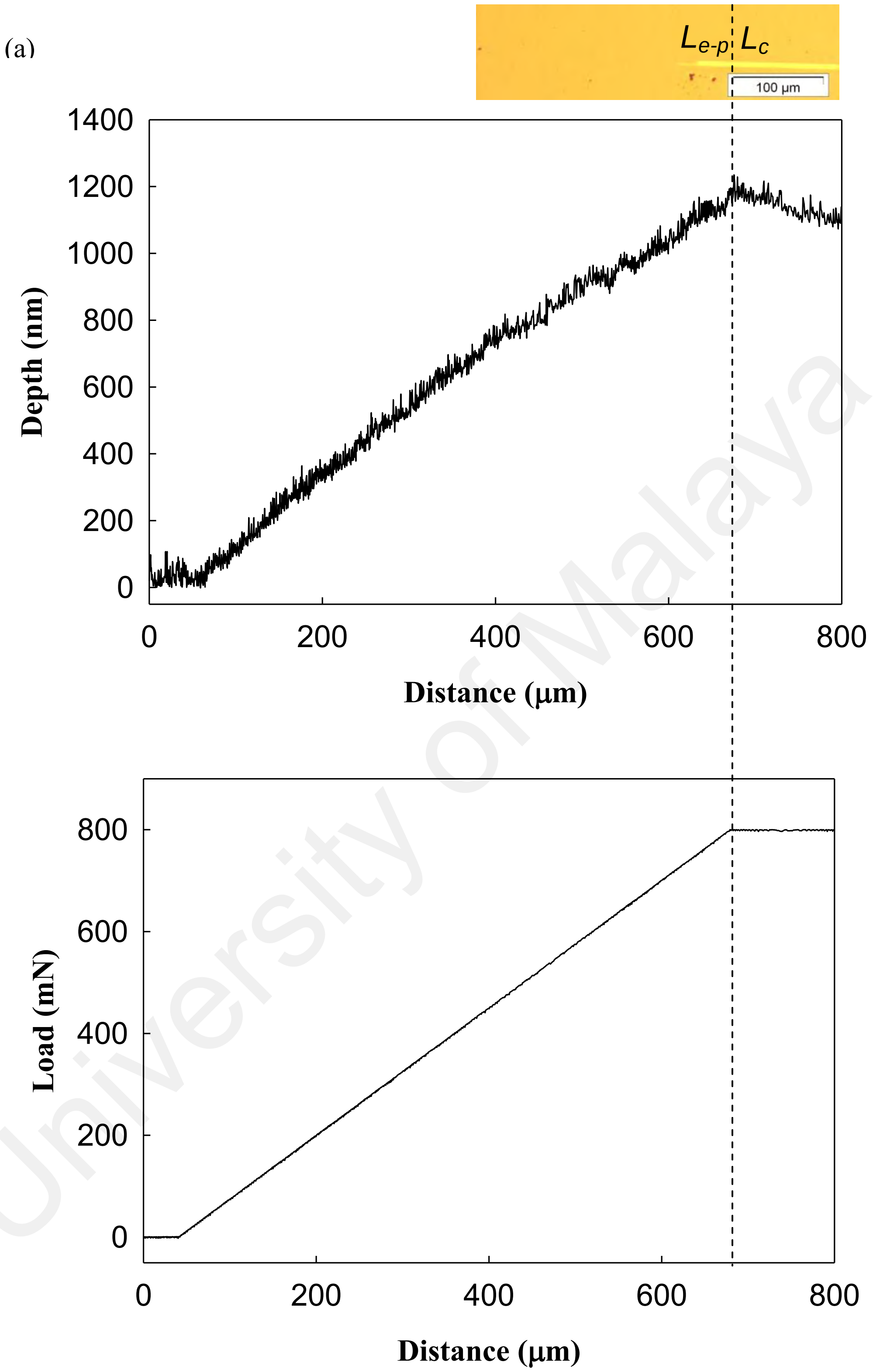

Figure 4.10: Optical micrograph of scratch tracks and graphs of depth versus distance and load versus distance of oxidized Nd samples at various durations: (a) 5 min;(b) 10 min; (c) 15 min; and(d) 20 min

(b)

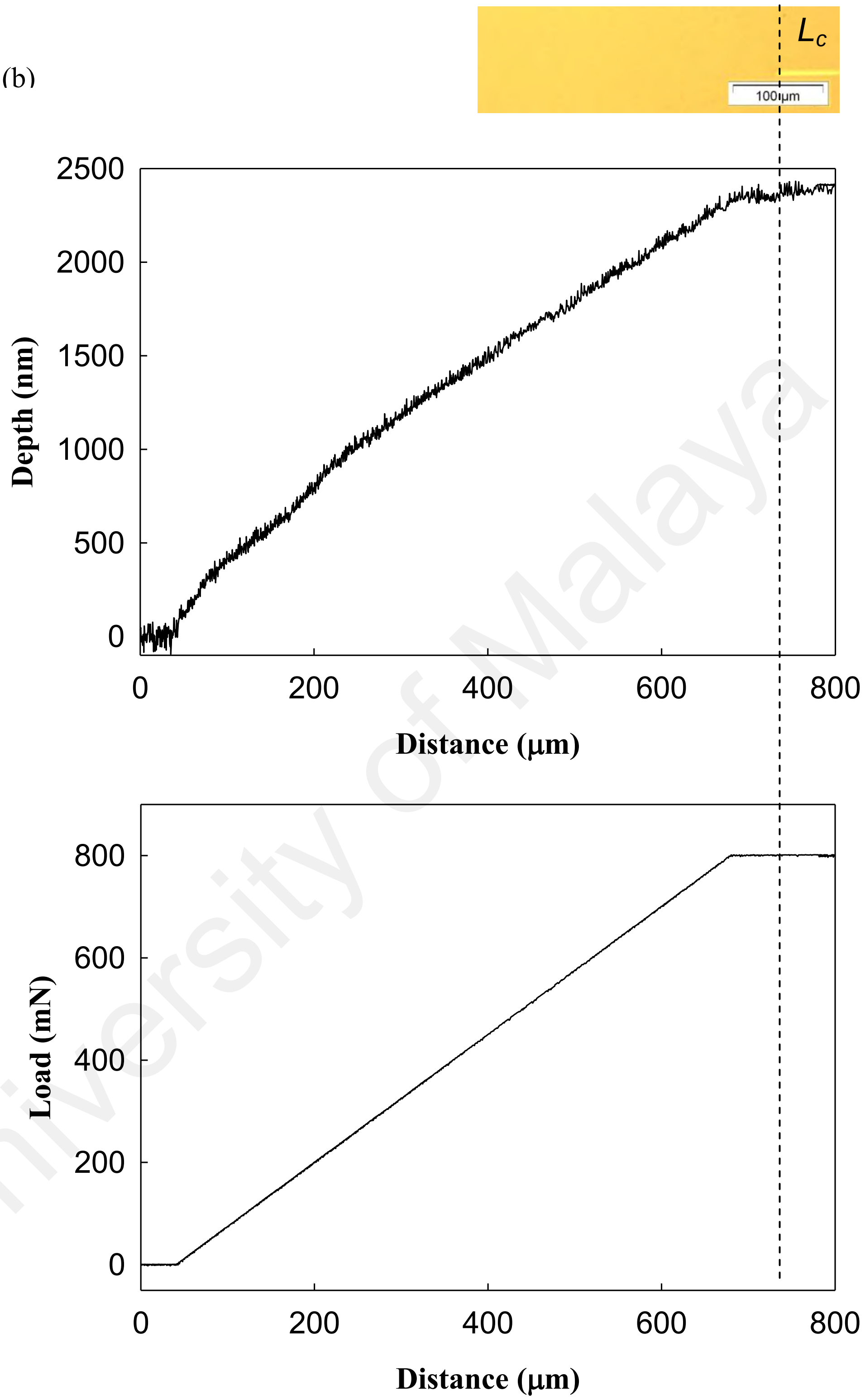

Figure 4.10: (*continued*) Optical micrograph of scratch tracks and graphs of depth versus distance and load versus distance of oxidized Nd samples at various durations: (a) 5 min;(b) 10 min; (c) 15 min; and(d) 20 min

(c)

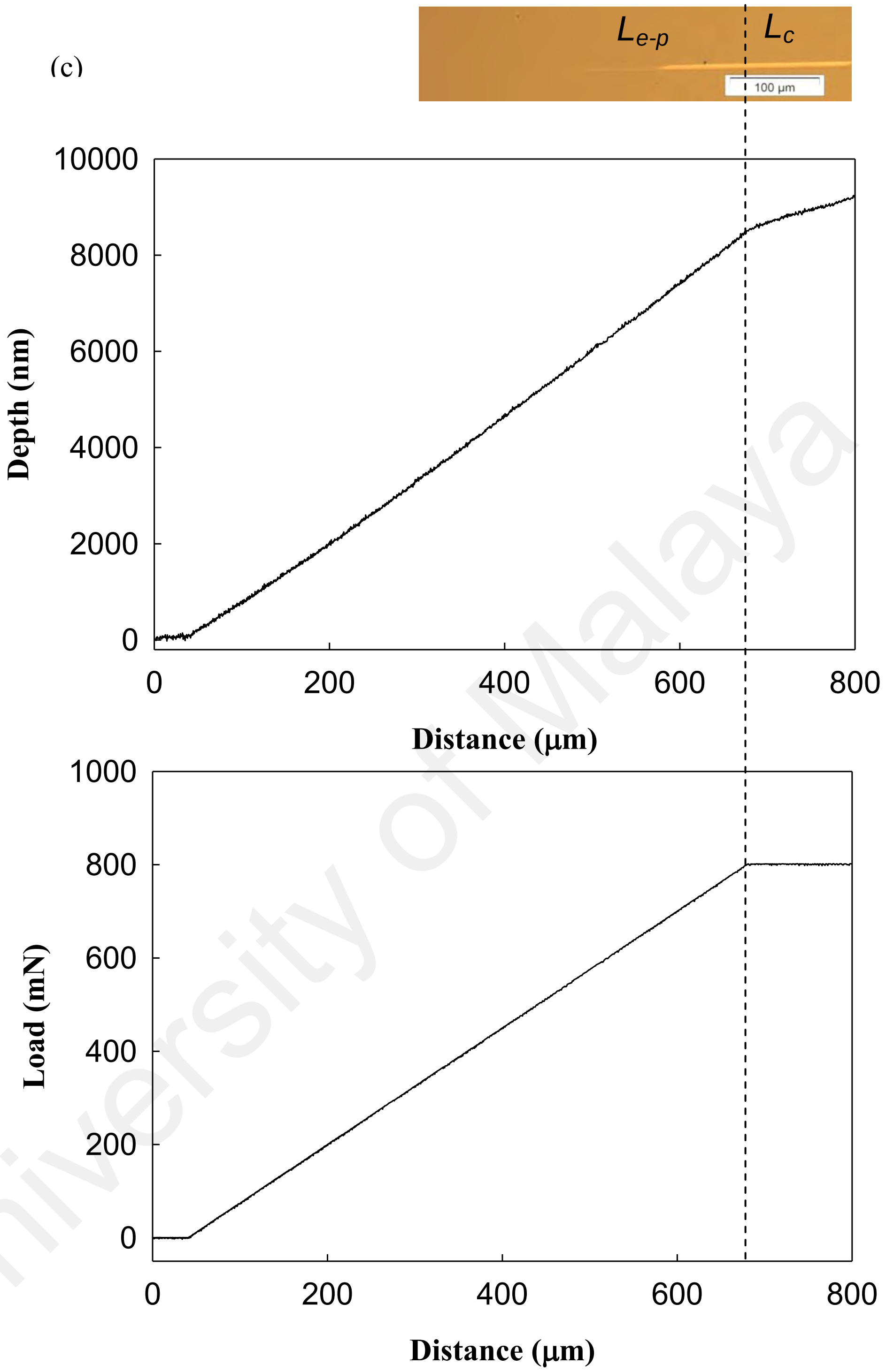

Figure 4.10: (*continued*) Optical micrograph of scratch tracks and graphs of depth versus distance and load versus distance of oxidized Nd samples at various durations: (a) 5 min;(b) 10 min; (c) 15 min; and (d) 20 min

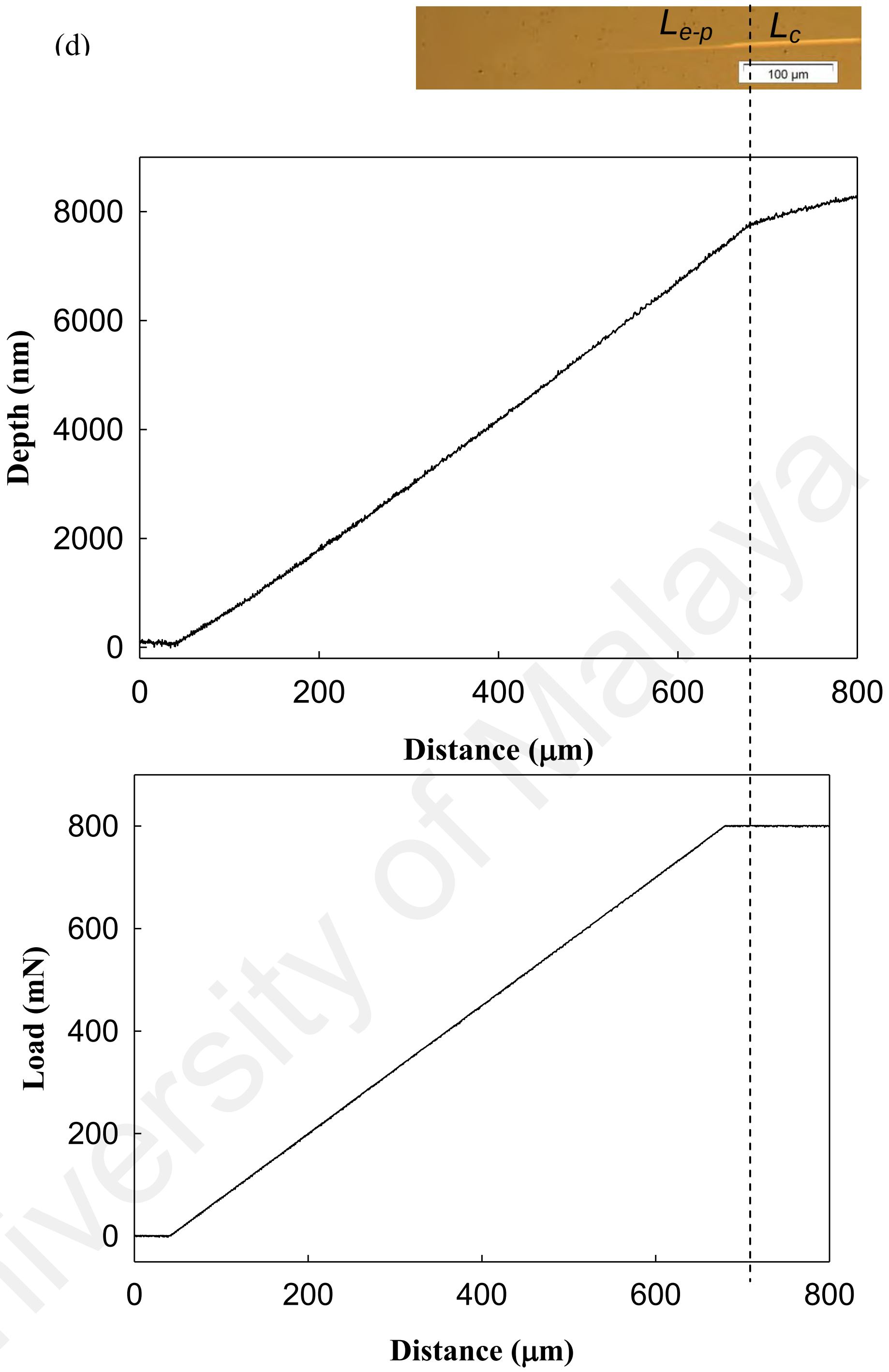

Figure 4.10: (*continued*) Optical micrograph of scratch tracks and graphs of depth versus distance and load versus distance of oxidized Nd samples at various durations (a) 5 min;(b) 10 min; (c) 15 min; and (d) 20 min

Table 4.2: $L_c$and scratch length of oxidized Nd samples at various durations

Oxidation duration (min)	**L_c (mN)**	**Scratch length (µm)**
5	789	184
10	799	70
15	787	362
20	791	311

4.2.6 Leakage Current Density versus Electrical Breakdown Field Characteristics

Figure 4.11 shows the J-E characteristics of the oxidized Nd samples at various durations (5 min, 10 min, 15 min, and 20 min).These samples posses double breakdowns. The sample oxidized for 10 min and 20 min possess poor J-E property, as they start with leakage. This can be a result of the almost similar oxide thickness of these samples, which are 8.21 nm (10 min) and 8.6 nm (20 min). Meanwhile, the sample oxidized for 15 min has an initial breakdown of 1.818 MV/cm at 8.118×10^{-6} A/cm^2, whereas the sample oxidized for 5 min has an initial breakdown of 5.4545 MV/cm at 4.178×10^{-5} A/cm^2. As the main aim of the alternative gate oxide is to produce lower leakage value, it is concluded that the sample oxidized for 15 min possesses the best J-E property. This can be attributed to the single and thinnest interfacial layer. Jeon et al. (1976) reported that the thinnest interfacial layer would result in better electrical property (Jeon et al., 2001). In addition, SiO_2 possesses a lower *k*-value (~3.9), which tends to reduce the overall *k*-value of the sample (E. Bugiel et al., 2005; G Lucovsky & Rayner, 2000). Thus, a thicker and separate SiO_2 layer has a poor effect on the electrical property of the sample. A comparison of a few published results of Nd_2O_3 is shown in Table 4.3.

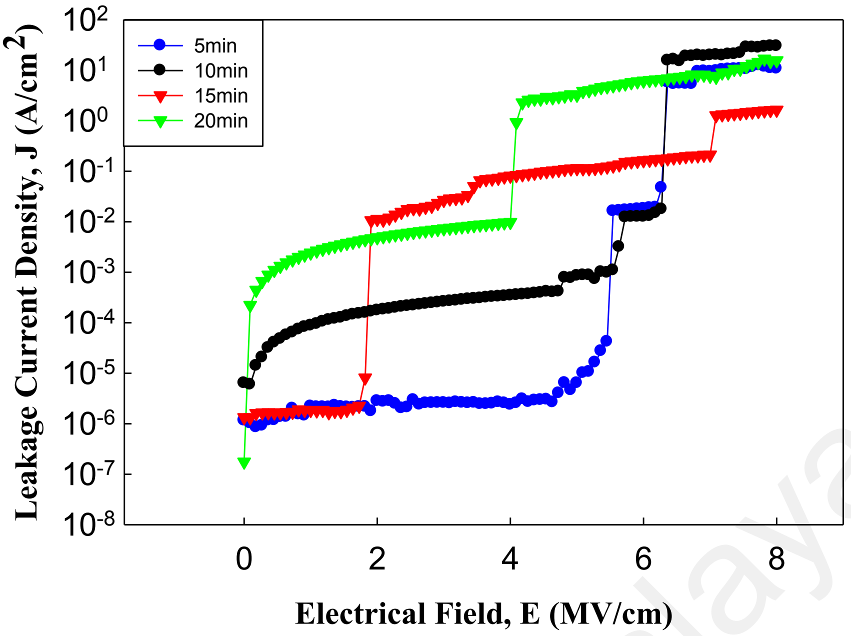

Figure 4.11: J-Echaracteristic of oxidized Nd samples at various durations (5 min,10 min, 15 min and 20 min)

Table 4.3: Electrical results comparison of previously published results

Method	**Oxide**	**IL**	**Thickness (nm)**	**E (MVcm^{-1})**	**J (A/cm^2)**	**Reference**
Metal organic chemical vapour deposition	Nd_2O_3	$Nd_2Si_2O_7$	35	1.4	10^{-4}	(Song & Rhee, 2005a)
Chemical solution deposition	Nd_2O_3	SiO_2	3.3	Not reported	10^{-4}	(Hardy et al., 2007)
RF sputtering	Nd_2O_3	N^+Poly-Si and wet oxide	27	3	10^{-4}	(C.H. Kao et al., 2010)
RF sputtering	Nd_2O_3	N^+Poly-Si and wet oxide	25	11	10^{-4}	(Demkov & Navrotsky, 2006)

Table 4.3: *(continued)* Electrical results comparison of previously published results

Method	**Oxide**	**IL**	**Thickness (nm)**	**E ($MVcm^{-1}$)**	**J (A/cm^2)**	**Reference**
RF sputtering followed by thermal oxidation	Nd_2O_3	SiO_2 + $Nd_2Si_2O_7$	5.82 - 14.1	1.8	10^{-6}	This work

The J-E measurement results were applied in performing a time-zero dielectric breakdown (TZDB) reliability test. Figure 4.12 shows the cumulative failure percentage of 100 capacitors. Samples oxidized for 5 min and 10 min were found to possess the highest breakdown voltage in the range of 3-5 MV/cm. However, the leakage values of these samples were higher than 10^{-6} A/cm^2. On the other hand, the lowest leakage value was recorded at 1.8 MV/cm for the sample oxidized for 15 min. Thus, the interface layer with the inclusion of $Nd_2Si_2O_7$ and SiO_2 has the best J-E characteristics. This observation is in contrast to the influence of the samarium silicate interface layer, which degrades the electrical properties of the oxide film (K. H. Goh, A. S. M. A. Haseeb, & Y. H. Wong, 2016b).

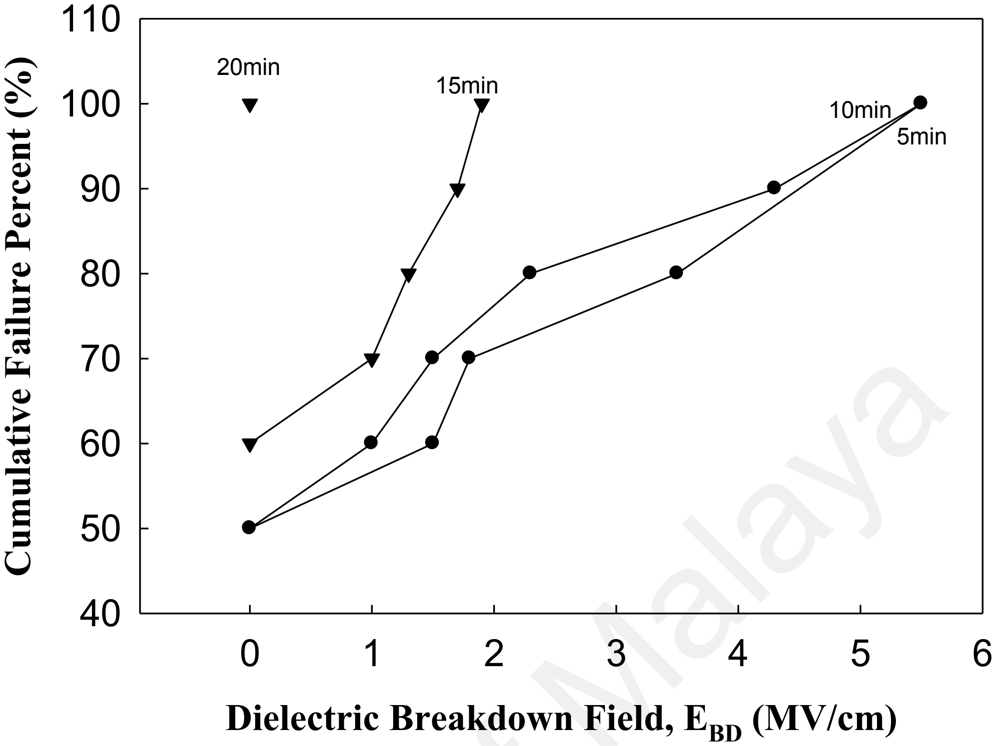

Figure 4.12: Cumulative failure percentage of the dielectric breakdown field (EBD) of oxidizedNd samples at various durations (5 min, 10 min, 15 min, and 20 min)

4.2.6.1 Fowler-Nordheim Tunneling Analysis

A FN regression plot of In (J/E^2) versus 1/E is shown in Figure 4.13. Meanwhile, Figure 4.14 shows the calculated $Ø_B$ from the FN regression plot. The highest $Ø_B$ is shown by the sample oxidized for 15 min, which results in the best I-V characteristics.

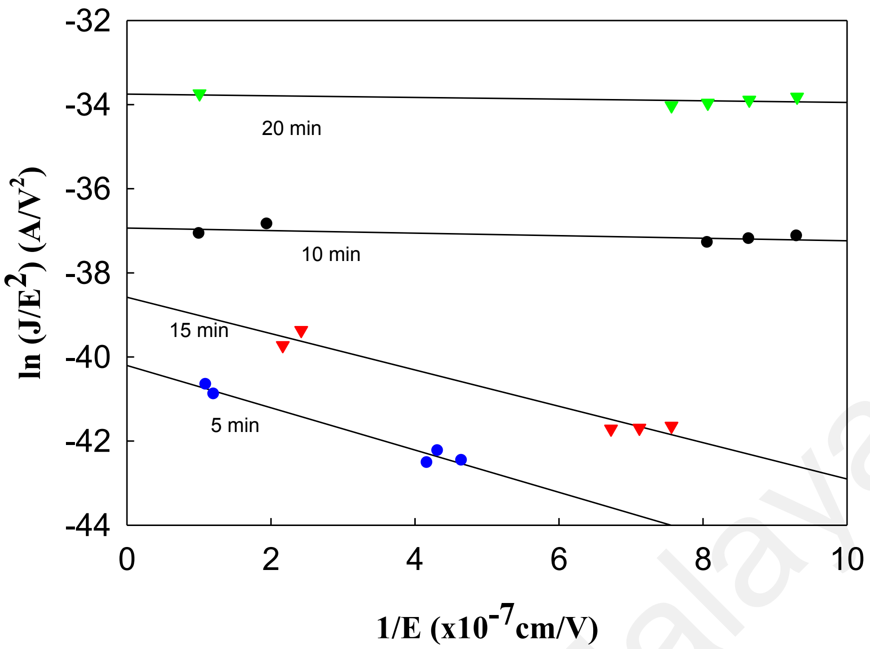

Figure 4.13: The F-N tunneling linear regression plot [In (J/E^2) versus 1/E] of oxidizedNd samples at various durations (5 min, 10min, 15 min, and 20 min)

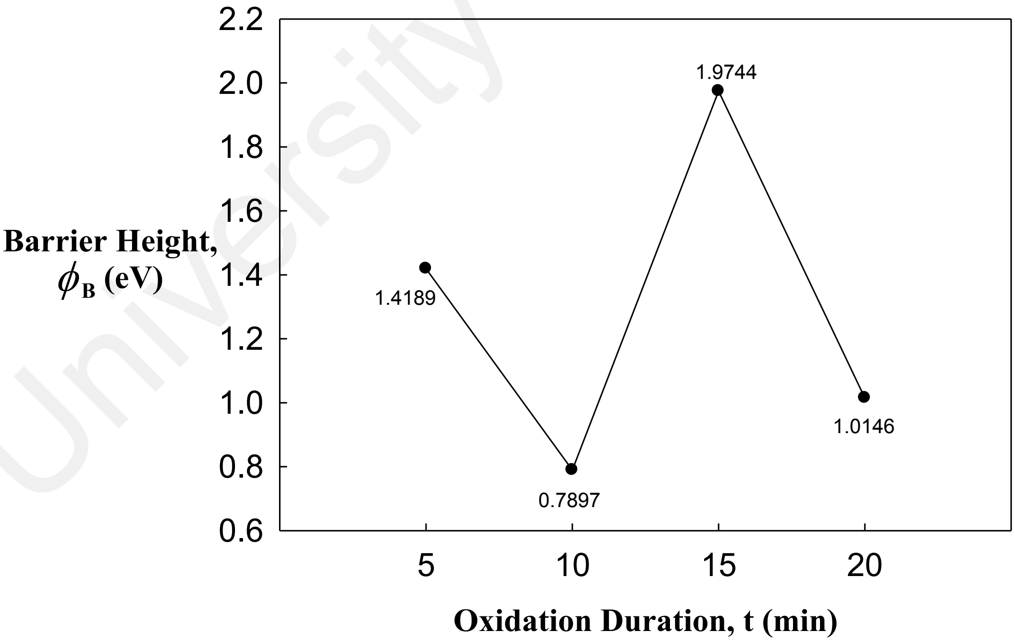

Figure 4.14: Barrier height values as a function of oxidizedNd samples at various durations (5 min, 10 min, 15 min, and 20 min)

4.2.7 Capacitance-Voltage Characteristics

Figure 4.15 shows the normalized capacitance value with the highest accumulation capacitance of each sample. This is followed with the highest capacitance accumulation and k-value of the oxidized Nd samples at various durations (5 min, 10 min, 15 min, and 20 min),as per Figure 4.16. Normalized capacitance reveals a negative bias depletion region and negatively shifted ΔV_{FB}. Thus, all the samples posses positive effective oxide charges (Yang et al., 2003). On the other hand, the highest accumulation capacitance is shown by the sample oxidized at 20 min. However, the sample with best J-E characteristics (oxidized for 15 min) possessed the lowest accumulation capacitance. As per Equation (3.12), because of the lowest accumulation capacitance and thickness, the sample also possesses the lowest k-value. It can be concluded that the sample with the interfacial layer of $Nd_2Si_2O_7$ and SiO_2possesses the lowest k-value. Although this value is the lowest of all the samples, it is still higher compared to previously published results, as the k-value of the sample with a thickness of less than 25 nm is 13 ± 2 (Jeon et al., 2001).

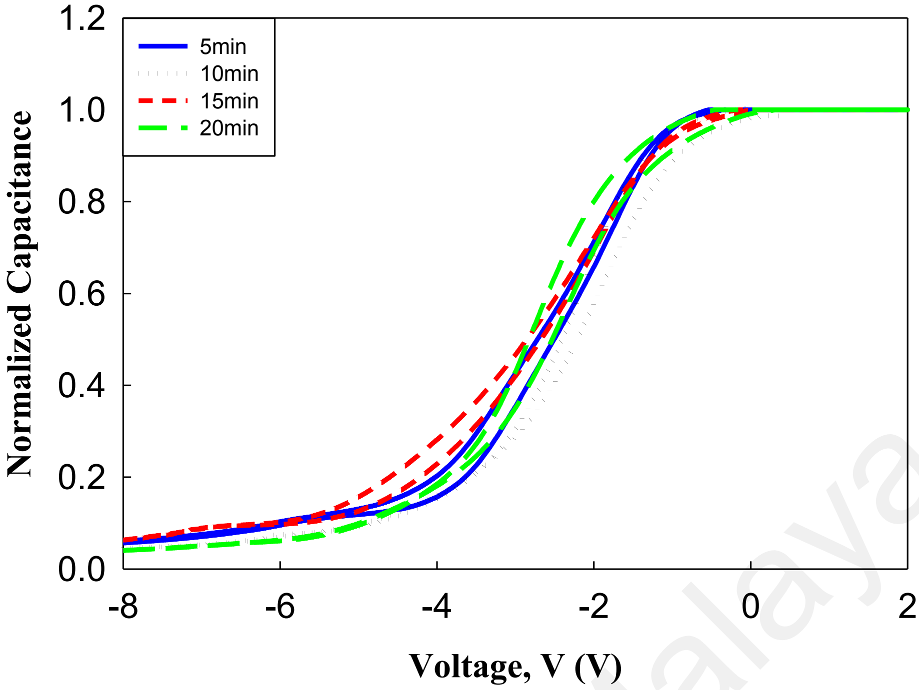

Figure 4.15: Normalized C-V curve of oxidized Nd samples at various durations (5 min, 10 min, 15 min, and 20 min)

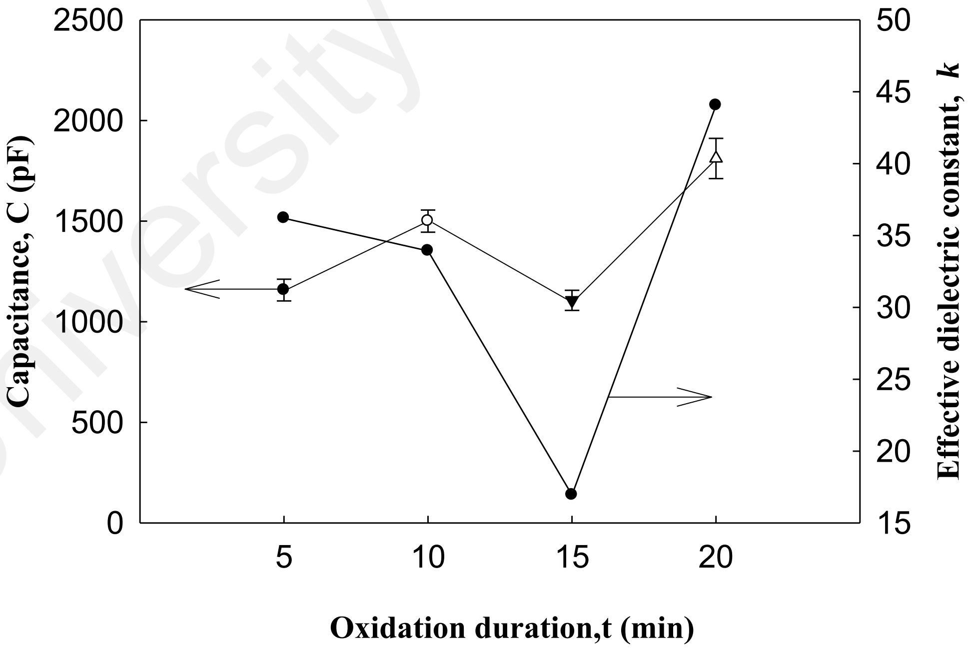

Figure 4.16: Capacitance accumulation and *k*-value of oxidized Nd samples at various durations (5 min, 10 min, 15 min, and 20 min)

4.2.7.1 Effective Oxide Charge, Slow Trap Density and Interface Trap Defect Density

Q_{eff} and STD of the oxidized Nd samples at various durations (5 min, 10 min, 15 min, and 20 min) are shown in Figure 4.17. An obvious relationship can be observed between the overall thickness of the oxide and interfacial layer, where Q_{eff} and STD also decreases as thickness decreases. Figure 4.18 shows the D_{it} values of the oxidized Nd samples at various durations (5 min, 10 min, 15 min, and 20 min). The lowest D_{it} is shown by the sample oxidized for 5 min. Pan et.al. (2007) also supports this observation, where SiO_2 and the silicate layer tended to decrease D_{it} (Pan et al., 2007).

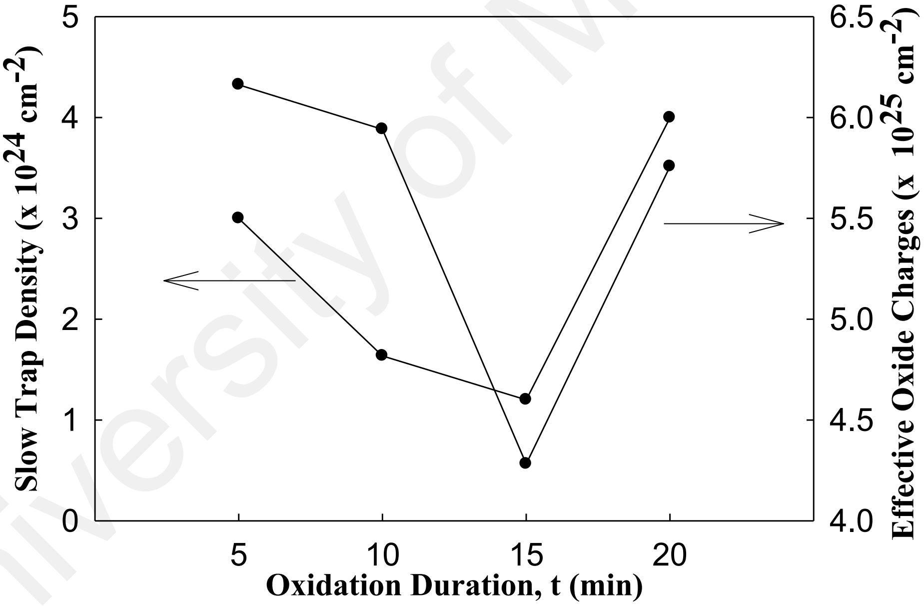

Figure 4.17: STD and Q_{eff} charges of the oxidized Nd samples at various durations (5 min, 10 min, 15 min, and 20 min)

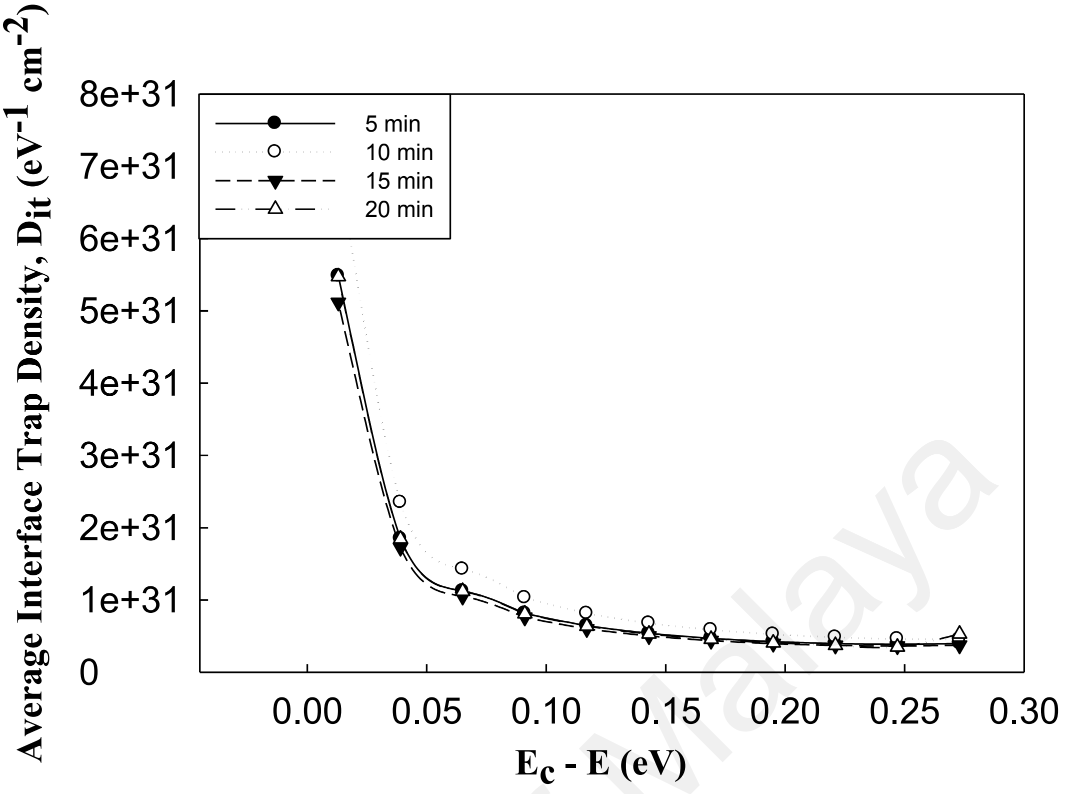

Figure 4.18: D_{it} of the oxidized Nd samples at various durations (5 min, 10 min, 15 min, and 20 min)

4.3 Effects of Thermal Oxidation Temperature on Sputtered Nd Thin Film on Si Substrate

4.3.1 XRD Analysis

Figure 4.19 shows the XRD patterns of the oxidized Nd samples at various temperatures (500°C, 700°C, 900°C, and 1100°C). Two strong peaks were observed at 33.0° and 69.0°. These peaks were identified as cubic c-Si(1 1 2) and c-Si(4 0 0). These peaks were confirmed based on ICSD reference code 98-001-6569.The cubic structure of c-Nd_2O_3 was detected at 68.8°, 74.9°, and 75.8°, corresponding to (118), (257), and (257), respectively. These peaks were confirmed based on ICSD 98-009-6204. Various peaks of SiO_2 of different phases, similar to different oxidation durations, were detected. There were four detected peaks belonging to m-SiO_2, two detected peaks belonging to h-SiO_2, and two detected peaks belonging to t-SiO_2.For m-SiO_2, the detected peaks were at diffraction angles of 46.2°, 47.8°, 54.6°, and 89.4°, corresponding to (226), (9 1 $\bar{3}$), (5 1 $\overline{13}$), and (201), respectively. These peaks were confirmed by ICSD 98-001-0176 and ICSD 98-002-4259. Peaks belonging to h-SiO_2 were detected at diffraction angles of 69.4°, 75.3°, and 75.6°, corresponding to (0 3 0), (1 0 4), and (3 0 2), respectively. These peaks were confirmed based on ICSD 98-001-6336, ICSD 98-001-6333, and ICSD 98-000-0174. Meanwhile, peaks belonging to t-SiO_2 were detected at 21.9° and 76.4°, corresponding to (0 1 1) and (0 4 0), respectively. These peaks were confirmed based on ICSD 98-000-9327.The peak of t-SiO_2 (0 1 1) was only detected for the sample oxidized at 1100°C. Five peaks belonging to o-$Nd_2Si_2O_7$ were detected at diffraction angles of 55.4°, 56.3°, 61.8°, 66.5°, and 67.4°, corresponding to (2 1 6), (3 1 3), (1 3 7), (1 6 0), and (2 0 8), respectively. These peaks were confirmed based on ICSD 98-001-6051. Detection of SiO_2 and the silicate layer results suggests that production of the interfacial layer occurs at oxidation temperatures less and more than 700°C.

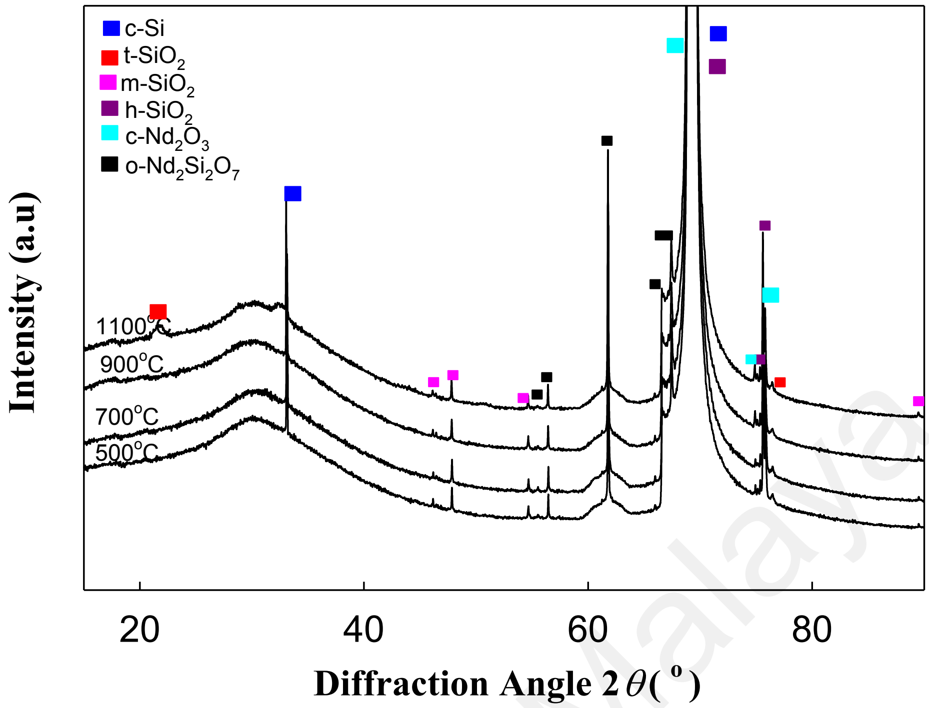

Figure 4.19: XRD patterns of the oxidized Nd samples at various temperatures (500°C, 700°C, 900°C, and 1100°C)

In order to study the effect of the oxide and interfacial layers on electrical property, the highest intensities of c-Nd_2O_3, m-SiO_2, h-SiO_2, t-SiO_2, and o-$Nd_2Si_2O_7$were investigated, as shown in Figure 4.20. The highest intensity of Nd_2O_3 was recorded by the sample oxidized at 700°C and the lowest was at 900°C. The sample oxidized at 700°C also possessed the highest intensity of o-$Nd_2Si_2O_7$. Meanwhile, the sample oxidized at 500°Cshowed the lowest intensity for interfacial layers except m-SiO_2. The highest intensity of t-SiO_2 and m-SiO_2 was shown by the sample oxidized at 1100°C.

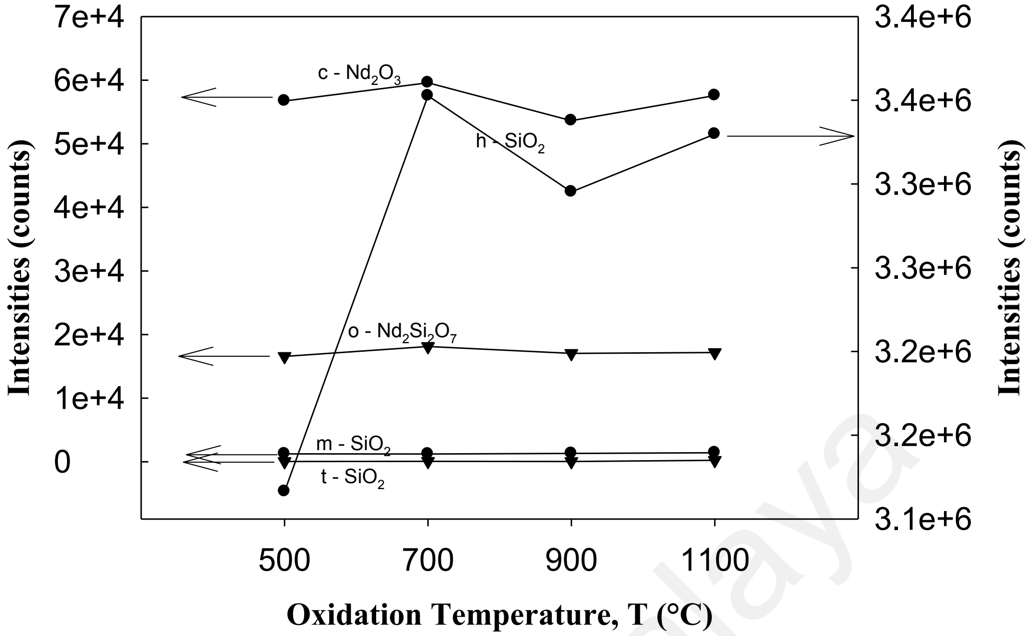

Figure 4.20: Highest intensities of c-Nd_2O_3, m-SiO_2, h-SiO_2, t-SiO_2, and o-$Nd_2Si_2O_7$ of the oxidized Nd samples at various temperatures (500°C, 700°C, 900°C, and 1100°C)

4.3.1.1 Williamson-Hall Analysis

The W-H analysis of the oxidized Nd samples at various temperatures (500°C, 700°C, 900°C, and 1100°C) is shown in Figure 4.21 with the crystallite size and microstrain presented in Figure 4.22. The sample oxidized at 500°C has the smallest microstrain and crystallite size for Nd_2O_3 and SiO_2. Meanwhile, the sample oxidized at 900°C has the smallest microstrain and crystallite size for $Nd_2Si_2O_7$.

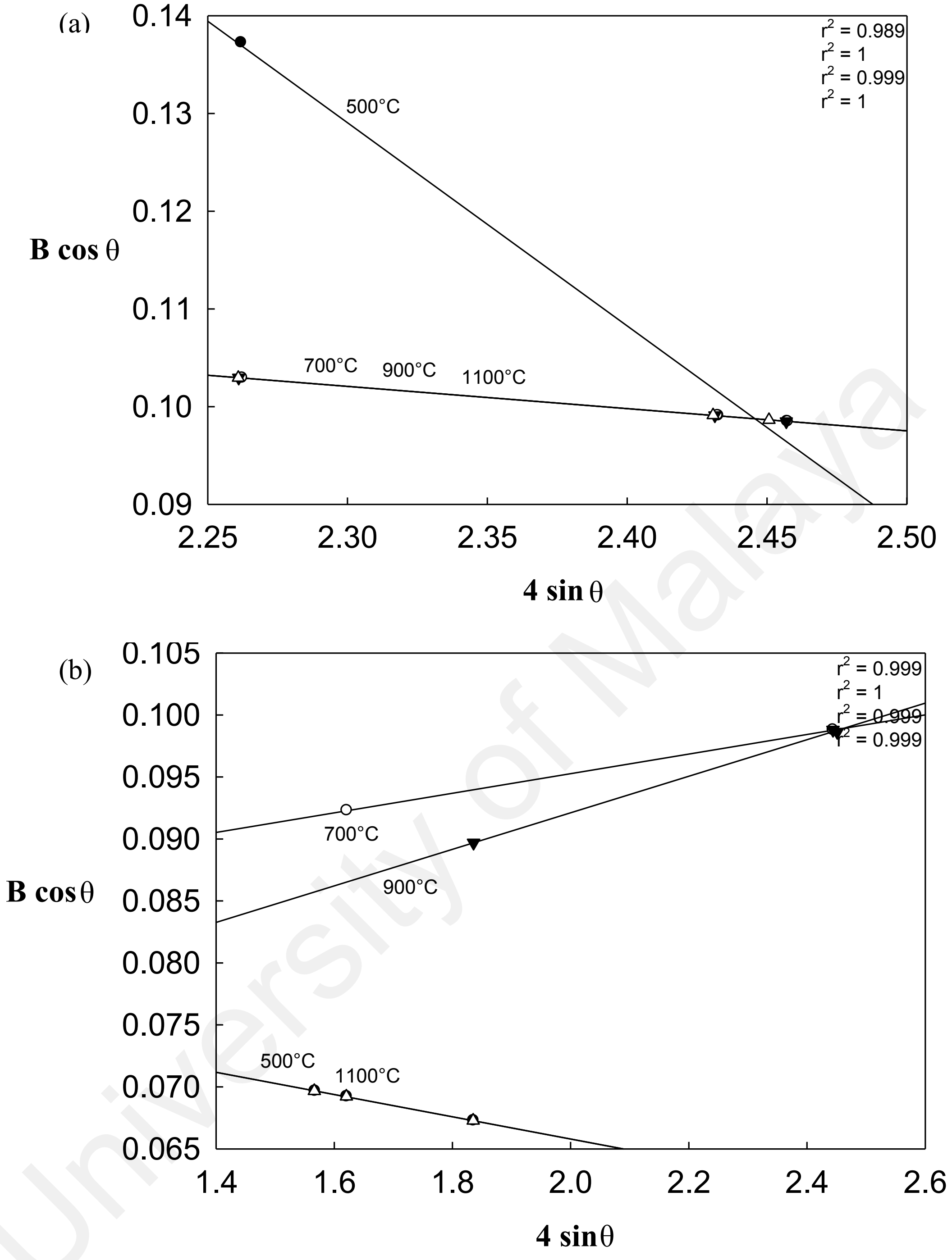

Figure 4.21: W-H plot of: (a) Nd_2O_3;(b) SiO_2; and (c) $Nd_2Si_2O_7$ of the oxidized Nd samples at various temperatures (500°C, 700°C, 900°C, and 1100°C)

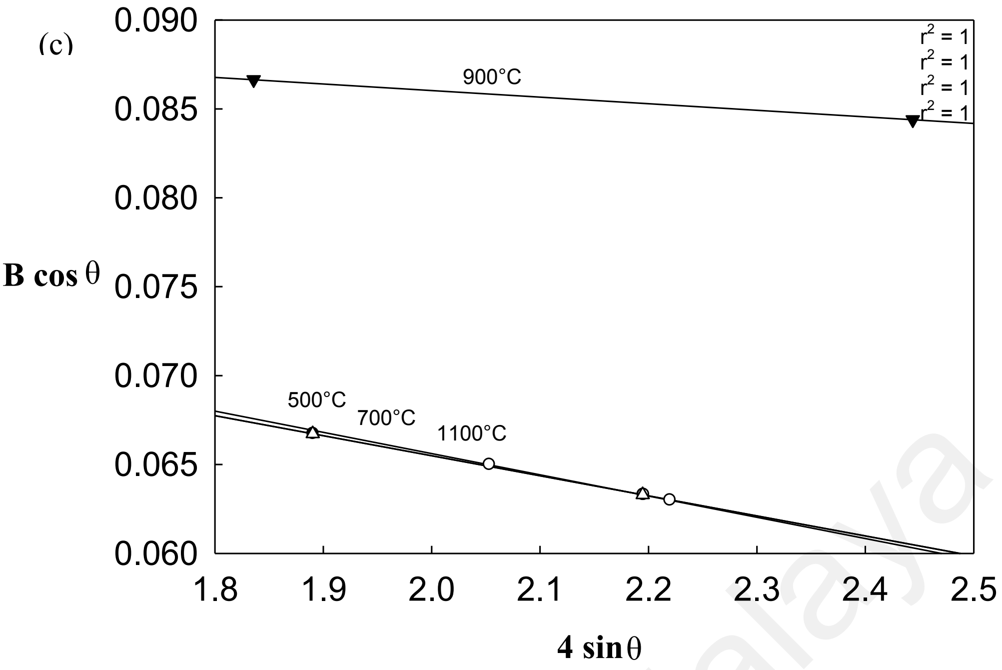

Figure 4.21: *(continued)* W-H plot of: (a) Nd_2O_3;(b) SiO_2; and (c) $Nd_2Si_2O_7$ of the oxidized Nd samples at various temperatures (500°C, 700°C, 900°C, and 1100°C)

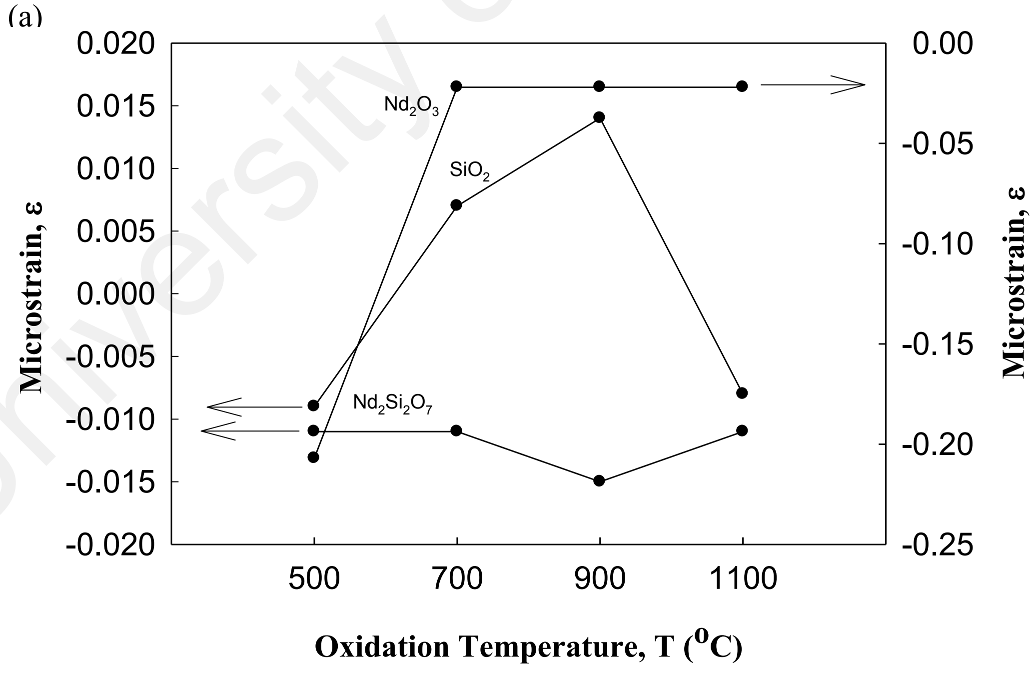

Figure 4.22: (a) Microstrain (b) crystallite size of Nd_2O_3, SiO_2 and $Nd_2Si_2O_7$ of the oxidized Nd samples at various temperatures (500°C, 700°C, 900°C, and 1100°C)

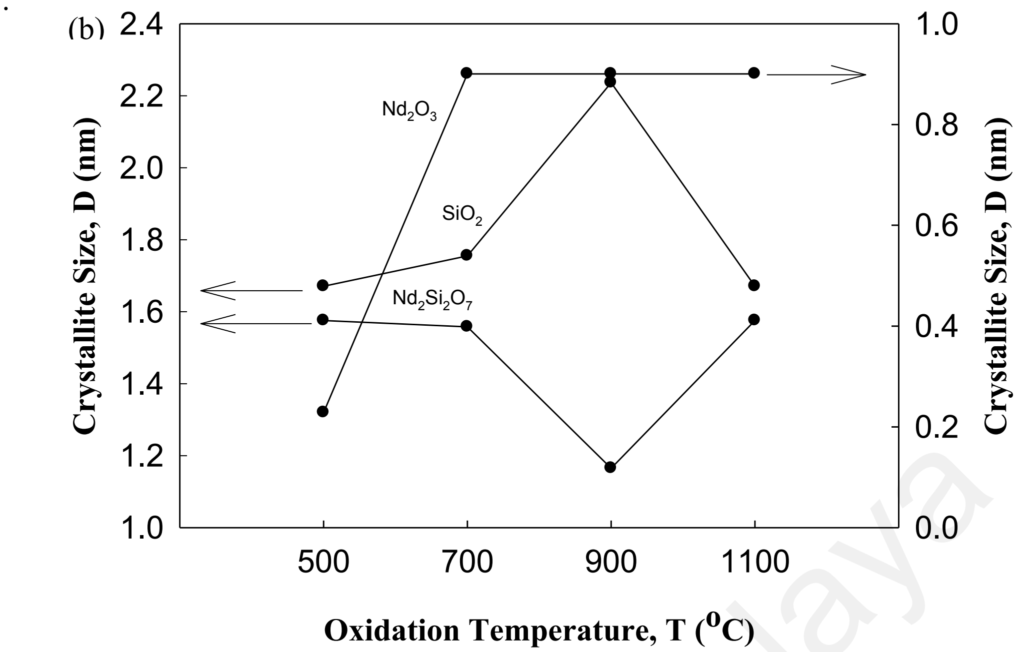

Figure 4.22: *(continued)*(a) Microstrain (b) crystallite size of Nd_2O_3, SiO_2 and $Nd_2Si_2O_7$ of the oxidized Nd samples at various temperatures (500°C, 700°C, 900°C, and 1100°C)

4.3.2 FTIR Analysis

The FTIR results of the oxidized Ndsamples at various temperatures (500°C, 700°C, 900°C, and 1100°C)are shown in Figure 4.23. A Si-Si vibration mode originating from the Si substrate was detected at 613cm^{-1} (Smith, 1998). The peak broadens as oxidation temperature increases up to900°C, but sharpens at 1100°C. A vibration mode attributed to Nd-O was detected at 558 cm^{-1} and 501cm^{-1}(Päiväsaari et al., 2005). Both peaks sharpen as oxidation temperature increases. A Si-O-Si assymmetric stretching mode was detected at 1204 cm^{-1} and 1041cm^{-1}(Kurniawan, Cheong, et al., 2011b). The intensity increases as temperature increases. A peak attributed to the rocking, bending, and stretching of Si-O was detected at 805cm^{-1}(Smith, 1998). A Si-O vibration mode was detected at 478cm^{-1} and 471cm^{-1}(Lippincott et al., 1958; Viana et al., 2001). Both peaks sharpen and broaden as oxidation temperature increases. A peak attributed to Si-O-Si bending was observed at 456cm^{-1}(Lippincott et al., 1958; Viana et al., 2001). The peak shifted at500°C and sharpness decreased as oxidation temperature increased from 700°C until 1100°C. A peak attributed to Si-O bend was detected at 443cm^{-1}, 431cm^{-1}, 419cm^{-1}, 411cm^{-1}, and 403cm^{-1}(Lippincott et al., 1958; Viana et al., 2001). Peaks 443cm^{-1} and 431cm^{-1} shifted at500°C. At the same time, both peaks sharpened as oxidation temperature increased. Meanwhile, peak 419cm^{-1} is only visible at900°C. On the other hand, peak 411cm^{-1} is not visible at 900°C. Lastly, peak 403cm^{-1} sharpened as oxidation temperature increased from 500°C to 700°Cthen decreased at 900°C and increased again at 1100°C. Nd silicate vibration was detected at 925 cm^{-1} (Ganesan et al., 2008; Smith, 1998). The peak exists as a broadened peak and the intensity decreased from 500°C to 700°C; but it increased again at a higher temperature.

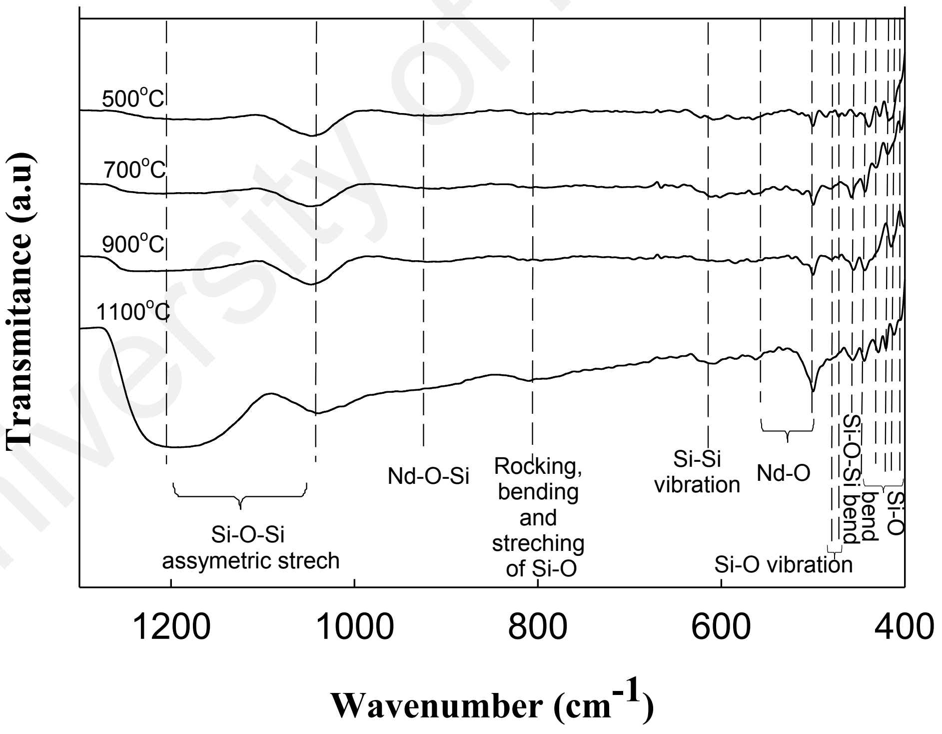

Figure 4.23: Transmittance spectra of oxidized Nd samples at various temperatures (500°C, 700°C, 900°C, and 1100°C)

4.3.3 Raman Analysis

Figure 4.24 shows the Raman analysis of the oxidized Nd samples at various temperatures (500°C, 700°C, 900°C, and 1100°C). A wavelength belonging to Si was detected at 525cm^{-1} (Wong & Cheong, 2011a). The intensity increased until 700°C and then decreased as temperature increased. Peaks belonging to Nd_2O_3 were detected at 112 cm^{-1} and 312 cm^{-1} (Kurniawan, Cheong, et al., 2011b; Nyquist & Kagel, 2012). The initial peak intensity increased up to 900°C and then decreased afterwards. Later, the peak intensity increased up to 700°C and then decreased as temperature increased. A peak belonging to SiO_2 was detected at 818cm^{-1} and 925cm^{-1} (Malinovsky, Novikov, Surovtsev, & Shebanin; Nyquist & Kagel, 2012). Peak 818cm^{-1} was only detected for the sample oxidized at 1100°C.This could be a result of additional t-SiO_2, as detected in the XRD analysis. Meanwhile, intensity of peak 925cm^{-1}increased until 700°C and then decreased as temperature increased. Peak 17cm^{-1} was assigned to neodymium silicate based on the XRD and FTIR analyses, as no reference was available for this peak. The intensity of this peak increased up to700°C and decreased at 900°C, later increasing again at 1100°C, similar to the intensity pattern of o-$Nd_2Si_2O_7$. The sample oxidized at 900°C shows the lowest intensity of silicate. The Raman findings support the existence of an interfacial layer in all samples, as per the XRD and FTIR analyses.

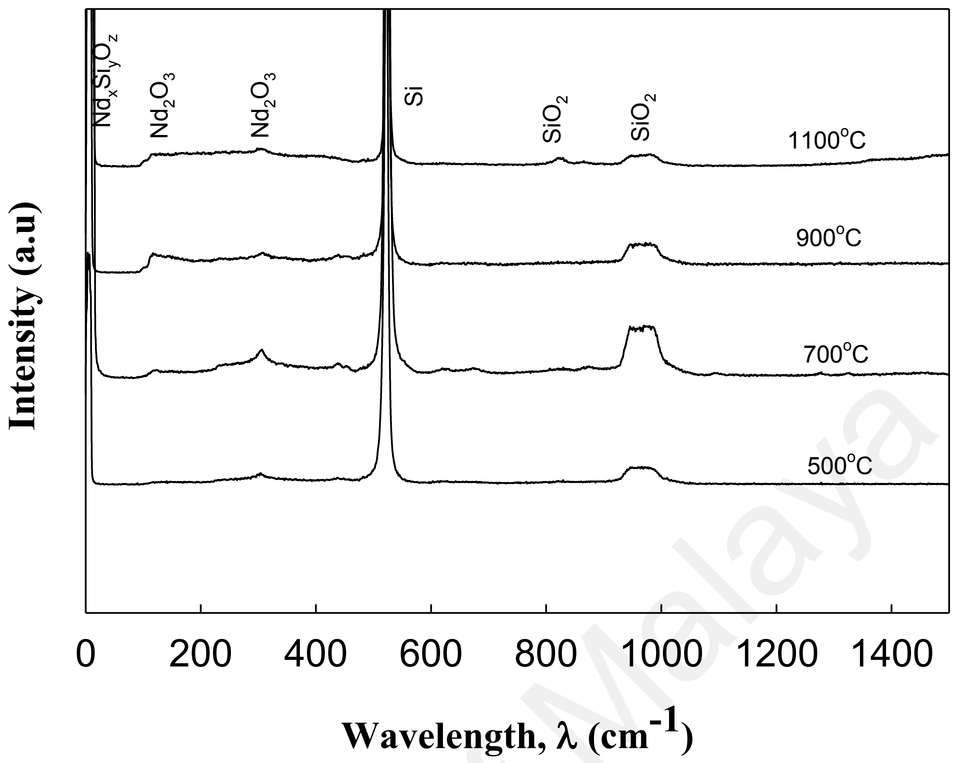

Figure 4.24: Raman spectra of the oxidized Nd samples at various temperatures (500°C, 700°C, 900°C, and 1100°C)

4.3.4 HRTEM Analysis

The sample oxidized at 700°C and 900°C underwent HRTEM and EDX analyses in order to understand the association between temperature on the Nd_2O_3 thickness and interfacial layer. Both samples recorded the highest and second-highest intensity for SiO_2 and $Nd_2Si_2O_7$.

Figure 4.25 shows the HRTEM analysis results. The oxide thickness of the sample oxidized at 900°C is higher than that at 700°C, at 7.37 nm and 5.32 nm, respectively. In addition, the thickness of the interfacial layer also increased when oxidation temperature increased from 700°C to 900°C, at 6.38 nm and 22.08 nm, respectively. Even though the silicate compound intensity of the sample oxidized at

700°C was higher compared to that of the 900°C, the interfacial layers are thinner. This thickened interfacial layer can be attributed to SiO_2.

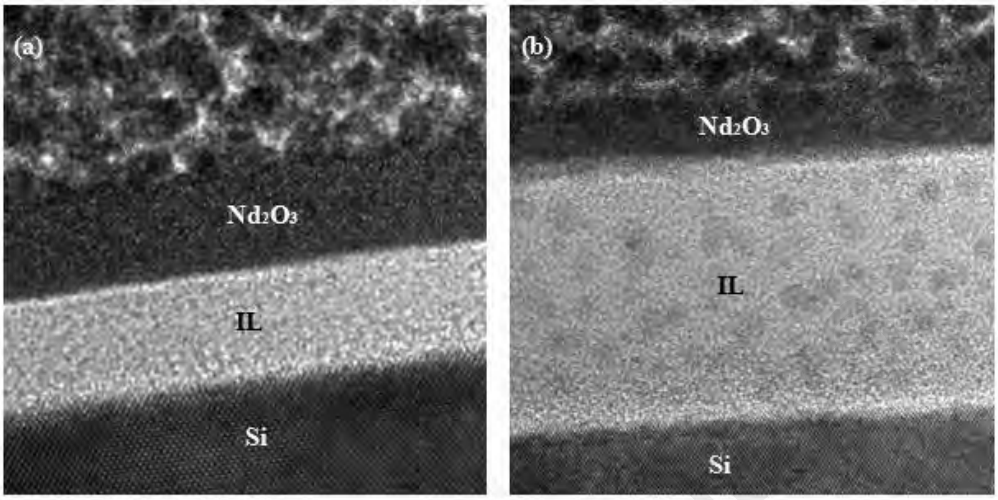

Figure 4.25: HRTEM images of oxidized Ndsamples at (a) 700°C (b) 900°C

The EDX analysis of the oxidized Nd sample at 900°C is shown in Figure 4.26. Si and O were detected at a depth profile of 37 nm. Meanwhile, Si, O and Nd were detected simultaneously at depth profile 59-67 nm. The findings prove the existence of an interfacial layer composed of Si-O and Nd-O-Si, as per the XRD, FTIR, and Raman analyses. In addition, the amorphous regions of the sample oxidized at 900°C is well distributed and visible compared to the sample oxidized at 700°C.

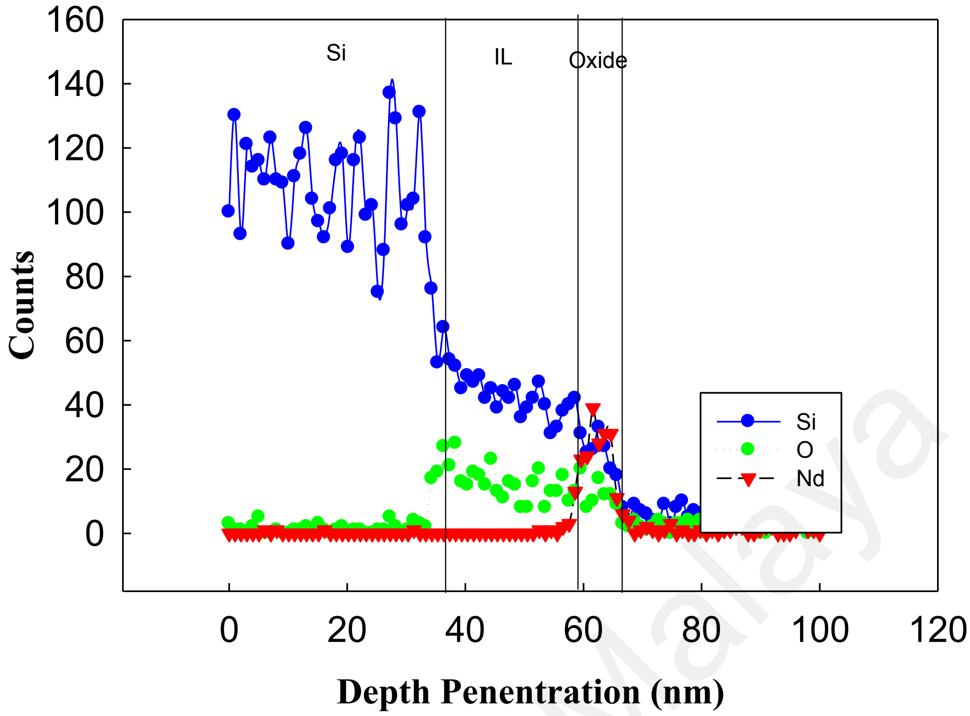

Figure 4.26: EDX composition analysis of the oxidized Nd sample at 900°C

4.3.5 Leakage Current Density versus Electrical Breakdown Field Characteristics

The J-E characteristics of the oxidized Nd samples at various temperatures (500°C, 700°C, 900°C, and 1100°C)are shown in Figure 4.27. Similar to the samples oxidized at various durations, these samples also posses double breakdowns except for the sample oxidized at 900°C. The analysis reveals that the sample oxidized at 900°C possesses the best J-E property where the breakdown voltage is 5.26 MV/cm at a J of2.019 × 10^{-6} A/cm^2. The leakage value is much lower compared to the values shown in Table 4.2. At the same time, the E value is higher compared to that of the sample oxidized at 700°C. In order to confirm these findings, accumulative failure was calculated and shown in Figure 4.28. For the sample oxidized at 900°C, the highest breakdown voltage is in the range of 4-8 MV/cm. However, the leakage value exceeds7

MV/cm at the breakdown voltage at more than 5.26 MV/cm. Thus, 5.26 MV/cm is assumed to be the best basis corresponding to the lowest leakage value.

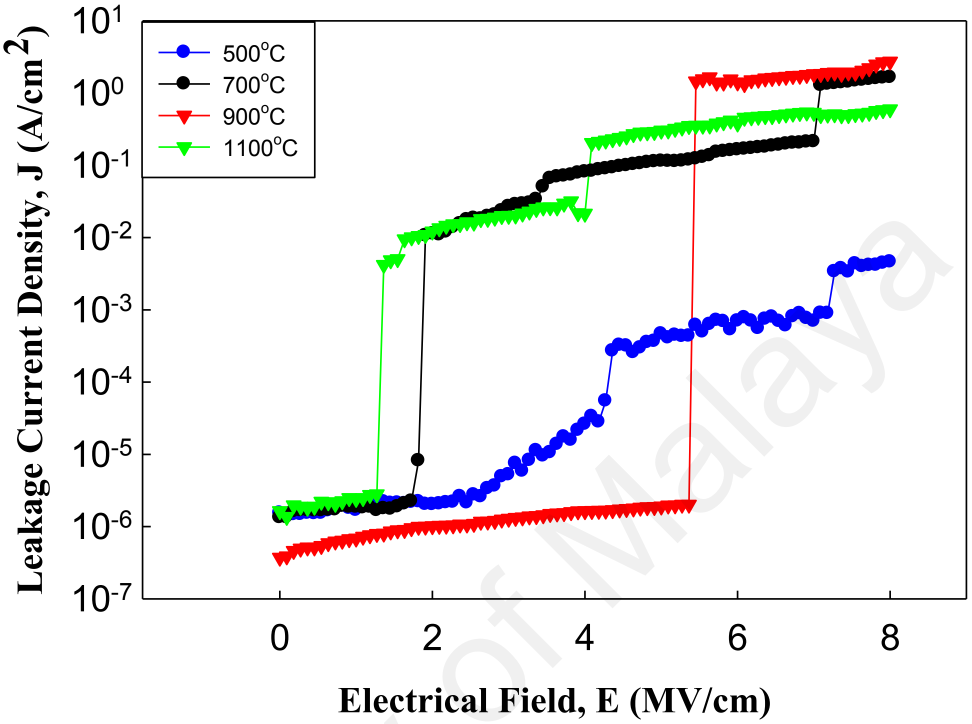

Figure 4.27: J-E characteristic of the oxidized Nd samples at various temperatures (500°C, 700°C, 900°C, and 1100°C)

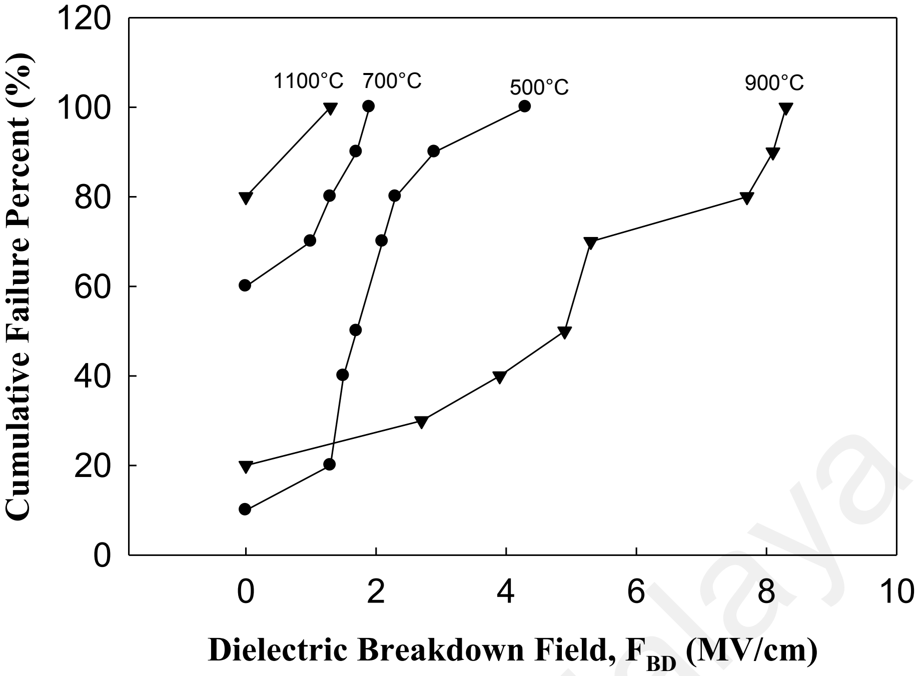

Figure 4.28: Cumulative failure percentage of the EBD of oxidized Nd samples at various temperatures (500°C, 700°C, 900°C, and 1100°C)

4.3.5.1 Fowler-Nordheim Tunneling Analysis

The J-E data was utilized to plot the F-N tunneling linear regression plot and to extract the $Ø_B$ between the conduction band edge and between the Si and interface. Figure 4.29 shows the F-N regression plot of In (J/E^2) versus 1/E. In the mean time, $Ø_B$ extracted from the F-N regression plot is shown in Figure 4.30. The sample oxidized at 900°C possesses the highest barrier height, which results in the best J-E characteristics.

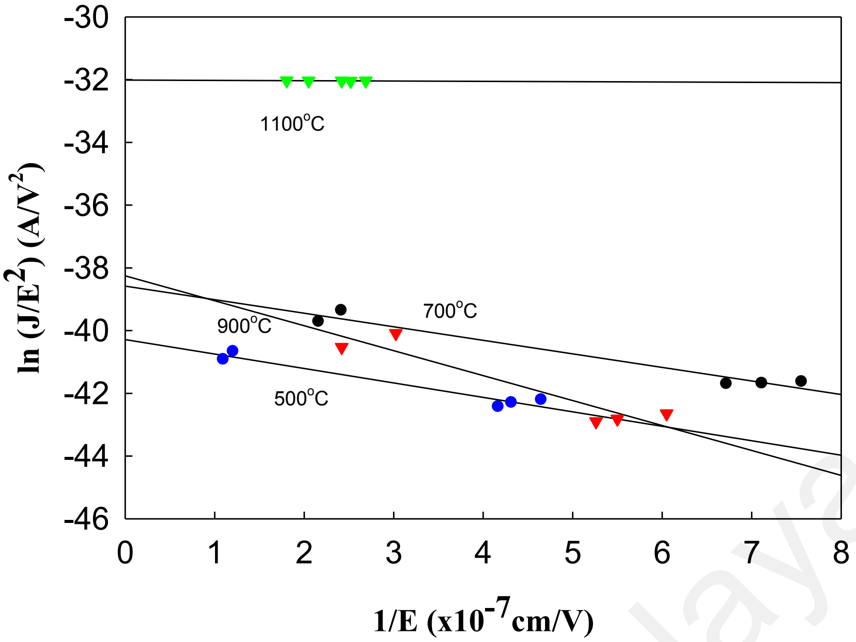

Figure 4.29: F-N tunneling linear regression plot [In (J/E^2) versus 1/E] of oxidized Nd samples at various temperatures (500°C, 700°C, 900°C, and 1100°C)

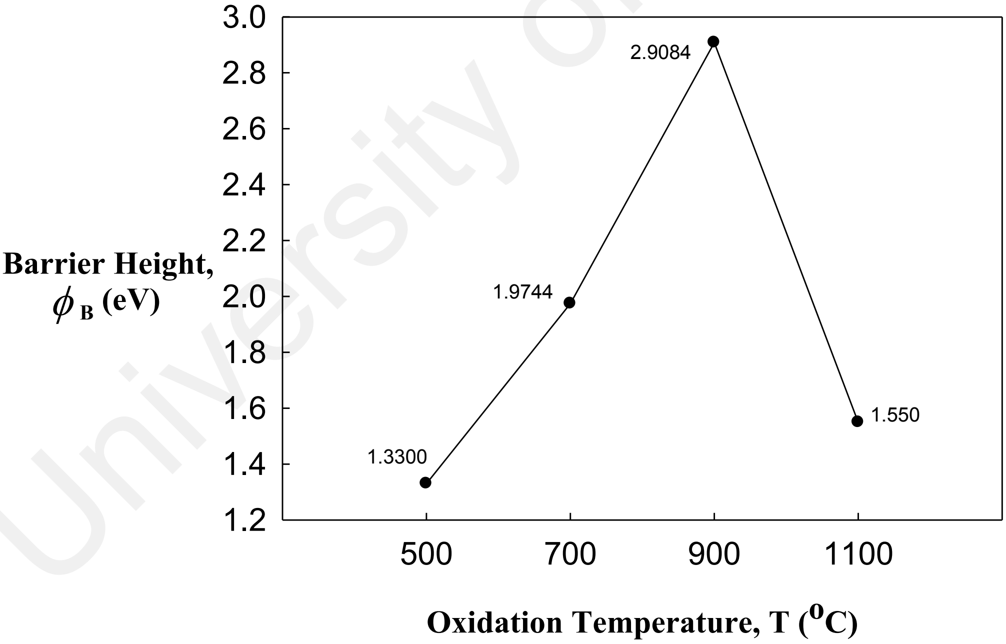

Figure 4.30: Barrier height values as a function of oxidized Nd samples at various temperatures (500°C, 700°C, 900°C, and 1100°C)

4.3.6 Capacitance-Voltage Characteristics

The normalized capacitance value with the highest accumulation capacitance for each sample is shown in Figure 4.31. Meanwhile, Figure 4.32 shows the highest capacitance accumulation of oxidized Nd samples at various temperatures (500°C, 700°C, 900°C, and 1100°C). As the oxidation temperature increases, the highest accumulation capacitance decreases. The *k*-value of the sample oxidized at 700°C and 900°C is 17 and 7, respectively.

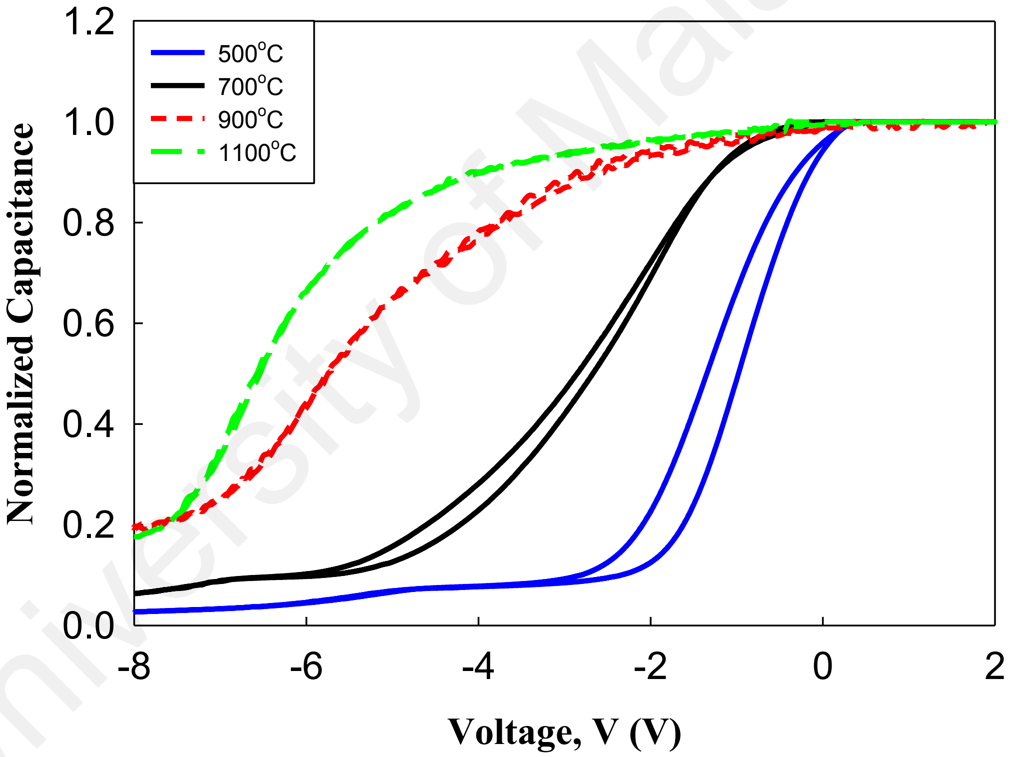

Figure 4.31: Normalized C-V curve of oxidized Nd samples at various temperatures (500°C, 700°C, 900°C, and 1100°C)

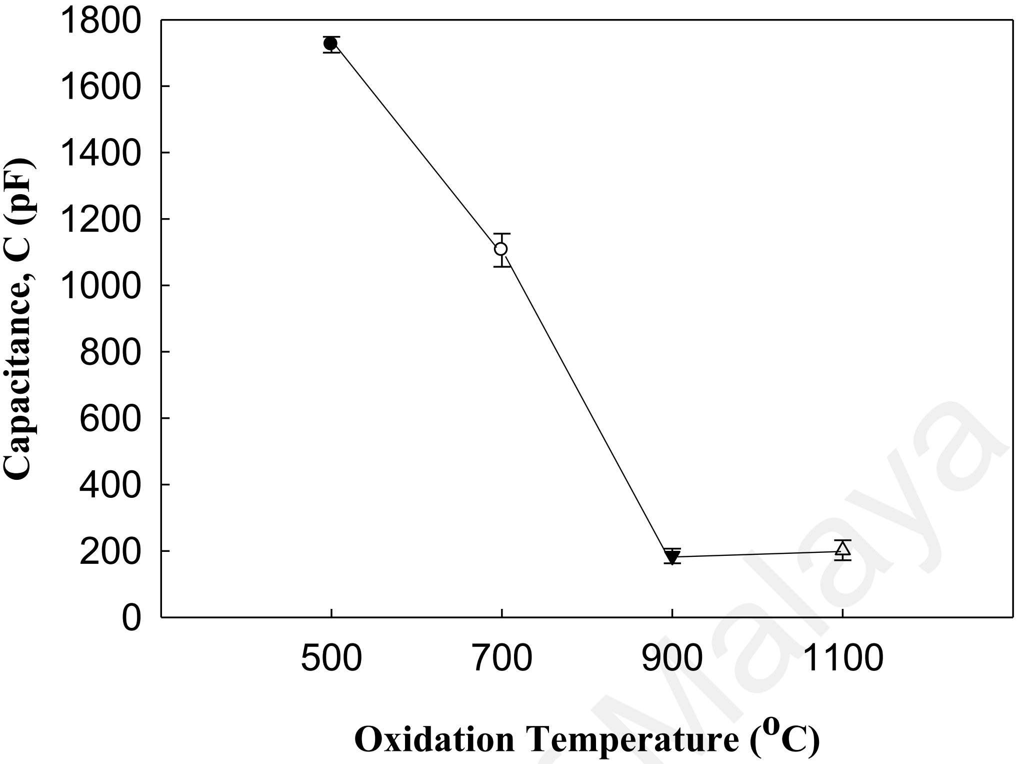

Figure 4.32: Capacitance accumulation value of oxidized Nd samples at various temperatures (500°C, 700°C, 900°C, and 1100°C)

In a previous report, the *k*-value was 14.3 when the interface layer thickness was1.9 ±.1.7 nm (Frohlich et al., 2006). On the other hand, Fromhold et.al. (1976) reported a *k*-value of 12.7 for an oxide thickness of 12.7(Fromhold Jr & Foster, 1976). These findings prove that both the oxide and interface layer thickness affects the *k*-value. The Nd_2O_3 produced through this work is lower compared to that of Fromhold et al. (1976). Thus, this work yields a higher *k*-value compared to the lower thickness. In addition, as temperature increases, hysteresis also decreases. At a higher oxidation temperature, the original SiO_2 has no blocking function since the Nd atoms are diffused further and the Si-O bonding is subjected to decomposition (Hsieh, Ko, Kuei, & Lee, 2006). Thus, it can be predicted that at 500°C, the SiO_2 still exists and produces a lower oxide thickness, which can lead to a lower *k*-value even at a higher capacitance. Meanwhile, at 1100°C, the thickness will be reduced further and a much lower *k*-value will be produced. Overall, the Nd silicate is responsible for improving electrical properties compared to the Sm silicate, which deteriorates the electrical properties of a Sm_2O_3 thin film (Goh et al., 2016b).

4.3.5.1 Effective Oxide Charge, Slow Trap Density and Interface Trap Defect Density

Figure 4.33 shows the Q_{eff} and STD of the oxidized Nd samples at various temperatures (500°C, 700°C, 900°C, and 1100°C). The results show that the sample oxidized at 900°C possesses the lowest Q_{eff} and a lower STD compared to the sample oxidized at 500°C and 700°C. Figure 4.34 shows the D_{it} values of the oxidized Nd samples at various temperatures (500°C, 700°C, 900°C, and 1100°C). The samples oxidized at 900°C and 1100°C have the lowest and similar average interface trap density. The C-V analysis shows that the sample oxidized at 900°C produced the best electrical result.

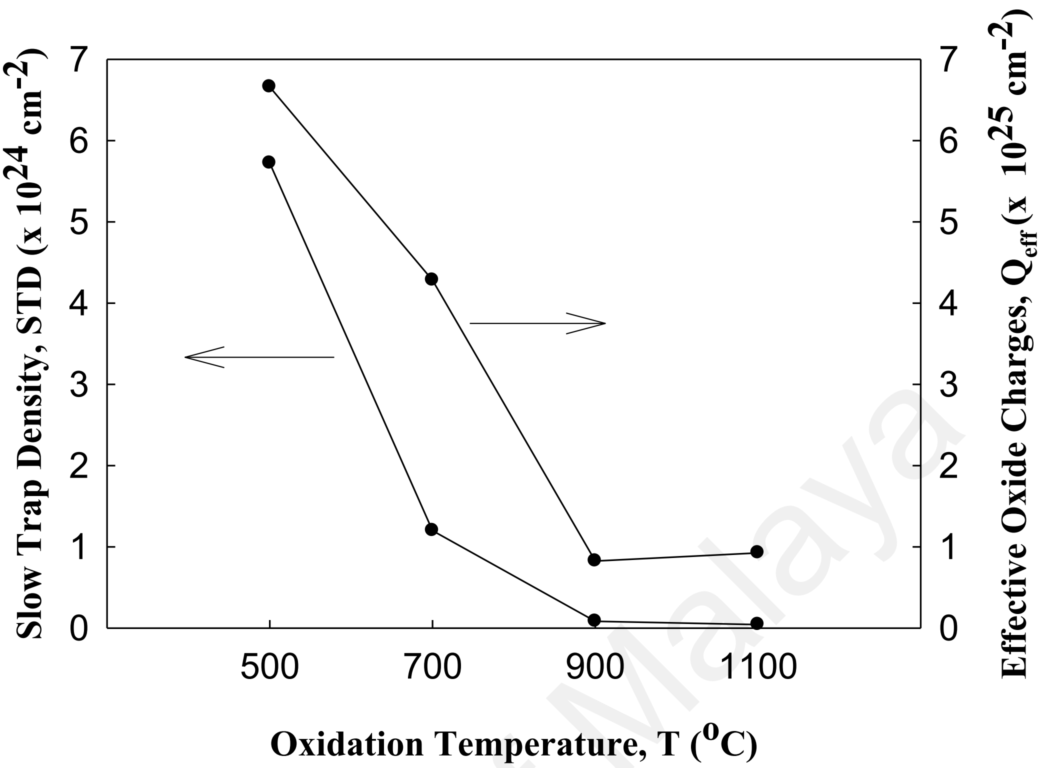

Figure 4.33: STD and Q_{eff} charges of oxidized Nd samples at various temperatures (500°C, 700°C, 900°C, and 1100°C)

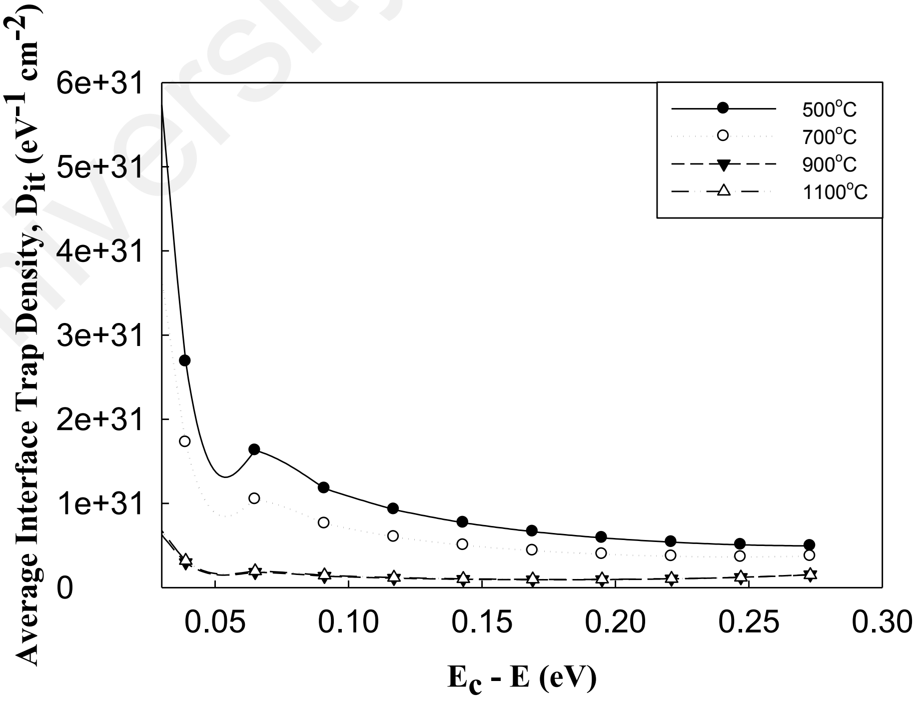

Figure 4.34: D_{it} of oxidized Nd samples at various temperatures (500°C, 700°C, 900°C, and 1100°C)

4.4 Effects of Thermal Oxynitridation Duration on Sputtered Nd Thin Film on Si Substrate

4.4.1 XRD Analysis

Figure 4.35 shows the XRD patterns of the oxynitrided Nd samples at various durations (5 min, 10 min, 15 min, and 20 min). Two strong peaks belonging to Si were detected at 33.0° and 69.0°. These peaks were confirmed as c-Si (1 1 2) and c-Si (4 00) based on ICSD 98-001-6569. Three peaks belonging to c-Nd_2O_3 were detected at 68.8°, 74.9°, and 75.8°. Based on ICSD 98-009-6204, these peaks were assigned to (1 1 8), (2 5 7), and (2 5 7), respectively. Three different phases of SiO_2 were detected. The peaks at 46.2°, 47.8°, 54.6°, and 89.4° were assigned to m-SiO_2, corresponding to (2 2 6), (9 1 $\bar{3}$), (5 1 $\overline{13}$), and (2 0 1), respectively. The peaks were identified based on ICSD 98-001-0176 and ICSD 98-002-425. In addition, peaks belonging to h-SiO_2 were identified at 69.4°, 75.3°, and 75.6°, corresponding to (0 3 0), (1 0 4), and (3 0 2), respectively. These peaks were confirmed based on ICSD 98-001-6336, ICSD 98-001-6333, and ICSD 98-000-0174. A single peak belonging to t-SiO_2 was detected at 76.4°, which was assigned to the (0 4 0) plane based on ICSD 98-000-9327. On the other hand, various planes of o-$Nd_2Si_2O_7$ were detected at 55.4°, 56.3°, 61.8°, 65.9°, 66.5°, and 67.4°, corresponding to (2 1 6), (3 1 3), (1 3 7), (0 6 2), (1 6 0), and (2 0 8), respectively. These peaks were confirmed based on ICSD 98-001-6051. Similar to the oxidized sample, the oxynitrided sample also possesses an interfacial layer consisting of SiO_2 and $Nd_2Si_2O_7$. At the same time, oxynitridation also produces crystalline Nd_2O_3, similar to zirconium oxynitride (ZrON),which produces crytstalline ZrO_2 under thermal oxynitridation (Wong, Atuchin, Kruchinin, & Cheong, 2014).

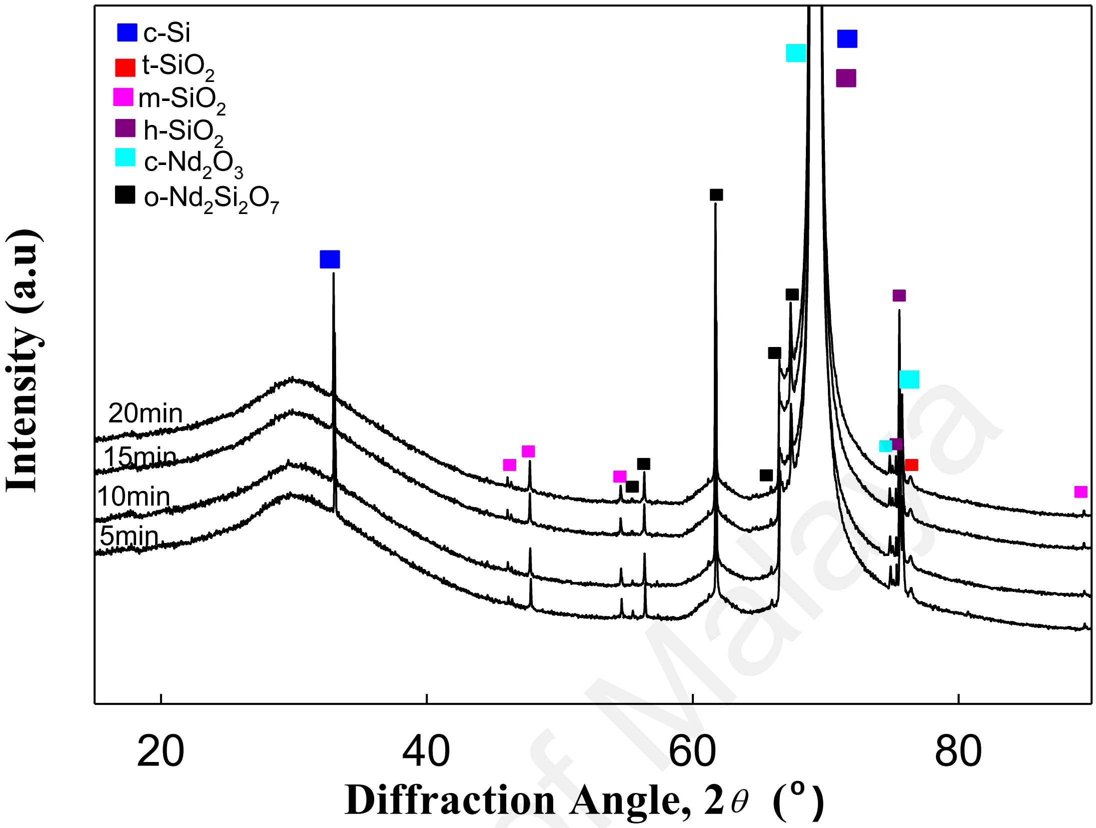

Figure 4.35: XRD patterns of oxynitrided Nd samples at various durations (5 min, 10 min, 15 min, and 20 min)

The highest intensities of c-Nd_2O_3, m-SiO_2, h-SiO_2, t-SiO_2, and o-$Nd_2Si_2O_7$ are shown in Figure 4.36. The sample oxynitrided for 15 min has the highest intensity for the entire interfacial compound. However, this sample also recorded the second-highest intensity of c-Nd_2O_3. As per Sections 4.2 and 4.3, the interfacial layer plays a vital role in determining electrical properties, so the percentage of interfacial layer to total thin film compound was calculated and shown in Figure 4.37. Overall, the interfacial percentage is as follows: 15 min > 10 min > 20 min > 5 min. Although N is present in the thermal oxynitrided ambient, it was not detected in the XRD analysis, in contrast to several other observations. N was detected in the XRD analysis of ZrON and hafnium oxynitride (HfON) (Ishikawa, Kamiyama, Kurosawa, Aoyama, & Nara, 2009; M. Signore, Rizzo, Mirenghi, Tagliente, & Cappello, 2007; M. A. Signore et al., 2010).

This could be due to the very small percentage of N being present in the nitrogen-incorporated neodymium oxide ($Nd_xO_yN_z$) (Ishikawa et al. (2009) found that HfON was produced on siliconoxynitride (SiON) (Ishikawa et al., 2009). On the other hand, Signore et al. (2007, 2010) produced ZrON via directly sputtering the N ambient (M. Signore et al., 2007; M. A. Signore et al., 2010). These methods contributed to a higher percentage of N, which led to its detection in the XRD analysis.

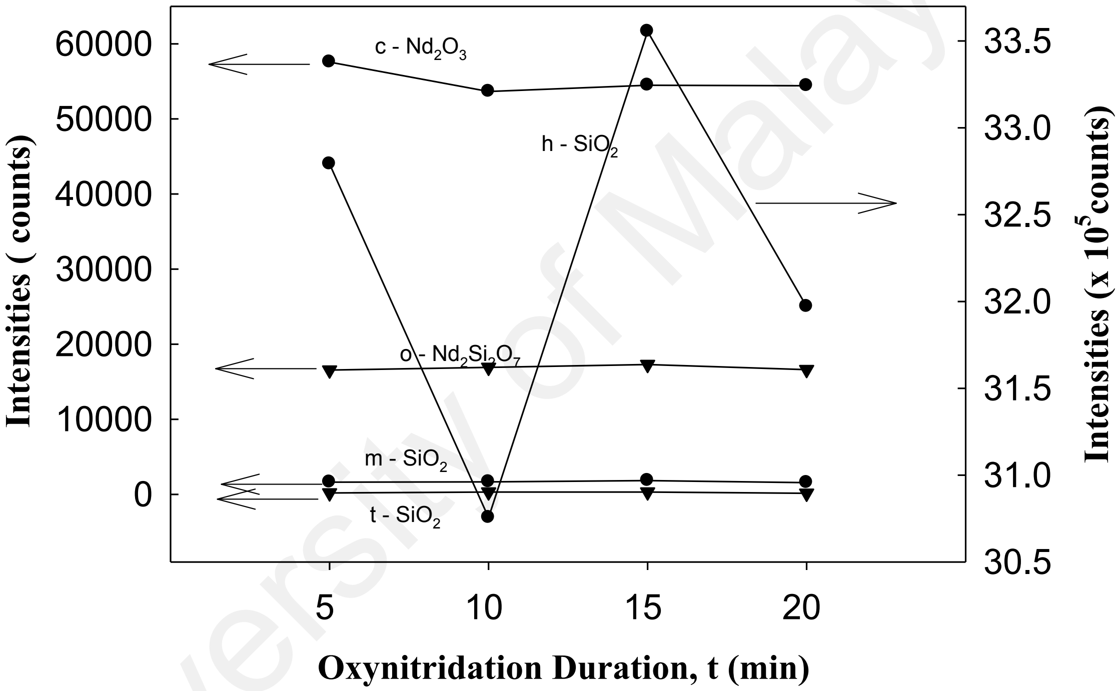

Figure 4.36: Highest intensities of c-Nd_2O_3, m-SiO_2, h-SiO_2, t-SiO_2, and o-$Nd_2Si_2O_7$ for oxynitrided Nd samples at various durations (5 min, 10 min, 15 min, and 20 min)

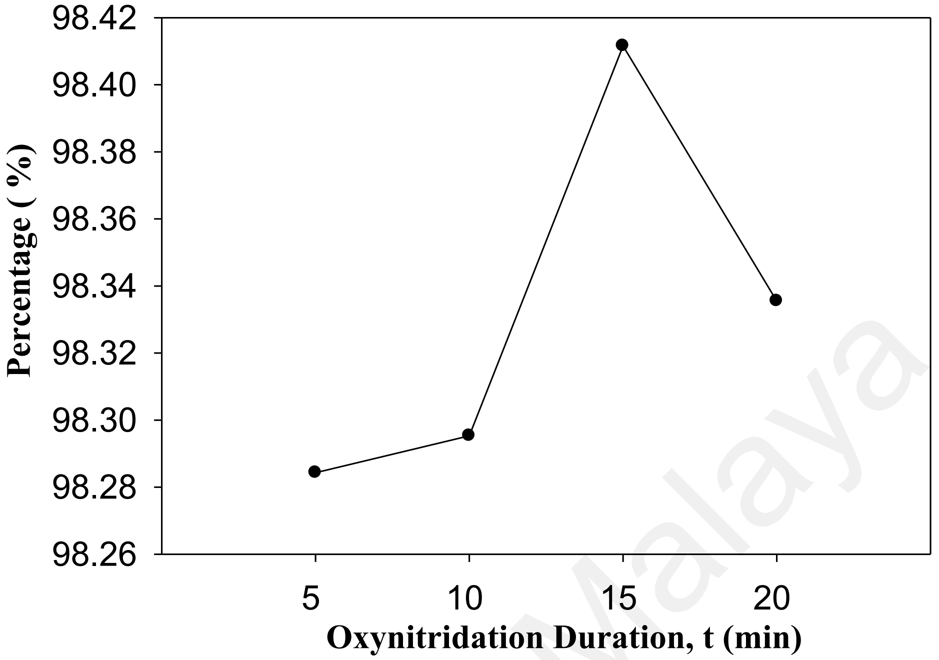

Figure 4.37: Percentage of interfacial compounds compared to the total detected thin film compounds of oxynitrided Nd samples at various durations (5min, 10min, 15min, and 20 min)

4.4.1.1 Williamson-Hall Analysis

Figure 4.38 shows Graph $\beta_{hkl}\cos\theta$ against $\sin\theta$, for Nd_2O_3, SiO_2, and $Nd_2Si_2O_7$, which were used to calculate crystallite size and microstrain in Figure 4.39. The crystallite size and microstrain for both Nd_2O_3 and SiO_2 are the same, which are 0.9003 nm and −0.022, for all the investigated durations. These indicate that homogeneous Nd_2O_3 and SiO_2 structures were produced. On the other hand, for $Nd_2Si_2O_7$, the crystallite size and microstrain at 5 min and 10 min are similar, which are 1.1850 nm and -0.015, respectively. Meanwhile, the crystallite size at 15 min and 20 min are also similar, which is 1.5937 nm. However, the microstrain for both these samples increased as duration increased. This shows that the silicate compound has a higher impact on the oxynitridation duration compared to Nd_2O_3 and SiO_2.

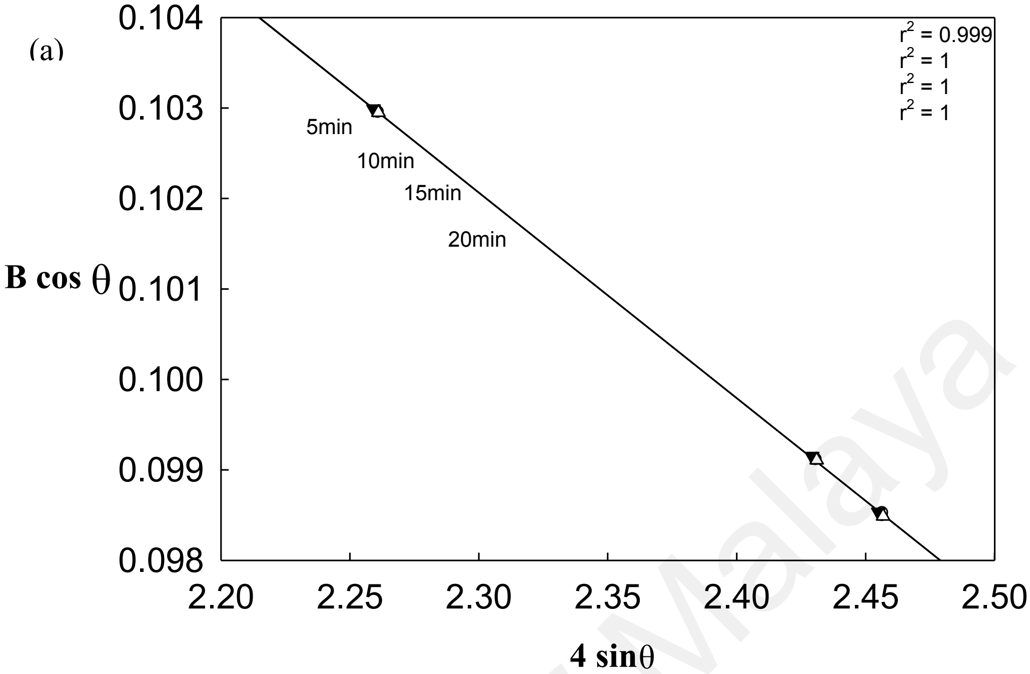

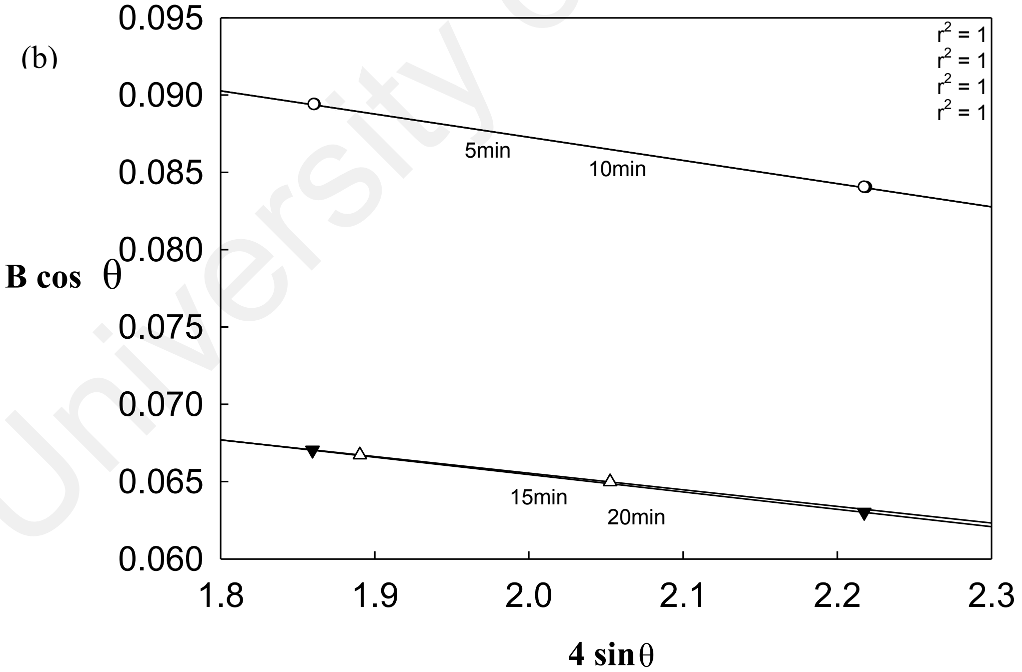

Figure 4.38: W-H plot of: (a) Nd_2O_3;(b) SiO_2; and (c) $Nd_2Si_2O_7$ of oxynitrided Nd samples at various durations (5 min, 10 min, 15 min, and 20 min)

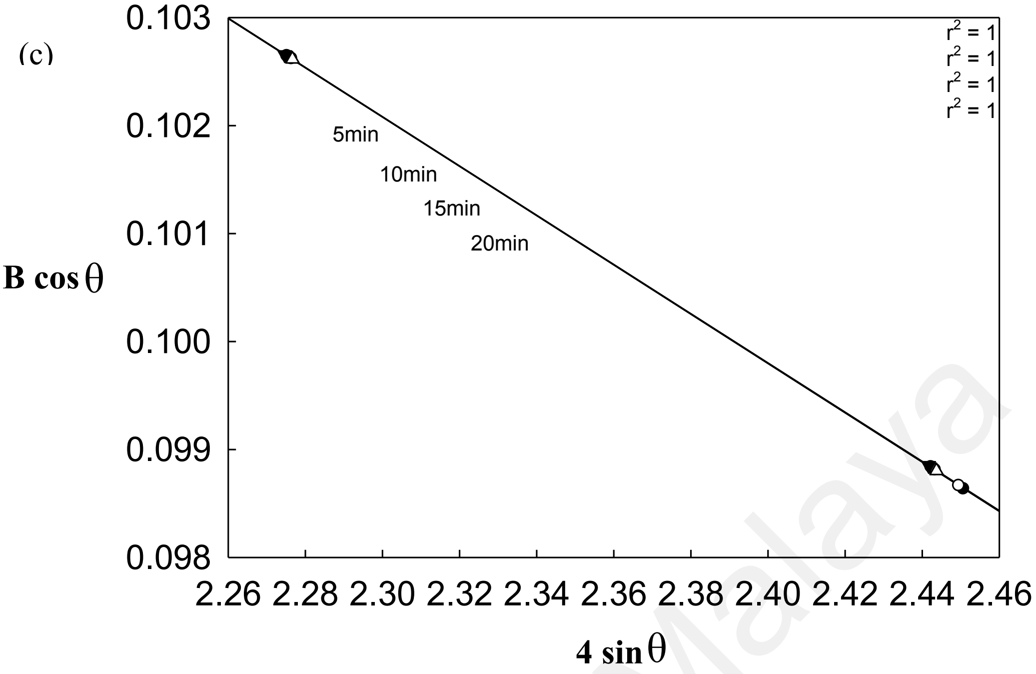

Figure 4.38: (*continued*) W-H plot of: (a) Nd_2O_3; (b) SiO_2; and (c) $Nd_2Si_2O_7$ of oxynitrided Nd samples at various durations (5 min, 10min, 15 min, and 20 min)

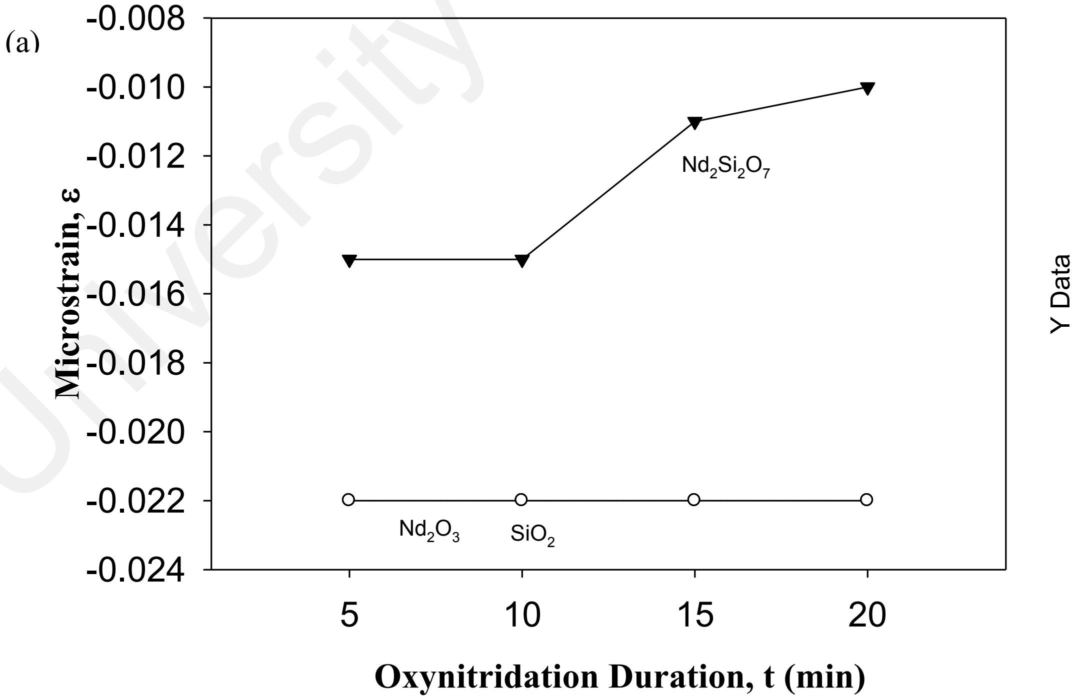

Figure 4.39: (a) Microstrain (b) crystallites size of Nd_2O_3, SiO_2, and $Nd_2Si_2O_7$ of oxynitrided Nd samples at various durations (5 min, 10 min, 15 min, and 20 min)

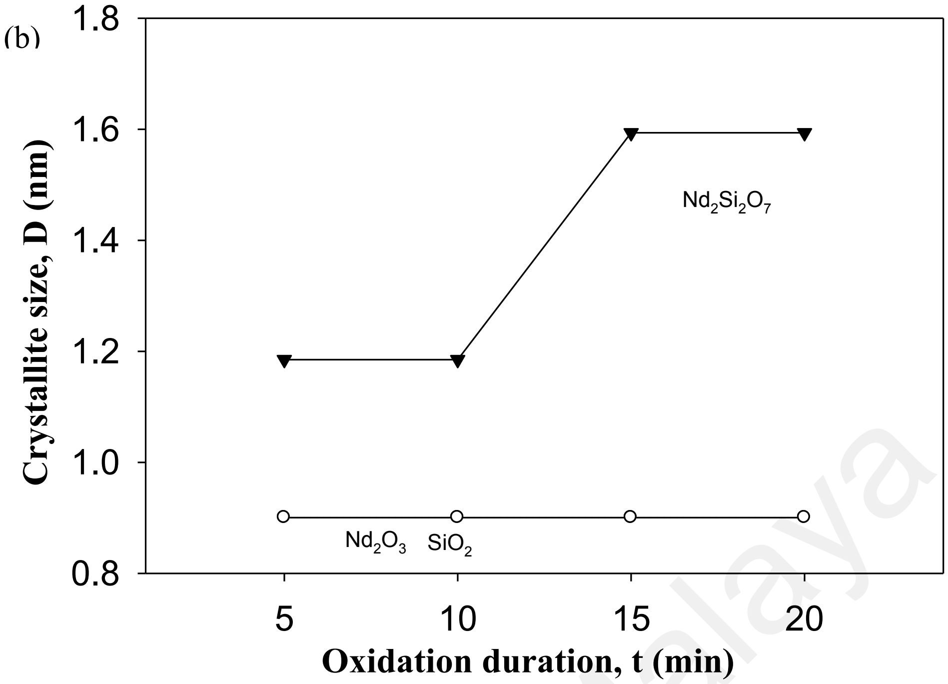

Figure 4.39: (*continued*) (a) Microstrain (b) crystallites size of Nd_2O_3, SiO_2, and $Nd_2Si_2O_7$ of oxynitrided Nd samples at various durations (5 min, 10 min, 15 min, and 20 min)

4.4.2 FTIR Analysis

Figure 4.40 shows the FTIR results of the oxynitrided Nd samples at various durations (5 min, 10 min, 15 min, and 20 min).The peak belonging to Si was detected as a Si-Si vibration mode at 613 cm^{-1}(Smith, 1998). This peak broadens as oxynitridation duration increases from 5 min to 10 min, and then sharpens at 15 min and 20 min. Peaks 502 cm^{-1} and 567 cm^{-1} were assigned to Nd-O (Päiväsaari et al., 2005). Peak 502 cm^{-1} shows a similar trend to that of the Si-Si vibration mode, where it broadens up until10 min and sharpens at 15 min. Meanwhile, peak 567cm^{-1} is only visible for the sample oxynitrided for 5 min. A similar interface layer compound, as shown in the XRD analysis, was detected. Peaks attributed to the Si-O-Si asymmetric stretch were detected at 1204 cm^{-1} and 1041 cm^{-1} (Kurniawan, Cheong, et al., 2011a). Both peaks broaden as oxynitridation duration increases. However, peak 1204 cm^{-1} disappears when oxynitrided for 20 min. A similar trend as peak 1204 cm^{-1} was also observed for peak Nd-O-Si at 925 cm^{-1}, where it broadens and disappears as oxynitridation duration increases. A peak attributed to the rocking, bending, and stretching of Si-O was detected at 805 cm^{-1}(Smith, 1998). This peak broadens and almost disappears as oxynitridation duration increases. Another peak belonging to Si-O was detected at the Si-O-Si bending at 456 cm^{-1}(Smith, 1998). The peak broadens as oxynitridation duration increases. A peak belonging to Si-O bend was detected at 413 cm^{-1} and 431 cm^{-1}(Lippincott et al., 1958; Viana et al., 2001). This initial peak sharpens as oxynitridation duration increases. However, the peak 431 cm^{-1} will only be visible for the sample oxynitrided for 15 min. The FTIR findings suggest that the tendency for interface layer formation decreases as oxynitridation duration increases. This observation is in contrast with the XRD analysis discussed in Section 4.4.1.

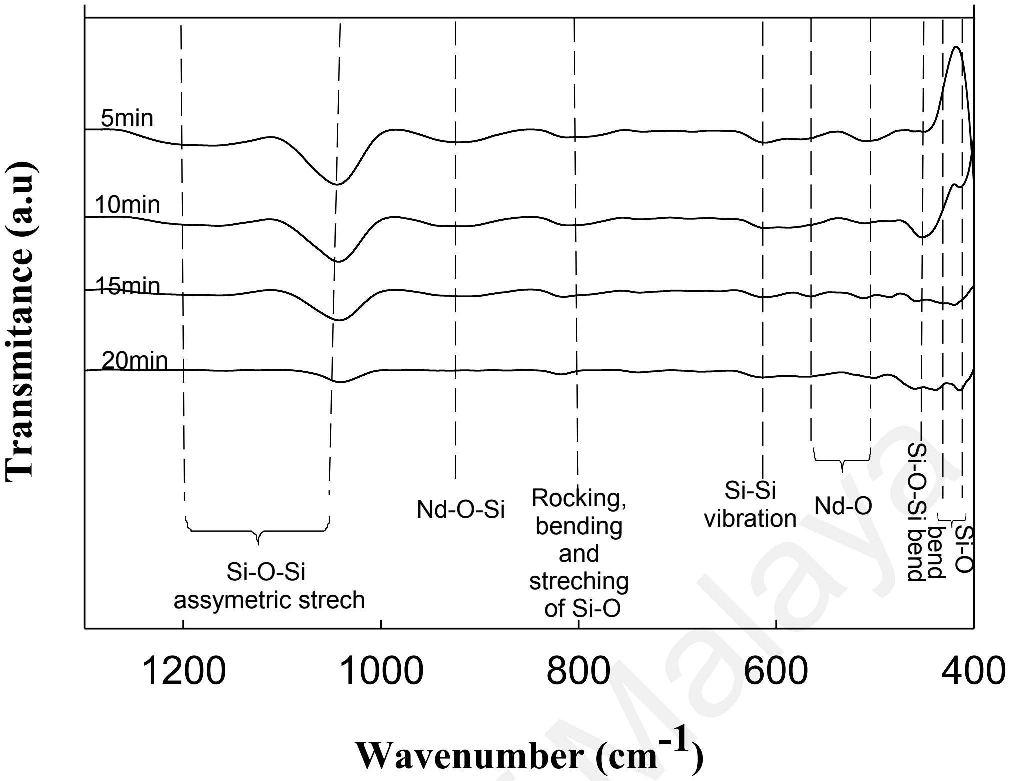

Figure 4.40: Transmittance spectra of oxynitrided Nd samples at various durations (5 min, 10 min, 15 min, and 20 min)

4.4.3 Raman Analysis

The Raman analysis results of the oxynitrided Nd samples at various durations (5 min, 10 min, 15 min, and 20 min) are shown Figure 4.41. Peak 525 cm^{-1} was assigned to Si (Wong & Cheong, 2011a). Six different peaks belonging to Nd_2O_3 were detected. These peaks were detected at 112 cm^{-1}, 225 cm^{-1}, 303 cm^{-1}, 434 cm^{-1}, 453 cm^{-1}, and 618 cm^{-1}(Jiang, Liu, Lin, Li, & Li, 2013; Kurniawan, Cheong, et al., 2011b; Nagai, Kitawaki, & Sato, 2013; Ubaldini & Carnasciali, 2008). However, all these peaks are only visible for the sample oxynitrided for 20 min. Peaks 303 cm^{-1} and 434 cm^{-1}were only visible for the sample oxynitrided for 5 min. These findings suggest that the sample oxynitrided at 20 min produces higher Nd_2O_3 when compared with the interfacial layer and followed by the sample oxynitrided at 5 min. An interfacial layer of SiO_2 and $Nd_xSi_yO_z$ was also detected. SiO_2 was detected at 925 cm^{-1} (Nyquist & Kagel,

2012) and $Nd_xSi_yO_z$ at 17 cm^{-1}. The intensity of peak SiO_2 decreased as oxynitrided duration increased up to 15 min and then increased at 20 min. Meanwhile, the silicate peak decreased as the oxynitrided duration increased to 10 min. However, this increased after 10 min. The sample oxynitrided for 10 min and 15 min produced much lower Nd_2O_3 when compared to the interfacial layer, as the peak of $Nd_2O_3$was not visible. The Raman findings are in agreement with the XRD findings.

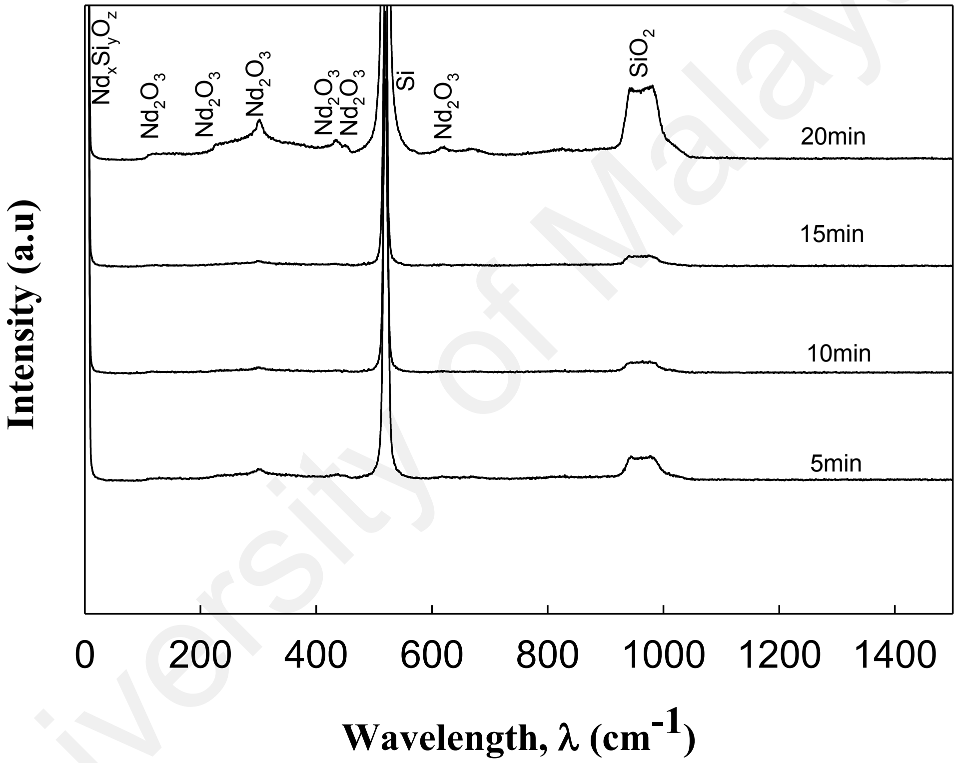

Figure 4.41: Raman spectra of oxynitrided Nd samples at various durations (5 min, 10 min, 15 min, and 20 min)

4.4.4 XPS Analysis

Depth profiling of thermally oxynitrided sample at various durations was conducted through XPS analysis. The wide scan detected the presence of Nd, Si, O, and N, which could not be detected through XRD, FTIR, or Raman analysis. Figure 4.42 shows the atomic percentage of Nd, Si, O, and N as a function of time for the oxynitrided Nd samples at various durations (5 min, 10 min, 15 min, and 20 min). The N element detected in these samples is less than 1%. The presence of N improves the crystallinity of the film (Iping et al., 2013). Additionally, the presence of N indicates the formation of $Nd_xO_yN_z$. In previous researches (Tong etal., 2006; Wong etal. 2012), a perfect stoichiometry of 1:2 (metal:O) was achieved (Tong, Jelenkovic, Liu, & Dai, 2006; Wong & Cheong, 2012b). However, a stoichimetry of 2:3 (Nd:O) could not be achieved due to a more than stable oxidation state. This can be exploited according to requirements, which is an added advantage of using this oxide (Scarel, Svane, & Fanciulli, 2007). As the etching time increases (depth increases from the surface), the presence of Nd, Si, O, and N were simultaneously detected. This indicates the presence of an interface layer consisting of nitrogen-incorporated neodymium silicate ($Nd_aSi_bO_cN_d$) (K. H. Goh, A. S. M. A. Haseeb, & Y. H. Wong, 2017b). As etching time increases, the atomic percentage of Si also increases whereas O decreases. However, the atomic percentage of Nd and N increases until 900 s, after which it decreases. This indicates that there will be oxynitride and Si boundaries. At this boundary, Nd, O, and N will completely disappear (Wong & Cheong, 2012b).

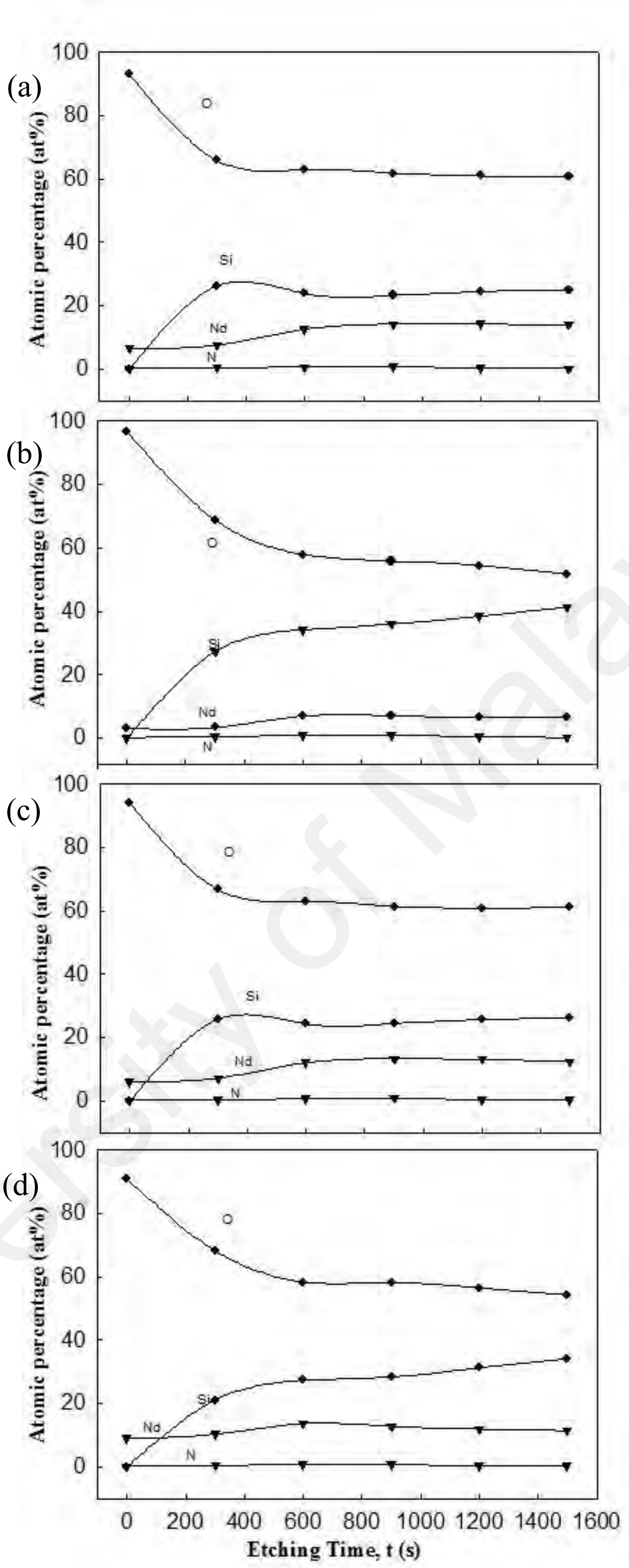

Figure 4.42: The atomic percentage of Nd, Si, O, and N as a function of time for oxynitrided Nd samples at various durations:(a) 5 min;(b) 10 min; (c) 15 min; and (d) 20 min

Figure 4.43 to Figure 4.46 show a summarized narrow scan of the core level of Nd, O, Si, and N as a function of etching time for oxynitrided Nd samples at various durations (5 min, 10 min, 15 min, and 20 min). The dotted line, which is the measured peak, was deconvoluted with the aid of a non-linear Gaussian-Lorentzian function using CasaXPS software (version 2.3.16).

Figure 4.43 shows the Nd 3*d* core level XPS spectra for oxynitrided Nd samples at various durations (5 min, 10 min, 15 min, and 20 min). Nd-O was detected at a binding energy between 983.2 eV-979.5 eV (C.H. Kao et al., 2010). A higher binding energy of 982.95 eV and 983.2 eV was detected for the sample oxynitrided for 5 min at an etching time of 300 s. However, further etching revealed that the higher binding energy had shifted to a lower binding energy. This indicates that 5 min is not sufficient to form higher intensity Nd-O compared to other samples. For the sample oxynitrided for 20 min a shift to lower binding energy (979.5 eV) was also observed, which indicates that formation of Nd-O decreased as oxynitridation duration increased. Overall, the intensities of these peaks increased until an etching time of 900 s and decreased at 1200 s. However, the sample oxynitrided for 20 min shows an increment of up to 600 s, which decreased afterwards, indicating poor formation of Nd-O for this sample.

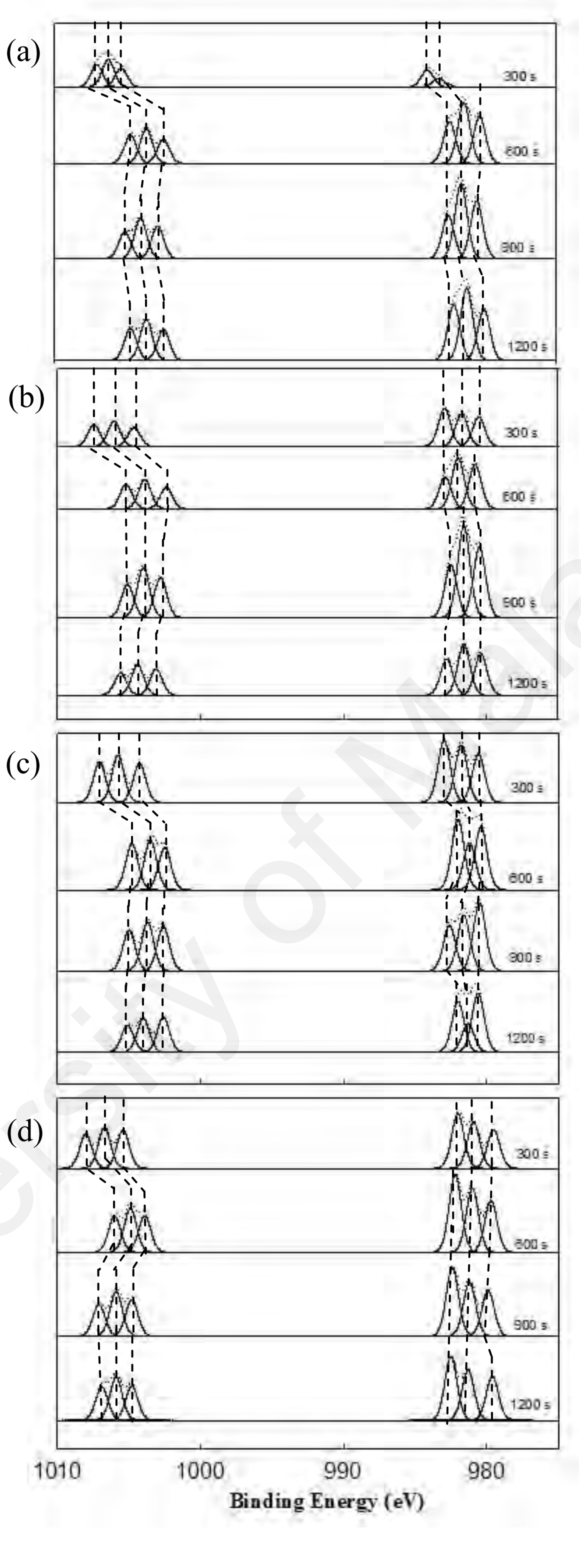

Figure 4.43: Nd 3*d* core level XPS spectra as a function of time for oxynitrided Nd samples at various durations: (a) 5 min; b) 10 min; (c) 15 min; and (d) 20 min

A few unidentified binding energies were detected in the range of 1008.2 eV and 1002.1eV. These binding energies originate from Nd-Si-O and Nd-Si-O-N bonding based on the atomic percentage analysis. These bonding energies also shifted to lower binding energies as etching time increased to 300 s to 600 s. Later, the lower binding energy increased to a higher one as etching time increased to 600 s to 900 s. Afterwards, this decreased to a lower binding energy as the etching time increased to 1200 s. Thus, it can be concluded that as the thickness increases, an interface layer will be formed as Nd tends to diffuse in to form $Nd_aSi_bO_cN_d$ bonding (Fissel et al., 2006) and oxynitrided Nd bonding. The thickness of the interface layer decreases as it approaches the Si substrate, as shown by the atomic percentage analysis. The intensity of the interface layer also increases as the oxynitridation duration increases up to 15 min and later decreases at 20 min. Thus, the formation of the interface layer reduces at 20 min.

Figure 4.44 shows O 1*s* core level XPS spectra for the oxynitrided Nd samples at various durations (5 min, 10 min, 15 min, and 20 min). The binding energy of Nd - O was detected at 530.8 eV,530.6 eV, and 529.5 eV (Frohlich et al., 2006; K. H. Goh, A. Haseeb, & Y. H. Wong, 2017a; J. Kim, Kim, & Kim, 2017; Pan et al., 2006b). For the sample oxynitrided for 5 min and 10 min, the intensity increased until an etching time of 900 s and later decreased. Meanwhile, for the sample oxynitrided for 5 min and 20 min the binding energies shifted to a higher binding energy. On the other hand, for the sample oxynitrided for 10 min and 15 min, the binding energies shifted to a lower binding energy. The binding energy assigned to nitrogen-incorporated silicate was detected at 531.8 eV and 532.2 eV (Chew et al., 2016; Pan et al., 2006b; Pan et al., 2007; Pan & Yu, 2009). The intensity of the sample oxynitrided for 5 min and 15 min was higher compared to the rest of the samples. The $Nd_aSi_bO_cN_d$ intensity detected at an etching time of 900 s for the sample oxynitrided for 15 min is higher compared to the rest of the sample. These indicate a thicker $Nd_aSi_bO_cN_d$ layer formation for this sample.

The binding energy of Si - O was detected at 533 eV (Pan et al., 2006b; Pan et al., 2007; Pan & Yu, 2009). This binding energy was detected at all etching times for the sample oxynitrided for 20 min. Meanwhile, for the rest of the samples, this was detected at the initial etching stages. A thicker Si- O layer was formed for the sample oxynitrided for 15 min compared to the sample oxynitrided for 5 min and 10 min. The binding energy assigned to N-O was detected at 531.5 eV. This bond was not detected at an etching time of 300 s. This indicates the formation of an interface layer consisting of an N element as it approaches Si.

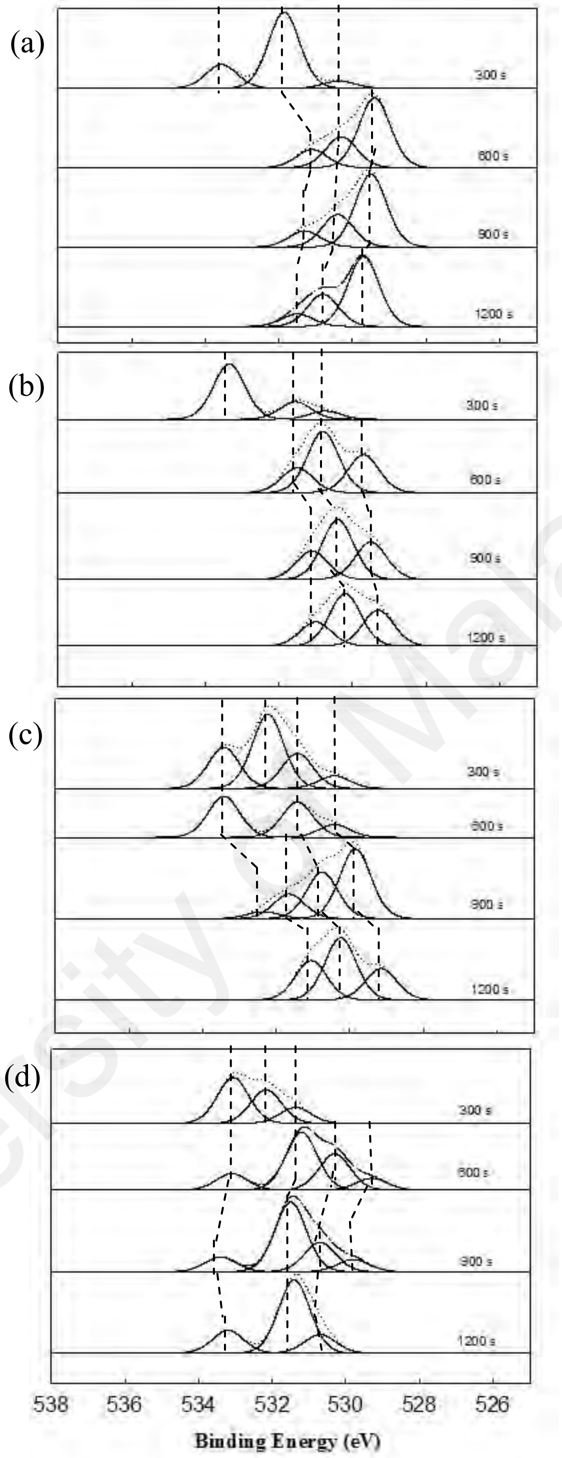

Figure 4.44: O 1*s* core level XPS spectra as a function of time for oxynitrided Nd samples at various durations: (a) 5 min; (b) 10 min; (c) 15 min; and (d) 20 min

Figure 4.45 shows the Si 2*p* core level XPS spectra for the oxynitrided Nd samples at various durations (5 min, 10 min, 15 min, and 20 min). The Si binding energy originates from the substrate detected at 99.6 eV (Pan et al., 2006b; Pan et al., 2007; Wong & Cheong, 2012c). This peak was detected at an etching time of 300 s for the sample oxynitrided for 5 min and 10 min. However, this was only detected at an etching time of 600 s for the sample oxynitrided for 15 min and 20 min. The intensity of this peak increased as etching time increased for the sample oxynitrided for 20 min. Meanwhile, for the sample oxynitrided for 15 min, the intensity reduced at an etching time of 1200 s. At the same time,a much lower binding energy was detected in the range of 97.2 eV and 96.4 eV for the sample oxynitrided for 5 min and 10 min. It could therefore be inferred that Si had moved deeper inside and a thicker $Nd_xO_yN_z$ layer was obtained for these two samples.

The binding energy related to Si-O, and Si-N was detected at 103.3 eV and 101.9 eV (Goh et al., 2017a; Pan et al., 2006b; Pan et al., 2007). The binding energy related to Si - O was detected within the range of 103.7 eV and 102.5 eV (Pan et al., 2006b; Pan et al., 2007; Tong et al., 2006). This was only detected at an etching time of 300 s for the sample oxynitrided for 10 min. Thus, the least amount of Si-O bonding was formed for this sample. For the sample oxynitrided for 5 min, the intensity decreased as etching time increased. Meanwhile, for the sample oxynitrided for 15 min, the intensity decreased until an etching time of 900 s but later increased as it approached 1200 s. However, for the sample oxynitrided for 20 min, the binding energy increased as etching time increased. On the other hand, the Si-N binding energy was detected throughout the $Nd_xO_yN_z$film for the sample oxynitrided for 15 min and 20 min. Meanwhile, for the sample oxynitrided for 5 min and 10 min, the binding energy was not detected at an etching time of 300 s. This indicates a better diffusion of N at a longer oxynitridation period. For a longer oxynitiration period (20 min), the intensity remains almost constant.

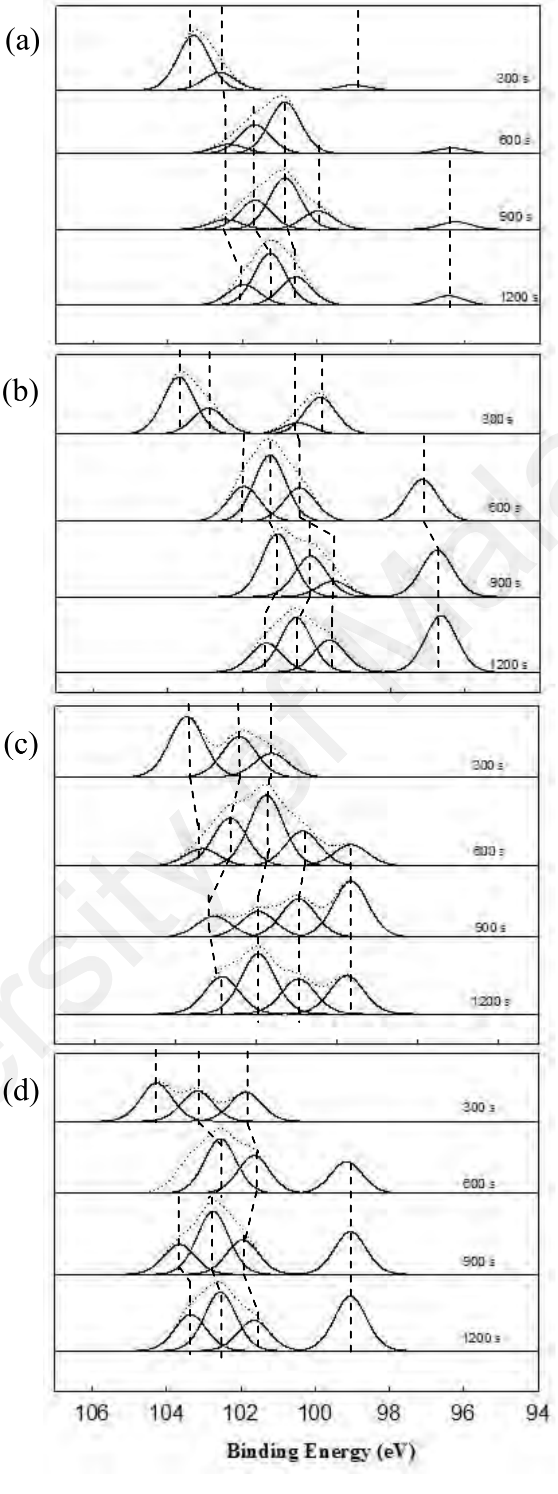

Figure 4.45: Si 2*p* core level XPS spectra as a function of time for oxynitrided Nd samples at various durations: (a) 5 min; (b) 10 min; (c) 15 min; and (d) 20 min

A few unidentified peaks were detected at 104.3 eV and in the range of 100.9 eV and 100.15 eV. These binding energies are attributed to Nd-Si-O. These binding energies were detected throughout the film, which was oxynitrided for 10 min, and was detected after an etching time of 300 s for the sample oxynitrided for 5 min and 15 min. However, the binding energy was only detected at the initial stage of etching for the sample oxynitrided for 20 min. The intensity of these binding energies decreased as the film approached the Si susbstrate for the sample oxynitrided for 15 min. However, for the sample oxynitrided for 5 min and 10 min, the binding energy increased as it approached the Si substrate.

Figure 4.46 shows the N 1*s* core level XPS spectra for oxynitrided Nd samples at various durations (5 min, 10 min, 15 min, and 20 min). The binding energies of ~402.5 eV, ~400 eV, and ~399.5 eV were attributed to N-O, Sm-N, and Si-N, respectively (Gholizadeh, Yu, & Wang, 2017; Goh et al., 2017a; J. C. Lee et al., 2003; Vaz et al., 2013; Wong & Cheong, 2011b, 2012c). N-O binding energies were not detected for the sample oxynitrided for 20 min; these were detected throughout the sample oxynitrided for 5 min and 15 min. For the sample oxynitrided for 5 min, the binding energies had shifted to a lower binding energy as the etching time increased. However, this binding energy was only detected at the final stage of etching for the sample oxynitrided for 10 min. The Nd-N and Si-N binding energy was not detected for the sample oxynitrided for 5 min. The Nd-N and Si-N binding energies were detected throughout the film oxynitrided for 10 min. For the sample oxynitrided for 15 min, Nd-N was detected at an etching time of 1200 s and Si - N was detected after an etching time of 300 s. However, Si-N binding energy was only detected after an etching time of 300 s. In addition, the Nd-N binding energy for the sample oxynitrided for 20 min had shifted to a lower binding energy and the Si-N binding energy had shifted to a higher binding energy as the etching time increased. This result shows the presence of

$Nd_xO_yN_z$ and an interface layer with incorporation of the N element. At the same time, no silicide bonding was detected.

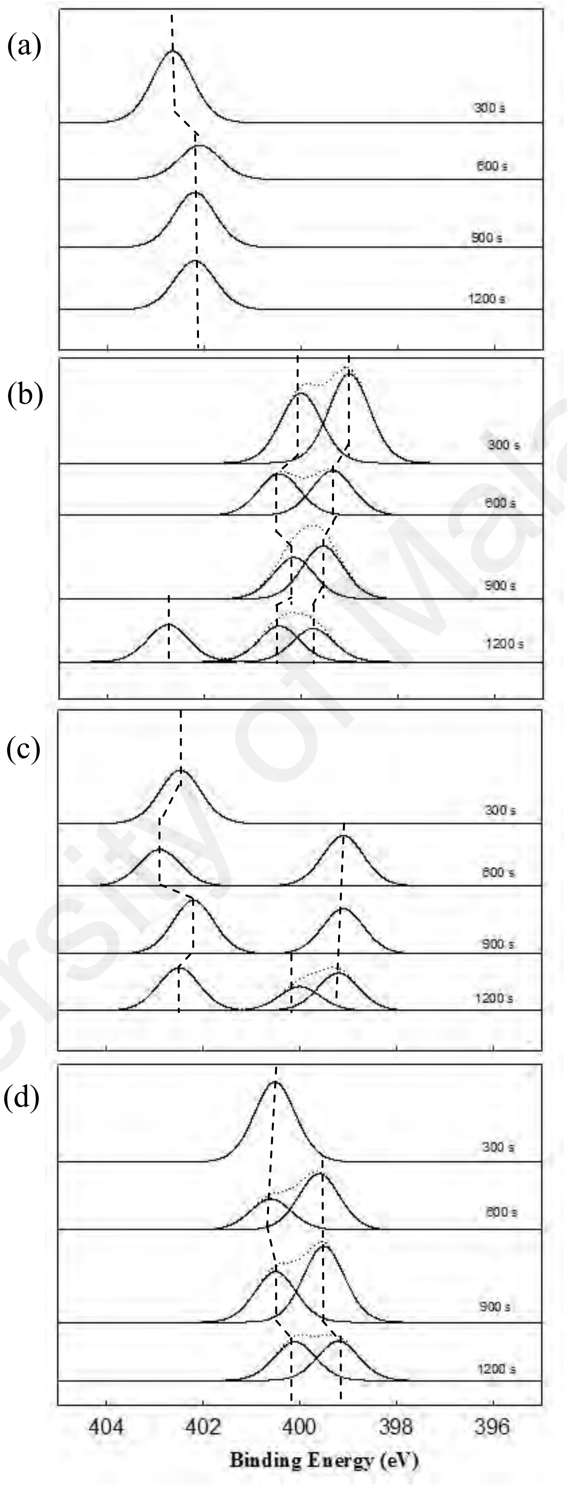

Figure 4.46: N 1*s* core level XPS spectra as a function of time for oxynitrided Nd samples at various durations: (a) 5 min; (b) 10 min; (c) 15 min; and (d) 20 min

4.4.5 HRTEM Analysis

As all samples produced almost similar results, a HRTEM analysis was performed on the sample oxynitrided for 15 min for which the result is shown in Figure 4.47. As predicted, the sample possesses a single interfacial layer between the Si and the oxide layer. The thickness of the $Nd_xO_yN_z$ layer and the interfacial layer are 4.87 nm and 8.83 nm, respectively. A similar growth was observed for samarium oxynitride and zirconium oxynitride, which was produced using a similar method (Goh et al., 2017a; Wong & Cheong, 2012b, 2012c). In addition, hafnium oxynitride also produced the same growth even with a different growth method, which is the co-sputtering of Hf in nitrogen, oxygen, and argon ambient, followed by PDA (Koike et al., 2003; J. C. Lee et al., 2003; Xu & Xu, 2008).

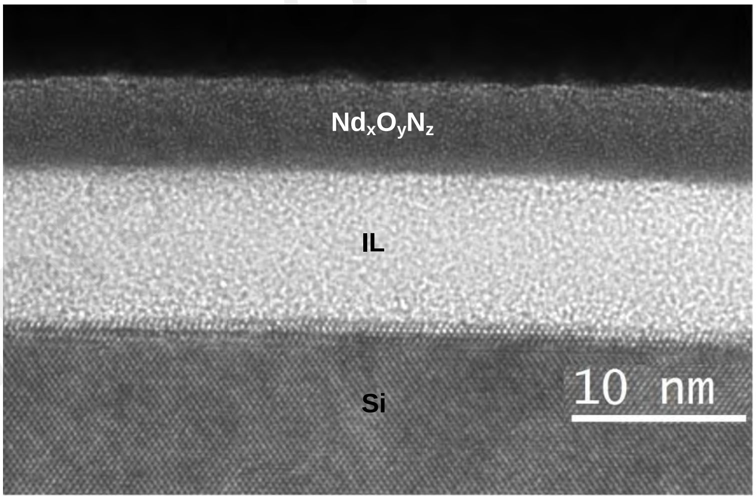

Figure 4.47: HRTEM image of oxynitrided Nd sample for 15 min

An oxynitridation model was proposed based on the structural analysis outlined in Sections4.4.1–4.4.5. Prior to that, the thickness of each layer for the sample oxynitrided for 5 min, 10 min, and 20 min was estimated based on the intensity of XPS analysis and thickness of the sample oxynitrided for 15 min, as per Equations (4.1) and (4.2):

$$\frac{\begin{array}{c}\mathrm{NdxOyNz}\\ \textit{thickness of sample}\\ \textit{oynitrided for } 15\ \textit{min}\end{array}}{\begin{array}{c}\mathrm{NdxOyNz}\\ \textit{thickness of sample}\\ \textit{oynitrided for}\\ 5\ \mathrm{min}, 10\ \textit{min},\ 20\ \textit{min}\end{array}} = \frac{\begin{array}{c}\mathrm{NdxOyNz}\\ \textit{intensity for overall sample}\\ \textit{oynitrided for } 15\ \textit{min}\end{array}}{\begin{array}{c}\mathrm{NdxOyNz}\\ \textit{intensity for overall sample}\\ \textit{oynitrided for } 5\ \textit{min}, 10\ \textit{min}, 20\ \textit{min}\end{array}} \tag{4.1}$$

$$\frac{\begin{array}{c}\mathrm{NdaSibOcNd}\\ \textit{thickness of sample}\\ \textit{oynitrided for } 15\ \textit{min}\end{array}}{\begin{array}{c}\mathrm{NdaSibOcNd}\\ \textit{thickness of sample}\\ \textit{oynitrided for}\\ 5\ \mathrm{min}, 10\ \textit{min},\ 20\ \textit{min}\end{array}} = \frac{\begin{array}{c}\mathrm{NdaSibOcNd}\\ \textit{intensity for overall sample}\\ \textit{oynitrided for } 15\ \textit{min}\end{array}}{\begin{array}{c}\mathrm{NdaSibOcNd}\\ \textit{intensity for overall sample}\\ \textit{oynitrided for } 5\ \textit{min}, 10\ \textit{min}, 20\ \textit{min}\end{array}} \tag{4.2}$$

Based on the calculation, the oxynitridation process is proposed as per Figure 4.48. The thickness of the $Nd_xO_yN_z$iis as follows: 20 min > 10 min > 5 min > 15 min. Meanwhile, the thickness of the interfacial layer is as follows: 5 min > 15 min > 20 min > 10 min. Overall, the sample oxynitrided for 5 min has the thickest $Nd_xO_yN_z$ and the sample oxynitrided for 10 min has the thinnest $Nd_xO_yN_z$.

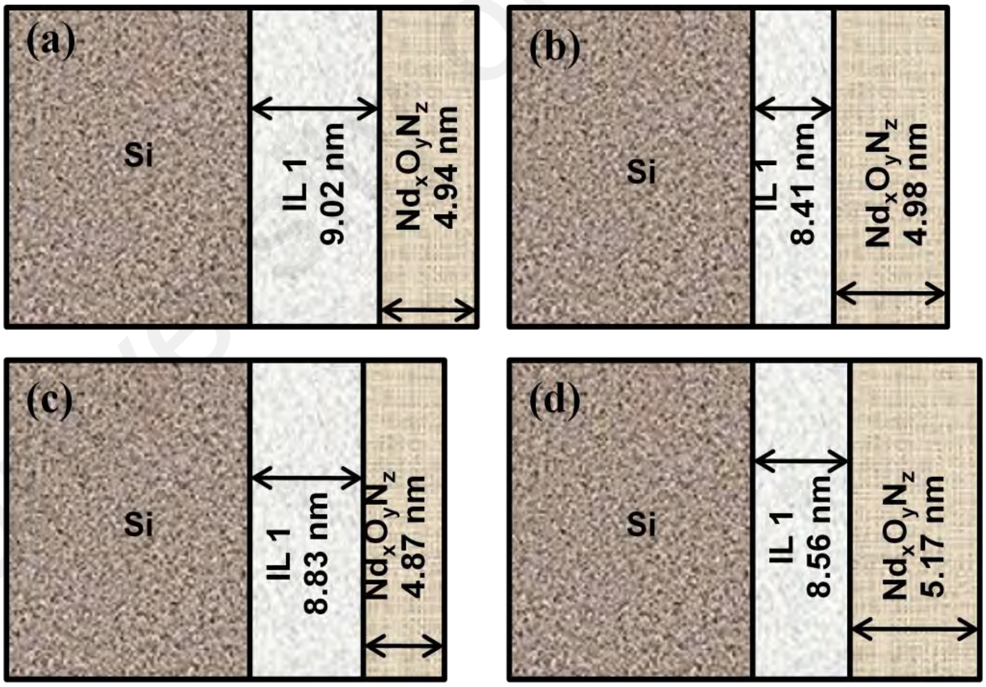

Figure 4.48: Layer distribution model for different oxynitridation durations: (a) 5 min; (b) 10 min; (c) 15min; and (d) 20 min

The N_2O decomposition mechanism can be simplified as per Equations (4.3)-(4.5) (Cui, Liu, Lin, & Ma, 2016; Kuboňová et al., 2017; L. Wu et al., 2015),

$$N_2O \rightarrow N_2 + O \tag{4.3}$$

$$N_2 + O \rightarrow 2NO \tag{4.4}$$

$$N_2O + O \rightarrow N_2 + O_2 \tag{4.5}$$

The decomposition of N_2O can be classified as a slower rate, as the adsorption of N_2O and desorption of O_2 is easier in the presence of transition metals (Kuboňová et al., 2017). Thus, at the initial oxynitridation duration (5 min), the decomposition is lesser. However, the decomposed N_2O may react with Nd to form $Nd_xO_yN_z$. At the same time, the inward diffusion of Nd, O and N, together with the outward diffusion of Si leads to the formation of a $Nd_aSi_bO_cN_d$.

On the other hand, at the final oxynitridation duration (20 min), a thicker $Nd_xO_yN_z$ was formed. This can be due to the longer decomposition period, which provides a higher intensity of O atoms, thus increasing the rate of adsorption of O atoms by Nd. However, when the thickness of oxide film increases, less N and O atoms can diffuse, leading to a thinner interfacial layer. Due to the thicker oxide layer, the sintering effect becomes less pronounced (Kang, 2004).

During oxynitridation durations of 10 min and 15 min, the temperature-aided sintering effect will lead to an overall thinner oxide formation (Kang, 2004). At 15 min, a thicker interfacial layer is formed compared to $Nd_xO_yN_z$, as the O atom has a larger atomic size compared to the N atom. Thus, more N atoms will diffuse in to form a thicker interfacial layer.

4.4.6 Leakage Current Density versus Electrical Breakdown Field Characteristics

The J-E characteristics of the oxynitrided Nd samples at various durations (5 min, 10 min, 15 min, and 20 min) are shown in Figure 4.49. All the samples possess double breakdown, where SB is in the range of ~10^{-6} A/cm^2. It can be concluded that the sample oxynitrided for 15 min has the best J-E characteristics, as it has the highest breakdown voltage of 3.909 MV/cm. The same trend is also observed for HB, where the breakdown voltage is 4.636 MV/cm.

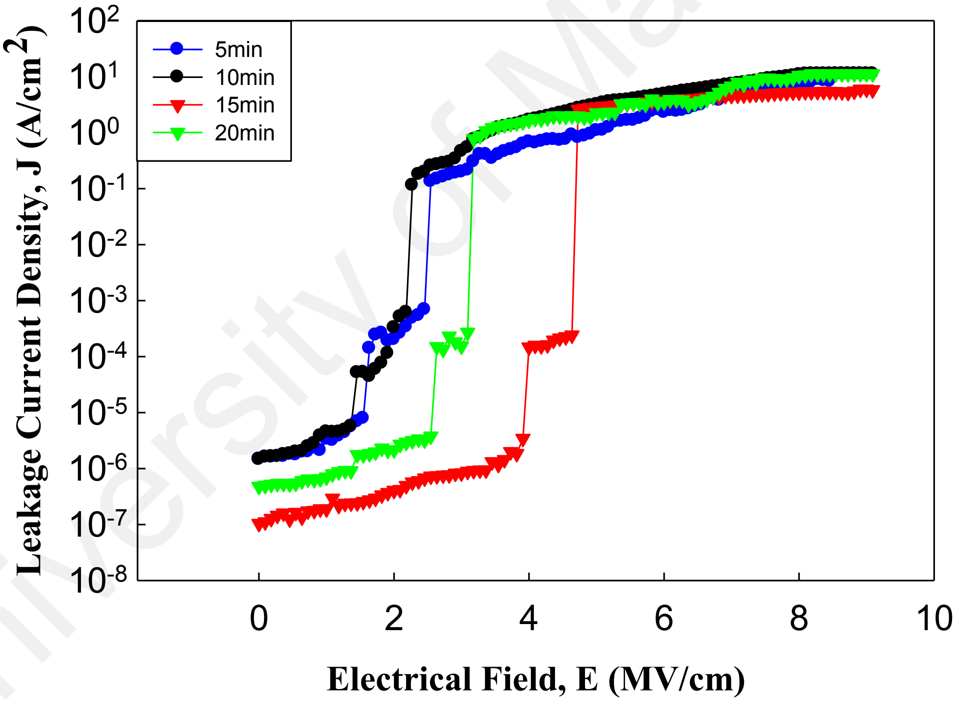

Figure 4.49: J-E characteristic of the oxynitrided Nd samples at various durations (5 min, 10 min, 15 min, and 20 min)

This result was compared with HfON, SiON, and ZrON, produced through various methods and shown in Table 4.4. $Nd_xO_yN_z$ possesses a much lower leakage value compared to SiON. At the same time, it also has a higher breakdown voltage than HfON and ZrON. This could be attributed to the higher *k*-value of Hf and Zr. In addition, the HfON interfacial layer does not consist of SiO_2, which is responsible for lowering the*k*-value of the oxide film (E. Bugiel et al., 2005; Frohlich et al., 2006; G Lucovsky & Rayner, 2000).

Table 4.4: J-E characteristics comparison of HfON, SiON, ZrON, and NdON

Method	**Oxide**	**IL**	**Thickness (nm)**	**E ($MVcm^{-1}$)**	**J (A/cm^2)**	**Refer-ence**
DC sputtering of Hf in Ar, O and N ambient followed by PDA	HfON	Silicon Nitride	12.2	3.3	10^{-7}	(Liu et al., 2008)
RF sputtering of Zr in Ar, O and N ambient followed by PDA	ZrON	Zirconium silicate + SiO_2	Not reported	2.0	10^{-8}	(Chew et al., 2016)
Plasma oxynitrid-ation	SiON	Not reported	14.5	-11.0	10^{-4}	(J. Kim et al., 2017)
Neutral beam	SiON	Not reported	14.3	~14.0	10^{-5}	(J. Kim et al., 2017)
RF sputtering of Nd followed by thermal oxynitrid-ation	$Nd_xO_yN_z$	$Nd_aSi_bO_cN_d$	13.7	3.0	10^{-6}	This current study

The TZBD reliability test result of thermal oxynitrided Nd samples at various durations (5 min, 10 min, 15 min, and 20 min) is shown in Figure 4.50. The highest breakdown voltage falls in the range of 4-5 MV/cm for the sample oxynitrided for 5 min, 15min, and 20 min. However, the leakage values of these samples are between ~ 10^{-4} - ~ 10^{-5}A/cm^2.

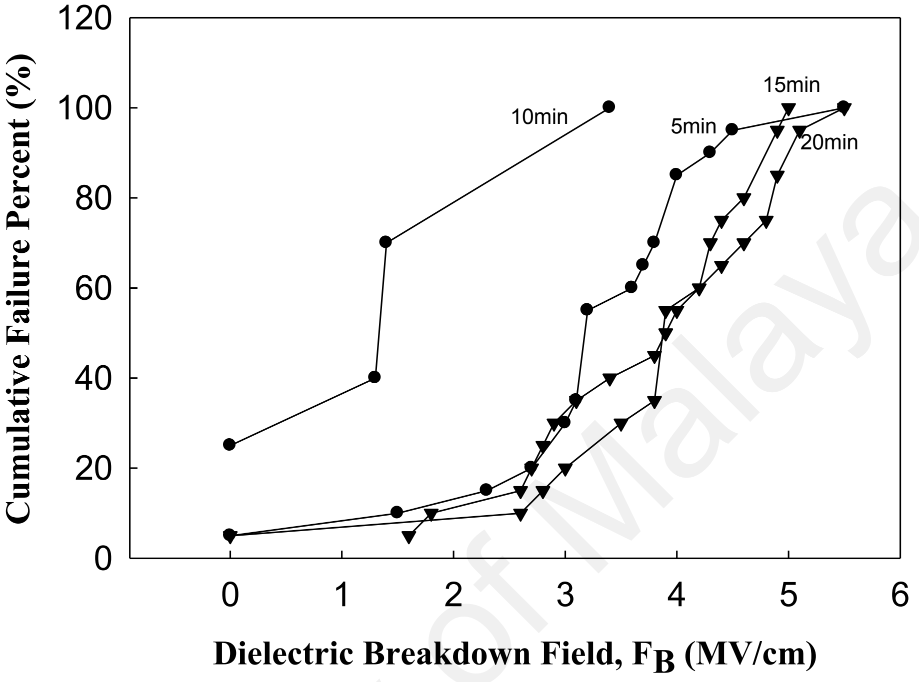

Figure 4.50: Cumulative failure percentage of the EBD of oxynitrided Nd samples at various durations (5 min, 10 min, 15 min, and 20 min)

4.4.6.1 Fowler-Nordheim Tunneling Analysis

Figure 4.51 shows the F-N regression plot of In (J/E^2) versus 1/E and followed by $Ø_B$ of the oxynitrided Nd samples at various durations (5 min, 10 min, 15 min, and 20 min) in Figure 4.52. The highest $Ø_B$ is recorded by the sample oxynitrided for 15 min, which also shows the best J-E characteristics.

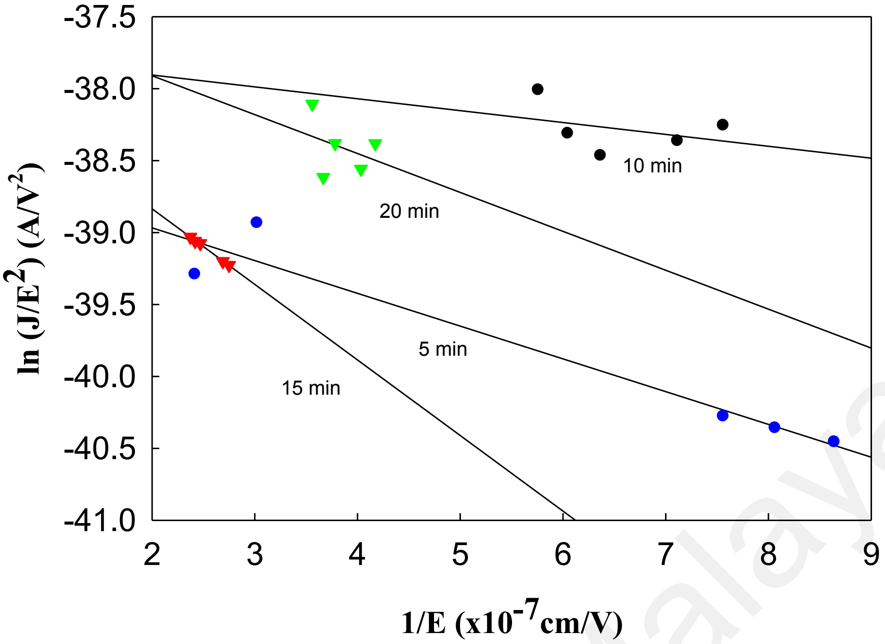

Figure 4.51: F-N tunneling linear regression plot [In (J/E^2) versus 1/E] of oxynitrided Nd samples at various durations (5 min, 10 min, 15 min, and 20 min)

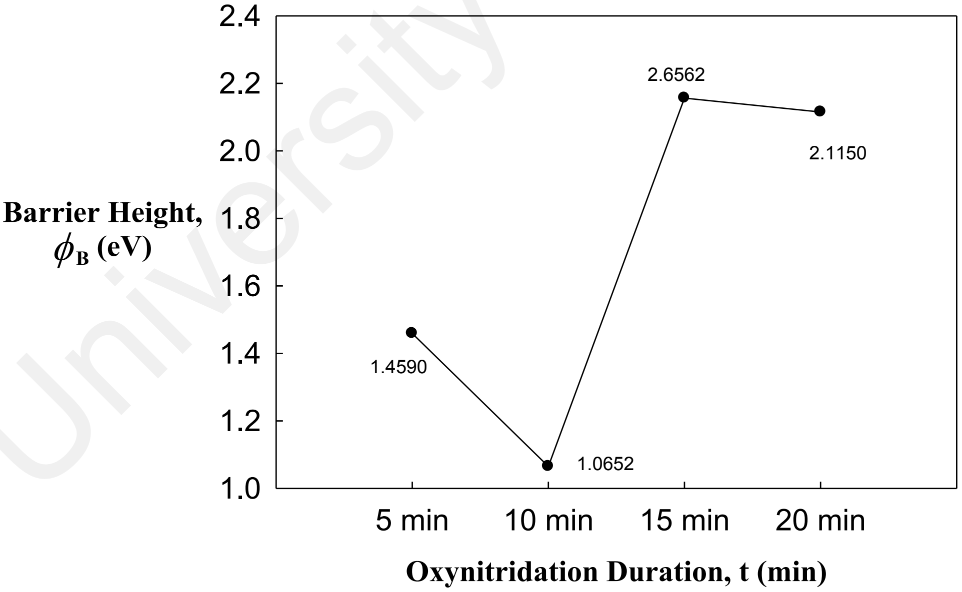

Figure 4.52: Barrier height values as a function of oxynitrided Nd samples at various durations (5 min, 10 min, 15 min, and 20 min)

4.4.7 Capacitance-Voltage Characteristics

The normalized capacitance value of oxynitrided Nd samples at various durations (5 min, 10 min, 15 min, and 20 min) is shown in Figure 4.53. All samples possessa negative depletion region with negative-shifted ΔV_{FB}. Figure 4.54 shows the highest capacitance accumulation and the k-value of oxynitrided Nds sample at various durations (5 min, 10 min, 15 min, and 20 min). Although the sample oxynitrided for 15 min possesses the best J-E characteristics, it has the lowest capacitance value and k - value. This sample also has a lower thickness than the sample oxynitrided for 5 min and 10 min, together with the lowest capacitance value that contributes to a lower k - value. Additionally, this k - value is also lower than SiO_2 (Vaz et al., 2013). C-V results will be further analyzed and discussed in Section 4.4.7.1 to confirm the findings of these J-E characteristics.

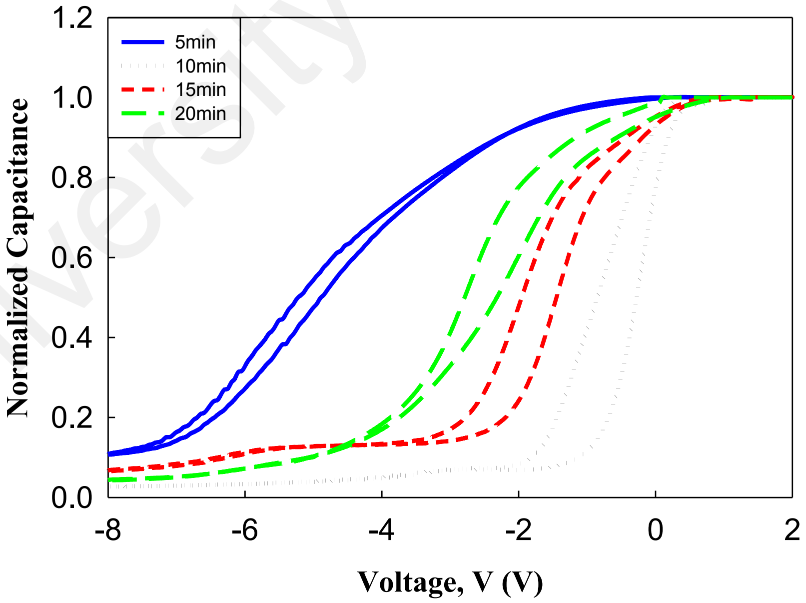

Figure 4.53: The normalized C-V curve of oxynitrided Nd samples at various durations (5 min, 10 min, 15 min, and 20 min)

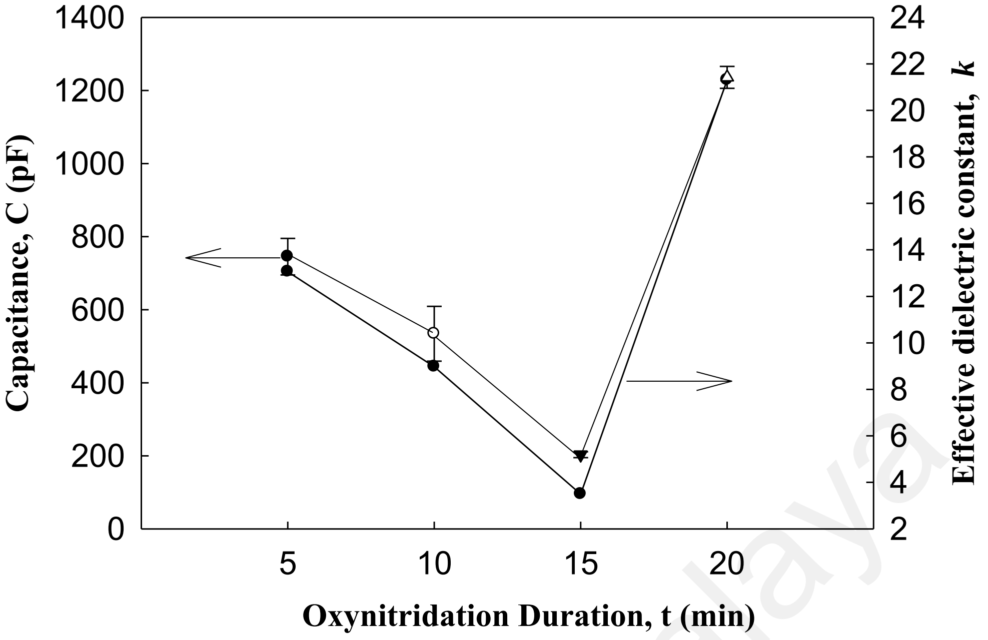

Figure 4.54: Capacitance accumulation and *k*-value of oxynitrided Nd samples at various durations (5 min, 10 min, 15 min, and 20 min)

4.4.7.1 Effective Oxide Charge, Slow Trap Density and Interface Trap Defect Density

Figure 4.55 shows the Q_{eff} and STD of the oxynitrided Nd samples at various durations (5 min, 10 min, 15 min, and 20 min) and followed by D_{it} in Figure 4.56. The sample oxynitrided for 15 min has the lowest Q_{eff} and STD. In addition, the sample oxynitrided for 15 min also possesses the lowest D_{it}. Thus, the sample oxynitrided for 15 min has the best C-V characteristics.

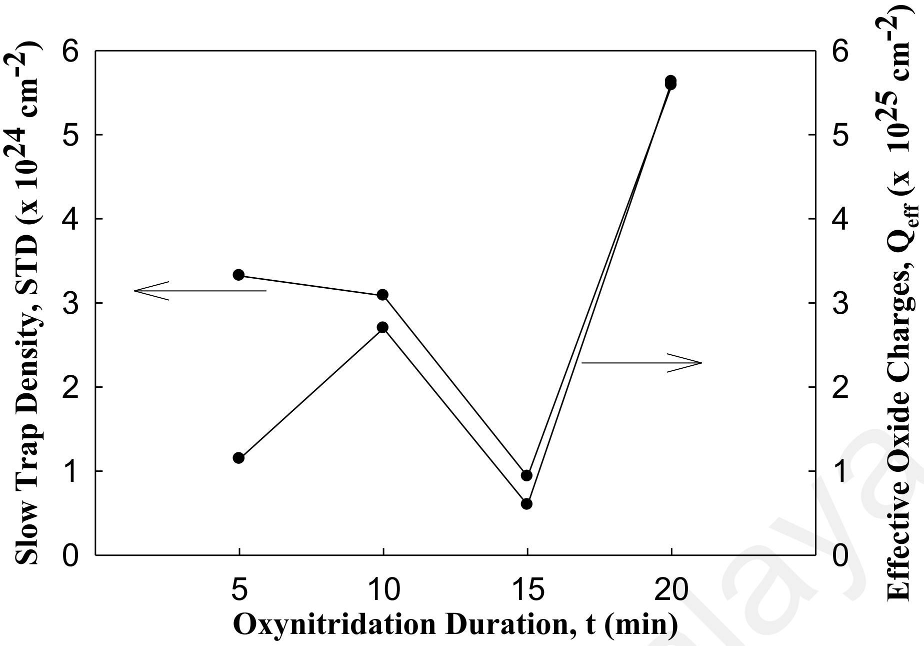

Figure 4.55: STD and Q_{eff} charges of the oxynitrided Nd samples at various durations (5 min, 10 min, 15 min, and 20 min)

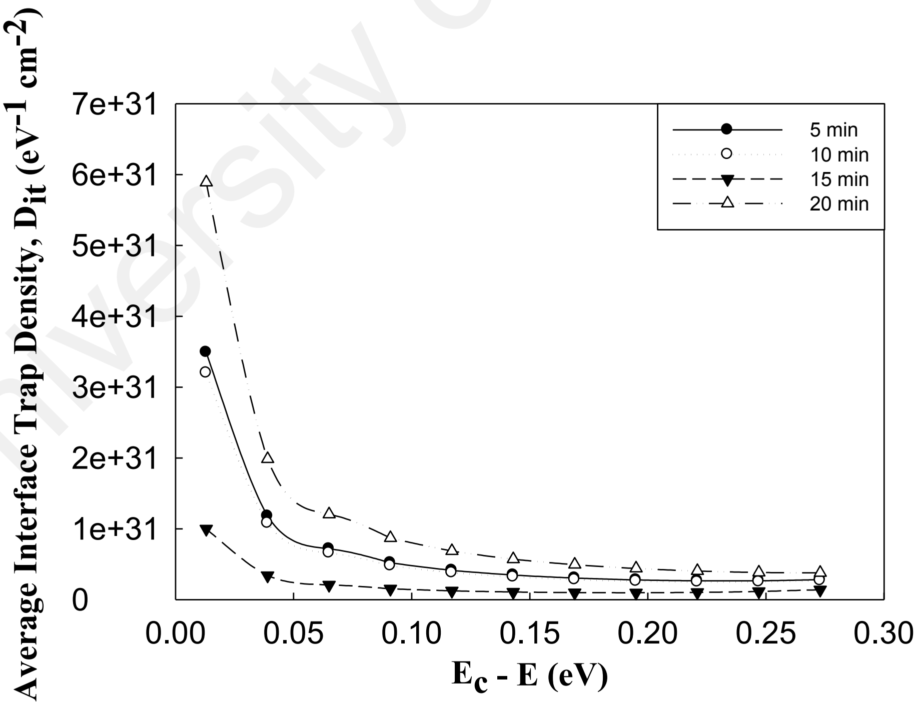

Figure 4.56: D_{it} of oxynitrided Nd samples at various durations (5 min, 10 min, 15 min, and 20 min)

4.5 Effects of Thermal Oxynitridation Temperature on Sputtered Nd Thin Film on Si Substrate

4.5.1 XRD Analysis

The XRD patterns of the oxynitrided Nd samples at various temperatures (500°C, 700°C, 900°C, and 1100°C) are shown in Figure 4.57. Two distinct peaks belonging to c-Si were detected at 33.0° and 69.0°, which belong to c-Si (1 1 2) and c-Si (4 0 0). These peaks were confirmed based on ICSD 98-001-6569. Three different peaks belonging to Nd_2O_3 were detected at 68.8°, 74.9°, and 75.8°. The peaks were assigned to c-Nd_2O_3 (1 1 8), c-Nd_2O_3 (2 5 7), and c-Nd_2O_3 (2 5 7), respectively, based on ICSD 98-009-6204.The interfacial layers of SiO_2 and Nd_2Si_2O were detected as various phase and planes. These findings are similar to the Zr and Sm thin films, which were oxynitrided, where SiO_2 and metal silicate compounds were detected (Goh et al., 2017a; Wong & Cheong, 2011a). Four different peaks belonging to m-SiO_2 were detected at 46.2°, 47.8°, 54.6°, and 89.4°belonging to (2 2 6), $(9\ 1\ \overline{3})$, $(5\ 1\ \overline{13})$, and (2 0 1), respectively. These peaks were matched based on ICSD 98-001-0176 and ICSD 98-002-425. Three peaks belonging to h-SiO_2 were detected at 69.4°, 75.3°, and 75.6°. The planes were identified as (0 3 0), (1 0 4),and (3 0 2) based on ICSD 98-001-6336, ICSD 98-001-6333, and ICSD 98-000-0174. Additionally, a single peak belonging to t-SiO_2(0 4 0) was detected at 76.4°and was confirmed based on ICSD 98-000-9327. Meanwhile, seven peaks belonging to o-Nd_2Si_2O were detected at 55.4°, 56.3°, 61.8°, 65.9°, 66.5°, 66.8°, and 67.4°. These peaks were assigned to (2 1 6), (3 1 3), (1 3 7), (0 6 2), (1 6 0), (3 2 5), and (2 0 8), respectively, and identified based on ICSD 98-001-6051. No peaks were detected for N or a N-incorporated compound, which can be attributed to the low content of N compared to Si, Nd, and O (Goh et al., 2017a).

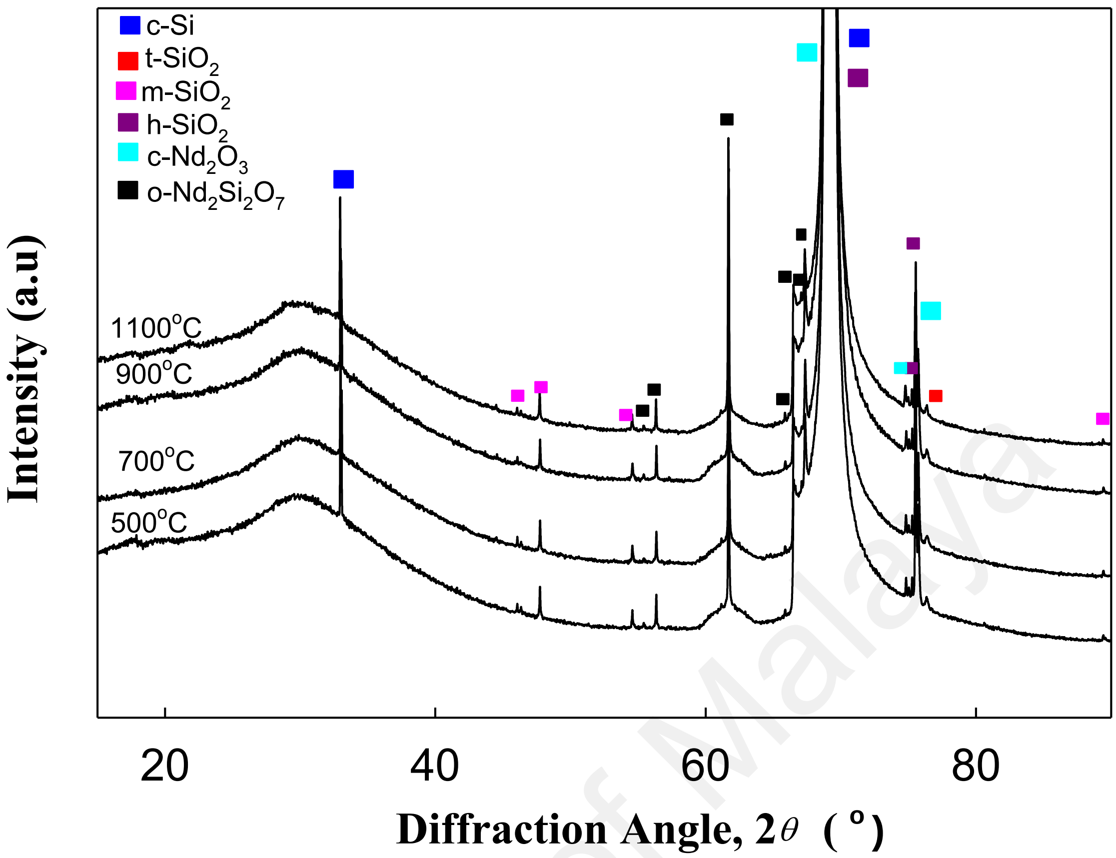

Figure 4.57: XRD patterns of oxynitrided Nd samples at various temperatures (500°C, 700°C, 900°C, and 1100°C)

Figure 4.58 shows the highest intensity for Nd_2O_3, SiO_2, and $Nd_2Si_2O_7$. All the samples recorded the highest intensity for h-SiO_2. The sample oxynitrided at 900°C shows the highest intensity for c-Nd_2O_3 and h-SiO_2. The sample also recorded the second-highest intensity for o-$Nd_2Si_2O_7$. On the other hand, the sample oxynitrided at 1100°C shows the lowest intensity for the entire compounds except t-SiO_2, which was recorded as the highest. As the interface plays a vital role in determining electrical properties, the percentage of interfacial layer to total thin film compound was calculated and shown in Figure 4.59. Overall, the highest percentage of interfacial compound is attributed to the sample oxynitrided at 700°C. In addition, the sample oxynitrided at 500°C and 900°C recorded the lowest and similar values, respectively.

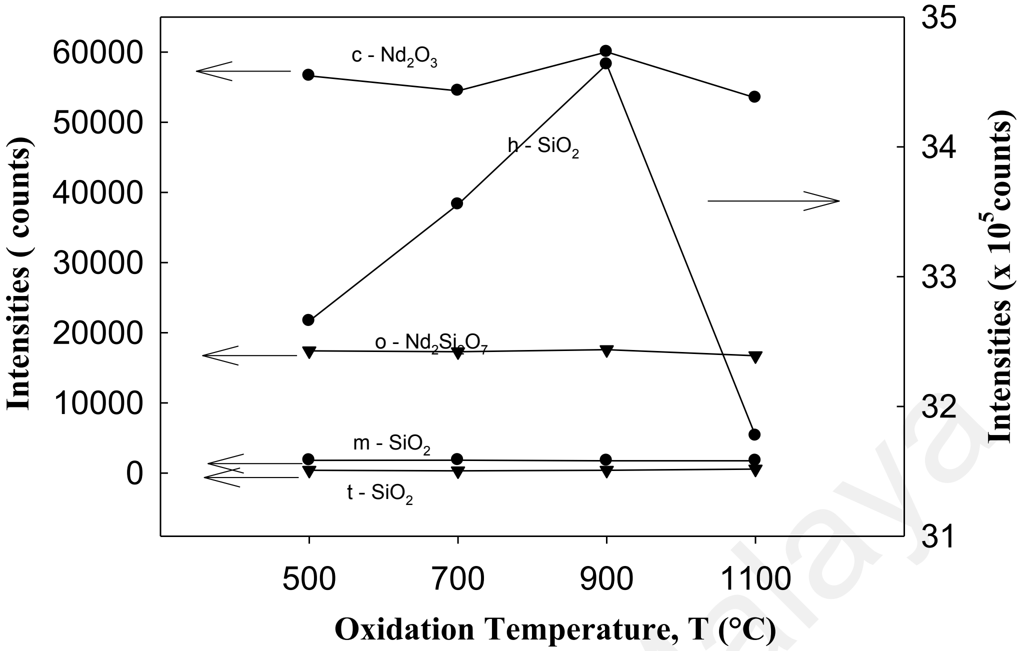

Figure 4.58: Highest intensities of c-Nd_2O_3, m-SiO_2, h-SiO_2, t-SiO_2, and o-$Nd_2Si_2O_7$ for oxynitrided Nd samples at various temperatures (500°C, 700°C, 900°C, and 1100°C)

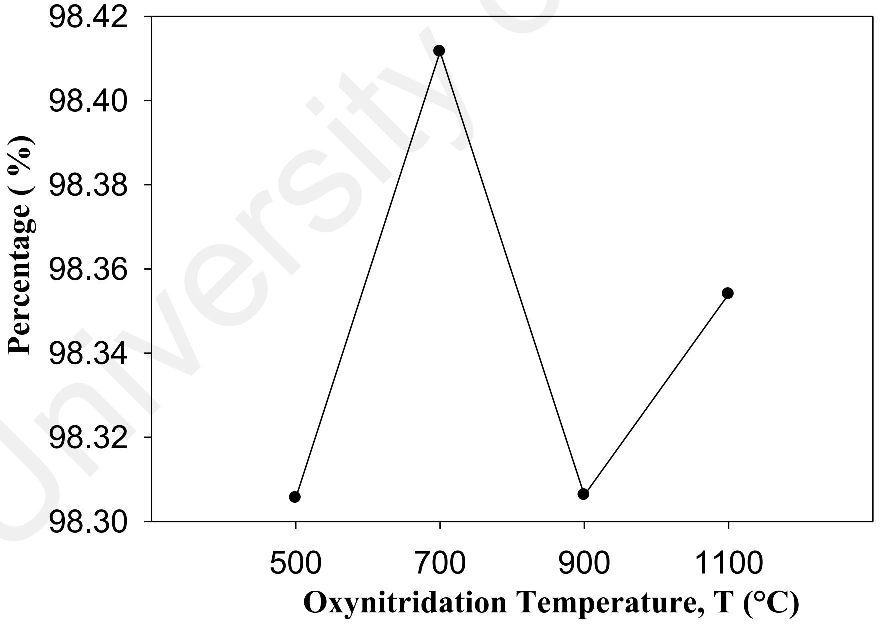

Figure 4.59: Percentage of interfacial compounds compared to total detected thin film compounds of oxynitrided Nd samples at various temperatures (500°C, 700°C, 900°C, and 1100°C)

4.5.1.1 Williamson-Hall Analysis

A W-H analysis was employed to determine microstrain and crystallite size, as shown in Figure 4.60. The calculated microstrain and crystallite size are shown in Figure 4.61. Both microstrain and crystallite size show a similar trend for all three compounds. SiO_2 shows similar microstrain values and crystallite sizes for all oxynitrided temperatures, which are -0.002 nm and 0.9003 nm, respectively. Meanwhile, for Nd_2O_3, microstrain and crystallite size increased as temperature increased from 500°C to 700°C and remained constant at -0.002 nm and 0.9003 nm, respectively, with a further increase in temperature. This shows that a higher temperature produces a more homogenous structure, which is similar to the finding on varied oxynitrided durations, as reported in Section 4.4.1.1. On the other hand, for $Nd_2Si_2O_7$, microstrain and crystallite size increased as temperature increased from 500°C to 700°C, and remained constant at 900°C, then decreased upon further temperature increase to 1100°C. This indicates that a better structure of silicate was achieved at moderate temperature, whereas a higher temperature tended to deteriorate the structure.

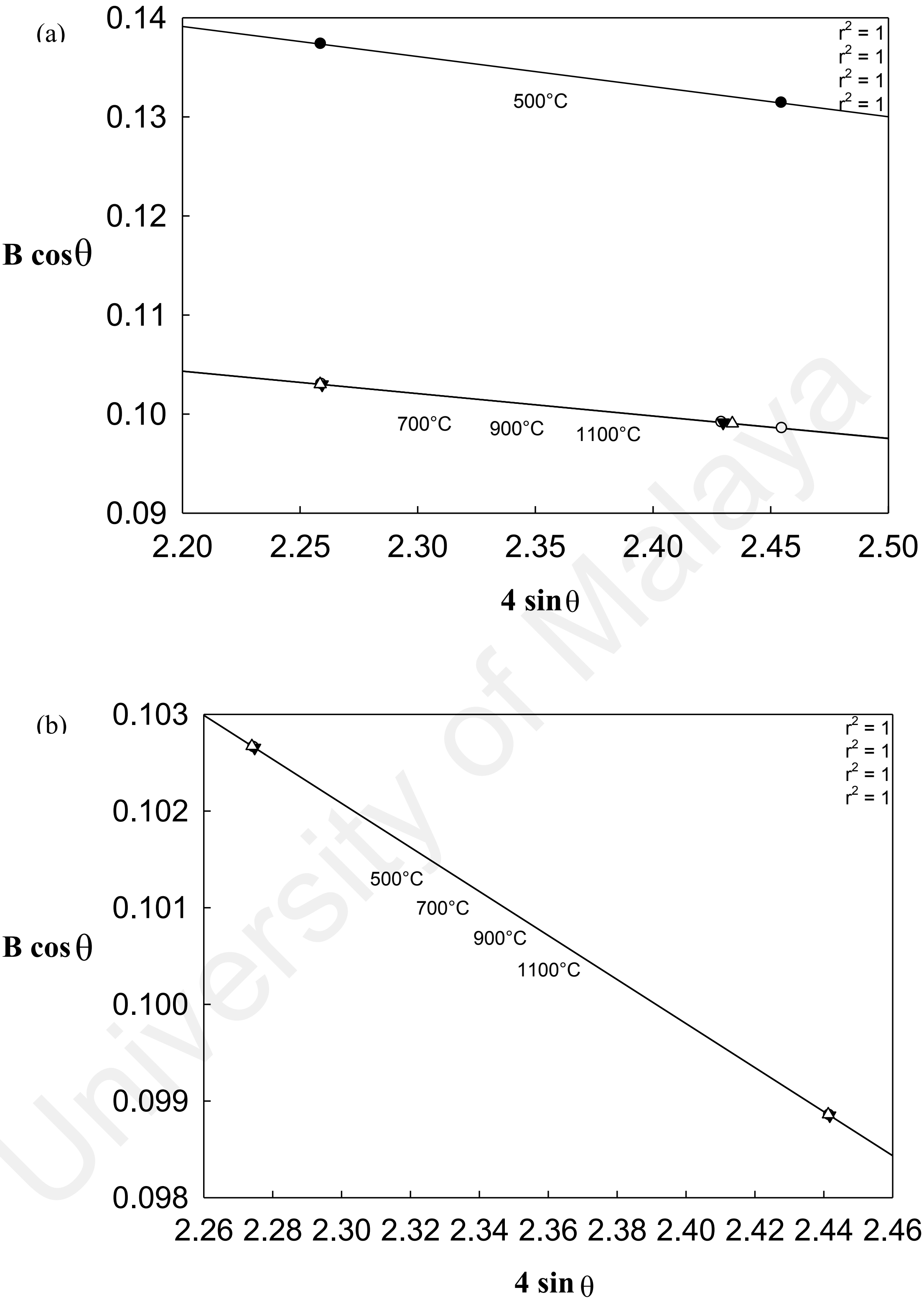

Figure 4.60: W-H plot of: (a) Nd_2O_3; (b) SiO_2; and (c) $Nd_2Si_2O_7$ of oxynitrided Nd samples at various temperatures (500°C, 700°C, 900°C, and 1100°C)

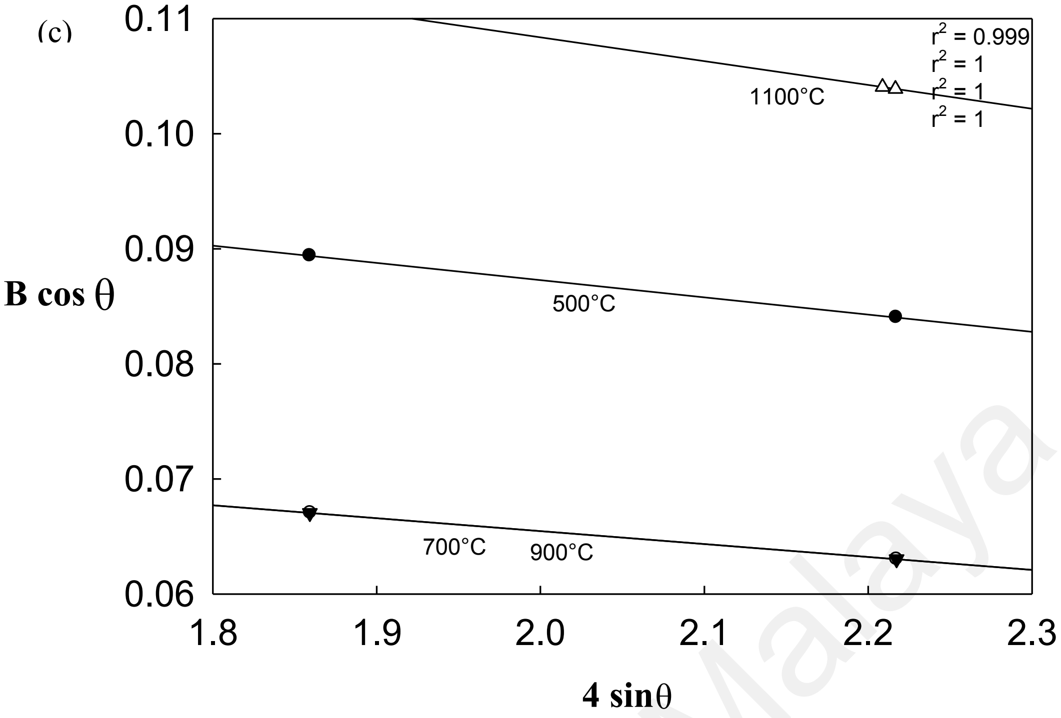

Figure 4.60:(*continued*) W-H plot of: (a) Nd_2O_3;(b) SiO_2; and (c) $Nd_2Si_2O_7$ of oxynitrided Nd samples at various temperatures (500°C, 700°C, 900°C, and 1100°C)

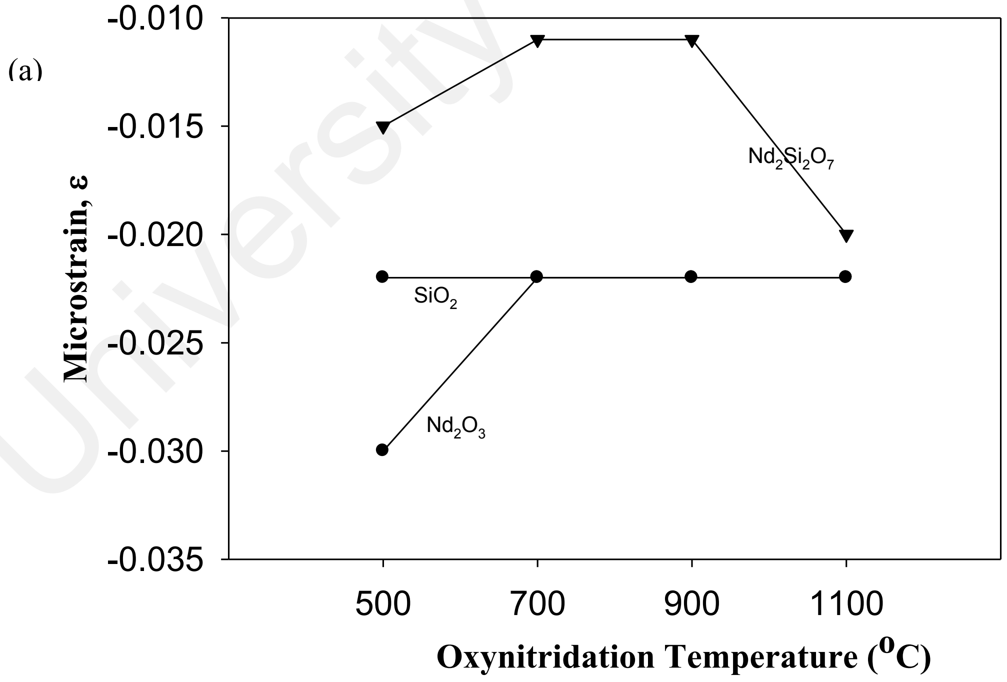

Figure 4.61: (a) Microstrain (b) crystallites size of Nd_2O_3, SiO_2, and $Nd_2Si_2O_7$ of oxynitrided Nd samples at various temperatures (500°C, 700°C, 900°C, and 1100°C)

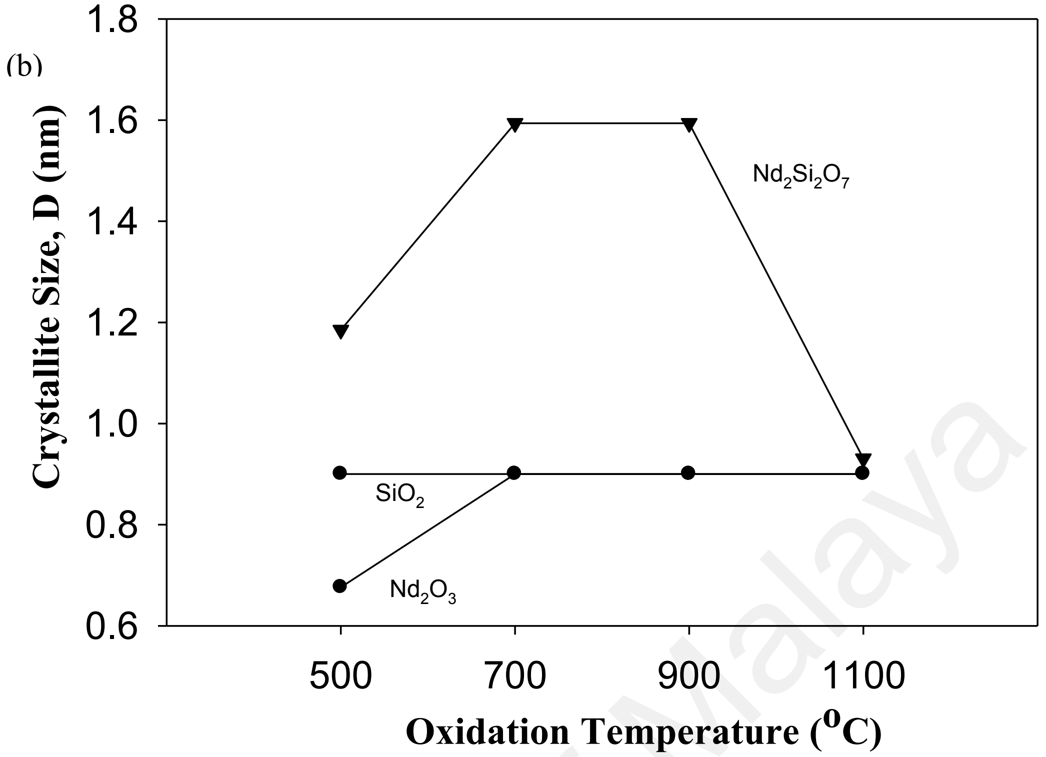

Figure 4.61: (*continued*) (a) Microstrain (b) crystallites size of Nd_2O_3, SiO_2, and $Nd_2Si_2O_7$ of oxynitrided Nd samples at various temperatures (500°C, 700°C, 900°C, and 1100°C)

4.5.2 FTIR Analysis

The FTIR results of the oxynitrided Nd samples at various temperatures (500°C, 700°C, 900°C, and 1100°C) are shown in Figure 4.62. A Si-Si vibration mode originating from Si was detected at 613 cm^{-1}(Smith, 1998). The peak broadens as the oxynitridation temperature increases from 500°C to 700°C. However, as the oxynitridation temperature increased to 900°C, it sharpens and then broadens again at 1100°C. Nd-O peaks were detected at 502 cm^{-1} and 567 cm^{-1} (Päiväsaari et al., 2005). Both peaks were less visible at a lower oxynitridation temperature of 500°C and 700°C. Both peaks sharpen as oxynitridation temperature increases. A few peaks belonging to the interfacial layer composed of Si-O and Nd-O-Si were detected. A Si-O-Si assymetric stretch mode was detected at 1243 cm^{-1}, 1204 cm^{-1}, and 1041 cm^{-1}

(Kurniawan, Cheong, et al., 2011b; Smith, 1998). Peak 1204 cm^{-1} was detected for the sample oxynitrided at 500°C and 700°C. At a higher temperature of 900°C and 1100°C, the peak broadens and shifts to 1243 cm^{-1}. On the other hand, peak 1041 cm^{-1} sharpens as oxynitridation temperature increases from 500°C to 700°C, and decreases at 900°C, later sharpening again at 1100°C. On the other hand, peaks belonging to Nd-O-Si were detected at 925 cm^{-1}. The peaks broaden as oxynitridation temperature increases from 500°C to 900°C and almost disappear at 900°C. The peaks become visible again at 1100°C. This indicates that the tendency for silicate compound formation decreases at a higher temperature. However, at too high a temperature, formation tends to increase. This is similar to the XRD findings, where it showed a lower interfacial layer percentage for oxynitridation temperatures of 500°C and 900°C. A peak attributed to the rocking, bending, and stretching of Si-O was detected at 805 cm^{-1}.This peak sharpens as oxynitridation temperature increases. A Si-O-Si bending peak was detected at 456 cm^{-1}. This peak shows a similar trend to that of peak Nd-O-Si, where it broadens as the oxynitridation temperature increases from 500°C to 900°C and disappears at 900°C. Later, it becomes visible again at 1100°C. Two more peaks attributed to the Si-O bend was detected at 431 cm^{-1} and 413 cm^{-1}. Peak 431 cm^{-1} is only visible at 700°C and 900°C. Meanwhile, peak 413 cm^{-1} broadens as the oxynitridation temperature increases from 500°C to 700°C and disappears at 900°C and 1100°C. This result indicates that the tendency for interface layer formation decreases as oxynitridation temperature increases, but a vice-versa effect was observed after 900°C, which is similar to the PDA treatment findings by Kao et.al. (2010) (C.H. Kao et al., 2010).

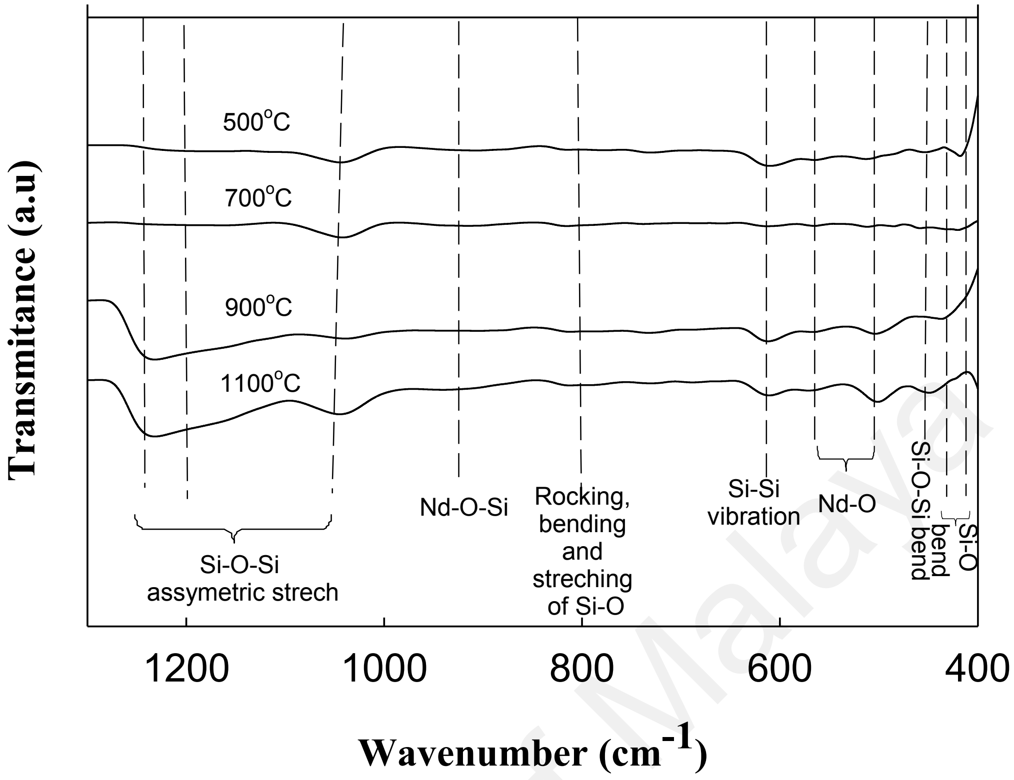

Figure 4.62: Transmittance spectra of oxynitrided Nd samples at various temperatures (500°C, 700°C, 900°C, and 1100°C)

4.5.3 Raman Analysis

Figure 4.63 shows the Raman analysis result of the oxynitrided Nd samples at various temperatures (500°C, 700°C, 900°C, and 1100°C). A peak originating from Si was detected at 525 cm^{-1}. A few peaks belonging to Nd_2O_3 were detected at 112 cm^{-1}, 225 cm^{-1}, 303 cm^{-1}, 434 cm^{-1}, 453 cm^{-1}, 618 cm^{-1}, and 668 cm^{-1} (Jiang et al., 2013; Kurniawan, Cheong, et al., 2011b; Nagai et al., 2013; Ubaldini & Carnasciali, 2008; Walrafen & Stone, 1975). Most of these peaks are not clearly visible for the sample oxynitrided at 700°C. This suggests that the sample oxynitrided at 700°C produces a lesser amount of oxides compared to the other compounds,SiO_2 and silicate. The oxide intensity increases at higher temperatures 900°C and 1100°C. Additionally, an interface layer of SiO_2 was detected at 925 cm^{-1} (Nyquist & Kagel, 2012); Meanwhile, $Nd_xSi_yO_z$

was detected at 17 cm^{-1}. The intensity of SiO_2 decreased as the oxynitridation temperature increased to 700°C and then increased again. The Raman findings are in agreement with the FTIR findings.

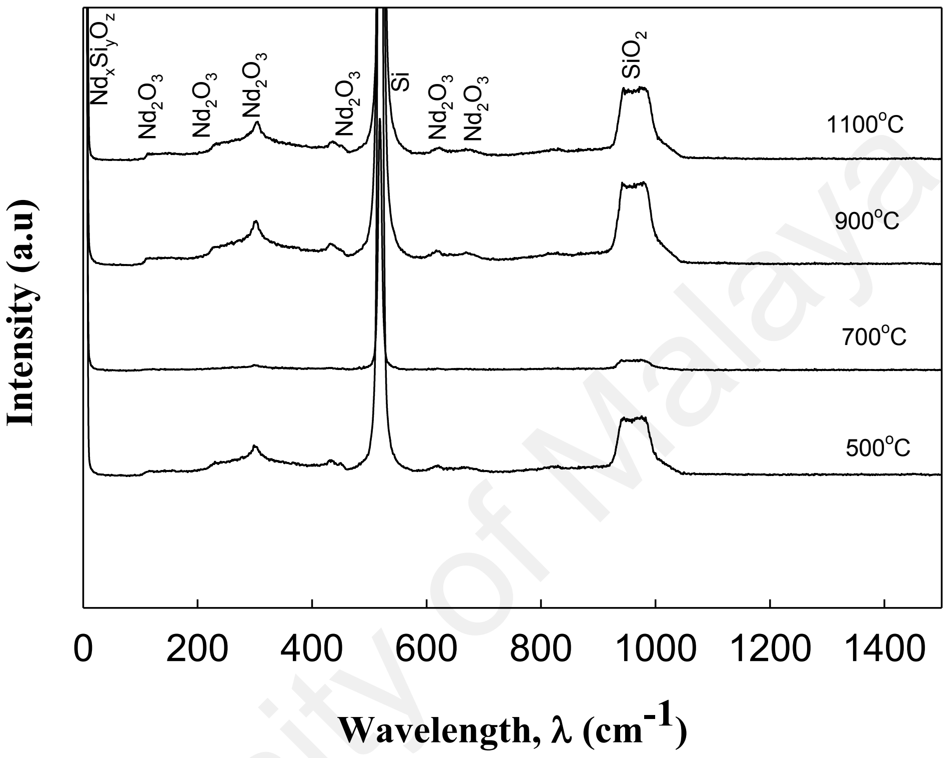

Figure 4.63: Raman spectra of oxynitrided Nd samples at various temperatures (500°C, 700°C, 900°C, and 1100°C)

4.5.4 XPS Analysis

The atomic percentage of Nd, Si, O, and N as a function of time for the oxynitrided Nd samples at various temperatures (500°C, 700°C, 900°C and 1100°C) is shown in Figure 4.64. The analysis enables the determination of surface composition and bonding stability. All samples show a similar trend, as discussed in Section 4.4.4. As the etching time increases, the atomic percentage of Si also increases. On the other hand, the atomic percentage of O decreases. However, the atomic percentage of Nd and N increases until 900s, after which it decreases. Nd, O, and N will continue to decrease until they totally disappear, except for Si. This indicates the appearance of the Si substrate as etching continues (Goh et al., 2017b; Wong & Cheong, 2012b). Additionally, with an increasing trend in Nd and N, Si shows a decreasing trend and vice versa. This shows that the higher the amount of Nd and N, the lower the Si diffusion rate. The sample oxidized at 500°C shows a slightly different pattern than that of Nd and Si, where the atomic percentage of Nd is higher than Si at 900 s. This indicates that at a lower temperature, the ratio of Si to Nd also lowers. The finding on N indicates the presence of an interfacial layer consisting of $Nd_aSi_bO_cN_d$.

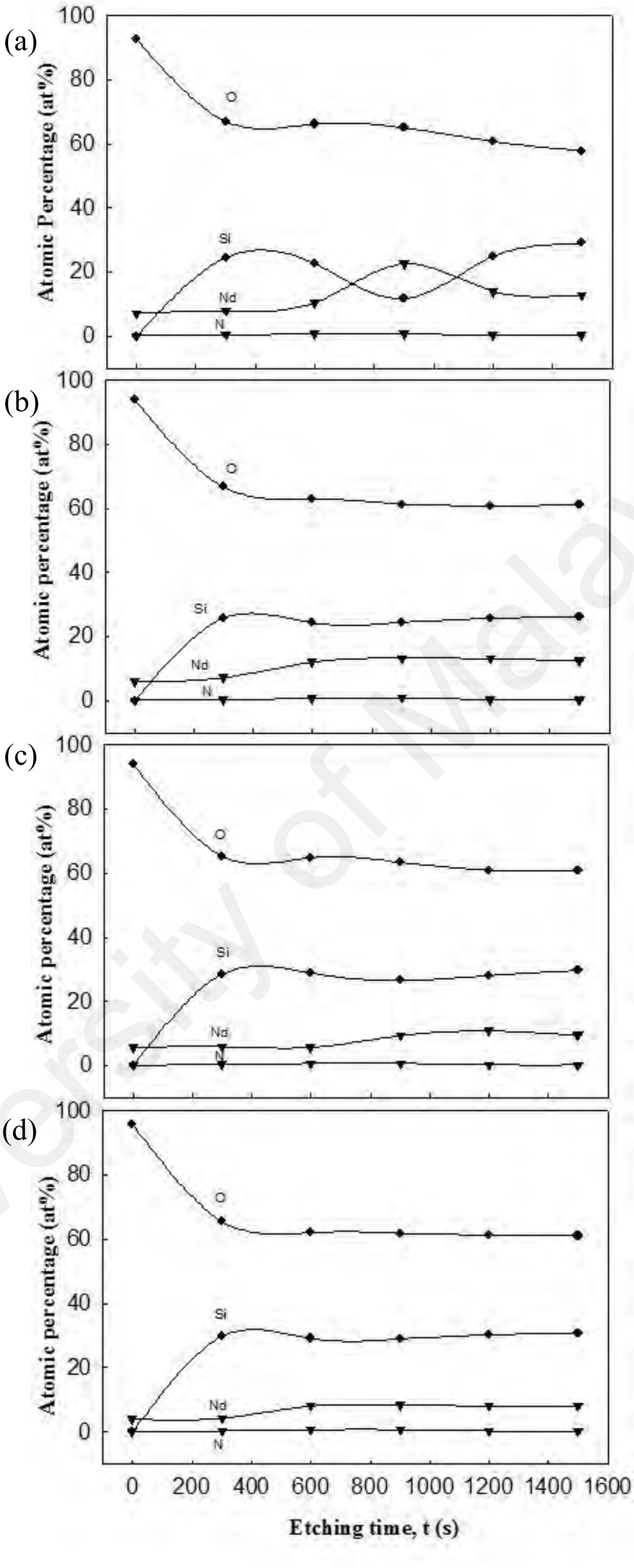

Figure 4.64: The atomic percentage of Nd, Si, O, and N as a function of time for oxynitrided Nd samples at various temperatures:(a) 500°C; (b) 700°C; (c) 900°C; (d) 1100°C

The summarized narrow scans of the core level of Nd, O, Si, and N as a function of etching time for the oxynitrided Nd samples at various temperatures (500°C, 700°C, 900°C, and 1100°C)are shown in Figure 4.65 - Figure 4.68. The measured peak, represented by the dotted line, was deconvoluted with the aid of a non-linear Gaussian-Lorentzian function via the CasaXPS software (version 2.3.16).

Figure 4.65 shows the Nd 3*d* core level XPS spectra for oxynitrided Nd samples at various temperatures(500°C, 700°C, 900°C, and 1100°C). The binding energy attributed to Nd-O was detected in the range of 983.0 eV-979.0 eV (C.H. Kao et al., 2010). These binding energies shifted to a higher binding energy as etching time increased for the sample oxynitrided at 900°C. However, this shifted to a lower binding energy at an oxynitridation temperature of 1100°C. At the same time, the sample oxynitrided at 900°C showed the highest intensity at an etching time of 300 s. In addition, for the samples oxynitrided 500°C, 700°C, and 900°C, the intensity of these peaks decreased at an ectching time of 600 s, increased again at 900 s, and then decreased again at 1200s. This indicates the non-uniform formation of Nd-O in these samples. For the sample oxynitrided at 1100°C, the intensity remains constant until an etching time of 900 s, but increased at 1200 s. This could be attributed to better bonding between Nd-O and the Si substrate.

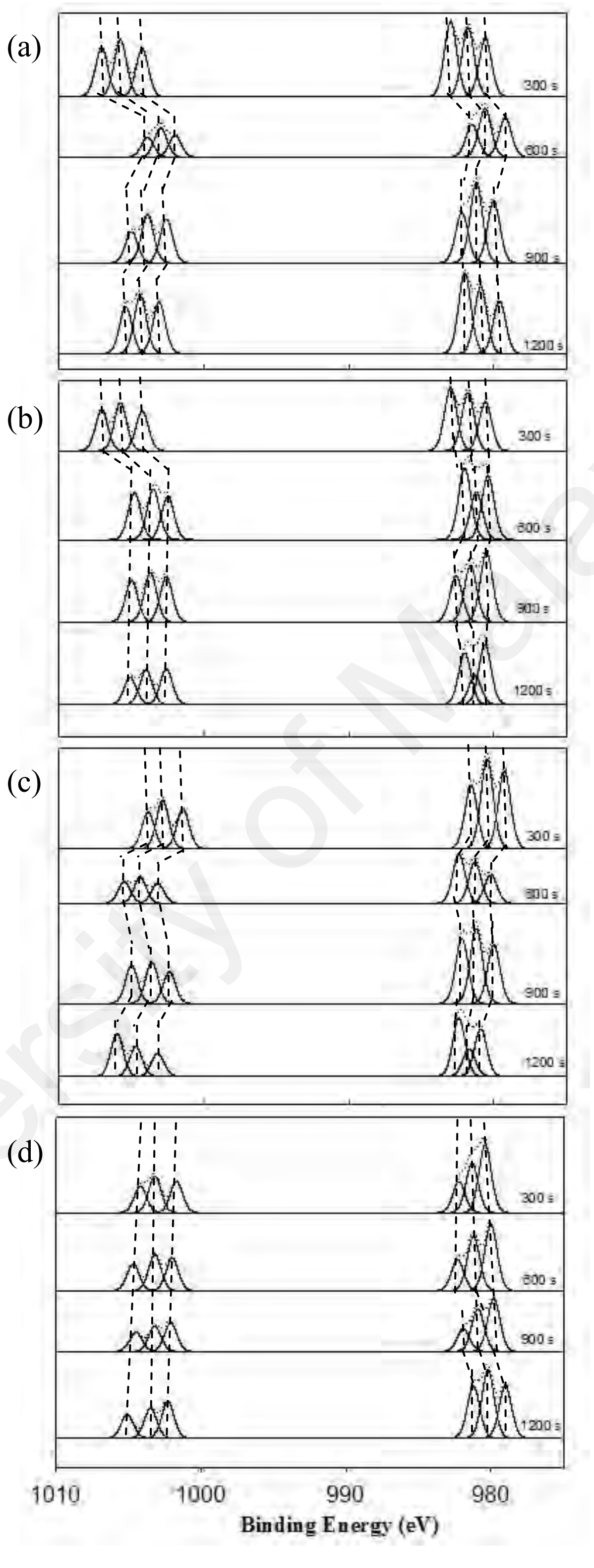

Figure 4.65: Nd 3*d* core level XPS spectra as a function of time for oxynitrided Nd samples at various temperatures: (a) 500°C; (b) 700°C; (c) 900°C; (d) 1100°C

Higher binding energies were detected in the range of 1007.0eV-1001.5 eV. Based on the atomic percentage analysis, it can be concluded that these originate from Nd-Si-O and Nd-Si-O-N. This also shows the presence of $Nd_aSi_bO_cN_d$ as an interface layer. For the sample oxynitrided 500°C and 700°C, the higher binding energy shifted to a lower binding energy as etching time increases. On the other hand, the binding energy remains constant for the sample oxynitrided at 1100°C. This sample also shows the lowest intensity for the interface layer. The sample oxynitrided at 900°C has the second lowest intensity peaks. In addition, the sample oxynitrided at 700°C and 900°C shows decreased intensity as etching approaches the substrate. However, a vice-versa pattern was observed for the sample oxynitrided at 500°C.

O 1*s* core level XPS spectra for oxynitrided Nd samples at various temperatures (500°C, 700°C, 900°C, and 1100°C) are shown in Figure 4.66. The binding energy attributedto Nd-O was detected at 530.8 eV, 530.6 eV, and 529.5 eV (Frohlich et al., 2006; Goh et al., 2017a; J. Kim et al., 2017; Pan et al., 2006b). For the sample oxynitrided at 500°C and 700°C, the binding energies shifted to a lower binding energy. On the other hand, the binding energy shifted to a higher binding energy for the sample oxynitrided at 900°C. This indicates a better formation of Nd-O at this temperature. The intensity of these peaks remains almost constant for the sample oxynitrided 1100°C. The $Nd_aSi_bO_cN_d$ binding energy was detected at 531.8 eV and 532.2 eV (Chew et al., 2016; Pan et al., 2006b; Pan et al., 2007; Pan & Yu, 2009). For all samples, the peaks had shifted to a lower binding energy as the etching time increased. Higher intensities of these binding energies were detected for the sample oxynitrided at 1100°C, which is attributed to the thicker interface layer formation in this sample. This peak is not detected at an etching time of 600 s for the sample oxynitrided at 700°C and 900°C. This leads to a lower intensity of $Nd_aSi_bO_cN_d$ for these samples. In addition, the intensity of these peaks decreases as etching time increases for the sample oxynitrided at 500°C. The binding energy of Si - O was detected at 533 eV (Pan et al., 2006b; Pan et al., 2007; Pan & Yu, 2009). This binding energy is only detected at an etching time of 300 s for the sample oxynitrided at 500°C. On the other hand, a vice-versa pattern was observed for the sample oxynitrided at 900°C and 1100°C, where the binding energy was only detected after an etching time of 300 s. This shows that Si diffused out from the substrate to form a thicker interface layer.

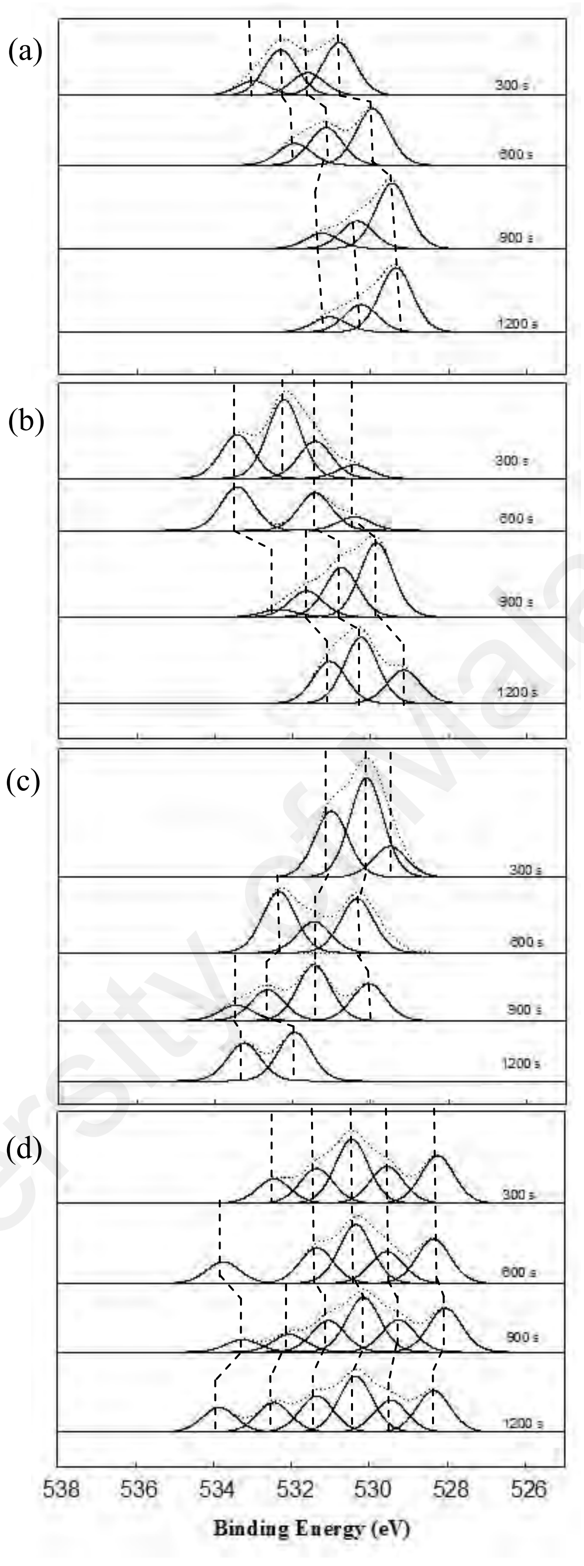

Figure 4.66: O 1*s* core level XPS spectra as a function of time for oxynitrided Nd samples at various temperatures: (a) 500°C; (b) 700°C; (c) 900°C; and (d) 1100°C

Figure 4.67 shows the Si 2*p* core level XPS spectra for oxynitrided Nd samples at various temperatures (500°C, 700°C, 900°C, and 1100°C). The binding energy originating from the Si substrate was detected at 99.6 eV (Pan et al., 2006b; Pan et al., 2007; Wong & Cheong, 2012c). For the sample oxynitrided at 500°C and 1100°C, the binding energies were detected throughout the etching time and shifted to a lower binding energy for the sample oxynitrided at 500°C. The binding energy was detected only at an etching time of 300 s for the sample oxynitrided at 900°C and was detected at a later etching time for the sample oxynitrided at 700°C.

The binding energy related to Si-O, and Si-N was detected at 103.3 eV and 101.9 eV(Goh et al., 2017a; Pan et al., 2006b; Pan et al., 2007). The binding energy related to Si-O was detected in the range of 103.9 eV and 102.1 eV(Pan et al., 2006b; Pan et al., 2007; Tong et al., 2006). For the sample oxynitrided at 900°C,vthe binding energy was detected after an etching time of 300 s compared to the rest of the sample, where the binding energy was detected throughout the sample. This is similar to the finding on Si-O binding energy through the O 1*s*narrow scan. This indicates that Si diffused out at a slower rate at this temperature compared to the rest of the samples. For the sample oxynitided at 500°C, the binding energy shifted to a lower binding energy and the intensity decreased as etching time increased. Meanwhile, the binding energy for Si-N was detected throughout the sample except for the sample oxynitrided at 900°C, where it was not detected at an etching time of 1200 s. The intensity also decreased as etching time increased. At the same time, the binding energy shifted to a lower binding energy for the sample oxynitrided at 500°C. On the other hand, the binding energy shifted to a lower binding energy for the sample oxynitrided at 700°C. At the highest temperature, the intensity remained almost constant, indicating better dissociation of N_2O at higher temperatures.

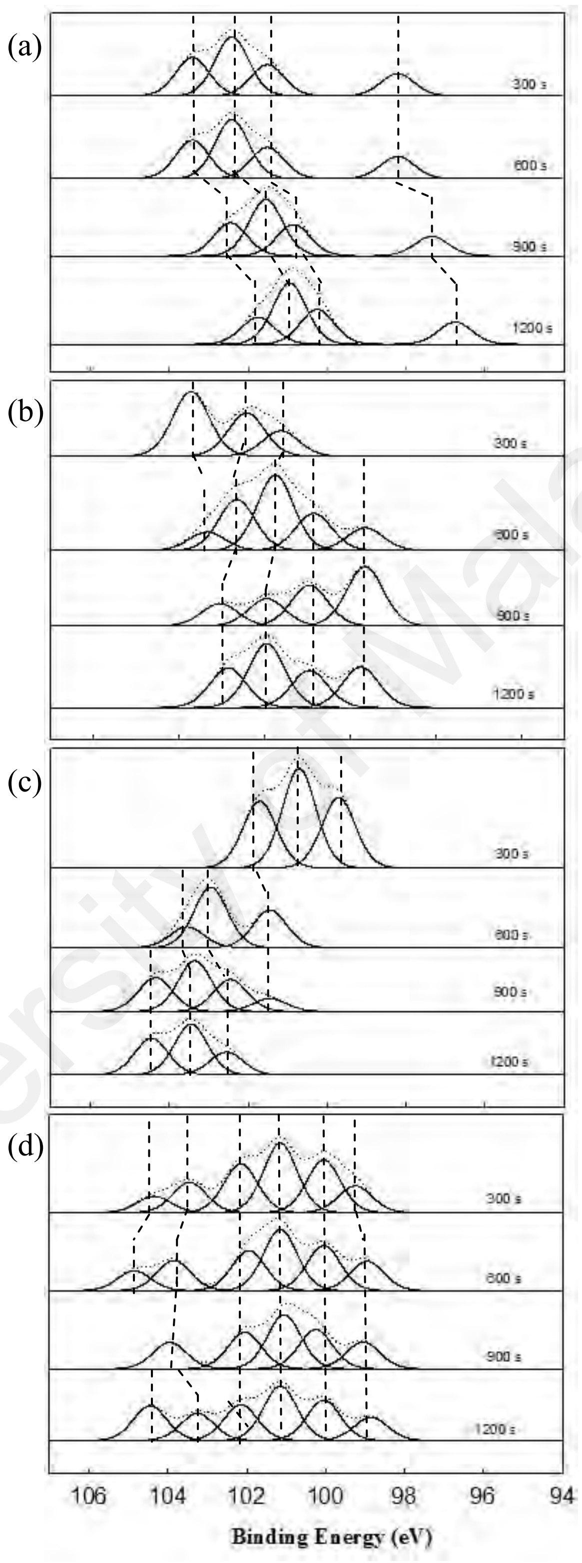

Figure 4.67: Si 2*p* core level XPS spectra as a function of time for oxynitrided Nd samples at various temperatures: (a) 500°C; (b) 700°C; (c) 900°C; and (d) 1100°C

The unindentified peaks at 104.3 eV and in the range of 100.9 eV and 100.15 eV is attributed to Nd-Si-O. These were detected throughout the sample oxynitrided at 1100°C. However, this was detected at a later etching time for the rest of the samples. This indicates that Si diffusion rate increases at a higher temperature, leading to a higher formation of $Nd_aSi_bO_cN_d$.

N 1*s* core level XPS spectra for oxynitrided Nd samples at various temperatures (500°C, 700°C, 900°C, and 1100°C) are shown in Figure 4.68. Binding energies of ~402.5 eV, ~400 eV and ~399.5 eV were assigned to N-O, Sm-N, and Si-N, respectively (Gholizadeh et al., 2017; Goh et al., 2017a; J. C. Lee et al., 2003; Vaz et al., 2013; Wong & Cheong, 2011b, 2012c). N-O binding energies were only detected for the sample oxynitrided at 1100°C. The binding energy of Sm-N and Si-N was detected throughout the sample oxynitrided at 900°C and then shifted to a lower binding energy after which it remained constant (including the intensity) after an etching time of 300 s. Thus, it can be inferred that uniform and better bonding of $Nd_aSi_bO_cN_d$ was achieved at this temperature. For the sample oxynitrided at 1100°C, the binding energy of both peaks and intensity remained constant until an etching time of 900 s. However, the binding energy of Si-N was not detected at an etching time of 1200 s.

Based on the narrow scan, all samples produced $Nd_xO_yN_z$ and an interface of $Nd_aSi_bO_cN_d$. The sample oxynitrided at 900°C produced better $Nd_aSi_bO_cN_d$ than the rest of the oxynitrided temperatures. In addition, no silicide formation was detected in all samples.

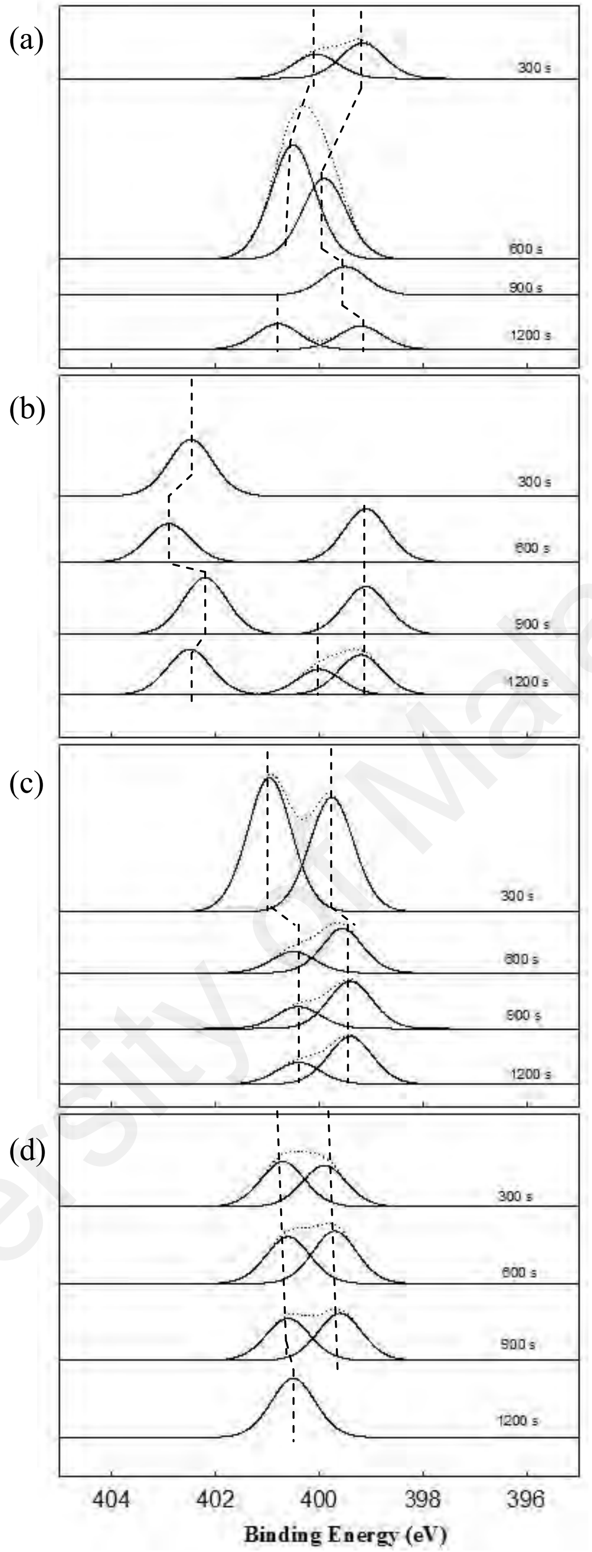

Figure 4.68: N 1*s* core level XPS spectra as a function of time for oxynitrided Nd samples at various temperatures: (a) 500°C; (b) 700°C; (c) 900°C; and (d) 1100°C

4.5.5 HRTEM Analysis

Structural analysis reveals that the sample oxynitrided at 900°C possessed the best interface layer. Therefore, this sample was selected to undergo HRTEM and EDX analyses for comparison with the sample oxynitrided at 700°C, as per Section 4.4.5. Figure 4.69 shows the HRTEM analysis of oxynitrided Nd samples at 700°C and 900°C, and followed by a comparison of the two outlined in Table 4.5.

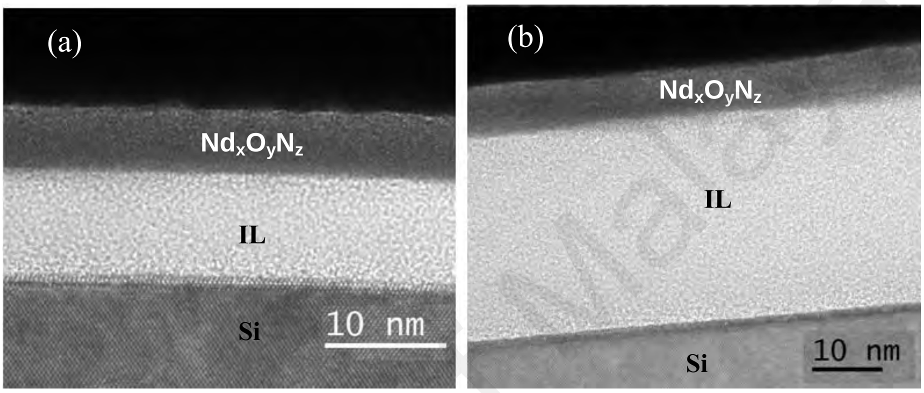

Figure 4.69: HRTEM images of the oxynitrided Nd samples at: (a) 700°C; and (b) 900°C

Table 4.5: Comparison betweenthe sample oxynitrided Nd at 700°C and the sample oxynitrided Nd at 900°C

Oxynitridation temperature (°C)	**Thickness of $Nd_xO_yN_z$ (nm)**	**Thickness of $Nd_aSi_bO_cN_d$ (nm)**
700	4.87	8.83
900	6.17	30.82

The thickness of $Nd_xO_yN_z$ for the sample oxynitrided 900°C is higher than that of 700°C. In addition, the thickness of $Nd_aSi_bO_cN_d$ for the sample oxynitrided at 900°C is almost 4 times higher than the sample oxynitrided at 700°C. This could be attributed to the different dissociation rate of N_2O as a result of varied temperature. The dissociation of N_2O is accelerated at a higher temperature due to a higher activation energy (Gholizadeh et al., 2017; Goh et al., 2017a). Thus, at 900°C, there is a higher amount of oxygen and nitrogen present. This leads to a thicker oxide and interface layer. A similar trend is also observed for samarium oxynitride ($Sm_xO_yN_z$), where the thickness of the oxide and interface layer increases with increased temperature (Goh et al., 2017a).

4.5.6 Leakage Current Density versus Electrical Breakdown Field Characteristics

Figure 4.70 shows the J-E characteristics of the oxynitrided Nd samples at various temperatures (500°C, 700°C, 900°C, and 1100°C). All samples possess double breakdown. The sample oxynitrided at 700°C, 900°C, and 1100°C possessed SB in the range of ~10^{-6} A/cm^2. Meanwhile, the sample oxynitrided at 500°C possessed SB at ~10^{-7} A/cm^2 and HB at ~10^{-7} A/cm^2. However, the breakdown voltage for this sample is only 1.181MV/cm and 2.281MV/cm. For the rest of the samples, the breakdown voltages for SB are more than 4.0MV/cm. The highest was for the sample oxynitrided at 900°C, which is 5.721 MV/cm. Meanwhile, the HB for this sample is ~10^{-4} A/cm^2 at a breakdown voltage of 8.525 MV/cm. Thus, it is concluded that the sample oxynitrided at 900°C has the best J-E characteristics. However, to confirm the findings, a TZBD reliability test was conducted; the results are shown in Figure 4.71. For the sample oxynitrided at 900°C, most of the breakdown falls in the range of 5.2-6.8 MV/cm. The same is true for the sample oxynitrided at 1100°C but its leakage value at this breakdown voltage is ~10^{-5} A/cm^2.

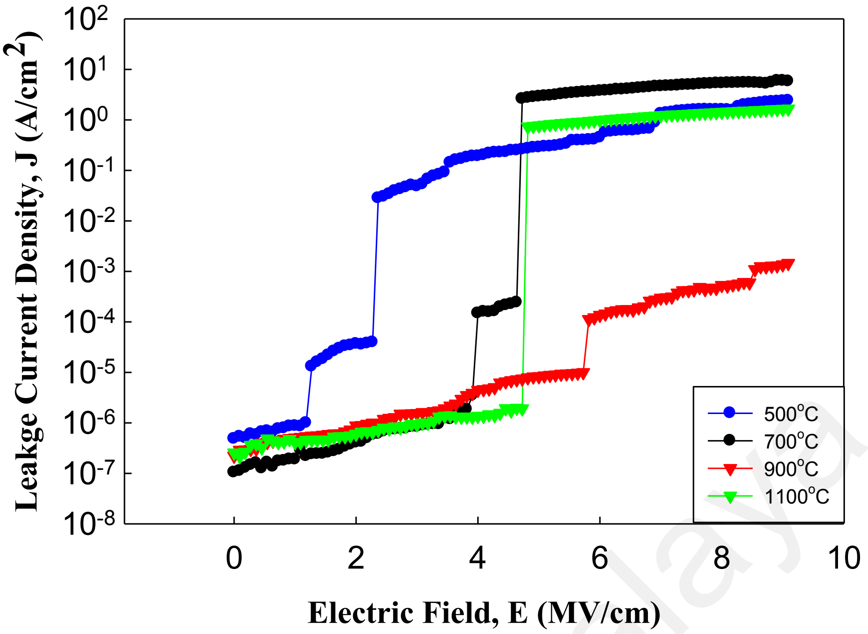

Figure 4.70: J-E characteristic of the oxynitrided Nd samples at various temperatures (500°C, 700°C, 900°C, and 1100°C)

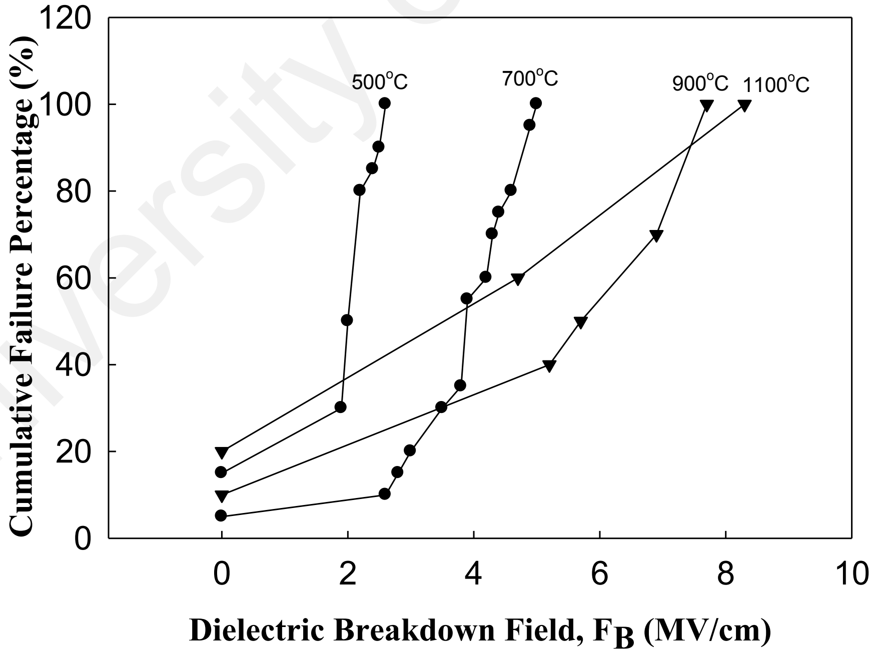

Figure 4.71: Cumulative failure percentage of the EBD ofoxynitrided Nd samples at various temperatures (500°C, 700°C, 900°C, and 1100°C)

4.5.6.1 Fowler-Nordheim Tunneling Analysis

Figure 4.72 shows the FN regression plot of In (J/E^2) versus 1/E of the oxynitrided Nd samples at various temperatures (500°C, 700°C, 900°C, and 1100°C). The $Ø_B$ of these samples is shown in Figure 4.73. As the sample oxynitrided at900°C possessed the best J-E characteristics, it also shows the highest $Ø_B$, which is 2.94 eV. This value is much higher than ZrON, where the highest value is ~2.0 eV (Wong & Cheong, 2012c).

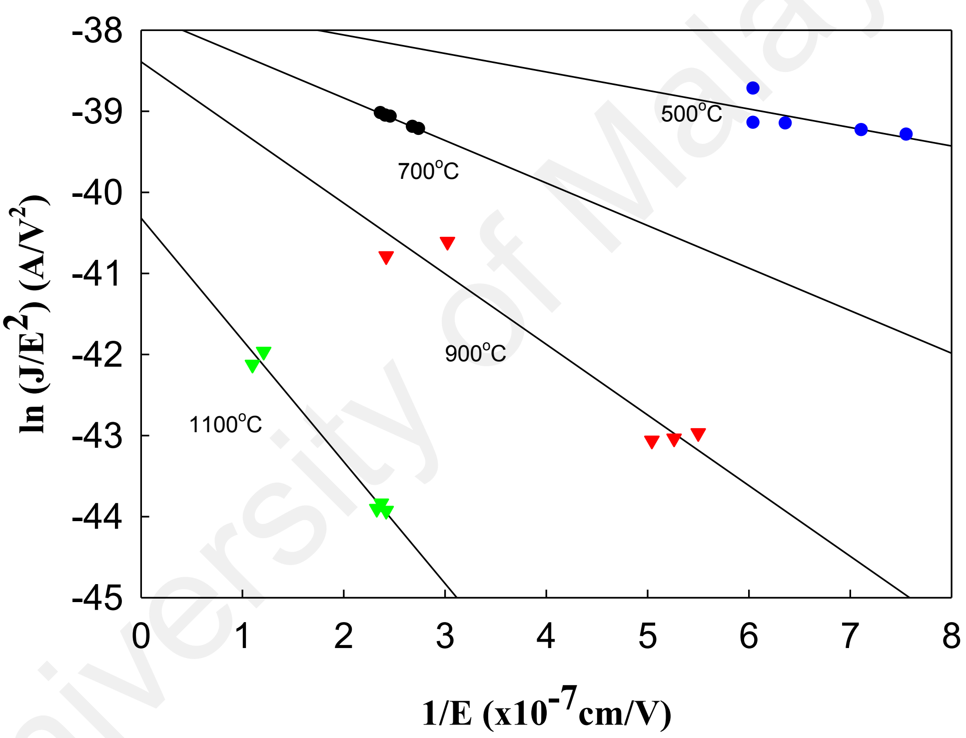

Figure 4.72: F-N tunneling linear regression plot [In (J/E^2) versus 1/E] of oxynitrided Nd samples at various temperatures (500°C, 700°C, 900°C, and 1100°C)

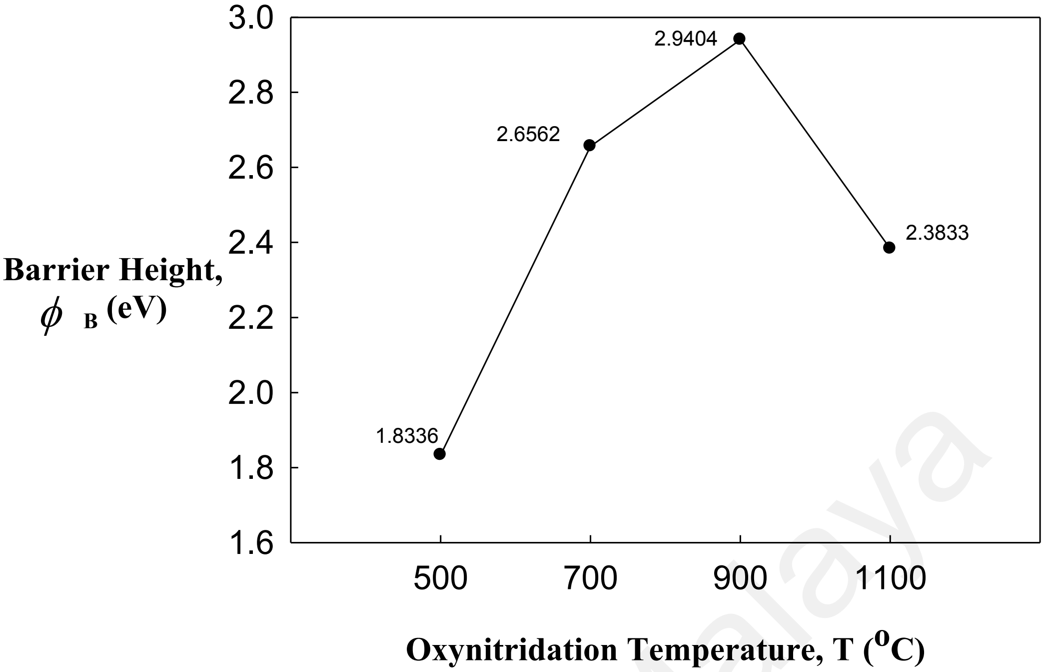

Figure 4.73: Barrier height values as a function of oxynitrided Nd samples at various temperatures (500°C, 700°C, 900°C, and 1100°C)

4.5.7 Capacitance-Voltage Characteristics

Figure 4.74 shows the normalized capacitance value of oxynitrided Nd samples at various temperatures (500°C, 700°C, 900°C, and 1100°C). The highest capacitance value of these samples is shown in Figure 4.75. Minimal hysteresis was observed for the sample oxynitrided at 1100°C and followed by the sample oxynitrided at900°C. All the samples possess a negative bias depletion region and negatively shifted ΔV_{FB}. Thus, these samples possessed positive effective oxide charges (Yang et al., 2003).On the other hand, the highest capacitance accumulation decreases as oxynitridation temperature increases up to 900°C and later increases again at 1100°C. Thus, the sample oxynitrided at 900°C has the lowest capacitance value. This observation is vice versa to the J-E characteristics results.

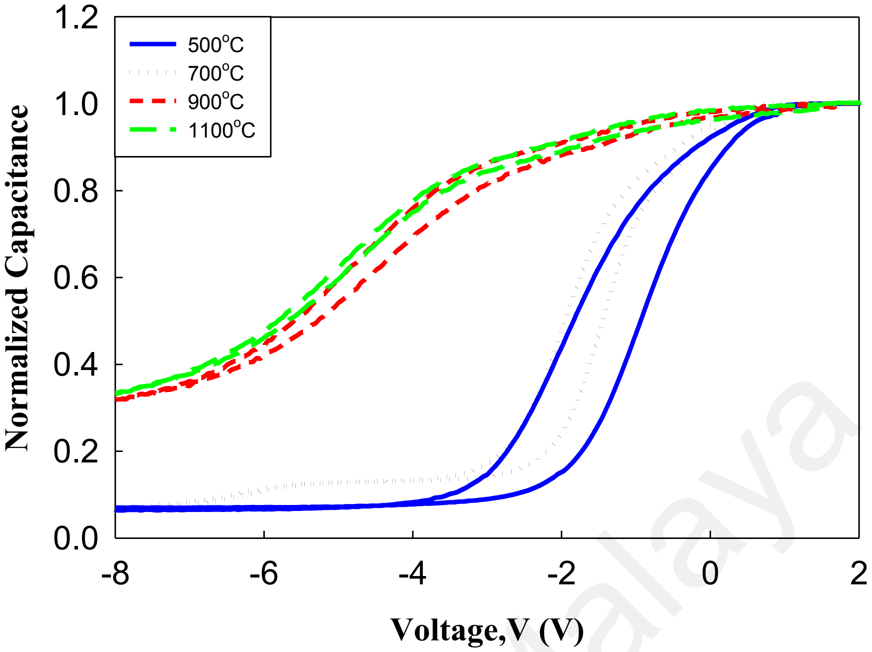

Figure 4.74: Normalized C-V curve of oxynitrided Nd samples at various temperatures (500°C, 700°C, 900°C, and 1100°C)

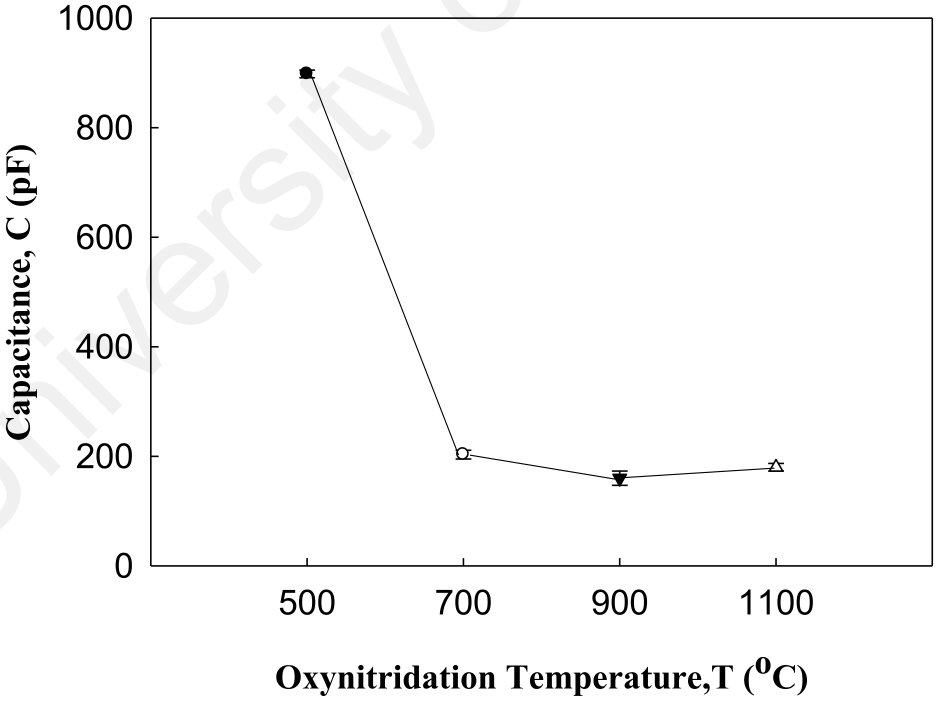

Figure 4.75: Capacitance accumulation value of oxynitrided Nd samples at various temperatures (500°C, 700°C, 900°C, and 1100°C)

Based on the measured thickness, the *k*-values of the sample oxynitrided at 700°C and 900°C were calculated, with the values being 3.49 and 7.43, respectively. The structural analysis revealed that the sample oxynitrided at 900°C has a more uniform $Nd_aSi_bO_cN_d$. The uniform structure is due to smaller size of nitrogen compared to oxygen. This enables nitrogen to fill in the voids that present in the thin film. This could be attributed to the higher *k*- value. Section 4.2 and Section 4.3 showed that the silicate layer contributes to better electrical properties. The C-V result was further analyzed to confirm the J-E findings, as the sample oxynitrided at 900°C possessed the lowest capacitance value.

4.5.7.1 Effective Oxide Charge, Slow Trap Density and Interface Trap Defect Density

Q_{eff} and STD of the oxynitrided Nd samples at various temperatures (500°C, 700°C, 900°C, and 1100°C) are shown in Figure 4.76. Meanwhile, Figure 4.77 shows the D_{it} values of these samples. The sample oxynitrided at 900°C possesses the lowest Q_{eff} and the second lowest STD. In addition, this sample also exhibited the lowest D_{it}. Based on this analysis, therefore, the sample oxynitrided at 900°C has the best C-V characteristics.

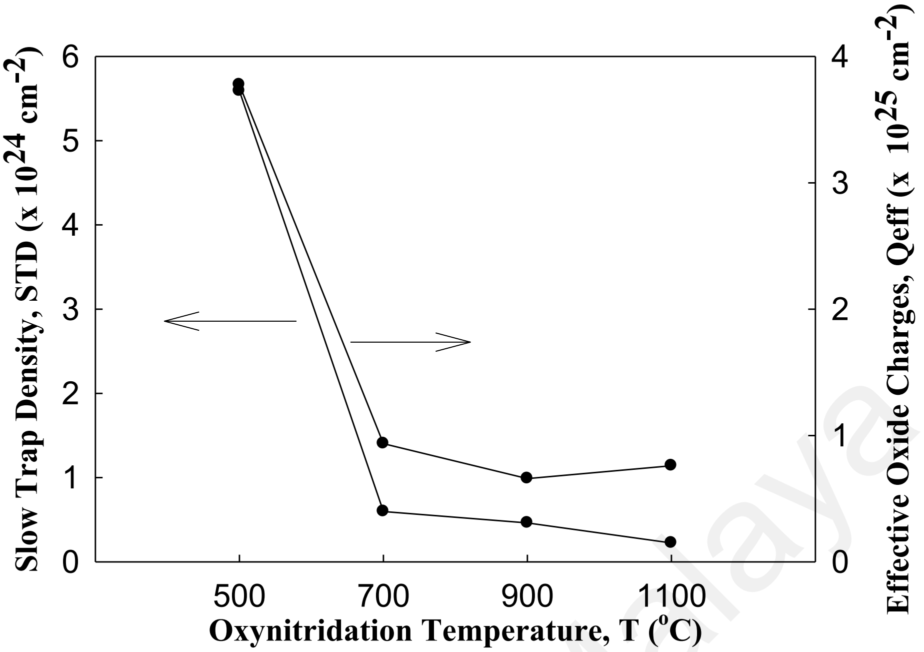

Figure 4.76: STD and Q_{eff} charges of oxynitrided Nd samples at various temperatures (500°C, 700°C, 900°C, and 1100°C)

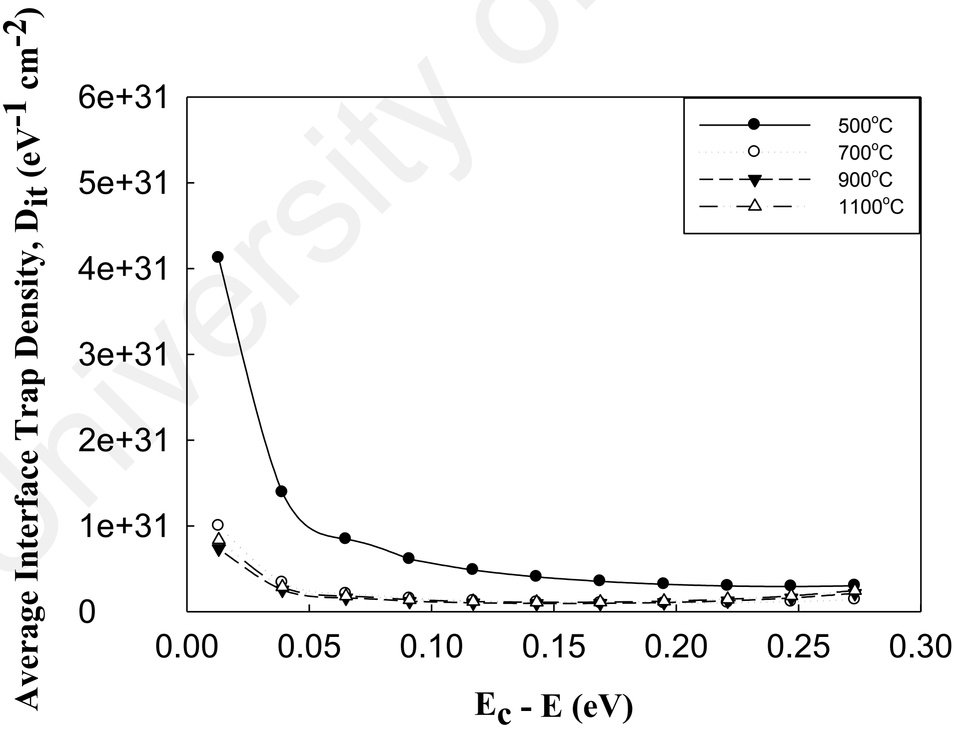

Figure 4.77: D_{it} of Nd oxynitrided samples at various temperatures (500°C, 700°C, 900°C, and 1100°C)

4.6 Comparison of Thermal Oxidation and Thermal Oxynitridation of Sputtered Nd Thin Film on Si Substrate

Upon completion of both thermal oxidation and thermal oxynitridation analysis in terms of physical, chemical, and electrical, the optimized parameters were determined and shown in Table 4.6. For both thermal oxidation and thermal oxynitridation, the optimized time and temperature were 15 min and 900°C, respectively.

Table 4.6: Optimized thermal oxidation and thermal oxynitridation parameter

Optimized parameter	**Thermal oxidation**	**Thermal oxynitridation**
Time (min)	15	15
Temperature (°C)	900	900

4.6.1 Physical and Chemical Properties

Table 4.7 shows a comparison of the physical and chemical properties of thermal oxidization and thermal oxynitridation at optimized parameter. Based on the XRD analysis, the main difference is in the number of peaks for $Nd_2Si_2O_7$. In addition, the crystallite size and microstrain of Nd_2O_3 remained constant. Meanwhile, for SiO_2, both crystallite size and microstrain decreased for thermal oxynitridation. This is an advantage, as SiO_2 is responsible for reducing the *k*-value. On the other hand, the crystallite size decreased and the microstrain increased for $Nd_2Si_2O_7$. During both FTIR and Raman analysis, the number of peaks for SiO_2 reduced for thermal oxynitridation. However, the number of peaks for Nd_2O_3 detected through Raman analysis for the thermal oxynitridation sample increased. Based on the HRTEM analysis, the oxide thickness decreased, while the interface layer thickness increased for thermal oxynitridation. Figure 4.78 shows a comparison of HRTEM analysis for thermal oxidation and thermal oxynitridation at optimum parameter. This revealed a denser oxide layer. It also showed that the oxidized sample exhibited anamorphous interface layer compared to the oxynitrided sample, which possessed a crystalline layer. Structural analysis revealed that nitrogen has a higher effect on the interface layer compared to the oxide layer.

Table 4.7: Comparison of the physical and chemical properties of thermal oxidization and thermal oxynitridation at optimum parameter

Characterization method	**Properties**	**Unit**	**Thermal oxidation**	**Thermal oxynitridation**
XRD	Plane of Nd_2O_3	-	(1 1 8), (2 5 7)	(1 1 8), (2 5 7)
	Plane of m-SiO_2	-	(2 2 6), $(9\ 1\ \bar{3})$, $(5\ 1\ \overline{13})$, (2 0 1)	(2 2 6), $(9\ 1\ \bar{3})$, $(5\ 1\ \overline{13})$, (2 0 1)
	Plane of h-SiO_2	-	(0 3 0), (1 0 4), (3 0 2)	0 3 0), (1 0 4), (3 0 2)
	Plane of t-SiO_2	-	(0 4 0)	(0 4 0)
	Plane of $Nd_2Si_2O_7$	-	(2 1 6), (3 1 3), (1 3 7), (1 6 0), (2 0 8)	(2 1 6), (3 1 3), (1 3 7), (0 6 2), (1 6 0), (3 2 5) (2 0 8)
	Crystallite size of Nd_2O_3	nm	0.9003	0.9003
	Crystallite size of SiO_2	nm	2.2363	1.5937
	Crystallite size of $Nd_2Si_2O_7$	nm	1.1651	0.9003
	Microstrain of Nd_2O_3	-	-0.0220	-0.0220
	Microstrain of SiO_2	-	0.0140	-0.0220
	Microstrain of $Nd_2Si_2O_7$	-	-0.0150	-0.0110

Table 4.7: *(continued)*Comparison of the physical and chemical properties of thermal oxidization and thermal oxynitridation at optimum parameter

Characterization method	**Properties**	**Unit**	**Thermal oxidation**	**Thermal oxynitridation**
FTIR	Number of Nd_2O_3 peaks	-	2	2
	Number of SiO_2 peaks	-	11	7
	Number of $Nd_2Si_2O_7$ peaks	-	1	1
Raman	Number of Nd_2O_3 peaks	-	3	6
	Number of SiO_2 peaks	-	2	1
	Number of $Nd_2Si_2O_7$ peaks	-	1	1
HRTEM	Thickness of oxide layer	nm	7.37	6.17
	Thickness of interface layer	nm	22.08	30.82
	Total thickness of thin film	nm	29.45	36.99

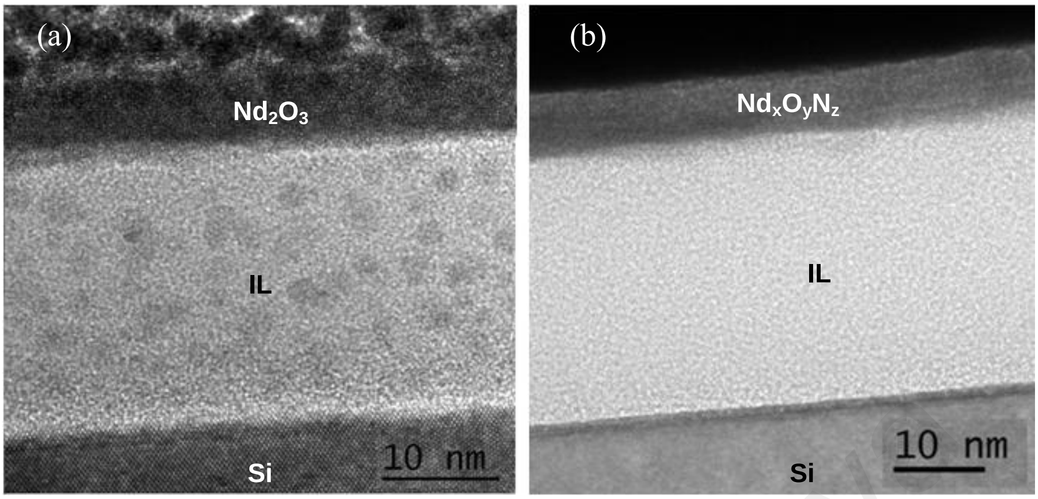

Figure 4.78: Comparison of HRTEM analysis at optimum parameter for (a) thermal oxidation (b) thermal oxynitridation

4.6.2 Electrical Properties

Table 4.8 shows the electrical properties of thermal oxidization and thermal oxynitridationat optimized parameter. Based on the J-E analysis, the thermal oxynitrided sample possessed higherbreakdown voltage and $Ø_B$, even though both samples had the same leakage value. Meanwhile, the thermal oxynitrided sample possessed lower capacitance and a higher STD value. However, it had higher *k*-value and lower Q_{eff} value. Thus, by considering both J-E and C-V analyses, thermal oxynitridation produces better electrical properties. This could be the result of nitrogen incorporation in the silicate interface layer improving the electrical properties rather than the oxide layer.

Table 4.8: Comparison of the electrical properties of thermal oxidization and thermal oxynitridation at optimum parameter

Characterization method	**Properties**	**Unit**	**Thermal oxidation**	**Thermal oxynitridation**
J-E	Breakdown voltage	MV/cm	5.260	5.721
	J	A/cm^2	10^{-6}	10^{-6}
	$Ø_B$	eV	2.91	2.94
C-V	C	pF	185	160
	k-value	-	7.03	7.43
	Q_{eff}	(10^{25}) cm^{-2}	0.8251	0.6594
	STD	(10^{24}) cm^{-2}	0.0839	0.4624
	D_{it}	eV^{-1}/cm^2	~ 10^{31}	~ 10^{31}

CHAPTER 5: CONCLUSION

5.1 Conclusion

The Nd-oxide and Nd-oxynitride were formed on Si substrate through thermal oxidation and thermal oxynitridation.The effect of thermal oxidation in an oxygen ambient at different oxidation duration and temperatures on physical and electrical properties was determined. In addition, the effect of thermal oxynitridationin an N_2O ambient at different oxynitridation duration and temperatures on physical and electrical properties were determined. The optimized parameter for both thermal oxidation and thermal oxynitridation were determined, and the properties were compared. The electrical properties were slightly improved with the incorporation of nitrogen. At the same time, the wear-resistant property of Nd-oxide film formed through different oxidation duration was investigated.Furthermore, a sketched model of the thermal oxidation and thermal oxynitridation at different durations were proposed to illustrate the formation of Nd-oxide and Nd-oxynitride.

5.1.1 Effects of Thermal Oxidation Durations and Temperatures on Sputtered Nd Thin Film on Si Substrate

Nd-oxide was successfully formed on Si substrate through thermal oxidation at different durations and temperatures. The sputtered Nd thin film on Si substrate was oxidized for different oxidation durations of 5 min, 10 min, 15 min, and 20 min at a constant temperature of 700°C. The Nd_2O_3 and interfacial layer consisting of SiO_2 and $Nd_2Si_2O_7$ were detected through XRD, FTIR, Raman, and HRTEM analyses. The sample oxidized for 15 min had the highest intensity for Nd_2O_3 and $Nd_2Si_2O_7$.HRTEM analysis also showed the presence of a single interfacial layer for the sample oxidized for 15 min and two distinct interfacial layers for the oxidation durations of 5 min, 10 min, and 20 min. Based on these findings, a sketched model was proposed. The sample oxidized for 15 min also had the lowest leakage value at ~10^{-6} A/cm^2, the highest barrier height of 1.97, the lowest slow trap density of 1.199 x 10^{24} cm^{-2}, the lowest effective oxide charges of 4.282 x 10^{25} cm^{-2}, and the lowest interface trap density.

On the other hand, the Nd thin film sputtered on Si substrate was successfully oxidized at different temperatures of 500°C, 700°C, 900°C, and 1100°C for a constant duration of 15 min to form Nd-oxide. The presence of Nd_2O_3 and an interfacial layer with SiO_2 and $Nd_2Si_2O_7$ was detected by the XRD, FTIR, Raman, HRTEM and EDX analyses. The broadening and shifting of this binding energy in FTIR showed the effect of temperature on these bonding. The sample oxidized at 700°C had the highest intensity for Nd_2O_3 and $Nd_2Si_2O_7$, as well as the highest crystallite size for SiO_2. HRTEM showed a thicker Nd-oxide and interfacial layer for the sample oxidized at 900°C compared to 700°C. The thickest thin film lead to the lowest leakage value of ~10^{-6} A/cm^2 at the highest breakdown voltage of 5.26 MV/cm and the highest barrier height of 2.91. In addition, this sample also had a higher *k*-value of 7.02. At the same time, it alsoexhibited the lowest effective oxide charges of 8.251 x 10^{24} cm^{-2} and the lowest interface trap density.

5.1.2 Effects of Thermal Oxynitridation Durations and Temperatures on Sputtered Nd Thin Film on Si Substrate

Thermal oxynitridation for different oxynitridation durations of 5 min, 10 min, 15 min, and 20 min at a constant temperature of700°C produced Nd-xoynitride on Nd thin film sputtered on Si. XRD, FTIR, Raman, and HRTEM analyses showed the presence of Nd-oxide and an interfacial layer of SiO_2 and $Nd_2Si_2O_7$. However, XPS analysis showed the presence of $Nd_xO_yN_z$ and $Nd_aSi_bO_cN_d$. The sample oxynitrided for 15 min had the highest interfacial compound intensities. The broadening and shifting in FTIR analysis are the least intense. Based on its electrical characterization, the sample oxynitrided for 15 min had the highest breakdown voltageat 3.91MV/cm with the lowest leakage value of ~10^{-6} A/cm^2, along with the highest barrier height of 2.66. Apart from that, the sample oxynitrided for 15 min also showed the lowest slow trap density of 3.084 x 10^{24} cm^{-2}, the lowest effective oxide charges of 5.979 x 10^{24} cm^{-2}, and the lowest interface trap density.

Besides that,Nd-oxynitride was successfully formed on the Nd sputtered Si substrate through thermal oxynitridation at different temperatures of 500°C, 700°C, 900°C, and 1100°C for a constant duration of 15 min. The presence of nitrogen was not detected through XRD, FTIR, Raman, and HRTEM. However, these analyses showed the presence of Nd_2O_3, along with SiO_2 and $Nd_2Si_2O_7$ as interfacial layers. The presence of $Nd_xO_yN_z$ and $Nd_aSi_bO_cN_d$ was confirmed through XPS analysis. The sample oxynitrided at 700°C had the highest intensity of interfacial compounds. However, the sample oxynitrided at 900°C exhibited the highest intensity for the oxide. All the samples, except the one oxynitrided at 500°C, had similar crystallite sizes and microstrains. In addition, the sample oxynitrided at 900°C had a thicker oxide and interfacial layer with a *k*-value of 7.43. Electrical characterization revealedthat the sample oxynitrided at 500°C had the lowest leakage ~10^{-7} A/cm^2, but also at the lowest breakdown voltage of 1.181 MV/cm. However, the sample oxynitrided at 900°C had the leakage value of ~10^{-6}A/cm^2 at the highest breakdown voltage of 5.721 MV/cm, the highest barrier height of 2.94, the lowest effective oxide charges of 6.594 x 10^{24} cm^{-2}, and the lowest interface trap density.

5.1.3 Comparison of Thermal Oxidation and Thermal Oxynitridation of Nd Sputtered Thin Film on Si Substrate

Based on the analysis, the optimized parameter for both thermal oxidation and thermal oxynitridation were 900°C and 15 min. The structural and electrical properties of these samples were compared. Both samples had the same leakage value, but the thermal oxynitrided sample had a higher breakdown voltage, higher barrier height, higher *k*-value, and the lowest effective oxide charges. This suggests that $Nd_xO_yN_z$ had better properties and can serve better as a replacement material for the existing SiO_2 compared to Nd_2O_3. This also proves that nitrogen reduces impurity penetration, which leads to the reduction of SiO_2 at the interface layer (J. C. Lee et al., 2003).

5.1.4 Wear-Resistant Property of Nd_2O_3 Formed Through Different Oxidation Durations

According to the scratch test analysis, all the thermal oxidation durations produced sample with scratch resistance upto 700 mN, whereby the critical load for these samples was more than 780 mN. In addition, the sample oxidized for 10 min had the highest critical load of 799 mN and the lowest scratch length of 70 µm. On the other hand, the sample oxidized for 15 min had the lowest critical load of 787 mN and the highest scratch length of 311 µm.

5.1.5 Establish Possible Mechanism Model for Oxidation and Oxynitridation

Based on the XRD, FTIR, Raman, HRTEM, and/or XPS physical and chemical analyses, the sketched model was proposed for different thermal oxidation and oxynitridation durations. For thermal oxidation, three-layerstacking was observed above

Si for the oxidation durations of 5 min, 10 min, and 20 min. Meanwhile, two-layer stacking was observed above Si for the sample oxidized for 15 min. On the other hand, thermal oxynitridation produced the sample with two-layer stacking above Si. Sintering effect due to thermal energy can be observed until the thermal oxidation and thermal oxynitridation duration of 5 min to 15 min. However, at 20 min, the sintering effect became less pronounce, as the amount of oxygen/nitrous oxide have increased.

5.2 Suggestion for Future Research

This research shows that Nd_2O_3 and $Nd_xO_yN_z$ have the potential to replace SiO_2. Based on this, the depth of understanding this material has to increase. The following ideas are proposed for future research:

i. The effect of thermal oxidation (durations and/or temperatures) and/or thermal oxynitridation (durations and/or temperatures) and duration on the physical, chemical, and electrical properties of Nd sputtered thin film on wide band gap substrate can be conducted for high power application;

ii. Thermal oxidized samples can undergo post-deposition annealing in nitrogen gas ambient to compare the physical, chemical, and electrical properties with $Nd_xO_yN_z$;

iii. The investigation of thermal oxynitridation can be further improved by studying the effects of different nitrous oxide concentration on the physical, chemical, and electrical properties of $Nd_xO_yN_z$;

iv. The wear-resistance property of thermal oxynitride samples should be investigated and compared with thermal oxidized samples; and

v. The reliability of Nd-oxide and Nd-oxynitride can be investigated by bias temperature instability (BTI) performance.

REFERENCES

Adamson, A. W. (1990). *Physical chemistry of surfaces*: Wiley.

Afanas' ev, V., Badylevich, M., Stesmans, A., Laha, A., Osten, H., Fissel, A., Schlom, D. (2008). Band offsets between Si and epitaxial rare earth sesquioxides (RE_2O_3, RE= La, Nd, Gd, Lu): Effect of 4f-shell occupancy. *Applied Physics Letters, 93*(19), 192105.

Aibin, H., & Qiuxia, X. (2009). Effects of silicon nitride diffusion barrier on germanium MOS capacitors with HfON gate dielectrics. *Journal of Semiconductors, 30*(10), 104002.

Ambriz-Vargas, F., Nouar, R., Kolhatkar, G., Sarkissian, A., Thomas, R., Gomez-Yáñez, Ruediger, A. (2017). RF-magnetron sputtering deposition of ultra-thin Hf0.5Zr$_0$.5O$_2$ films for non-volatile memory applications. *Materials Today: Proceedings, 4*(7, Part 1), 7000-7010.

Aydogan Gokturk, P., Salzner, U., Nyulászi, L., Ulgut, B., Kocabas, C., & Suzer, S. (2017). XPS-evidence for in-situ electrochemically-generated carbene formation. *Electrochimica Acta, 234*, 37-42.

Bugiel, E., Fissel, A., Czernohorsky, M., Laha, A., & Osten, H. J. (2007). Integration of Functional Epitaxial Oxides into Silicon: A TEM Investigation. *Microscopy and Microanalysis, 13*(S03), 304-305.

Bugiel, E., Osten, H. J., Fissel, A., Kirfel, O., & Czernohorsky, M. (2005). TEM investigations of epitaxial high-α dielectrics on silicon. In A. G. Cullis & J. L. Hutchison (Eds.), *Microscopy of Semiconducting Materials* (Vol. 107, pp. 343-346): Springer Berlin Heidelberg.

Busani, T., Devine, R., & Gonon, P. (2006). Structural Effects in the Dielectric Constant of Rare-Earth Oxides: Nd_2O_3. *ECS Transactions, 1*(5), 331-340.

Bushroa, A., Rahbari, R., Masjuki, H., & Muhamad, M. (2012). Approximation of crystallite size and microstrain via XRD line broadening analysis in TiSiN thin films. *Vacuum, 86*(8), 1107-1112.

Chew, C. C., Goh, K. H., Gorji, M. S., Tan, C. G., Ramesh, S., & Wong, Y. H. (2016). Breakdown field enhancement of Si-based MOS capacitor by post-deposition annealing of the reactive sputtered ZrOxNy gate oxide. *Applied Physics A, 122*(2), 66.

Chin, W. C., Cheong, K. Y., & Hassan, Z. (2010). Sm_2O_3 gate dielectric on Si substrate. *Materials Science in Semiconductor Processing, 13*(5), 303-314.

Chiu, F.-C., Lee, C.-Y., & Pan, T.-M. (2009). Current conduction mechanisms in Pr_2O_3/ oxynitride laminated gate dielectrics. *Journal of applied physics, 105*(7), 074103.

Chow, T. P., & Tyagi, R. (1993). *Wide bandgap compound semiconductors for superior high-voltage power devices.* Paper presented at the Power Semiconductor Devices and ICs, 1993. ISPSD'93., Proceedings of the 5th International Symposium on.

Cui, Y., Liu, H., Lin, Y., & Ma, Z. (2016). Metal phosphate-supported RuOx catalysts for N_2O decomposition. *Journal of the Taiwan Institute of Chemical Engineers, 67*, 254-262.

Dakhel, A. (2004a). Characterisation of Nd_2O_3 thick gate dielectric for silicon. *Physica status solidi CH, 201*(4), 745-755.

Dakhel, A. (2004b). Characterisation of Nd_2O3 thick gate dielectric for silicon. *Physica status solidi (a), 201*(4), 745-755.

Dakhel, A. (2004c). Electrical conduction processes in neodymium oxide thin films prepared on Si (1 0 0) substrates. *Journal of alloys and compounds, 376*(1), 38-42.

Dakhel, A. A. (2004). Mott-hopping processes in neodymium oxide thin films prepared on Si(100) substrates. *Crystal Research and Technology, 39*(5), 404-407.

Degraeve, R., Groeseneken, G., De Wolf, I., & Maes, H. (1995). Oxide and interface degradation and breakdown under medium and high field injection conditions: A correlation study. *Microelectronic Engineering, 28*(1-4), 313-316.

Demkov, A. A., & Navrotsky, A. (2006). *Materials Fundamentals of Gate Dielectrics*: Springer Netherlands.

Depla, D., Mahieu, S., & De Gryse, R. (2008). Depositing aluminium oxide: a case study of reactive magnetron sputtering *Reactive Sputter Deposition* (pp. 153-197): Springer.

DiMaria, D. (1999). Defect generation under substrate-hot-electron injection into ultrathin silicon dioxide layers. *Journal of Applied Physics, 86*(4), 2100-2109.

DiMaria, D., & Stasiak, J. (1989). Trap creation in silicon dioxide produced by hot electrons. *Journal of Applied Physics, 65*(6), 2342-2356.

Dumin, D. J. (2002). *Oxide Reliability: A Summary of Silicon Oxide Wearout, Breakdown, and Reliability*: World Scientific.

Escoubas, S., Brillet, H., Mesarotti, T., Raymond, G., Thomas, O., & Morin, P. (2008). Local strains induced in silicon channel by a periodic array of nitride capped poly lines investigated by high resolution X-ray diffraction. *Materials Science and Engineering: B, 154*, 129-132.

Fan, X., Liu, H., Fei, C., Zhong, B., Wang, X., & Wang, Q. (2015). Observation of Optical Properties of Neodymium Oxide with Spectroscopic Ellipsometry. *Journal of Electronic Materials, 44*(8), 2592.

Fan, X., Liu, H., & Zhang, X. (2014a). Identification of optimal ALD process conditions of Nd_2O_3 on Si by spectroscopic ellipsometry. *Applied Physics A, 114*(2), 545-550.

Fan, X., Liu, H., & Zhang, X. (2014b). Identification of optimal ALD process conditions of NdO on Si by spectroscopic ellipsometry. *Applied Physics A: Materials Science & Processing, 114*(2).

Fang, T.-H., Chang, W.-J., & Lin, C.-M. (2005). Nanoindentation and nanoscratch characteristics of Si and GaAs. *Microelectronic engineering, 77*(3), 389-398.

Fissel, A., Elassar, Z., Kirfel, O., Bugiel, E., Czernohorsky, M., & Osten, H. (2006). Interface formation during molecular beam epitaxial growth of neodymium oxide on silicon. *Journal of Applied Physics, 99*(7), 074105.

Fitzgerald, A. G., Storey, B. E., & Fabian, D. J. (1993). *Quantitative Microbeam Analysis*: Taylor & Francis.

Franchi, S. (2013). Chapter 1 - Molecular beam epitaxy: fundamentals, historical background and future prospects. In M. Henini (Ed.), *Molecular Beam Epitaxy* (pp. 1-46). Oxford: Elsevier.

Frohlich, K., Luptak, R., Dobrocka, E., Husekova, K., Cico, K., Rosova, A., Espinos, J. (2006). Characterization of rare earth oxides based MOSFET gate stacks prepared by metal-organic chemical vapour deposition. *Materials Science in Semiconductor Processing, 9*(6), 1065-1072.

Fromhold Jr, A., & Foster, W. (1976). An experimental investigation of the dielectric properties of thermally evaporated rare earth oxides for use in thin film capacitors. *Active and Passive Electronic Components, 3*(1), 51-62.

Fu, W.-E., Chang, Y.-Q., Chang, C.-W., Yao, C.-K., & Liao, J.-D. (2013). Mechanical properties of ultra-thin HfO_2 films studied by nano scratches tests. *Thin Solid Films, 529*, 402-406.

Ganesan, M., Dhananjeyan, M., Sarangapani, K., & Renganathan, N. (2008). Lithium ion conduction in sol–gel derived lithium samarium silicate solid electrolyte. *Journal of Alloys and Compounds, 450*(1), 452-456.

Gavartin, J., Shluger, A., Foster, A. S., & Bersuker, G. (2005). The role of nitrogen-related defects in high-k dielectric oxides: Density-functional studies. *Journal of applied physics, 97*(5), 053704.

Geetha, D., Joice Sophia, P., Radhika, R., & Arivuoli, D. (2017). Evaluation of nanoindentation and nanoscratch characteristics of GaN/InGaN epilayers. *Materials Science and Engineering: A, 683*(Supplement C), 64-69.

Geetha, D., Sophia, P. J., Radhika, R., & Arivuoli, D. (2017). Evaluation of nanoindentation and nanoscratch characteristics of GaN/InGaN epilayers. *Materials Science and Engineering: A, 683*, 64-69.

George, J. (1992). *Preparation of Thin Films*: Taylor & Francis.

George, S. M. (2009). Atomic layer deposition: an overview. *Chemical reviews, 110*(1), 111-131.

Gholizadeh, R., Yu, Y.-X., & Wang, Y. (2017). N_2O Adsorption and Decomposition over ZnO (0001) Doped Graphene: Density Functional Theory Calculations. *Applied Surface Science*.

Goh, K. H., Haseeb, A., & Wong, Y. H. (2016a). Physical and electrical properties of thermal oxidized Sm_2O_3 gate oxide thin film on Si substrate: Influence of oxidation durations. *Thin Solid Films, 606*, 80-86.

Goh, K. H., Haseeb, A., & Wong, Y. H. (2017a). Structural characteristics of samarium oxynitride on silicon substrate. *Journal of Alloys and Compounds, 722*, 729-739.

Goh, K. H., Haseeb, A. S. M. A., & Wong, Y. H. (2016b). Effect of Oxidation Temperature on Physical and Electrical Properties of Sm_2O_3 Thin-Film Gate Oxide on Si Substrate. *Journal of Electronic Materials, 45*(10), 5302-5312.

Goh, K. H., Haseeb, A. S. M. A., & Wong, Y. H. (2017b). Structural characteristics of samarium oxynitride on silicon substrate. *Journal of Alloys and Compounds, 722*(Supplement C), 729-739.

Gopalan, S., Dutta, S., Ramesh, S., & Prathapan, R. (2017). *Al_20_3 thin films on Silicon and Germanium substrates for CMOS and flash memory applications.* Paper presented at the AIP Conference Proceedings.

Grill, A., & Neumayer, D. A. (2003). Structure of low dielectric constant to extreme low dielectric constant SiCOH films: Fourier transform infrared spectroscopy characterization. *Journal of applied physics, 94*(10), 6697-6707.

Guo, Z., & Tan, L. (2009). *Fundamentals and applications of nanomaterials*: Artech House.

Han, D., Kang, J., Lin, C., & Han, R. (2003). Reliability characteristics of high-K gate dielectrics HfO_2 in metal-oxide semiconductor capacitors. *Microelectronic engineering, 66*(1), 643-647.

Hansen, P.-A., Fjellvåg, H., Finstad, T., & Nilsen, O. (2013). Structural and optical properties of lanthanide oxides grown by atomic layer deposition (Ln= Pr, Nd, Sm, Eu, Tb, Dy, Ho, Er, Tm, Yb). *Dalton Transactions, 42*(30), 10778-10785.

Hardy, A., Van Elshocht, S., D'Haen, J., Douhéret, O., De Gendt, S., Adelmann, C., Bender, H. (2007). Aqueous chemical solution deposition of ultrathin lanthanide oxide dielectric films. *Journal of materials research, 22*(12), 3484-3493.

Havey, K., Zabinski, J., & Walck, S. (1997). The chemistry, structure, and resulting wear properties of magnetron-sputtered NbN thin films. *Thin Solid Films, 303*(1-2), 238-245.

Herman, M. A., & Sitter, H. (2012). *Molecular beam epitaxy: fundamentals and current status* (Vol. 7): Springer Science & Business Media.

Houssa, M., Pantisano, L., Ragnarsson, L.-Å., Degraeve, R., Schram, T., Pourtois, G., Heyns, M. (2006). Electrical properties of high-κ gate dielectrics: Challenges, current issues, and possible solutions. *Materials Science and Engineering: R: Reports, 51*(4), 37-85.

Hsieh, L.-Z., Ko, H.-H., Kuei, P.-Y., & Lee, C.-Y. (2006). Growth evolution of ZrO_2 from deposited Zr metal during thermal oxidation. *Japanese journal of applied physics, 45*(10R), 7680.

Iping, S., Kouichiro, O., Kazunari, K., Kouichi, M., Daisuke, Y., Giichiro, U., Naho, I. (2013). Effects of Nitrogen on Crystal Growth of Sputter-Deposited ZnO Films for Transparent Conducting Oxide. *Japanese Journal of Applied Physics, 52*(11S), 11NB03.

Ishikawa, D., Kamiyama, S., Kurosawa, E., Aoyama, T., & Nara, Y. (2009). Extended Scalability of HfON/SiON Gate Stack Down to 0.57 nm Equivalent Oxide Thickness with High Carrier Mobility by Post-Deposition Annealing. *Japanese Journal of Applied Physics, 48*(4S), 04C004.

Jayanti, S., Yang, X., Lichtenwalner, D. J., & Misra, V. (2010a). Technique to improve performance of Al_2O_3 interpoly dielectric using a La_2O_3 interface scavenging layer for floating gate memory structures. *Applied Physics Letters, 96*(9), 092905.

Jayanti, S., Yang, X., Lichtenwalner, D. J., & Misra, V. (2010b). Technique to improve performance of Al_2O_3 interpoly dielectric using a La_2O_3 interface scavenging layer for floating gate memory structures. *Applied Physics Letters, 96*, 092905.

Jeon, S., Im, K., Yang, H., Lee, H., Sim, H., Choi, S., Hwang, H. (2001). *Excellent electrical characteristics of lanthanide (Pr, Nd, Sm, Gd, and Dy) oxide and lanthanide-doped oxide for MOS gate dielectric applications.* Paper presented at the Electron Devices Meeting, 2001. IEDM'01. Technical Digest. International.

Jian, S.-R., Teng, I.-J., Yang, P.-F., Lai, Y.-S., Lu, J.-M., Chang, J.-G., & Ju, S.-P. (2008). Surface morphological and nanomechanical properties of PLD-derived ZnO thin films. *Nanoscale Research Letters, 3*(5), 186.

Jiang, S., Liu, J., Lin, C., Li, X., & Li, Y. (2013). High-pressure x-ray diffraction and Raman spectroscopy of phase transitions in Sm_2O_3. *Journal of Applied Physics, 113*(11), 113502.

Jin, P., He, G., Fang, Z. B., Liu, M., Xiao, D. Q., Gao, J., Zhang, M. (2017). Annealing-temperature-modulated optical, electrical properties, and leakage current transport mechanism of sol–gel-processed high-k HfAlOx gate dielectrics. *Ceramics International, 43*(3), 3101-3106.

Jinxing, W., Laha, A., Fissel, A., Schwendt, D., Dargis, R., Watahiki, T., Osten, H. J. (2009, 5-8 Jan. 2009). *Structural and strain relaxation study of epitaxially grown nano-thick Nd<inf>2</inf>O<inf>3</inf>/Si(111) heterostructure.* Paper presented at the Nano/Micro Engineered and Molecular Systems, 2009. NEMS 2009. 4th IEEE International Conference on.

Jones, A. C., Aspinall, H. C., Chalker, P. R., Potter, R. J., Kukli, K., Rahtu, A., Leskelä, M. (2004). Some recent developments in the MOCVD and ALD of high-κ dielectric oxides. *Journal of Materials Chemistry, 14*(21), 3101-3112.

Jones, A. C., Aspinall, H. C., Chalker, P. R., Potter, R. J., Kukli, K., Rahtu, A., Leskelä, M. (2005). Recent developments in the MOCVD and ALD of rare earth oxides and silicates. *Materials Science and Engineering: B, 118*(1), 97-104.

Kääriäinen, T., Cameron, D., Kääriäinen, M.-L., & Sherman, A. (2013). *Atomic layer deposition: principles, characteristics, and nanotechnology applications*: John Wiley & Sons.

Kakushima, K., Tsutsui, K., Ohmi, S.-I., Ahmet, P., Rao, V. R., & Iwai, H. (2007). Rare earth oxides in microelectronics *Rare earth oxide thin films* (pp. 345-365): Springer.

Kang, S. J. L. (2004). *Sintering: Densification, Grain Growth and Microstructure*: Elsevier Science.

Kano, K. (1998). *Semiconductor Devices*: Prentice Hall.

Kao, C.H., Chan, T., Chen, K. S., Chung, Y.-T., & Luo, W.-S. (2010). Physical and electrical characteristics of the high-k Nd_2O_3 polyoxide deposited on polycrystalline silicon. *Microelectronics Reliability, 50*(5), 709-712.

Kao, C. H., Chen, H., Liao, Y.-C., Deng, J. Z., Chu, Y. C., Chen, Y. T., & Chang, H. W. (2014). Comparison of high-κ Nd_2O_3 and $NdTiO_3$ dielectrics deposited on polycrystalline silicon substrates. *Thin Solid Films, 570*, 412-416.

Kim, H., Marshall, A., McIntyre, P. C., & Saraswat, K. C. (2004). Crystallization kinetics and microstructure-dependent leakage current behavior of ultrathin HfO_2 dielectrics: In situ annealing studies. *Applied Physics Letters, 84*(12), 2064-2066.

Kim, J., Kim, D. C., & Kim, Y.-W. (2017). Characteristics of silicon oxynitride films grown by using neutral-beams and inductively coupled plasma. *Thin Solid Films, 642*, 281-284.

Klein, N. (1966). The mechanism of self-healing electrical breakdown in MOS structures. *IEEE Transactions on Electron Devices, 13*(11), 788-805.

Klein, N. (1971). Switching and breakdown in films. *Thin Solid Films, 7*(3-4), 149-177.

Koike, M., Ino, T., Kamimuta, Y., Koyama, M., Kamata, Y., Suzuki, M., Tsunashima, Y. (2003). *Effect of Hf-N bond on properties of thermally stable amorphous HfSiON and applicability of this material to sub-50nm technology node LSIs.* Paper presented at the Electron Devices Meeting, 2003. IEDM'03 Technical Digest. IEEE International.

Kosola, A., Päiväsaari, J., Putkonen, M., & Niinistö, L. (2005). Neodymium oxide and neodymium aluminate thin films by atomic layer deposition. *Thin Solid Films, 479*(1), 152-159.

Kuboňová, L., Peikertová, P., Kutláková, K. M., Jirátová, K., Słowik, G., Obalová, L., & Cool, P. (2017). Catalytic activity of cobalt grafted on ordered mesoporous silica materials in N_2O decomposition and CO oxidation. *Molecular Catalysis, 437*, 57-72.

Kumar, A. (2012). Leakage current controlling mechanism using high k dielectric + metal gate. *International Journal of Information Technology and Knowledge Management*, 191-194.

Kurniawan, T., Cheong, K., Razak, K., Lockman, Z., & Ahmad, N. (2011a). Oxidation of sputtered Zr thin film on Si substrate. *Journal of Materials Science: Materials in Electronics, 22*(2), 143-150.

Kurniawan, T., Cheong, K. Y., Razak, K. A., Lockman, Z., & Ahmad, N. (2011b). Oxidation of sputtered Zr thin film on Si substrate. *Journal of Materials Science: Materials in Electronics, 22*(2), 143-150.

Kurniawan, T., Wong, Y. H., Cheong, K. Y., Moon, J. H., Bahng, W., Razak, K. A., Kim, N.-K. (2011). Effects of post-oxidation annealing temperature on ZrO_2 thin film deposited on 4H-SiC substrate. *Materials Science in Semiconductor Processing, 14*(1), 13-17.

Laha, A., Fissel, A., Bugiel, E., & Osten, H. (2007a). Epitaxial multi-component rare earth oxide for high-K application. *Thin Solid Films, 515*(16), 6512-6517.

Laha, A., Fissel, A., Bugiel, E., & Osten, H. J. (2007b). Epitaxial multi-component rare earth oxide for high-K application. *Thin Solid Films, 515*(16), 6512-6517.

Laha, A., Fissel, A., & Osten, H. (2013). Effective control on flat band voltage of epitaxial lanthanide oxide based metal oxide semiconductor capacitors by interfacial carbon. *Applied Physics Letters, 102*(20), 202902.

Larkin, P. (2011). *Infrared and Raman Spectroscopy: Principles and Spectral Interpretation*: Elsevier Science.

Lee, B. H., Kang, L., Nieh, R., Qi, W.-J., & Lee, J. C. (2000). Thermal stability and electrical characteristics of ultrathin hafnium oxide gate dielectric reoxidized with rapid thermal annealing. *Applied Physics Letters, 76*(14), 1926-1928.

Lee, B. H., Oh, J., Tseng, H. H., Jammy, R., & Huff, H. (2006). Gate stack technology for nanoscale devices. *materials today, 9*(6), 32-40.

Lee, J. C., Cho, H., Kang, C., Rhee, S., Kim, Y., Choi, R., Abkar, M. (2003). *High-k dielectrics and MOSFET characteristics.* Paper presented at the Electron Devices Meeting, 2003. IEDM'03 Technical Digest. IEEE International.

Lincot, D., & Hodes, G. (2006). *Chemical Solution Deposition of Semiconducting and Non-Metallic Films: Proceedings of the International Symposium*.

Lippincott, E. R., Van Valkenburg, A., Weir, C. E., & Bunting, E. N. (1958). Infrared studies on polymorphs of silicon dioxide and germanium dioxide. *Journal of Research of the National Bureau of Standards, 61*(1), 61.

Liu, Y., Shim, S. I., Wang, X. W., Lee, L.-S., Tsai, M.-J., & Ma, T. P. (2008). High-quality high-k HfON formed with plasma jet assisted PVD process and application as tunnel dielectric for flash memories. *Microelectronic Engineering, 85*(1), 45-48.

Lucovsky, G. (2005). Electronic Structure and Chemical Bonding in High-k Transition Metal and Lanthanide Series Rare Earth Alternative Gate Dielectrics: Applications to Direct Tunneling and Defects at Dielectric Interfaces *Materials Fundamentals of Gate Dielectrics* (pp. 109-177): Springer.

Lucovsky, G., & Rayner, G. (2000). Microscopic model for enhanced dielectric constants in low concentration SiO_2-rich noncrystalline Zr and Hf silicate alloys. *Applied Physics Letters, 77*(18), 2912-2914.

Lupták, R., Fröhlich, K., Rosová, A., Hušeková, K., Ťapajna, M., Machajdík, D., Mansilla, C. (2005). Growth of gadolinium oxide films for advanced MOS structure. *Microelectronic Engineering, 80*, 154-157.

Malinovsky, V. K., Novikov, V. N., Surovtsev, N. V., & Shebanin, A. P. Investigation of amorphous states of SiO_2 by Raman scattering spectroscopy. *Physics of the Solid State, 42*(1), 65-71.

May, G. S., & Spanos, C. J. (2006). *Fundamentals of Semiconductor Manufacturing and Process Control*: Wiley.

Murphy, D. B., & Davidson, M. W. (2012). *Fundamentals of Light Microscopy and Electronic Imaging*: Wiley.

Nagai, T., Kitawaki, S.-I., & Sato, N. (2013). Low Temperature Chlorination of by Mechanochemical Method. *Materials Sciences and Applications*, 419-431.

Neamen, D. A. (2003). *Semiconductor Physics and Devices: Basic Principles*: McGraw-Hill.

Nyquist, R. A., & Kagel, R. O. (2012). *Handbook of infrared and raman spectra of inorganic compounds and organic salts: infrared spectra of inorganic compounds* (Vol. 4): Academic press.

Oniki, Y., Iwazaki, Y., Hasumi, M., Ueno, T., & Kuroiwa, K. (2008). Fabrication of High-k/Si Structure Using Metal Deposition Followed by Oxidation. *ECS Transactions, 16*(5), 139-145.

Osburn, C., & Ormond, D. (1974). SodiumInduced BarrierHeight Lowering and Dielectric Breakdown on SiO_2 Films on Silicon. *Journal of The Electrochemical Society, 121*(9), 1195-1198.

Osten, H. J., Bugiel, E., Czernohorsky, M., Elassar, Z., Kirfel, O., & Fissel, A. (2007). Molecular beam epitaxy of rare-earth oxides *Rare earth oxide thin films* (pp. 101-114): Springer.

Osten, H. J., Bugiel, E., Kirfel, O., Czernohorsky, M., & Fissel, A. (2005). MBE growth and properties of epitaxial metal oxides for high-κ dielectrics. *Journal of crystal growth, 278*(1), 18-24.

Päiväsaari, J., Putkonen, M., & Niinistö, L. (2005). A comparative study on lanthanide oxide thin films grown by atomic layer deposition. *Thin Solid Films, 472*(1), 275-281.

Pan, T.-M., Lee, J.-D., Shu, W.-H., & Chen, T.-T. (2006a). Structural and electrical properties of neodymium oxide high-k gate dielectrics. *Applied physics letters, 89*(23), 2908.

Pan, T.-M., Lee, J.-D., Shu, W.-H., & Chen, T.-T. (2006b). Structural and electrical properties of neodymium oxide high-k gate dielectrics. *Applied Physics Letters, 89*(23), 232908.

Pan, T.-M., Lee, J.-D., & Yeh, W.-W. (2007). Influence of oxygen content on the structural and electrical characteristics of thin neodymium oxide gate dielectrics. *Journal of Applied Physics, 101*(2), 024110.

Pan, T.-M., Lin, C.-W., Lin, J.-C., Su, S.-H., Kuo, H.-M., & Chien, Y.-K. (2009). *Influence of oxygen content on the structural and pH-sensitive properties of thin* Nd_2O_3 *electrolyte-insulator-semiconductor.* Paper presented at the Sensors, 2009 IEEE.

Pan, T.-M., & Lin, J.-C. (2009). Effects of Post-Deposition Annealing and Oxygen Content on the Structural and pH-Sensitive Properties of Thin NdO Films. *Sensors Journal, IEEE, 9*(10), 1173-1180.

Pan, T.-M., & Yu, T.-Y. (2009). Comparison of the structural properties and electrical characteristics of Pr_2O_3, Nd_2O_3 and Er_2O_3 charge trapping layer memories. *Semiconductor Science and Technology, 24*(9), 095022.

Pierret, R. F. (1990). *Field Effect Devices*: Addison-Wesley Publishing Company.

Pierson, H. O. (1999). *Handbook of chemical vapor deposition: principles, technology and applications*: William Andrew.

Pisecny, P., Husekova, K., Frohlich, K., Harmatha, L., Soltys, J., Machajdik, D., Jakabovic, J. (2004). Growth of lanthanum oxide films for application as a gate dielectric in CMOS technology. *Materials Science in Semiconductor Processing, 7*(4), 231-236.

Prabhu, Y. T., Rao, K. V., Kumar, V. S. S., & Kumari, B. S. (2014). X-ray analysis by Williamson-Hall and size-strain plot methods of ZnO nanoparticles with fuel variation. *World Journal of Nano Science and Engineering, 4*(01), 21.

Rahmawati, E., Ekawita, R., Budiman, M., Abdullah, M., & Khairurrijal, K. (2012). A Low Cost C8051F006 SoC-Based Quasi-Static CV Meter for Characterizing Semiconductor Devices. *TELKOMNIKA (Telecommunication Computing Electronics and Control), 10*(4), 733-740.

Rathee, D., Kumar, M., & Arya, S. K. (2010). CMOS Development optimization, scaling issue and replacement with high-k material for future microelectronics. *International Journal of Computer Application, 8*(5), 10.

Rodriguez, J. A., & Fernández-García, M. (2007). *Synthesis, Properties, and Applications of Oxide Nanomaterials*: Wiley.

Salmani-Jelodar, M., Ilatikhameneh, H., Kim, S., Ng, K., & Klimeck, G. (2015). Optimum high-k oxide for the best performance of ultra-scaled double-gate MOSFETs. *arXiv preprint arXiv:1502.06178*.

Sano, T., & Ohmi, S.-i. (2011). In situ formation of HfN/HfSiON gate stacks with 0.5 nm equivalent oxide thickness utilizing electron cyclotron resonance plasma sputtering on three-dimensional Si structures. *Japanese journal of applied physics, 50*(4S), 04DA09.

Sarma, R., Saikia, D., Saikia, P., Saikia, P., & Baishya, B. (2010). Pentacene based thin film transistors with high-k dielectric Nd_2O_3 as a gate insulator. *Brazilian Journal of Physics, 40*(3), 357-360.

Scarel, G., Svane, A., & Fanciulli, M. (2007). Scientific and Technological Issues Related to Rare Earth Oxides: An Introduction. In M. Fanciulli & G. Scarel (Eds.), *Rare Earth Oxide Thin Films* (pp. 1-14). Berlin, Heidelberg: Springer Berlin Heidelberg.

Schlom, D. G., Chen, L. Q., Pan, X., Schmehl, A., & Zurbuchen, M. A. (2008). A thin film approach to engineering functionality into oxides. *Journal of the American Ceramic Society, 91*(8), 2429-2454.

Schmitt, J., & Flemming, H.-C. (1998). FTIR-spectroscopy in microbial and material analysis. *International Biodeterioration & Biodegradation, 41*(1), 1-11.

Schroder, D. K. (1987). *Advanced MOS devices*: Addison-Wesley Longman Publishing Co., Inc.

Schroder, D. K. (2006). *Semiconductor Material and Device Characterization*: Wiley.

Schwartz, R. W., Schneller, T., & Waser, R. (2004). Chemical solution deposition of electronic oxide films. *Comptes Rendus Chimie, 7*(5), 433-461.

Shatzkes, M., Av- Ron, M., & Anderson, R. (1974). On the nature of conduction and switching in SiO_2. *Journal of Applied Physics, 45*(5), 2065-2077.

Shi, Y., Ma, T., Prasad, S., & Dhanda, S. (1998). Polarity-dependent tunneling current and oxide breakdown in dual-gate CMOSFETs. *IEEE Electron Device Letters, 19*(10), 391-393.

Shima, A., & Ryuzaki, D. (2007). ULSI devices: current status and future prospects of research and development. *Hitachi Review, 56*(3), 25.

Signore, M., Rizzo, A., Mirenghi, L., Tagliente, M., & Cappello, A. (2007). Characterization of zirconium oxynitride films obtained by radio frequency magnetron reactive sputtering. *Thin Solid Films, 515*(17), 6798-6804.

Signore, M. A., Rizzo, A., Tapfer, L., Piscopiello, E., Capodieci, L., & Cappello, A. (2010). Effect of the substrate temperature on zirconium oxynitride thin films deposited by water vapour–nitrogen radiofrequency magnetron sputtering. *Thin Solid Films, 518*(8), 1943-1946.

Smith, B. C. (1995). *Fundamentals of Fourier Transform Infrared Spectroscopy*: Taylor & Francis.

Smith, B. C. (1998). *Infrared Spectral Interpretation: A Systematic Approach*: Taylor & Francis.

Song, M.-K., & Rhee, S.-W. (2005a). Direct liquid injection metal organic chemical vapor deposition of Nd_2O_3 thin films using Tris(2,2,6,6-tetramethyl-3,5-heptanedionato) neodymium. *Thin Solid Films, 492*(1–2), 19-23.

Song, M.-K., & Rhee, S.-W. (2005b). Direct liquid injection metal organic chemical vapor deposition of Nd_2O_3 thin films using Tris (2, 2, 6, 6-tetramethyl-3, 5-heptanedionato) neodymium. *Thin Solid Films, 492*(1), 19-23.

Strong, A. W., Wu, E. Y., Vollertsen, R. P., Sune, J., Rosa, G. L., Sullivan, T. D., & Rauch, S. E. (2009). *Reliability Wearout Mechanisms in Advanced CMOS Technologies*: Wiley.

Suehle, J. S. (2002). Ultrathin gate oxide reliability: Physical models, statistics, and characterization. *IEEE Transactions on Electron Devices, 49*(6), 958-971.

Sun, Q.-Q., Laha, A., Ding, S.-J., Zhang, D. W., Osten, H. J., & Fissel, A. (2008a). Observation of near interface oxide traps in single crystalline Nd_2O_3 on Si (111) by quasistatic CV method. *Applied Physics Letters, 93*(8), 83509.

Sun, Q.-Q., Laha, A., Ding, S.-J., Zhang, D. W., Osten, H. J., & Fissel, A. (2008b). Observation of near interface oxide traps in single crystalline Nd_2O_3 on Si (111) by quasistatic C-V method. *Applied physics letters, 93*(8), 083509.

Sze, S. M. (2001). *Semiconductor Devices: Physics and Technology*: Wiley.

Tahir, D., Lee, E. K., Oh, S. K., Tham, T. T., Kang, H. J., Jin, H., Lee, J. C. (2009). Band alignment of atomic layer deposited (ZrO_2) x (SiO_2) 1− x gate dielectrics on Si (100). *Applied Physics Letters, 94*(21), 212902.

Tao, J., Xu, M., Li, C., & Zhu, X. (2012). Influence of plastic deformation on evolution of defect structures, microhardness and electrical conductivity of copper. *Materials Technology, 27*(1), 82-84.

Tasaki, Y., Satoh, M., Yoshizawa, S., Kataoka, H., & Hidaka, H. (1997). New liquid precursors of yttrium and neodymium for metalorganic chemical vapor deposition. *Japanese journal of applied physics, 36*(11R), 6871.

Terasawa, N., Akimoto, K., Mizuno, Y., Ichimiya, A., Sumitani, K., Takahashi, T., Nabatame, T. (2005). Crystallization process of high-k gate dielectrics studied by surface X-ray diffraction. *Applied surface science, 244*(1), 16-20.

Tong, K. Y., Jelenkovic, E. V., Liu, W., & Dai, J. Y. (2006). Nitridation of hafnium oxide by reactive sputtering. *Microelectronic Engineering, 83*(2), 293-297.

Török, P., & Kao, F. J. (2013). *Optical Imaging and Microscopy: Techniques and Advanced Systems*: Springer Berlin Heidelberg.

Tseng, H.-H. (2010). The Progress and Challenges of Applying High-k/Metal-Gated Devices to Advanced CMOS Technologies. *Solid State Circuits Technologies, edited by Jacobus W. Swart*.

Tummula, R., Rymaszewski, E., & Klopfenstein, A. G. (1997). Microelectronics Packaging Handbook-Semiconductor Packaging. *Part II, 407*.

Ubaldini, A., & Carnasciali, M. M. (2008). Raman characterisation of powder of cubic RE_2O_3 (RE= Nd, Gd, Dy, Tm, and Lu), Sc_2O_3 and Y_2O_3. *Journal of Alloys and Compounds, 454*(1), 374-378.

Umeda, K., Tomita, T., & Taniguchi, K. (1997). Silicon dioxide breakdown induced by SHE (substrate hot electron) injection. *Electronics and Communications in Japan (Part II: Electronics), 80*(8), 11-19.

van der Heide, P. (2011). *X-ray Photoelectron Spectroscopy: An introduction to Principles and Practices*: Wiley.

Vaz, F., Martin, N., & Fenker, M. (2013). *Metallic Oxynitride Thin Films by Reactive Sputtering and Related Deposition Methods: Processes, Properties and Applications*: Bentham Science Publishers.

Venkateswarlu, K., Bose, A. C., & Rameshbabu, N. (2010). X-ray peak broadening studies of nanocrystalline hydroxyapatite by Williamson–Hall analysis. *Physica B: Condensed Matter, 405*(20), 4256-4261.

Viana, C. E., da Silva, A. N. R., & Morimoto, N. I. (2001). Analysis of SiO_2 thin films deposited by PECVD using an oxygen-TEOS-argon mixture. *Brazillian Journal of Physics, 31*, 299-303.

Vogel, E. M., Suehle, J. S., Edelstein, M. D., Wang, B., Chen, Y., & Bernstein, J. B. (2000). Reliability of ultrathin silicon dioxide under combined substrate hot-electron and constant voltage tunneling stress. *IEEE Transactions on Electron Devices, 47*(6), 1183-1191.

Walrafen, G. E., & Stone, J. (1975). Raman Spectral Characterization of Pure and Doped Fused Silica Optical Fibers. *Applied Spectroscopy, 29*(4), 337-344.

Wang, J., Laha, A., Fissel, A., Schwendt, D., Dargis, R., Watahiki, T., Osten, H. J. (2009). *Structural and strain relaxation study of epitaxially grown nano-thick Nd_2O_3/Si (111) heterostructure.* Paper presented at the NEMS.

Watanabe, H., Kamiyama, S., Umezawa, N., Shiraishi, K., Yoshida, S., Watanabe, Y., Yasutake, K. (2005). Role of nitrogen incorporation into Hf-based high-k gate dielectrics for termination of local current leakage paths. *Japanese journal of applied physics, 44*(10L), L1333.

Wilk, G. D., Wallace, R. M., & Anthony, J. (2001). High-κ gate dielectrics: Current status and materials properties considerations. *Journal of applied physics, 89*(10), 5243-5275.

Wong, Y. H., Atuchin, V. V., Kruchinin, V. N., & Cheong, K. Y. (2014). Physical and dispersive optical characteristics of ZrON/Si thin-film system. *Applied Physics A, 115*(3), 1069-1072.

Wong, Y. H., & Cheong, K. Y. (2010). ZrO_2 thin films on Si substrate. *Journal of Materials Science: Materials in Electronics, 21*(10), 980-993.

Wong, Y. H., & Cheong, K. Y. (2011a). Thermal oxidation and nitridation of sputtered Zr thin film on Si via N_2O gas. *Journal of Alloys and Compounds, 509*(35), 8728-8737.

Wong, Y. H., & Cheong, K. Y. (2011b). Thermal oxidation and nitridation of sputtered Zr thin film on Si via N_2O gas. *Journal of Alloys and Compounds, 509*(35), 8728-8737.

Wong, Y. H., & Cheong, K. Y. (2012a). Effects of oxidation and nitridation temperatures on electrical properties of sputtered Zr thin film based on Si in N_2O ambient. *Electronic Materials Letters, 8*(1), 47-51.

Wong, Y. H., & Cheong, K. Y. (2012b). Formation of Zr-oxynitride thin films on 4H-SiC substrate. *Thin Solid Films, 520*(22), 6822-6829.

Wong, Y. H., & Cheong, K. Y. (2012c). Properties of thermally oxidized and nitrided Zr-oxynitride thin film on 4H–SiC in diluted N_2O ambient. *Materials Chemistry and Physics, 136*(2), 624-637.

Wu, E. Y., Abadeer, W., Han, L.-K., Lo, S.-H., & Hueckel, G. R. (1999). *Challenges for accurate reliability projections in the ultra-thin oxide regime.* Paper presented at the Reliability Physics Symposium Proceedings, 1999. 37th Annual. 1999 IEEE International.

Wu, L., Qin, W., Hu, X., Ju, S., Dong, C., & Yang, Y. (2015). Decomposition and reduction of N_2O on CaS (100) surface: A theoretical account. *Surface Science, 632*, 83-87.

Xu, G., & Xu, Q. (2008). *Thermal stability of HfON, HfSiON and HfTaON gate dielectrics.* Paper presented at the Solid-State and Integrated-Circuit Technology, 2008. ICSICT 2008. 9th International Conference on.

Yacobi, B. G. (2003). *Semiconductor Materials: An Introduction to Basic Principles*: Springer US.

Yacobi, B. G. (2006). *Semiconductor Materials: An Introduction to Basic Principles*: Springer US.

Yang, C.-W., Fang, Y.-K., Chen, C., Chen, S., Lin, C., Lin, C., Yao, L.-G. (2003). Effect of polycrystalline-silicon gate types on the opposite flatband voltage shift in n-type and p-type metal-oxide-semiconductor field-effect transistors for high-k-HfO_2 dielectric. *Applied Physics Letters, 83*(2), 308-310.

Yau, W.-H., Tseng, P.-C., & Lian, D. (2011). Nanoscratch study of ZnO thin films deposited using radio frequency magnetron sputtering. *Nuclear Instruments and Methods in Physics Research Section B: Beam Interactions with Materials and Atoms, 269*(12), 1450-1454.

Yeo, Y.-C., King, T.-J., & Hu, C. (2003). MOSFET gate leakage modeling and selection guide for alternative gate dielectrics based on leakage considerations. *IEEE Transactions on Electron Devices, 50*(4), 1027-1035.

Yeo, Y.-C., Lu, Q., & Hu, C. (2001). MOSFET gate oxide reliability: Anode hole injection model and its applications. *International Journal of High Speed Electronics and Systems, 11*(03), 849-886.

Zaumseil, P., & Schroeder, T. (2005). A complex x-ray characterization of epitaxially grown high-K gate dielectrics. *Journal of physics D: Applied Physics, 38*(10A), A179.

Zeman, M., Fulton, C., Lucovsky, G., Nemanich, R., & Yang, W.-C. (2006). Thermal stability of TiO_2, ZrO_2, or HfO_2 on Si (100) by photoelectron emission microscopy. *Journal of applied physics, 99*(2), 023519.

Zeng, H., Wu, Y., Zhang, J., Kuang, C., Yue, M., & Zhou, S. (2013). Grain size-dependent electrical resistivity of bulk nanocrystalline Gd metals. *Progress in Natural Science: Materials International, 23*(1), 18-22.

Zhang, S., Sun, D., Fu, Y., & Du, H. (2005). Toughness measurement of thin films: a critical review. *Surface and Coatings Technology, 198*(1), 74-84.

Zhao, C., Zhao, C., Werner, M., Taylor, S., & Chalker, P. (2012). Advanced CMOS gate stack: Present research progress. *ISRN Nanotechnology, 2012*.

LIST OF PUBLICATIONS AND PAPERS PRESENTED

Hetherin, K., Ramesh, S., & Wong, Y. H. (2017a). Effects of thermal oxidation duration on the structural and electrical properties of Nd_2O_3/Si system. *Applied Physics A, 123*(8), 510. (Published)

Hetherin, K., Ramesh, S., & Wong, Y. H. (2017b). Formation of neodymium oxide by thermal oxidation of sputtered Nd thin film on Si substrate. *Journal of Materials Science: Materials in Electronics, 28*(16), 11994-12003. (Published)

Hetherin, K., Ramesh, S., & Wong, Y. H., *Influence of Thermal Oxidation Duration on Physical, Chemical and Electrical Properties of* Nd_2O_3 *on Si Substrate,* Advances in Material and Processing Technologies Conference, Kuala Lumpur, Malaysia, 8-11 Nov 2015. (Attended)